Dissertation

Submitted to the
Combined Faculty of Natural Sciences and Mathematics
Heidelberg University, Germany
for the degree of
Doctor of Natural Sciences

Put forward by
M.Sc. Thomas Krengel
Born in Esslingen am Neckar

Oral examination: 21.02.2020

550,000 years of marine climate variability in the western Mediterranean Sea revealed by cold-water corals

Referees:

Prof. Dr. Norbert Frank

Prof. Dr. Oliver Friedrich

550.000 years of marine climate variability in the western Mediterranean Sea revealed by cold-water corals

Cold-water corals (CWC) are common throughout the Alboran Sea (AS; western Mediterranean Sea), however large coral mound provinces have only been discovered along the Moroccan margin. During research cruise MSM36 "MoccoMeBo", the Bremen drill rig MeBo successfully drilled 70 m long coral bearing cores, including the cores from the East Melilla Coral Province (EMCP) presented here. Using the high precision U-series dating method, the two cores presented here provided a unique insight into the mound evolution over 550 ka. For the second time ever, a CWC mound has been fully penetrated and thus the timing of the onset of coral growth in this location could be determined. The other mound, potentially drilled to only half its height (70 m), may provide a first estimate of the basin-wide onset of coral growth in the AS. However, the discontinuous temporal evolution of both mounds revealed unprecedented complex age-depth profiles and thus two different mound evolution models over several full glacial-interglacial cycles are proposed. The predominantly interglacial evolution of CWC occurrence in the AS provided close constraints of the climate conditions during interglacial periods facilitating vigorous coral growth. Changes in climate conditions towards glacial periods determined the decline of flourishing coral growth, leading to a glacial demise of CWC in the AS.

Based on the Li/Mg proxy, the past temperature variability of the near Bottom Water Temperature (nBWT) was closely regarded. For the first time, a high-resolution nBWT record in the AS was conducted and compared with published Sea Surface Temperatures (SST). The observed variability in temperature suggests a common global driver of SST variability and coral occurrence in the AS.

MSM36 “MoccoMeBo” was motivated by the hypotheses of a “Gibraltar seesaw pattern”, describing the long-term development of predominantly glacial CWC growth in the Gulf of Cádiz (GoC) and predominantly interglacial CWC growth in the AS. Combined U-series records from both sides of the Strait of Gibraltar, may have revealed a common global driver of the observed seesaw pattern and thus, may have unveiled a most possible onset of CWC growth in the Mediterranean Region during the Mid-Pleistocene Transition.

Lastly, the evolution of seawater $\delta^{234}U$, an indicator of the global weathering rate and crucial for the high precision U-series dating method, was closely investigated. Contrary to the general assumption of a global $\delta^{234}U$, a Mediterranean Sea offset, compared to the Atlantic $\delta^{234}U$, is presented. Furthermore, the combined Atlantic and Mediterranean records, comprised of over 1500 published and unpublished data provide unique insights into the $\delta^{234}U$ evolution over several full glacial-interglacial cycles.

550.000 Jahre mariner Klimavariabilität im westlichen Mittelmeer aus der Perspektive von Kaltwasserkorallen

Kaltwasserkorallen (CWC) sind im gesamten Alborán Meer (AS; westliches Mittelmeer) verbreitet, jedoch wurden große, so genannte Korallen-Mound Provinzen nur am marokkanischen Rand entdeckt. Während der Forschungsschiffreise MSM36 "MoccoMeBo" bohrte das Bremer Bohrgerät „MeBo“ erfolgreich 70 m lange Kerne durch diese Korallen-Mounds, darunter auch die hier vorgestellten Kerne aus der East Melilla Coral Province (EMCP). Mithilfe der hochpräzisen Uran-Thorium-Datierungsmethode gewährten die beiden Kerne einen einzigartigen Einblick über 550.000 Jahre in die Entwicklung der untersuchten Korallen-Mounds. Zum zweiten Mal wurde ein untersuchter Mound vollständig durchbohrt, womit der Zeitpunkt des Beginns des Korallenwachstums an diesem Mound bestimmt werden konnte. Für den anderen Mound, der wahrscheinlich nur bis zur Hälfte (70 m) durchbohrt wurde, konnte eine erste Abschätzung für den Beginn von Korallenwachstum im gesamten AS liefern. Die diskontinuierliche zeitliche Entwicklung beider Mounds ergab jedoch beispiellos komplexe Wachstumsprofile und lieferte somit zwei verschiedene Mound-Entwicklungsmodelle über mehrere vollständige Eiszeit-Warmzeit-Zyklen. Die überwiegend warmzeitliche Entwicklung von CWC im AS ermöglichte eine engere Einschränkung der Klimabedingungen, welche für ein blühendes Korallenwachstum erforderlich sind. Eine Veränderung der klimatischen Verhältnisse während Kaltzeiten verschlechterte die Wachstumsbedingungen, führte zu einem Rückgang der blühenden Korallenriffe und leitete ein kaltzeitliches Absterben der CWC im AS ein.

Basierend auf dem Li/Mg-Proxy wurde die vergangene Temperaturvariabilität nahe des Meeresbodens (nBWT) genau untersucht. Zum ersten Mal wurde eine hochauflösende nBWT-Rekonstruktion im AS durchgeführt und mit bereits veröffentlichten Meeresoberflächen-temperaturen (SST) verglichen. Die beobachtete Variabilität der Temperatur lässt darauf schließen, dass die SST-Variabilität und das Vorkommen von Korallen im AS einen gemeinsamen klimatologischen Ursprung besitzen.

Die Hypothese eines „Gibraltar-Wippmusters“ motivierte die Forschungsschiffreise MSM36 „MoccoMeBo“. Die Hypothese beschreibt die langfristige Entwicklung des überwiegend kaltzeitlichen CWC-Wachstums im Golf von Cádiz (GoC) und des überwiegend warmzeitlichen CWC-Wachstums im AS. Die Betrachtung aller verfügbaren datierten Korallen über 550.000 Jahre aus dem GoC und dem AS könnte auf einen gemeinsamen globalen Treiber des beobachteten Wippmusters hinweisen. Auf Grund dieser Erkenntnisse wird der Beginn von Korallenwachstum im Mittelmeerraum während dem Übergang im mittleren Pleistozän (MPT) vermutet.

Abschließend wurde die Entwicklung des Meerwassers $\delta^{234}U$ betrachtet, einem Indikator für die globale Verwitterungsrate und entscheidend für die hochpräzise Uran-Thorium-Datierung Methode. Entgegen der allgemeinen Annahme eines globalen $\delta^{234}U$-Wertes wurde ein Unterschied zwischen Mittelmeer und dem Atlantischen Ozean entdeckt. Darüber hinaus bieten die kombinierten atlantischen und mediterranen $\delta^{234}U$-Rekonstruktionen, die aus über 1500 veröffentlichten und unveröffentlichten Daten bestehen, einzigartige Einblicke in die Entwicklung des $\delta^{234}U$-Wertes über mehrere vollständige Eiszeit-Warmzeit-Zyklen.

Content

1 Foreword

The concern of a warming world led scientists beyond the daily pattern of the weather, towards long-term climate observations and eventually to climate models, which can predict the climate of the near future. These models are based on different earth systems, in particular, the physics of ocean-atmosphere circulation and the chemistry of the carbon cycle (Henderson 2002). Precise models are difficult to construct since both systems are very complex and sensitive to changing conditions. To approach the sensitivity and complexity, scientists rely on modern instrumental observations and paleoclimatological work with so-called “proxies”. The latter aims for the often indirect, but quantitative, reconstruction of past environmental conditions and climate (e.g. Wefer 1999).

Paleoclimate reconstructions can be carried out on a broad range of natural archives, like ice, speleothems, tree rings, pollen, loess, marine and lacustrine sediments as well as tropical coral reefs. More recently it was discovered that, in contrast to tropical coral reefs, which are restricted to shallow water depth, cold-water corals can build unexpected large topographic features on the deep seafloor throughout the global ocean (Roberts 2009, Freiwald et al. 2017). Drilling such mounds provides piles of fossil corals that can serve as climate archives to study past climate change in the mid-depth ocean. With 70% of the Earth’s surface being water, the role of the ocean in the climate system is crucial. To retrieve its past changes is the aim of paleoceanography, a field that has become central to paleoclimatology. One of the primary archives utilized in paleoceanography are marine sediments used for nearly a century (Hubbard and Wilder 1930, Schott 1938, Emiliani and Milliman 1966) and can potentially provide continuous records of climate, spanning many millions of years (Bradley 2015). However, common limitations are (i) low sedimentation rates at open ocean locations and thus poor time resolution, (ii) the mixing of sediments by bioturbation, which may further weaken time resolution. (iii) Locations with strong currents may either transport allochthonous sediment towards the location or autochthonous sediment somewhere else, which makes these locations almost unusable (Wefer 1999, Bradley 2015).

Since the 1970s, scientists have introduced cold-water corals (CWC) as an additional climate archive (e.g. Weber 1973, Emiliani et al. 1978). Corals in general, warm- or cold-water, offer a broad variety of advantages, which very few archives can keep up with. First CWC-pioneers investigated stable isotopes in solitary CWC from the central North Atlantic to prove profound changes in intermediate-water circulations coinciding with major climate changes (Smith et al. 1997). The authors concluded that, using CWC as archives, previously unavailable records of climate change might become accessible or new types of proxies may

be developed (e.g. temperature, water mass tracer). Other pioneers discovered a major CWC province which lead to the first long term record of discontinuous coral growth, spanning over 2 million years (Henriet et al. 1998, Kano et al. 2007) and proved the possibility of ocean ventilation reconstructions, using combined U-series and ^{14}C dating (Adkins 1998, Mangini et al. 1998). Today, over two decades later, these visionary studies set the framework for intense work on CWC ecosystems, their climate-related growth and dependency for certain environmental parameters, leading to a better understanding of the climate system.

CWC as a climate archive stand out due to their global distribution and broad depth range, from a mere few meters to abyssal depths and from the Norwegian Sea (70°N) to the Ross Sea in Antarctica (78°24'S) (Freiwald et al. 2017). Longevity and temporal resolution provide records on sub decadal level (potentially even higher) which span as much as 200 years on a single sample. Due to the relatively high growth rates of some coral species, which range from 2-26 mm/year (Gass and Roberts 2006, Henriques 2014, Büscher et al. 2017), corals may provide a much higher time resolution than most other oceanic archives (Stanley and Cairns 1988, Adkins et al. 2004, Freiwald and Roberts 2005, Cairns 2007, Sherwood and Risk 2007, Orejas et al. 2008). So-called framework forming CWC build reefs, which over long periods with episodes of consecutive coral growth and sediment input, these reefs build up to CWC mounds. Mounds can extend over several km in lengths, hundreds of m in width and height. Several dating methods (e.g. U-series and ^{14}C dating) and multiple ocean parameter proxies (e.g. Li/Mg temperature; εNd water mass tracer) were developed over the last decades, applicable on both solitary and framework forming CWC.

The interest in CWC grew immensely, due to the many possibilities in climate reconstructions they offered, resulting in a fast rising number of publications and numerous research cruises (e.g. Ferdelman et al. 2006, Freiwald et al. 2009, Hebbeln et al. 2009, Hebbeln et al. 2015). In 2014, one of these research cruises, MSM36 "MoccoMeBo", was conducted in the westernmost part of the Mediterranean Sea (MED), the Alboran Sea (AS), and in the Gulf of Cadiz (GoC), which is connected via the Strait of Gibraltar (SoG; Hebbeln et al. 2015). One major objective of the cruise was to gain detailed insight into coral mound initiation and development over time in both locations (Hebbeln et al. 2015). The hypothesis of a "seesaw" pattern, with glacial coral occurrence in the Gulf of Cadiz and interglacial coral occurrence in the AS, was reinforced by long cores, revealing the proposed pattern over several glacial-interglacial cycles (Krengel 2016). However, the initiation of corals and the development of mounds and ridges in the AS remained elusive. Drilled with the MARUM drill rig "MeBo", a unique data set comprised of two 70 m long cores was recovered and builds the

foundation of the work presented here. The following approaches, which provide important information for the climate variability in this area, are investigated in this work:

- This unique data set will be used to decipher the temporal evolution of coral growth in the AS over 550 ka and the climatic drivers of vigorous coral growth and its decline within the Mediterranean Region (Chapter 3).
- Based on the Li/Mg proxy, the past temperature variability of the near Bottom Water Temperature (nBWT) will be regarded to conduct a high-resolution nBWT record to unravel driver of SST variability and coral occurrence in the Alboran Sea (Chapter 4).
- The long-term evolution of interglacial coral growth in the AS will be compared with the glacial coral growth evolution of the GoC, to decipher the climatic drivers of the Gibraltar seesaw pattern and to further constrain the timing of the onset of coral growth in the AS (Chapter 5).
- The evolution of seawater $\delta^{234}U$ is an indicator of the global weathering rates. Especially in this marginal sea, valuable information for the Atlantic circulation and turnover rates during climate changes is expected from the variability in coral $\delta^{234}U$ (Chapter 6).

2 Background and Methods

Cold-Water Corals (CWC) are nonsymbiotic-living animals. Some species, so-called scleractinian CWC, produce calcium carbonite skeletons (Cairns 2007). These aragonite skeletons are affected by the chemical composition of the seawater they live in. The prevailing environmental parameters like pH and temperature are recorded in the chemical composition of the skeletons (Smith et al. 2000, Rüggeberg et al. 2008, Case et al. 2010, McCulloch et al. 2012, Raddatz et al. 2013, Montagna et al. 2014, Raddatz et al. 2014). Upon death, the aragonite skeleton is preserved, holding clues to the environmental conditions in which it formed in, providing an exceptional archive. Alas, one cannot directly measure oceanic parameters or other physical properties of a bygone world, a so-called proxy variable is therefore used (short: proxy). A proxy is "a measurable property of an environmental/geological record which, through mathematical or statistical treatment, can be related with a stated uncertainty to one or a combination of physical, chemical, or biological environmental factors during its formation" (Hillaire-Marcel and De Vernal 2007).

A number of diverse proxies exist which can be used to reconstruct seawater temperature from cold-water corals. For example, reconstructions can be derived from the stable isotope ratio of O and C (Smith et al. 1997), which however are strongly affected by the calcification process itself (Adkins et al. 2002, Lutringer et al. 2005). Alternative approaches are, the elemental composition of Li/Mg (e.g. Case et al. 2010, Hathorne et al. 2013, Raddatz et al. 2013, Montagna et al. 2014), clumped isotopes (e.g. Ghosh et al. 2006, Eiler 2011) or Na/Ca (Schleinkofer et al. 2019). Using proxies to detect environmental changes is a powerful tool if however the age of a fossil coral can be precisely constrained by means of ^{14}C or U-series dating. CWC incorporate large amounts of uranium into the aragonite skeleton (~2-5 ppm, approximately a factor of 10^3 more than in seawater). Thus, through U-series dating, CWC can be dated accurately (Mangini et al. 1998, Lomitschka and Mangini 1999, Cheng et al. 2000, Hua et al. 2001, Frank et al. 2004, Frank et al. 2005, Schröder-Ritzrau et al. 2005, Frank et al. 2009, Frank et al. 2011, Wefing et al. 2017).

The following sections will give detailed insight into the geology, the present-day hydrography of the Mediterranean Sea, Cold-water corals and their capacity to engineer coral mounds as well as regarding the absolute dating method and the temperature reconstruction, applied throughout this work.

2.1 Geology of the Mediterranean Sea

The Mediterranean Sea (MED) is a semi-enclosed basin encompassing an area of ca. 2.5 million km² (Lionello et al. 2004). Its average water depth is 1500 m albeit reaching maximum water depth of up 5100 m in the Ionian Sea (Bethoux et al. 1999). Its only connection to the open ocean is the narrow Straits of Gibraltar (SoG) (sill depth ~300 m, width ~13 km) to the west which links the MED directly to the Atlantic Ocean (Malanotte-Rizzoli 2001). An additional narrow and shallow connection exists between the MED and the Black Sea (Fig. 2.1) to the east through the Marmara Sea (Skliris 2014).

The geological evolution of the MED is characterized by phases of subduction, spreading, rifting and collision of (micro-) plates since the Mesozoic (250-65 Ma) (Picotti et al. 2014). This tectonic activity resulted in the formation of two major sub-basins: (1) the Eastern Mediterranean Basin (EMS), and (2) Western Mediterranean Basin (WMS; Picotti et al. 2014). Both major basins are further subdivided into smaller sub-basins: the EMS is subdivided, starting counter-clockwise in the west, into the Ionian, Levantine, Aegean and the Adriatic basin (Robinson et al. 2001). The spreading of the basins started earlier than in the WMS, therefore the basins are generally older, of potentially pre-Jurassic to Cretaceous age (>200 to 70 Ma), and deeper than the WMS, which is of Miocene to Pliocene age (23-3 Ma) (Picotti et al. 2014). The WMS is also divided into sub-basins: to the west, the first sub-basin is the Alboran and the Algerian (16-8 Ma) followed counter-clockwise by Tyrrhenian (7-2 Ma), Ligurian-Provencal and the Balearic basin (20-15 Ma). The Strait of Sicily (SoS) (width: ~35 km, sill depth: ~300 m) connects both major sub-basins (EMS and WMS) (Robinson et al. 2001, Millot and Taupier-Letage 2005, Picotti et al. 2014).

2.2 Hydrography of the Mediterranean Sea

The modern hydrography of the MED is dominated by its evaporation-precipitation balance and its exchange with the adjacent North Atlantic (Malanotte-Rizzoli 2001, Millot and Taupier-Letage 2005). Across the MED, evaporation exceeds freshwater input from river run-off and precipitation and thus causes a concentration in salinity (Skliris 2014). This buoyancy drive facilitates the inflow of less dense Atlantic water (AW; see Chapter 2.2.1) at the surface and the outflow of dense Mediterranean Outflow Water (MOW; see Chapter 2.2.3). In contrast to its modern setting the MED was gradually cut off from the Atlantic Ocean during the Messinian (7.2-5.33 Ma) which diminished the inflow of AW, resulting in basin-wide evaporate depositions (Willett et al. 2006, Roveri et al. 2014). Since the reopening of the SoG at the end of the Messinian Crisis (~5.33 Ma; Krijgsman et al. 1999, Roveri et al. 2014) the

hydrographic conditions of the MED developed into its present-day form (Picotti et al. 2014). In the following, the prevailing dominant water masses of the MED are discussed in detail.

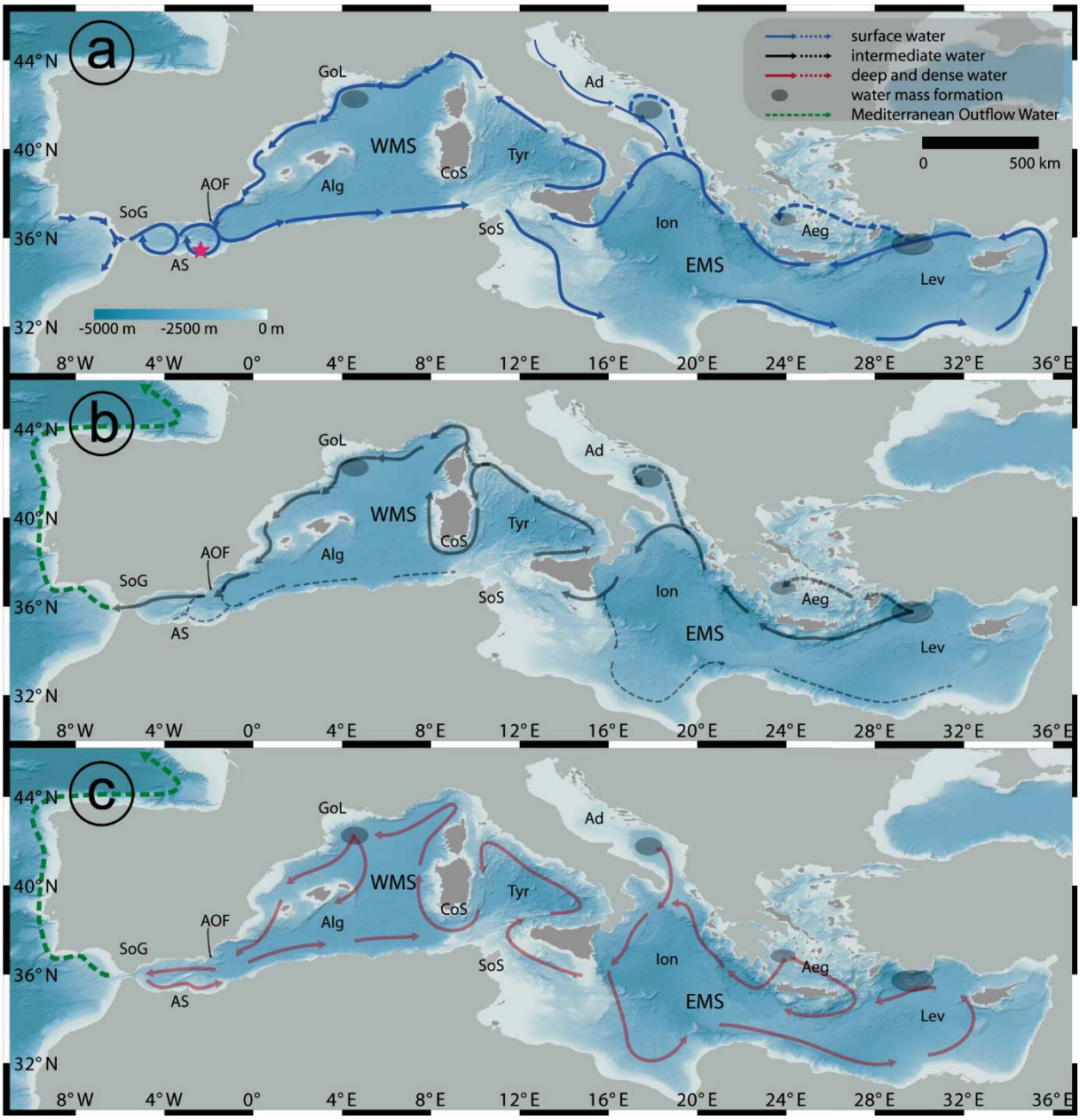

Fig. 2.1: Map of the Mediterranean Sea: a) Surface water flow path. b) Intermediate water mass formation sites and flow paths. c) Deep and dense water mass formation and flow path (Water mass formation and flow paths modified after: Millot and Taupier-Letage 2005, Hernández-Molina et al. 2006, Hernández-Molina et al. 2014). Red star: Location of the East Melilla Coral Province (EMCP). Important abbreviations: Western Mediterranean Sea (WMS); Alboran Sea (AS); Strait of Gibraltar (SoG); Almeria-Oran-Front (AOF).

2.2.1 Surface Water Circulation

Forced by the anticyclonic surface circulation and the sinking sea level, due to evaporation, in the Mediterranean Sea, Atlantic Water (AW) enters the Strait of Gibraltar (SoG). The AW at SoG, with physical parameters of 15-16 °C, 36-37 psu, forms an up to 200 m deep jet with an inflowing rate of ~1 SV. After entering the MED, the temperature and salinity of AW are constantly modified while progressing through the MED through admixing of other surface water masses, evaporation, air-sea interactions and thus becomes Modified Atlantic Water (MAW). MAW is directed north-eastwards along the Spanish margin, describing a quasi-permanent, clockwise gyre, the West Alboran Gyre (WAG) (Millot 1999). At the south-eastern Spanish margin, inflowing MAW mixes with saltier and denser resident MAW outflowing the Algerian basin along the eastern Spanish border (Fig. 2.1a). Both water masses are deflected towards the south, where the mostly anticyclonic, East Alboran Gyre (EAG) is formed. Entrained MAW flowing southwards, towards Algeria and then along the southern coast of the Alboran Sea towards Melilla. On the eastern edge of EAG, where MAW and the older resident MAW converge, the strong, geostrophic "Almeria-Oran-Front" (AOF) is formed (Tintore et al. 1988).

The front is characterized by increased high primary productivity (Lohrenz et al. 1988, Tintore et al. 1988). West of the AOF, the MAW becomes more saline (up to 37-38 psu) due to enhanced evaporation and thus increases in density of σ=28-29. MAW resides into depths of 200 m in the centre of the Alboran basin, as shallow as 50 m along the Spanish coast and as deep as 300 m at the AOF. At the Algerian coast, MAW deflects into two streams. The smaller stream is entrained into the EAG, while the more important stream flows along the Algerian coast towards the east and is called the Algerian Current (AC) (Millot 1985). Progressing east, this narrow and often unstable current (30-50 km wide, 200-400 m deep) follows the slope towards the SoS (Millot and Taupier-Letage 2005). The AC widens and thins out along its path (Benzohra and Millot 1995) and generates either small and short-lived eddies or big open-sea eddies called the Algerian Eddies (Millot 1999, Malanotte-Rizzoli 2001). At the SoS, MAW splits into two pathways: (1) the Tyrrhenian vein passes the SoS and flows along Sicily and the Italian Peninsula, where it continues along the northern slope of WMS (Millot and Taupier-Letage 2005). (2) The second pathway flows through the SoS and along-slope of the southern EMS. This Libyan vein traverses further east as the so-called Libyan-Egyptian Current. The current creates small eddies at first, which are later replaced by well-structured and energetic eddies (Millot and Taupier-Letage 2005). MAW, forced by the Libyan-Egyptian Current, flows along slope the Levantine Basin where it is deflected in a north-western

direction and thus forms smaller streams penetrating also into the Aegean Sea (Millot and Taupier-Letage 2005). Further to the west, the MAW flows along the Greek shoreline, towards the Italian peninsula, entraining into the Adriatic Sea. Along Sicily's shoreline, MAW rejoins the northward propagating Tyrrhenian vein (Millot 1999). The Tyrrhenian vein flows further along the northern slope of the Ligurian, the Provençal, the Gulf of Lions (GoL) and the Catalan. Bypassing Corsica to the west, the Tyrrhenian vein becomes the Northern Current and is involved in the formation of Winter Intermediate Water (WIW) in the Liguro-Provençal and involved in the formation of West Mediterranean Deep Water (WMDW) within the Gulf of Lion (Millot and Taupier-Letage 2005). The Northern Current then flows along the Spanish coast to conclude a basin-wide western gyre within the Alboran Sea providing the above-mentioned resident MAW involved in the AOF.

2.2.2 Intermediate Water Circulation

The majority (90%) of the inflowing AW at the SoG is subsequently involved in intermediate or deep-water formation whilst the remaining 10% are being evaporated (Millot and Taupier-Letage 2005). In the EMS, roughly ¾ of the MAW volume is transformed in intermediate and deep-water masses, whereas only ¼ is further transformed in the WMS as elucidated in this section (Millot and Taupier-Letage 2005). The Levantine Intermediate Water (LIW) (Fig. 2.1b), formed in the northern Levantine Basin is the warmest, saltiest and in volume greatest water mass formed in the MED (Millot and Taupier-Letage 2005). It can be tracked as far west as the SoG and is characterized by temperatures between 14.5 to 15.5 °C, salinities of ca. 39 psu and densities of σ=29 (Lascaratos 1993, Millot and Taupier-Letage 2005). The formation of LIW is driven by intense winter cooling of MAW which subsequently sinks isopycnally to depths of 100-500 m and thus forms LIW (Millot and Taupier-Letage 2005).

Forced by the Coriolis Effect, the newly formed LIW flows north-west, along the Cretan Arc islands, passing the Adriatic Sea, the Italian peninsula and the SoS before entering the western basin. The sills into the Aegean Sea and the Adriatic Sea are deep enough for LIW to also partially flow into these sub-basin, where LIW mixes with MAW to form Aegean Deep Water (AeDW) and Adriatic Deep Water (AdDW), respectively (Millot and Taupier-Letage 2005). After passing the SoS, LIW flows around the Tyrrhenian Basin at 200-600 m water depth, passing along the western slope of the islands of Corsica and Sardinia before joining a vein of LIW that flows through the Channel of Corsica with a sill depth of 400 m (Millot and Taupier-Letage 2005). Flowing underneath the Northern Current, the LIW constantly admixes with overlying MAW continuously becoming fresher (Millot 2013). Further to the west, LIW

flows along the northern slope into the Alboran Sea, where a portion of LIW is redirected into the Algerian Basin, flowing below the Algerian Current (Millot 1999). However, the main LIW vein flows towards the SoG along the northern Alboran Basin. With a sill depth of 300 m, most LIW exits the MED, mixes with Mediterranean DW and flows as Mediterranean Outflow Water (MOW) into the Atlantic Ocean.

Other intermediate water masses, such as the Cretan Intermediate Water and the Winter Intermediate Water, originating in the Aegean and the Liguro-Provençal area respectively, are difficult to differentiate from surrounding water masses, due to similar physical properties and the low amount of formed water mass volume (Millot and Taupier-Letage 2005).

2.2.3 Deep Water Circulation

In total, four deep water masses can be recognized within the MED (Fig. 2.1c), two in each Mediterranean basin. In the EMS, the Aegean Deep Water, also known as Cretan Deep Water (AeDW) is warmer and saltier (14 °C and 38.9 psu) than the Adriatic Deep Water AdDW (12.9 to 13.8 °C and 38.65-38-88 psu) (Gacic et al. 1996, Theocharis et al. 1999, Budillon et al. 2010). This is due to two aspects: (1) the overlying MAW is warmer and saltier in the Aegean Sea and (2) the LIW is being formed in the vicinity of the Aegean and thus has undergone less mixing (Millot and Taupier-Letage 2005). Both deep water masses, with similar densities of σ=29.15 and σ=29.2 respectively, cascade down into depths of similar density of the Levantine, Cretan and Ionian Basin and keep circulating along the slope, forced by the Coriolis Effect (Millot and Taupier-Letage 2005). The combination of the deep EMS basins (4000-5000 m) and the shallow SoS limits the communication of AeDW/AdDW with the intermediate and deep water masses in the WMS basins (Millot 1987, Astraldi et al. 2001).

Only the upper layers of both eastern deep-water masses pass through the SoS and subsequently cascade down into the Tyrrhenian Sea, mixing with resident waters at depths reaching 1900-2000 m (Sparnocchia et al. 1999). This leads to the formation of the Tyrrhenian Dense Water (TDW) (12.97 °C; 38.495 psu; Fuda et al. 2002), which follows a basin-wide gyre and enters the Algerian Basin at the Channel of Sardinia. It continues its path along the slope Sardinia towards the Ligurian and the Provençal and into the Alboran and the Algerian Sea. Within the WMS basin, the so-called Western Mediterranean Deep Water (WMDW) is formed in the Gulf of Lions during wintertime, with physical properties of 12.7 °C, 38.40 psu and σ=29.1 (Skliris 2014). Winter cold spells facilitate MAW and LIW to significantly cool down and traverse to depths of 2000-2500 m (Millot and Taupier-Letage 2005, Skliris 2014). Flowing underneath the TDW, WMDW circulates through a basin-wide gyre, along the Catalan and

into the Alboran Sea, where the less dense part of both water masses are uplifted and mix with LIW (Millot 1999). This combined water mass then, further flows towards the SoG and exits the MED as Mediterranean Outflow Water (MOW) (Hernández-Molina et al. 2014). After the SoG, the dense MOW cascades down the continental slope and flows along the Spanish coast towards the North-East Atlantic (Hernández-Molina et al. 2014). The more dense parts of TDW and WMDW circulate along slope the deep Alboran Sea into the Algerian basin, where it is partially trapped in depths exceeding 2700-2900 m (Millot and Taupier-Letage 2005b).

2.3 Cold-Water corals: nomenclature, ecology and mound formation

2.3.1 Nomenclature

The Great Barrier Reef with over 400 different warm-water (tropical) coral species and over thousands of other species has been discovered by James Cook in 1770 and is probably the most known coral reef worldwide. However, roughly 65% of the known (as of 2007) 5160 coral species dwell in depths greater than 50 m (Roberts 2009). These corals were not shallow warm-water corals, but so-called "deep-sea corals" or "cold-water corals". Since both names are equally used in literature, the term CWC is used in this study. Defined by Cairns (2007) corals, in general, are '*animals in the cnidarian classes [...] that produce calcium carbonate (aragonitic or calcitic) secretions resulting in continuous skeleton [...]*'. This definition encompasses among many other species, the in this study investigated species of Scleractinia (stony corals). The differences between warm-water and cold-water corals are not only the water temperature in which they thrive in or the depth they are generally found at, but also the dependency on the symbioses with photosynthetic dinoflagellates (zooxanthellae). Warm-water corals, found in maximal depths of up to 150 m, live in symbioses with zooxanthellae which are an important source of the necessary energy for metabolism, growth and reproduction (Lohr et al. 2007, Roberts 2009). CWC live non-symbiotic, so-called azooxanthellate, with 90% of the species occurring in deep, up to abyssal depths waters, where photosynthesis is not possible anymore.

Some species live solitary, like the scleractinian species *Desmophyllum dianthus*. However, most are colonial, like *Lophelia pertusa* (*Desmophyllum pertusum*) and *Madrepora oculata*. *Lophelia pertusa* is molecularly and morphologically overwhelmingly similar to the genera *Desmophyllum* (Addamo et al. 2016). It has been proposed to address the coral species as *Desmophyllum pertusum*. In this thesis, the old denomination *Lophelia pertusa* will be used, to be consistent with the cited publications and to avoid confusion, however, the new denomination is added in brackets. Azooxanthellate species (n=711 species) are distinguished by non-framework forming (n=693) and framework forming (n=18) (Roberts 2009).

This study solely focuses on two species of the latter order, namely:

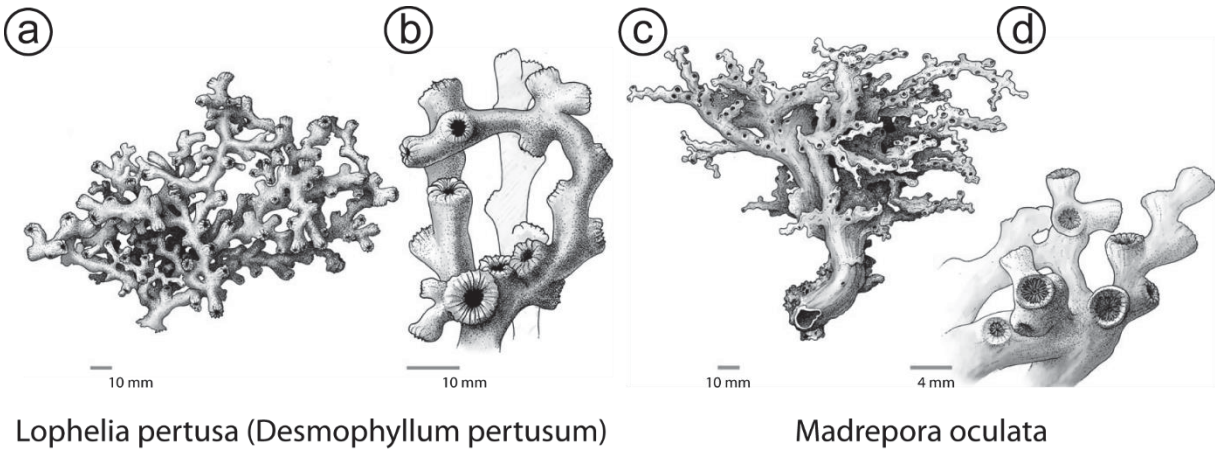

Fig. 2.2: Drawings of the scleractinian CWC species L. pertusa (D. pertusum) (a, b) and M. oculata (c, d). (a, c): formed coral framework. (b, d) Detailed close up of individual corallites. Scale bars: 10 mm (a-c), 4 mm (d). Modified after Roberts (2009).

2.3.2 Ecology

CWC are so-called suspension feeders, settling on hard ground substrate and prospering in the presence of zooplankton and phytodetritus (Duineveld et al. 2004, Kiriakoulakis et al. 2004). The food supply is provided by both, the marine productivity at the ocean's surface and by a turbulent hydrodynamic regime (Duineveld et al. 2004, Mienis et al. 2007, White 2007) delivering food particles to the coral polyps. CWC are commonly found on topographically elevated positions, substantiating the necessity of high energetic regimes and strong bottom currents (White et al. 2005, Dorschel et al. 2007). Certain physico-chemical properties have shown to be crucial for flourishing CWC colonies. The occurrence of *M. oculata* (53-1950 m) is associated with a temperature range of 4 to 13 °C with maximum temperatures of 25 °C (Keller and Os'kina 2008). *L. pertusa* (*D. pertusum*) (39-2775 m) thrives at temperatures ranging from 4 to 14 °C (Roberts et al. 2006, Freiwald et al. 2009) with maximum temperatures of 26 °C. Salinities of 31.7 to 38.8 psu and dissolved oxygen values from 0.2 to 7.2 ml/l (Hanz et al. 2019), yet flourishing conditions for *L. pertusa* between 3 and 5 ml/l (Freiwald 2002), have been reported (Davies et al. 2008, Roberts 2009). Pycnoclines, formed along water mass boundaries and resultant internal waves have shown to play an important role in ensuring continuous coral growth. Along the boundary layer, particles are concentrated and energetic regimes created, transporting food and sediment towards the corals (White et al. 2005, Mienis et al. 2007, Dullo et al. 2008, Flögel et al. 2014, Rüggeberg et al. 2016, Wang et al. 2019). Annual growth rates for *L. pertusa and M. oculata* are estimated to range between 3 to 34 mm/a (Roberts 2009 and references therein, Henriques 2014, Büscher et al. 2017).

2.3.3 Coral mound formation

Carbonate mounds (Coral mounds) are elevated seafloor structures, comprised of *"stratified sequences of reef deposits separated by non-reef (typical seafloor) sedimentary units and erosion surfaces"* (Roberts 2009*)*. At the beginning of every mound stands the settlement of individual coral larvae on hard substrata (Roberts et al. 2006). If favourable environmental conditions prevail, corals grow and form colonies simultaneously as new coral larvae settle (Roberts 2009). Growing colonies will eventually intermingle and form coral "thickets" (Squires 1964), comprised of dead corals at the bottom and live corals at the top, they attract large biodiversity of fish, sponges and other species as recently demonstrated in the Alboran Sea (Corbera et al. 2019). Bioerosion, sponges and fungi feeding on the dead corals at the base, is an important factor in producing coral rubble which acts as new substrata for coral larvae to settle or is incorporated to form packstones and stabilize the structure (Roberts 2009). Coral thickets only grow into coppice and eventually reefs/mounds, if hemipelagic material gets trapped within the coral framework as the reef grows (Roberts 2009). Reefs redirect bottom water currents through the structure, increase turbulences and create small-scale eddies around it, resulting in a reduced sediment-carrying capacity of currents around the corals. The deposition and trapping of bedload and suspended sediment around and within the growing reef is enhanced (De Mol et al. 2002, Huvenne et al. 2009, Titschack et al. 2015). Flügel (2013) described this increase in sediment accumulation, called baffling, as a crucial factor for a three-dimensional relief. Therefore, coral mounds are restricted to the continental margins, where terrigenous sediment is supplied (Hebbeln 2019).

As mentioned above, coral mounds are ideally comprised of stratigraphic sequences of reef deposits, separated by non-reef sedimentary units. With changing environmental conditions over glacial-interglacial cycles or if the mound out grows optimal hydrographic conditions, coral growth may become stagnate and the reef may die completely (Roberts 2009). The remaining topographic seafloor structure then (i) can be buried by off mound sedimentation, (ii) can be partially eroded or (iii) new coral larvae can resettle on the elevated structure to form new colonies and reef structures (Fig. 2.3).

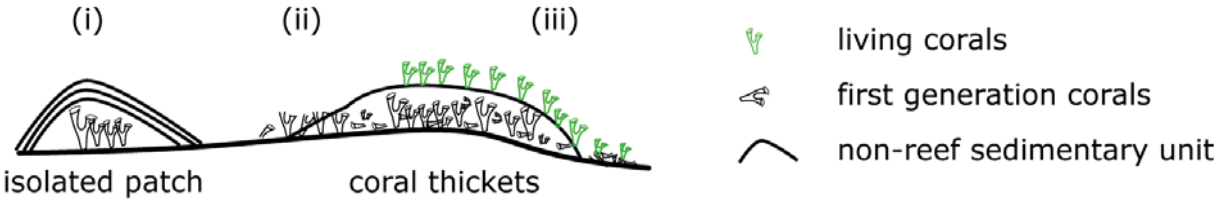

Fig. 2.3: Unfavourable coral growth conditions may lead to (i) isolated patches buried by off mound sedimentation or (ii) partially eroded. Restored favourable conditions may lead to (iii) a resettlement of coral larvae on previous grow periods.

Mounds can be found as an isolated feature or as part of a cluster of numerous mounds, so-called Coral Mound Provinces (CMP) (De Mol et al. 2002, Wheeler et al. 2007, Wienberg et al. 2018). With repeated reef growth and sedimentation, mounds can span several thousand to millions of years of discontinuous coral growth (Freiwald et al. 2004, Roberts et al. 2006, Kano et al. 2007) and extend horizontally over several kilometres. Vertically, mounds and ridges can range from a few meters up to >300 m and can potentially have multiple peaks (Mienis et al. 2006, Roberts 2009). Ideally, mounds grow in conical shapes, however these are rarely found in nature. More common are current-aligned, oval to arcuate and elongated shaped mounds as found in the northeast Atlantic and the Mediterranean Sea (Fig. 2.7) (Wheeler et al. 2007, Hebbeln 2019).

Today, flourishing coral colonies are observed in the Gulf of Mexico (Matos et al. 2017), on the Angolan margin (Hebbeln et al. 2016), on the Norwegian shelf (Mortensen et al. 2001), and on over 1000 mounds in the Northeast Atlantic along the Irish and British margins (Roberts et al. 2006). Dead coral colonies, with merely a few patches of live corals, have been observed off Mauritania, off Brazil, along the Atlantic-Moroccan margin and within the Alboran Sea (Hebbeln et al. 2009, Wienberg et al. 2009, Mangini et al. 2010, Eisele et al. 2011, Hebbeln et al. 2019).

CWC colonies and mounds have been subject to many studies (e.g. De Mol et al. 2002, Schröder-Ritzrau et al. 2003, Frank et al. 2004, Dorschel et al. 2005, Rüggeberg et al. 2005, Dorschel et al. 2007, Kano et al. 2007, Wheeler et al. 2007, van de Flierdt et al. 2010, Wienberg et al. 2010, Eisele et al. 2011, Raddatz et al. 2011, Fink et al. 2013). Age data, obtained from fossil coral fragments, has linked the growth and demise of corals to variations in the climate system (e.g. Kano et al. 2007). Flourishing mound growth during full interglacial periods was found between 70°N and 50°N along the eastern Atlantic margin and within the Mediterranean Sea (Frank et al. 2011 and references therein, Fink et al. 2013), whereas growth during glacial periods was found between 50°N and 20°N (Frank et al. 2011 and references therein). Frank et al. (2011) proposed an ice age paced north-south oscillation of environmental conditions necessary for reef development, potentially co-occurring with changes in the polar front, displacing cold, nutrient-rich intermediate waters and surface productivity. The only known locations, with coral growth during full glacial-interglacial cycles are on the Angolan margin, with documented coral growth since the last glacial period up to the present-day (Hebbeln et al. 2016, Wefing et al. 2017).

2.4 Radiogenic age determination

Since the middle of the 20th century, radiogenic dating methods have been established and used in different application areas. Rb-Sr dating, established by (Hahn et al. 1943) is commonly used to date igneous rocks, meteorites, even lunar samples from the Apollo missions (Murthy et al. 1971). This dating method is limited by a minimum sample age of some hundred thousand years but can be used to date back to hundreds of millions of years (Faure 1977). Another widely used and well-known method has been developed and used by Anderson and Libby (1951). Radiocarbon dating, using the radioactive carbon isotope ^{14}C, is commonly used for organic material such as bones, wood, shells and corals. Recent to young periods (from 1950 to 50 ka ago) can be precisely dated. Uranium-series (U-series) dating, the suitable method for this study, is capable of precisely reconstructing calcitic samples for the past 600 ka, with the limit of application at 800 ka. This geochronological tool is based on a systematic radioactive disequilibrium in the ^{238}U decay chain (Barnes et al. 1956), decaying from ^{238}U to ^{230}Th with α- and β^--decays (Fig. 2.4).

The residence time of U in seawater is estimated to be 380 ka, which is considerably longer, then the ocean's global mixing time (~1000 a). U is therefore distributed homogenously in the oceans. On the other hand, Th is poorly soluble in water and highly particle reactive. Consequently, it has a residence time in the ocean of only 40 a. It is removed from the water column by adsorption or reverse scavenging processes (e.g. Vogler et al. 1998).

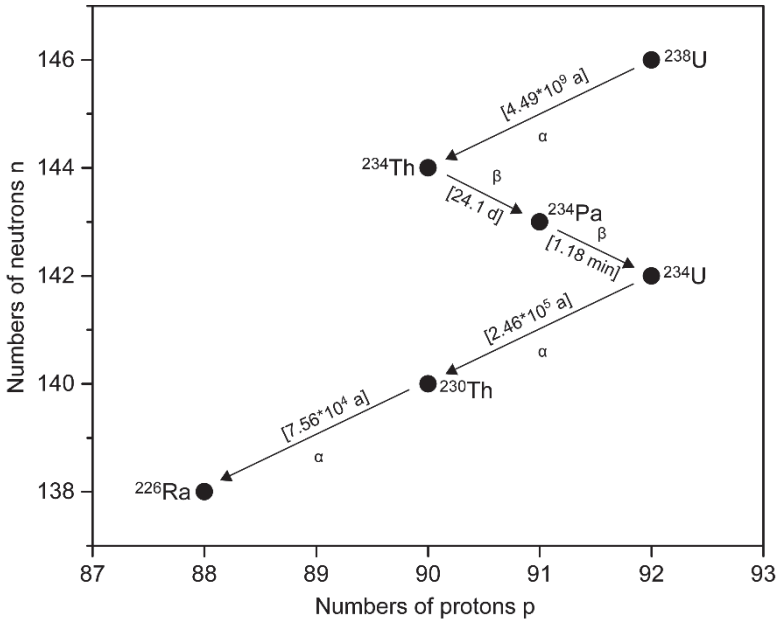

Fig. 2.4: U-series decay chain with half-lives for ^{234}U and ^{230}Th. In this figure revised half-lives from Cheng et al. (2013) are used. However, U-series ages in this study were done with half-lives from Cheng et al. (2000).

The short-lived daughter nuclides ^{234}Th and ^{234}Pa are not considered in the following equation as their half-lives are several orders of magnitude smaller than those of ^{238}U and ^{234}U (Fig. 2.4 [brackets]). Therefore, only the activity ratios of ($^{230}Th/^{238}U$) and ($^{234}U/^{238}U$) are necessary to determine the age of the sample. The isotopic decay constants are noted as λ_i. The initial activity ratio in the sample carbonate is $(^{230}Th/^{238}U)_i$ and the measured activity ratio is $(^{230}Th/^{238}U)_t$, the sample age is given as t. Derived from (Ivanovich 1994), the *marine age equation* is formed:

$$\left(\frac{^{230}Th}{^{238}U}\right)_t = 1 + \left[\left(\frac{^{230}Th}{^{238}U}\right)_i - 1\right] \cdot e^{-\lambda_{230}t} + \left[\left(\frac{^{234}U}{^{238}U}\right)_i - 1\right] \cdot \frac{\lambda_{230}}{\lambda_{230} - \lambda_{234}} \cdot (1 - e^{(\lambda_{234} - \lambda_{230})t}) \quad \text{E2.1}$$

The ratio ($^{234}U/^{238}U$) is often given in δ notation (E2.2), expressing the deviation from radioactive equilibrium in ‰:

$$\delta^{234}U = \left(\frac{\left(^{234}U/^{238}U\right)_t - \left(^{234}U/^{238}U\right)_{eq}}{\left(^{234}U/^{238}U\right)_{eq}}\right) \cdot 1000 = \left(\left(\frac{^{234}U}{^{238}U}\right)_t - 1\right) \cdot 1000$$

E2.2

Natural geochemical processes, like oxidation/reduction, scavenging processes, adsorption or crystallization cause isotopic and elemental fractionation in seawater, initiating a state of disequilibrium between mother and daughter nuclides. These isotopic signatures and trace elements are incorporated during growth when marine calcifiers precipitate $CaCO_3$ from surrounding seawater. In any U-bearing, naturally occurring calcite or aragonite, if it remained unaltered, the disequilibrium can be measured and dated by using the U-series age equation. Some 800 ka after formation a state of secular equilibrium is eventually established, which marks the limits of this age determination method. During the formation of calcitic tests (e.g. foraminifera or coccolithophores) or aragonitic skeletons (CWC), U atoms take up slots in the crystal lattice structure. Calcite forms as rhombohedral crystals, whereas aragonite forms as orthorhombic crystals. The dominant U molecule in seawater, uranyl carbonate is in octahedral system and more compatible with the latter (Shen and Dunbar 1995, Reeder et al. 2001). The different crystal lattices are responsible for varying U concentrations in foraminifera tests of 0.02-0.05 ppm and 2-5 ppm in coralline skeletons (Ku 1965, Russell et al. 1994). In addition, the ratio of U/Ca in coral skeletons is dependent on the pH and controlled by the carbonate ion concentration in seawater (Anagnostou et al. 2011, Inoue et al. 2011, Raddatz et al. 2014). Upon death, no more U is incorporated into the marine organism skeleton and through the decay of ^{238}U, ^{230}Th increases.

As mentioned above, ^{230}Th is particle reactive and only resides on a short timescale in the water column and is scavenged quickly. Yet reported values suggest an increase of ^{230}Th in depth from $^{230}Th/^{232}Th$ values of 0-30 ranging from 0-400 m (Vogler et al. 1998, Cheng et al. 2000). Accordingly, the initial ^{230}Th concentration in coral skeletons cannot be assumed to be zero, which consequently leads to a ^{230}Th correction for the amount of Th which did not derive from radioactive decay in a closed system. The initial activity ratio of $^{230}Th/^{238}U$ is accordingly adopted as:

$$\left(\frac{^{230}Th}{^{238}U}\right)_i = \left(\frac{^{232}Th}{^{238}U}\right)\left(\frac{^{230}Th}{^{232}Th}\right)_i$$

E2.3

Due to the long half-lives of ^{232}Th and ^{238}U, exceeding the coral age by several orders of magnitude, the activity ratio ($^{232}Th/^{238}U$) since the formation of the sample material can be assumed constant and $(^{230}Th/^{232}U)_i$ can be taken from water column measurements (Cheng et al. 2000) or via isochron techniques.

As mentioned above, it is of utmost necessity for U-series measurements, that the sample remains unaltered after death. Coral alterations comprise of carbonate dissolution, secondary aragonite precipitation, boring organisms, pore fillings, recrystallization and ferromanganese coatings on the skeleton (e.g. Lomitschka and Mangini 1999, Allison et al. 2007). These alterations can affect the geological U-series clock when removing or adding additional U and Th to the skeleton. Ferromanganese coatings, acquired on the surface of the skeletons contain, in addition to U, a high concentration of $^{230}Th_i$. These coatings can be effectively removed through physical and chemical cleaning and do not alter the skeleton itself. Other alterations are difficult to quantify through microscopic studies of the skeleton or geochemical analyses.

One approach to confirm the samples closed system nature or open system behaviour, is the *seawater evolution curve* (E2.5), depending on $\delta^{234}U$ (E2.2) and assuming $(^{230}Th/^{238}U) = 0$. In the case of closed system behaviour, the sample follows the evolution curve throughout time, whereas deviations from the curve reflect open system behaviour. (Fig. 3.3a and 3.5a).

$$\left[\left(\frac{^{234}U}{^{238}U}\right)_t - 1\right] = \left[\left(\frac{^{234}U}{^{238}U}\right)_i - 1\right] \cdot e^{-\lambda_{234} t}$$

E2.4

$$\left(\frac{^{230}Th}{^{238}U}\right)_t = 1 - e^{-\frac{\lambda_{230}}{\lambda_{234}} \ln\left(\frac{\delta^{234}U}{\delta^{234}U_i}\right)} + \frac{\lambda_{230}}{\lambda_{230} - \lambda_{234}} \cdot \left(1 - e^{\frac{\lambda_{230} - \lambda_{234}}{\lambda_{234}} \ln\left(\frac{\delta^{234}U}{\delta^{234}U_i}\right)}\right) \cdot \frac{\delta^{234}U}{1000}$$

E2.5

Due to the α-recoil effect and chemical fractionation processes, ^{234}U is preferably leached from source rocks (Chabaux et al. 2003). Resulting in activity ratios of $^{234}U/^{238}U$ in rivers showing large deviations from secular equilibrium, up to several hundred or thousand permille (Dunk et al. 2002, Chabaux et al. 2003). River run-off into the ocean results in a present-day, globally enriched activity ratios of $^{234}U/^{238}U = 1.1468$ or $\delta^{234}U = 146.8‰$ (Andersen et al. 2010). Henderson (2002) proposed this $\delta^{234}U$ value has been stable with a variation of ± 15‰, for the past 360 ka. The long residence time of U in seawater (380 ka) suggests long feedback times on external input of U. Robinson et al. (2004) investigated the effects of rainfall and weathering on seawater $\delta^{234}U$ during glacial cycles. Simple mass balance models indicate a variation of up to 10‰ during the last 80 ka. Therefore Robinson et al. (2004) suggested a revaluation of rejected data varying significantly from the established modern seawater $\delta^{234}U$.

Most importantly, various studies suggested lower seawater $\delta^{234}U$ values during the last glacial (Cutler et al. 2004, Robinson et al. 2004, Esat and Yokoyama 2006, Thompson et al. 2011), as well as large and rather rapid changes of the U isotope budget over the last 30 ka (Chen et al. 2016). Potential triggers for varying seawater $\delta^{234}U$ are changes in ocean mixing, the reduction of weathering during glacial periods and the meltwater discharge during early deglacial periods (Chen et al. 2016). Additionally, changes in weathering patterns, exposure and the size of mangrove forests, which are known as reductive U storing environments, may play a role (Robinson et al. 2004, Esat and Yokoyama 2006).

2.5 Li/Mg temperature

In the scientific community, a growing number of studies developed temperature proxies, e.g. $\delta^{18}O$, Δ_{47} (so-called clumped isotopes), Sr/Ca, Mg/Ca, U/Ca on carbonate skeletons of biomineralizing organisms like foraminifera tests, tropical to temperate (warm-water) corals as well as cold-water corals (Beck et al. 1992, Shen and Dunbar 1995, Mitsuguchi et al. 1996, McCulloch 1999, Montagna et al. 2007, Saenger et al. 2012). The temperature of the oceans controls, among other physical and chemical parameters, the ocean circulation and dissolution of CO_2, as well as a wide range of biogeochemical processes, determining the structure of aquatic ecosystems and their food webs (Montagna et al. 2014). However, isotopic and elemental ratio data of skeleton samples alike have been proven to be influenced by vital effects, salinity or pH, resulting in the dilution of the primary environmental signal (Sinclair 2005, Sinclair et al. 2006, Hathorne et al. 2013).

The search for a temperature proxy less influenced by vital effects led Marriott et al. (2004) to investigate the Li/Ca ratios on the tropical scleractinian coral species *Porites*, showing a negative gradient of 4.9±1.8% per °C with seawater temperature. Compared to Sr/Ca, with a gradient of only 0.7% per °C (Corrège 2006), another proxy used for paleothermometry, the sensitivity of Li/Ca to seawater temperature changes is thus much greater in Li/Ca, therefore, making it an ideal tool to reconstruct temperature variability during the geological past. Using the well-established Mg/Ca proxy on benthic foraminifera combined with Li/Ca ratios, Bryan and Marchitto (2008) significantly improved the correlation with seawater temperature. Based on these findings, Case et al. (2010) presented Li/Mg ratios on corals, correlating with R^2=0.62 with temperature allowing thus for a reconstruction precision as good as ±1.6 °C on (paleo)-temperatures. It was further demonstrated, that the skeleton Li/Mg ratio is independent of salinity and carbonate ion concentration (Raddatz et al. 2013, Montagna et al. 2014). Further studies have improved these earlier findings of the Li/Mg vs. water mass temperature relationship, but also demonstrated that the Li/Ca as well as Mg/Ca ratios in aragonite lattice are possibly influenced by the corals' growth rate and calcification process in addition to seawater temperature (e.g. Raddatz et al. 2013). Experimental work on inorganic calcite precipitation by Füger et al. (2019) confirms this empirical bias when incorporating Li in calcite at variable precipitation rate and pH. Since corals regulate pH internally (Adkins et al. 2003, McCulloch et al. 2012) and the global pH value in the ocean has changed only little by 0.3±0.1 since the last glacial period (Sanyal et al. 1995), the effect of pH on Li/Ca and Mg/Ca ratios in coral skeletons can be considered small but may be considered individually on local hydrographic scales.

Combining the findings of the latter mentioned studies, Hathorne et al. (2013) investigated Li/Mg ratios on *Porites* and presented a negative correlation with local seawater temperatures. Further, a single exponential relationship between Li/Mg and seawater temperature, valid for multiple biogenic aragonites has been proposed (Hathorne et al. 2013). Investigating 49 coral specimen, from shallow to deep-water (8-880 m), from tropical to cold-water (0-26 °C) as well as tank cultured specimen, Montagna et al. (2014) established a highly substantiated interspecies, exponential negative correlation (R^2=0.975) of Li/Mg with temperature, with a typically achievable precision of ±0.9 °C (Fig. 2.5).

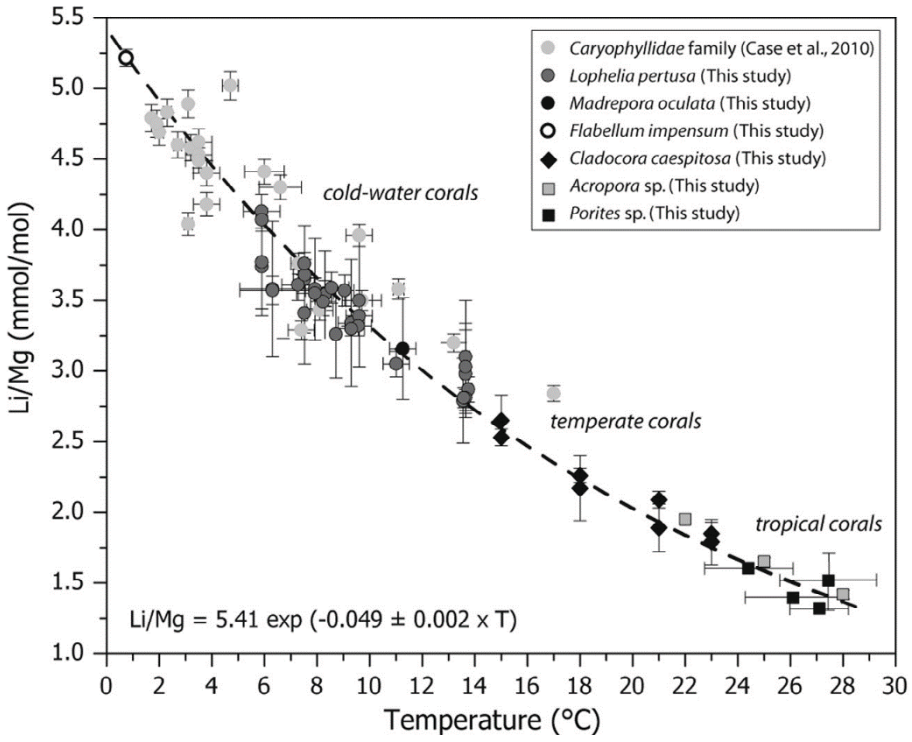

Fig. 2.5: Li/Mg temperature calibration curve (Montagna et al. 2014).

In addition, Montagna et al. (2014) investigated the inter-skeletal, micro-scale variations and differences of Li/Mg compared to Li/Ca and Mg/Ca in the thecal wall of *L. pertusa* (*D. pertusum*). The latter two ratios are heavily influenced by crystal-growth and show elevated values in the fast-growing centre of calcification (COC) compared to fibrous aragonite overlying the COC (Case et al. 2010, Raddatz et al. 2013). The fibrous part of the thecal wall, characterized by low Li/Ca and Mg/Ca potentially reflects lower growth rates, close to thermodynamic equilibrium and likely shows unbiased environmental signals, being best suited for geochemical analyses (Montagna et al. 2014).

The Li/Mg temperature proxy has been successfully applied on CWC specimens of the species *L. pertusa* (*D. pertusum*) off the coast of Norway (Raddatz et al. 2016). Similar patterns were found in reconstructed Li/Mg bottom water temperatures compared to the established foraminifera (species: *Neoglobquadrina pachyderma* (sinistral) cold-water planktonic foraminifera) Mg/Ca Sea Surface Temperature (SST) proxy and faunal assemblages (Raddatz et al. 2014, Raddatz et al. 2016).

Recent studies have shown more structural difficulties concerning organic green bands and diagenetic calcite deposits within the aragonite coral skeleton (e.g. Cuny-Guirriec et al. 2019 and references therein). The former, found in some tropical corals specimen, revealed anomalously high Mg/Ca ratios and consequently low Li/Mg values, overestimating temperatures by 15 °C. Whereas the calcite deposits have been found in CWC, affecting the Li/Mg temperature sensitivity by ~1.5 °C/1% calcite (Cuny-Guirriec et al. 2019). Based on the fundamental work of Montagna et al. (2014), a revised Li/Mg temperature calibration was recently published by Cuny-Guirriec et al. (2019; Fig 2.6), confirming the findings of Montagna et al. (2014) and refining the exponential calibration with a correlation of R^2=0.99.

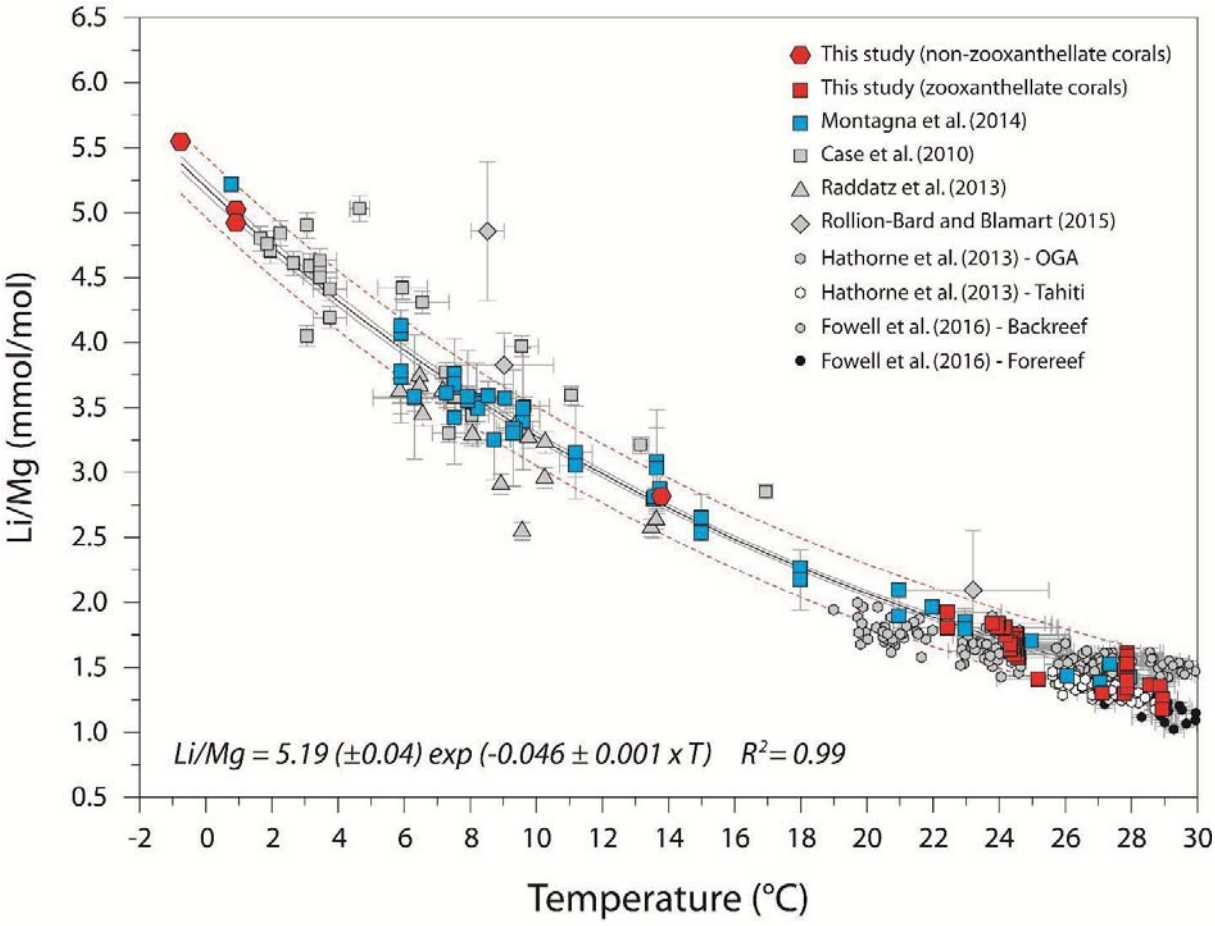

Fig. 2.6: Revised Li/Mg temperature calibration curve (Cuny-Guirriec et al. 2019). Calibration curve is comprised of warm water and cold-water corals.

The uncertainty of the temperature estimates increase with rising temperatures (±0.9 °C at 1 °C, ±1.5 °C at 12 °C and ±2.6 °C at 25°C), this results in highest uncertainties with temperature reconstruction on corals from tropical areas. The interspecies overall uncertainty across Antarctic to tropical environments is stated with a standard error of ±1.0. Here, the improved calibration was used to determine ambient water temperatures bathing the studied CWC based on their skeleton Li/Mg ratios (see Chapter 4).

2.6 Methods: Observation tools and coring gear

2.6.1 Multibeam Echosounder

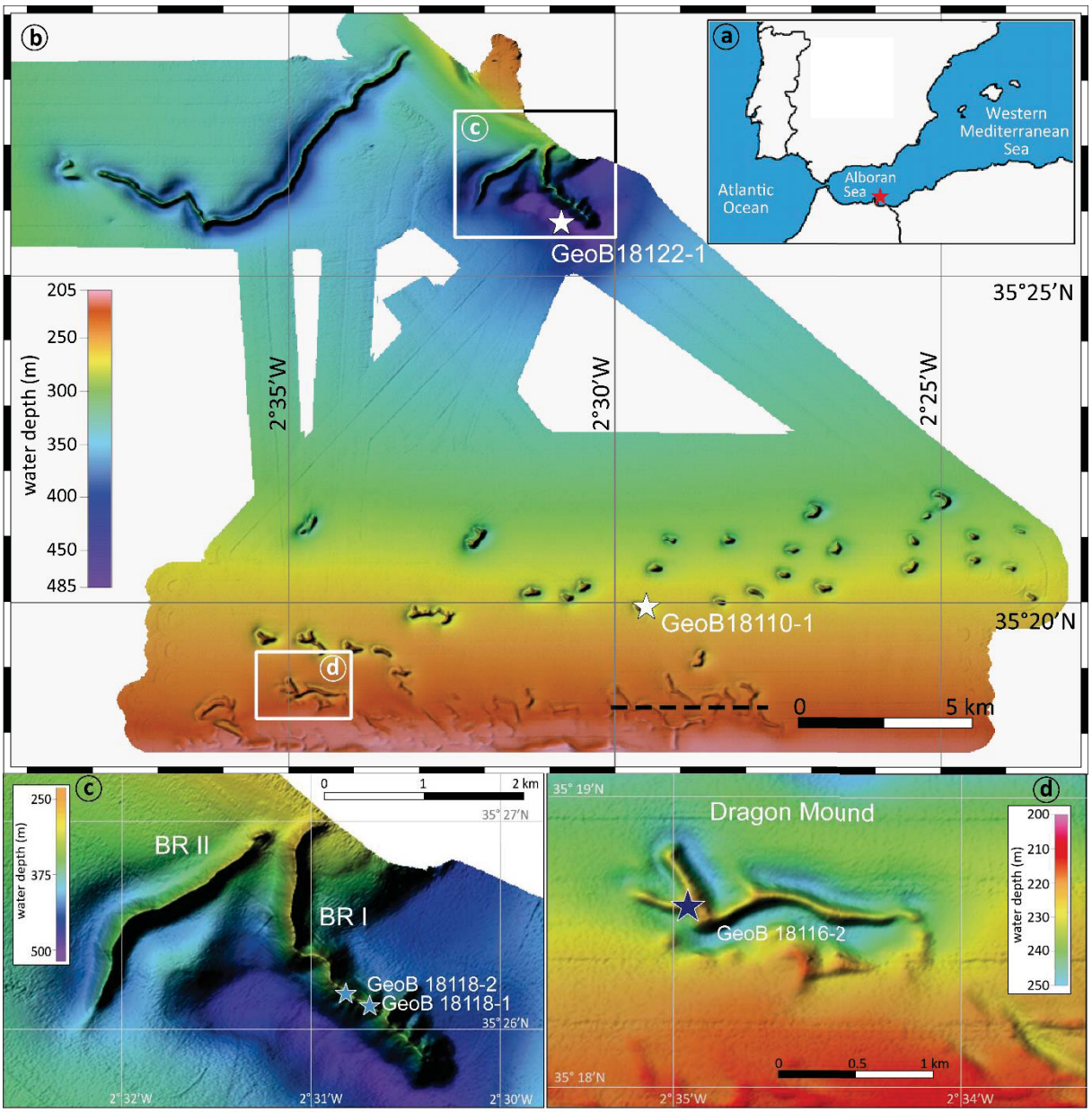

Fig. 2.7: (a) Overview map, including the location of EMCP in the Alboran Sea. (b) Multi-beam bathymetric map of the EMCP with a 25 m grid resolution. Box (c) and (d) show a close up of the core locations (GeoB18118-1, GeoB18118-2 and GeoB18116-2) and the mound topography. White stars indicate the locations of CTD stations (GeoB18122-1 and GeoB18110-1) used in Chapter 4. Parasound profile (Fig. 2.8) is indicated by black dashed line. (c) Topography of Brittlestar I (BR I) and on mound core locations GeoB18118-1 and GeoB18118-2. (d) Topography of Dragon Mound (DM) and on mound core location GeoB18116-2. Map is modified after (Hebbeln 2019).

Highly resolved maps of the seafloor, revealing topographic features like coral mound structures (Fig. 2.7), are produced by using a ship-mounted Multibeam Echosounder. The data, used for Fig. 2.7 was produced during MSM36, where depending on deep or shallow to medium water depths, low (12 kHz) and high (95 kHz) frequencies and pulse lengths between 0.2-2 ms were used to achieve resolutions as low as 2-8 m (Hebbeln et al. 2015). The seafloor is then scanned in predefined grids. The result, as seen in Fig. 2.7 is a map with different shaped structures of various sizes and their highly defined erosional moats around them (Hebbeln 2019).

2.6.2 Parasound

Using parasound prior to the drilling verifies the coral bearing nature of seafloor structures. Two primary high-frequency signals are emitted towards the seafloor. A secondary low frequency, reflected from the seafloor is received by ship-mounted detectors (piezo-crystals). Fig. 2.8 displays a parasound profile showing seafloor sediment structures and partially buried coral mounds in the Alboran Sea. Undisturbed, homogenously deposited sediments show the same reflection time (black areas) whereas inhomogeneous, disturbed sediments and coral mounds, where parasound is deflected, are displayed in white.

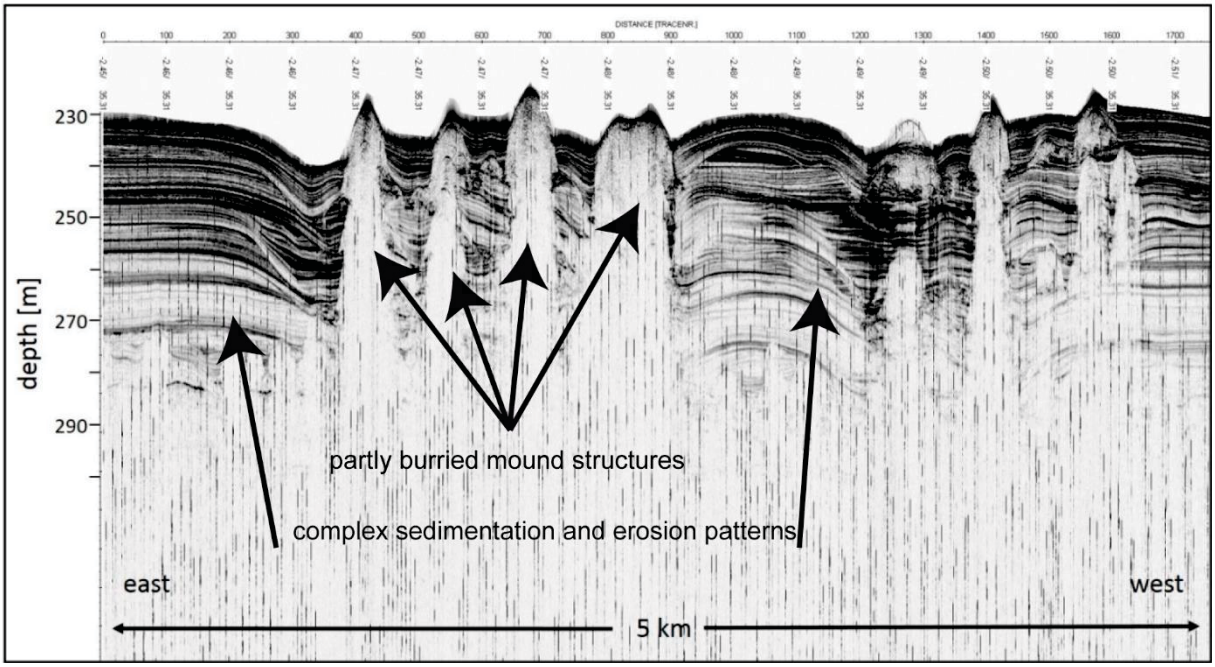

Fig. 2.8: Parasound Profile, shown by dashed line in the multi-beam map (Fig. 2.7). Multi beam map shows elongated and partly buried mounds. Parasound reveals "christmas tree" like structures of the mound and a complex pattern of erosion and sedimentation in off-mound sediments. The given depth is based on a uniform sound velocity of 1500 m/s Modified after Hebbeln et al. (2015).

2.6.3 Coring gear

Upon finding a suitable location, depending on the research question, various sampling methods have been used in the last decades to retrieve coral samples. For an in-situ impression of the seafloor and the state of corals on-site, Remotely Operated Vehicles (ROV) are deployed, providing live-video transects of the location (Fig. 2.9a). Additionally, equipped with robotic arms and sample boxes, ROVs can selectively collect single coral specimen (Fig. 2.9b). Using a Van Veen Grab Sampler or box-corer, both devices close upon impact on the seafloor, retrieve undisturbed surface samples of 20 to 50 cm depth below seafloor (Fig. 2.9c). Studying the spatial distribution of coral growth in mounds, commonly Gravity Corers (GC) are used (Fig. 2.9d). A metal pipe (Ø12 cm) of various lengths (5-10-15 m) is attached to an up to 2 t heavy weight (so-called "bomb"). The metal pipe is fitted inside with a plastic liner, which after successfully deploying the GC contains a full of corals and/or sediment sequence. The tip of the metal pipe is closed off by the core catcher, a sharp-bladed metal sheet. Hanging outboard from a winch, the GC is released with up to 1 m/s towards the seafloor, where it penetrates the coral mound. Depending on the density of the sediment and the speed of penetration, the GC can over-penetrate or get stuck. Aboard, the liner is commonly cut in 1 m segments and sawn into 2 halves, one for the archive and one for scientific analysis (Fig. 2.9f and 2.9g).

As previously mentioned, coral mounds can built up 300 m or higher representing thousands or even millions of years of coral growth. The first 5 to 10 m sampled by GCs, mostly reflect the last reef growth phases of the mound but do not show the long term development of the mound. To gain more insight and possibly drill to the base of a coral mound, one approach is the use of a drillship, like the JOIDES RESOLUTION. During IODP Expedition 307, Challenger Mound, on the Irish Margin was successfully drilled to the base (155 m) and revealed discontinuous coral growth over 2.6 Ma (Kano et al. 2007). Another, less costly method with less logistical effort, is the MARUM seafloor drill rig MeBo (MeeresbodenBohrgerät; Fig. 2.9e) (Freudentahl and Wefer 2010, Wefer and Freudentahl 2016), as used in the research cruise MSM36 MoccoMeBo (Hebbeln et al. 2015). Equipped with two core barrel magazines, each barrel, including a plastic liner within, has a length of 2.35 m and a drill head for coring (Fig. 2.10). MeBo can drill 70-77 m with the old configuration (Hebbeln et al. 2015) or up to 200 m with the modern setup (MeBo2).

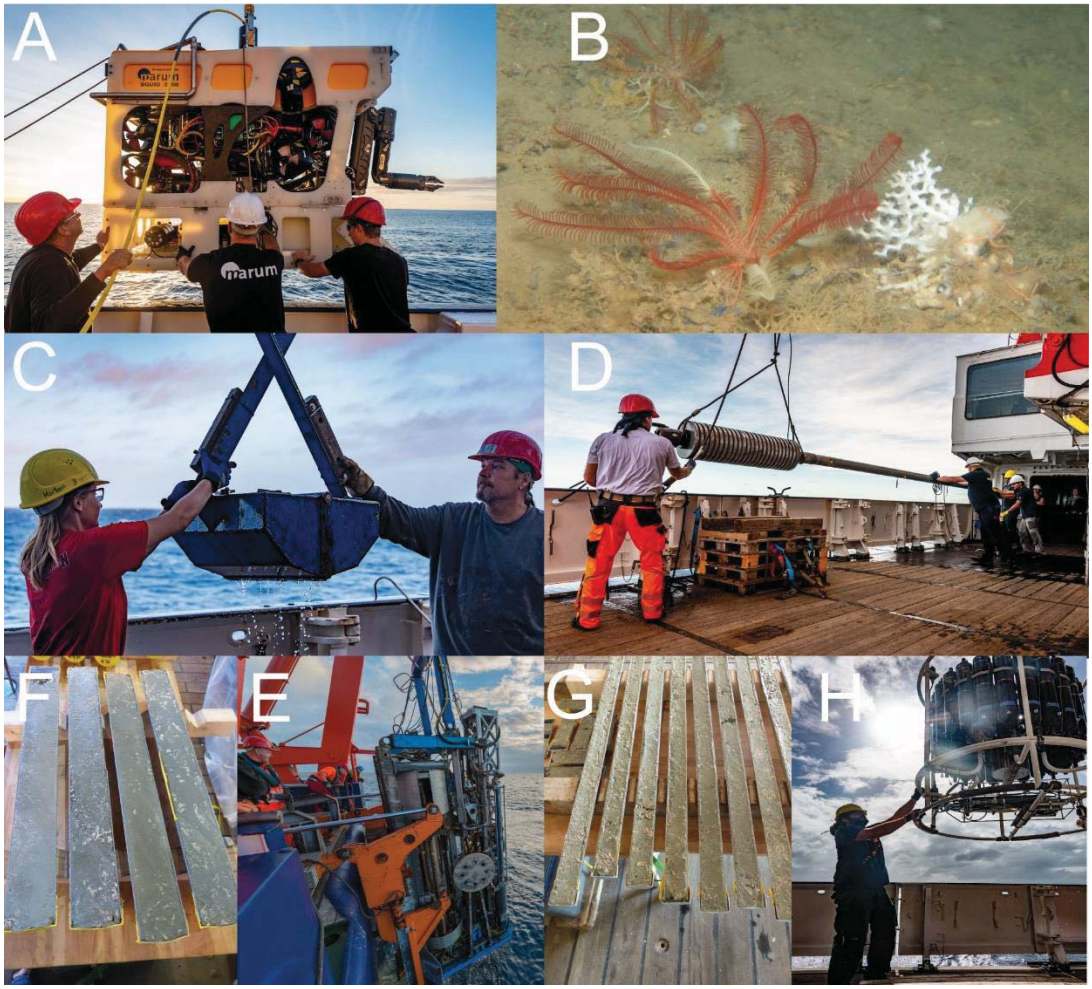

Fig. 2.9: Variety of introduced sampling gear. (a) ROV used during M151. (b) live corals in the Alboran Sea (Hebbeln et al. 2009). (c) Grab sampler used during M151. (d) Gravity Core (M151). (e) Opened coral bearing gravity cores (MS36). (f) MeBo, recovered after deployment. (g) MeBo coring rods unopened (MS36). (h) Opened coral bearing MeBo cores (MS36). Pictures were taken during different research cruises (MS38 and M151). Copyright belongs to Volker Diekamp, Thorsten Klein, ROV Cherokee, MARUM.

MeBo is deployed from the back of a ship and lowered by a 2000 m long winch onto the seafloor. Safely landing MeBo on a coral mound is difficult, since a flat angle of maximal 2° is necessary to maintain an upright position for drilling (Freudentahl and Wefer 2010, Wefer and Freudentahl 2016). Once landed and stabilized, a full 70 m drill takes up more than 24 h. Changes in the sediment fraction towards finer sediment down the core and adjustments in water pressure, necessary for the drilling process can lead to the loss of core material. Individual core barrels show a recovery as low as 29% in GeoB18116-2 (Fig. 3.4) and 5.5% in GeoB18118-2 (Fig. 3.6a and 3.6b).

Back on board, the core barrel magazine is emptied. The plastic liners are cut in 1.2 m sections, depending on the recovery of the individual liner. The CoreCatcher (CC) is stored in a short liner piece (Fig. 210). If the core is bearing corals, it is frozen prior to sawing, to preserve the core stratigraphy, while splitting it into two halves (Fig. 2.9g). During the research cruise MSM 36, several coral mounds were drilled and a total of 382 m core material was retrieved (Hebbeln et al. 2015).

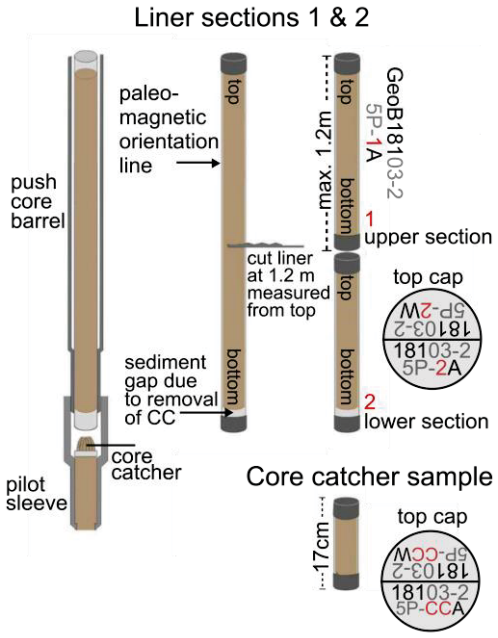

Fig. 2.10: Scheme of MeBo core handling. One core barrel is split in two parts of maximum 1.2 m. The CoreCatcher (CC) is stored in an individual barrel. All core segments are labelled horizontally with Work (W) and Archive (A) halves. Modified after the standard scheme for MeBo cores of the MARUM, used in Hebbeln et al. (2015).

A Conductivity-Temperature-Depth (CTD) profiler with 24 water bottle rosette (Fig. 2.9h) is commonly used to determine the chemical properties of the water masses surrounding the cored mound. Additional sensors beside the name-giving sensors, dissolved oxygen and chlorophyll-a, are usually equipped as well.

3 Climatic and paleoceanographic constraints on long-term cold-water coral growth in the Alboran Sea

3.1 Introduction

Scleractinian framework-forming cold-water corals (CWC) are distributed all over the world's oceans (Roberts 2009, Freiwald et al. 2017) and can form extended geo-bioconstructions known as coral mounds (Roberts et al. 2006, Wienberg and Titschack 2017). The most prominent framework-forming species *L. pertusa* (*D. pertusum*) and *M. oculata* are capable of tolerating a broad range of physico-chemical conditions in the ocean (Freiwald 2002, Roberts et al. 2006, Keller and Os'kina 2008, Freiwald et al. 2009, Hanz et al. 2019). The most important factors influencing the occurrence of CWC are food supply, temperature, salinity, oxygen concentrations, water mass density, pH and aragonite saturation, as well as bottom water dynamics and hard substrate (e.g. Freiwald 2002, Davies et al. 2008, Dullo et al. 2008, Davies and Guinotte 2011, Flögel et al. 2014). Strong near-bottom hydrodynamics and enhanced productivity benefit mound development (Dorschel et al. 2005, Rüggeberg et al. 2007, Wienberg et al. 2010, Eisele et al. 2011, Matos et al. 2015), whereas low dissolved oxygen concentrations appear to hamper coral mound formation (Wienberg et al. 2018). Another important parameter in invigorating or limiting mound formation is the water column structure and water mass circulations at intermediate depth (White and Dorschel 2010, Frank et al. 2011, Raddatz et al. 2014, Matos et al. 2017, Wienberg et al. 2018). Due to the sessile nature of CWC, food particles must be delivered from the surface or through advection by ambient hydrodynamics (internal tides and waves, downwelling, geostrophic currents and mixing processes) (White et al. 2005, Mienis et al. 2007, Davies et al. 2009, Taviani et al. 2016, Wang et al. 2019). However recent studies suggested a rather seasonal diet for CWC than a constant food supply (Van Engeland et al. 2019).

If favourable conditions predominate, successive generations of corals may build up to reefs and consequently to coral mounds (Roberts 2009). However, only a sufficient supply of sediment incorporated into the coral framework and thus supporting it can lead to the three-dimensional structures of CWC mounds. Due to their dependency on sediment supply, coral mounds are so far only recorded on the continental margins (Roberts et al. 2006, Roberts 2009, Hebbeln et al. 2016, Wienberg and Titschack 2017). CWC mounds may form oval to elongated shapes or even ridge-like structures, extending over several hundreds to thousands of meters and may vary in height from a few to hundreds of meters (van Weering et al. 2003, Mienis et al. 2007, Wheeler et al. 2007). In the Atlantic and the Mediterranean Sea, coral mounds, usually found in water depths between 200 to 1000 m, are often arranged in clusters or coral mound

provinces. Consisting of up to hundreds or thousands of mounds, these clusters and provinces shape the seafloor topography (De Mol et al. 2002, Wheeler et al. 2007, Roberts 2009, Wienberg and Titschack 2017, Hebbeln et al. 2019). Mound development can last over periods of thousands to millions of years and provide a unique archive, containing a record of the hydro-environmental variability that prevailed during coral growth and mound formation (Kano et al. 2007, Frank et al. 2011, Raddatz et al. 2014). Distinct patterns of discontinuous coral growth have been found in various mound provinces in the NE Atlantic, most likely the growth patterns are closely related to major climate changes, such as glacial-interglacial variability (Kano et al. 2007, Frank et al. 2011, Raddatz et al. 2014). In detail, CWC growth was predominantly observed during interglacial and interstadial periods, whereas in the Gulf of Cádiz and off Mauretania, CWC growth was predominantly observed during glacial periods (Dorschel et al. 2005, Kano et al. 2007, Wienberg et al. 2010, Eisele et al. 2011, Frank et al. 2011).

In the Mediterranean Sea, most coral mounds are found within the Alboran Sea, along the Moroccan margin (Comas et al. 2009, Lo Iacono et al. 2014, Hebbeln et al. 2019). Parallel to the margin and spanning an area of over 500 km², the Melilla Coral Province is found just north of the Spanish enclave Melilla. The Coral Province is divided into the East and West Melilla Coral Province (EMCP and WMCP; Van Rooij et al. 2013, Lo Iacono et al. 2014). A growing number of studies provided information on CWC occurrence in the Alboran Sea over the past 15 ka and provided first implications on environmental forcing, invigorating and limiting coral growth in the area (Fink et al. 2013, Stalder et al. 2015, Stalder et al. 2018, Wang et al. 2019, Feenstra et al. 2020). High CWC aggregation rates between 70-420 cm/ka during the Bølling-Allerød interstadial and the Early Holocene were correlated: (i) enhanced productivity in AS (Fink et al. 2013), (ii) cold/dense and well-oxygenated bottom water conditions (Stalder et al. 2015). Thirdly (iii) a closer proximity to water mass boundaries, supplying corals with food particles (Wang et al. 2019) and (iv) increased fluvial input, supplying sediment and organic matter (Feenstra et al. 2020).

Although several studies closely investigated the last thriving growth period of CWC in the Alboran Sea and provided possible environmental parameters for enhanced or suppressed CWC growth, the question of a regional to global forcing mechanism remains. Since the Alboran Sea provides vast CWC mounds under the influence of Atlantic and Mediterranean exchange, this area provides a unique environment to study such phenomena. Consequently, the aims of this study are (i) to provide a unique long-term growth history of CWC in the EMCP over the last 550 ka, which is based on the possibility to assess drill cores and collect

an unprecedented amount of U-series ages on pristine coral fragments. As well as (ii) to link the derived temporal pattern of mound formation to basin-wide oceanographic and atmospheric environmental changes over several full glacial-interglacial cycles.

3.2 Regional setting

The Alboran Sea is encompassed by North Africa in the south and by the Iberian Peninsula in the north. In the west, through the narrow Strait of Gibraltar (SoG) (300 m sill depth), the Alboran Sea is connected to the Atlantic Ocean and opens to the east into the Algerian Basin. Three distinct water masses, the Modified Atlantic Water (MAW), the Levantine Intermediate Water (LIW) and the West Mediterranean Deep Water (WMDW) are found in the Alboran Sea (Millot and Taupier-Letage 2005). CTD data obtained close to the sample locations, match the published physical parameters of MAW and LIW (Fig. 4.2) with water mass boundaries of MAW/LIW residing in 250 and 160 m water depth. The core locations within the EMCP are marked in Fig. 3.1a. Mound topography is shown in Fig. 3.1b and Fig. 3.1c.

The Mediterranean Sea is generally characterized as oligotrophic (Morán and Estrada 2001, d'Ortenzio and Ribera d'Alcalà 2009). The Alboran Sea, considered an exception, shows the highest marine productivity and quasi-permanent areas of upwelling. These dynamics are controlled by local hydrography, like vertical mixing along the northern edge of the West Alboran Gyre (WAG), along the Almeria Oran Front on the eastern side of the East Alboran Gyre (EAG) (Fig. 2.1) as well as atmospheric circulation, causing wind-induced upwelling (Garcia-Gorriz and Carr 1999, Sarhan 2000, Dafner et al. 2003, d'Ortenzio and Ribera d'Alcalà 2009). Biogenic material is transported both vertically and horizontally within the gyres in the Alboran Sea (Sarhan 2000, Baldacci et al. 2001). Sediments found in the Alboran Sea are comprised of aeolian dust, transported from the Sahara (Stuut et al. 2009, Terhzaz et al. 2018) and fluvial input, originating primarily from the Iberian Peninsula and the Moroccan hinterland (Fabres et al. 2002, Terhzaz et al. 2018). The largest Moroccan river, Moulouya River, with a pre-dam sediment load of 12-13 megaton/year (Mt/a), enters the Alboran Sea some 50 km east of the investigated location (Snoussi et al. 2002). The river drains predominantly through sedimentary bedrocks of the high and low Atlas Mountains (Snoussi et al. 2002).

Along the Moroccan margin, a large amount of CWC mounds were discovered over the last decade (Comas and Pinheiro 2007, Lo Iacono et al. 2014, Lo Iacono et al. 2018). Based on the geographical position from west to east three coral provinces, the West Melilla Coral Province (WMCP), the most prominent East Melilla Coral Province (EMCP) and the Cabliers Mounds

were created. Today, coral occurrence is limited to the EMCP with isolated patches of corals and to the Cabliers Mounds with flourishing coral reefs (Hebbeln et al. 2009, Corbera et al. 2019). The EMCP within the grey box (Fig. 3.1a) is comprised of three subsections. In the northern section (light blue star), predominantly large coral ridges were found (Fig. 3.1b). The middle section is comprised of oval to arcuate coral mounds and in the southern section (dark blue star, Fig. 3.1c) mainly elongated, partly buried ridges were found (Hebbeln 2019).

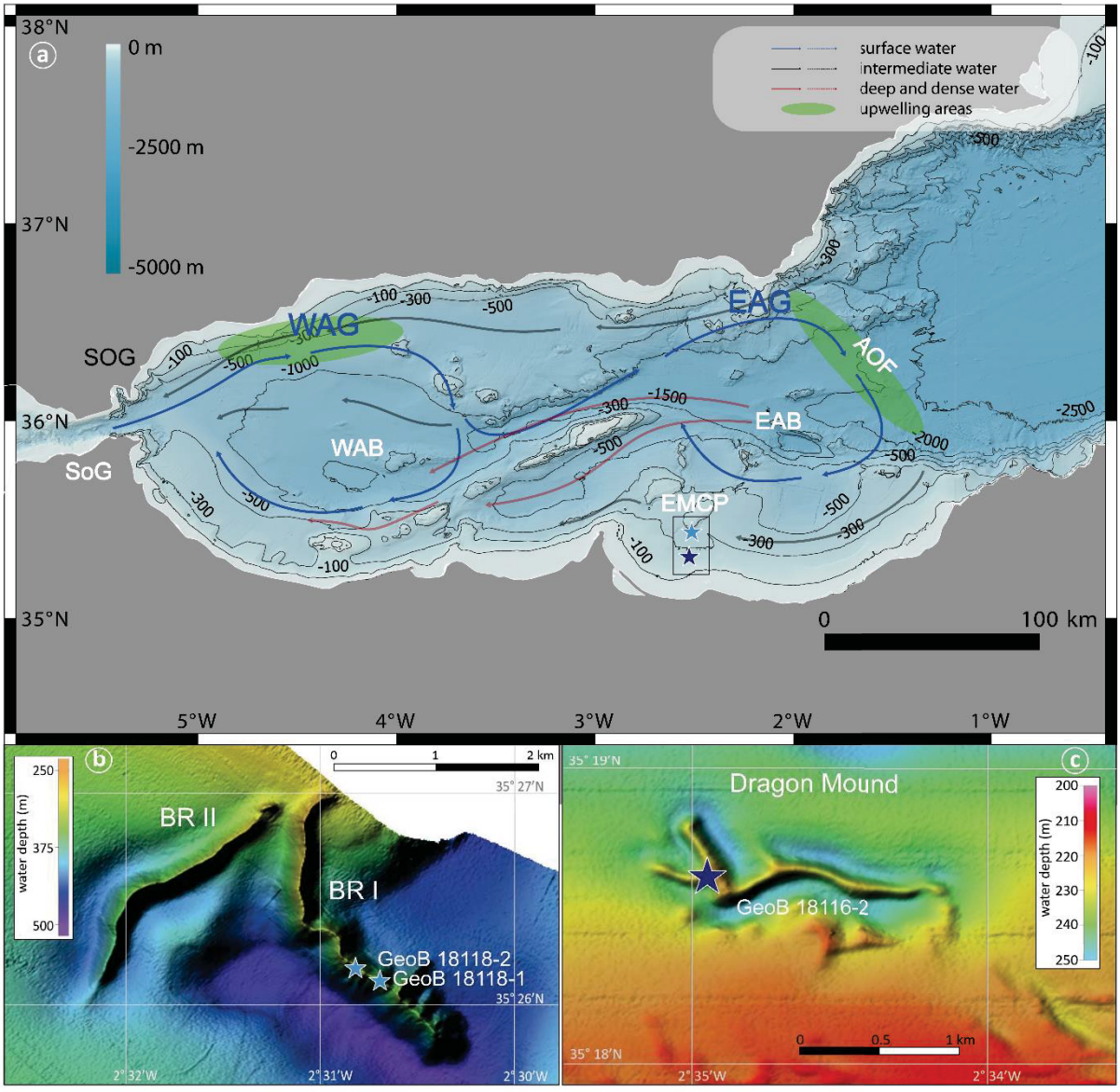

Fig. 3.1: Map of the Alboran Sea and the core locations (a) General overview of the Alboran Sea with water mass flow paths including surface to deep water. Green shaded areas show upwelling with high productivity. (b) Topography of Brittlestar I (BR I) and on mound core locations GeoB18118-1 and GeoB18118-2. (c) Topography of Dragon Mound (DM) and on mound core location GeoB18116-2. Map is modified after (Hebbeln 2019).

3.3 Material and Methods

3.3.1 Samples

In this study, three on-mound cores, collected in 2014 during MSM-36 "MoccoMeBo" cruise aboard the RV Maria S. Merian (Hebbeln et al. 2015), are presented. Two cores GeoB18118-1 and GeoB18118-2 originate from Brittlestar Ridge I (Fig. 3.1b). The gravity core (GC) GeoB18118-1 (35°26.139'N, 2°30.765'W), with a recovery of 873 cm is located in 332 m water depth. In close proximity to the GC, in 329 m water depth is a 5298 cm long MeBo core GeoB18118-2 (35°26.160'N, 2°30.810'W). The second location is south of Brittlestar I. GeoB18116-2 in 236 m water depth (Fig. 3.1c) is a 7147 cm long MeBo core on the partially buried Dragon Mound (35°18.642'N, 2°34.933'W; Hebbeln 2019). Before cutting the cores lengthwise with a saw, the cores were frozen for 24 hours to preserve the sediment and therein embedded coral fragments in place. Based on qualitative visual core descriptions on board, coral fragments were sampled for paleoceanographic multi-proxy analyses in the labs at MARUM, Bremen.

Table 3.1: Metadata of sampling stations (GC – Gravity Corer; MeBo – Bremen drill rig) visited during MSM36 in the Alboran Sea (EMCP – East Melilla Coral Province).

Station	Area	Gear	Latitude [°N]	Longitude [°W]	Water depth [m]	Recovery [cm]
GeoB18118-1	EMCP	GC	35°26.139	2°30.765	332	873
GeoB18118-2	EMCP	MeBo	35°26.160	2°30.810	329	5298
GeoB18116-2	EMCP	MeBo	35°18.642	2°34.933	236	7147

3.3.2 U-series dating sample preparation

The conventional column chromatography method as described in Wefing et al. (2017) was used to extract and purify U and Th from coral samples. The samples were bathed in an ultrasonic water bath and mechanically cleaned, using a sandblaster and Dremel drill. The clean sample material (~50–75 mg) was leached and dissolved in 7M HNO_3. A TriSpike, containing the artificial isotopes ^{229}Th, ^{233}U and ^{236}U, was added to the sample solution. The extraction was done in 1.5 ml columns, filled with 250 µl UTEVA resin and washed with Milli-Q. The column was loaded with 7M HNO_3 and the sample added, consequently the sample was washed in 3 steps of 0.5 ml HNO_3. The sample was eluted into the sample beaker by washing the sample once with Milli-Q and eluted with 0.5 ml steps of 1.5 ml 1M HCl and 1.5 ml 3M HCl. The column was filled with Milli-Q to keep it moist overnight, the sample then was evaporated and re-dissolved in 300 µl 7M HNO_3. Loaded with 7M HNO_3, the second column was processed exactly like the first column with the exception of an additional final

step. 1.5 ml of 1M HF was added in 3 steps and the sample evaporated afterwards. To prepare the sample for the analysis on the Multi Collector-Inductively Coupled Plasma-Mass Spectrometer (MC-ICP-MS), it was dissolved in 2 ml of 1% HNO_3 and 0.05% HF. Blanks were proceeded in the same way as samples, excluding the washing procedure in the beginning and blanks were dissolved in 0.3 ml 1% HNO_3 and 0.05% HF solution for analysis. Analytical blanks achieved values of 0.05 fg for ^{230}Th, 0.3 fg for ^{234}U and 0.005 ng for ^{238}U (80 measurements over 3 years; Heidelberg U-series CWC age database). The mean chemical yield for U is at 98±4% and for Th at 88±8% (Wefing 2016).

Before 08/2015 samples (n=42) were measured on an iCap - Inductively Coupled Plasma Quadrupole - Mass Spectrometer (iCap -ICP-Q-MS) and are marked with (*) in table 3.2. The extraction protocol solely differs in the final dissolution of samples in 0.5M HNO_3, whereas the blanks were treated the same.

3.3.3 Analysis

The isotopes ^{229}Th, ^{230}Th, ^{232}Th, ^{233}U, ^{234}U, ^{235}U and ^{236}U were measured on a Thermo Fisher Neptune Plus MC-ICP-MS at the Institute for Environmental Physics, Heidelberg University (Germany), using a standard bracketing technique (e.g. Arps 2017, Wefing et al. 2017) with the HU-1 standard (Cheng et al. 2000). Achieved HU-1 standard reproducibility is $^{234}U/^{238}U = 0.9997±0.0003$ and $^{230}Th/^{238}U= 1.002±0.005$ (Arps 2017). Average precisions of 1‰ for U ratios and 2.6‰ for Th ratios were achieved (2 SD uncertainty). Coral ages were calculated using the re-determined half-life values of ^{230}Th, ^{234}U, ^{238}U from (Cheng et al. 2000) and references therein.

3.3.4 Quality control

Evaluating the measurement results, the first criteria of quality control is the amount of measured ^{232}Th. Frank et al. (2004), measuring on a thermal ionization mass spectrometer, suggested an upper limit of 10 ng/g for ^{232}Th so that the age correction stays within the uncertainty of the measurement. Since measurements in this study were mainly done on a Neptune Plus MC-ICP-MS, a higher precision of sub-‰ (i.e. ε-) levels were achieved. Hemsing (2017) suggested an upper limit of 1 ng/g for such an improved precision to minimize the effect of ^{232}Th age corrections for corals ranging from recent to 60 ka. However, Hemsing (2017) used an artificial upper limit of 5 ng/g, since using an upper limit of 1 ng/g would have led to a 50% loss of discussable data and the author's samples showed no open system behaviour. Regarding the range of ages (500 to 8 ka) presented in this study, a stepwise

extension of the upper limit for ^{232}Th appears to be necessary, which on first glance may appear an awkward choice. Ages, from recent to 10 ka, show age corrections higher than the measurement uncertainties for ^{232}Th values as low as 1.12 ng/g. therefore an upper limit of 1 ng/g seems appropriate. Only one coral (78 ka) was dated in the age range (~60 ka) of Hemsing (2017), with ^{232}Th values of 3 ng/g, which still is within the uncertainty of the measurement (±100 a), yet an upper limit of 2.5 ng/g seems to be more fitting for corals of that age range with high ε-precisions. Further obtained ages, with ^{232}Th values above the proposed 1ng/g limit, show elevated Th values of up to 7.8 ng/g and range between 140 and 540 ka. Additionally, ^{232}Th contamination is a residue from cleaning, not a strict indication of diagenesis or CWC alteration. Discarded data with ^{232}Th values > 10 ng/g – 20 ng/g show corrections of 0.9 to 2 ka. The former proposed upper limit of 10 ng/g by Frank et al. (2004) is a sensible limit for high ε-precision measurements ranging between 100 ka and 550 ka. Since elevated ^{232}Th values attest for not sufficiently clean coral samples, measurements above this upper limit should be discarded nevertheless. Analysed samples in this study stay well below 10 ng/g. The stepwise increasing limits of 1 ng/g (≤10 ka), 2.5 ng/g (≤100 ka) and 10 ng/g (≥100 ka) have been used for all samples presented in this study.

The second criteria of quality control is the seawater evolution curve of δ^{234}U and the activity ratio ^{230}Th/^{238}U (Fig. 3.3a and 3.5a). The curve is displayed with an initial 10‰ variation of seawater δ^{234}U. CWC within the ±10‰ variation range are considered to show closed system behaviour. After applying both quality control criteria 206 of 278 coral ages remain for discussion, with over 85% below the mentioned 1 ng/g limit for ^{232}Th.

3.3.5 Mound Aggregation Rate

The Mound Aggregation Rate (MAR) is calculated by clustering dated coral fragments down core. From each cluster, the oldest and youngest ages, as well as the highest and lowest depth are taken to determine the MAR (cm/ka) (Fig. 3.2).

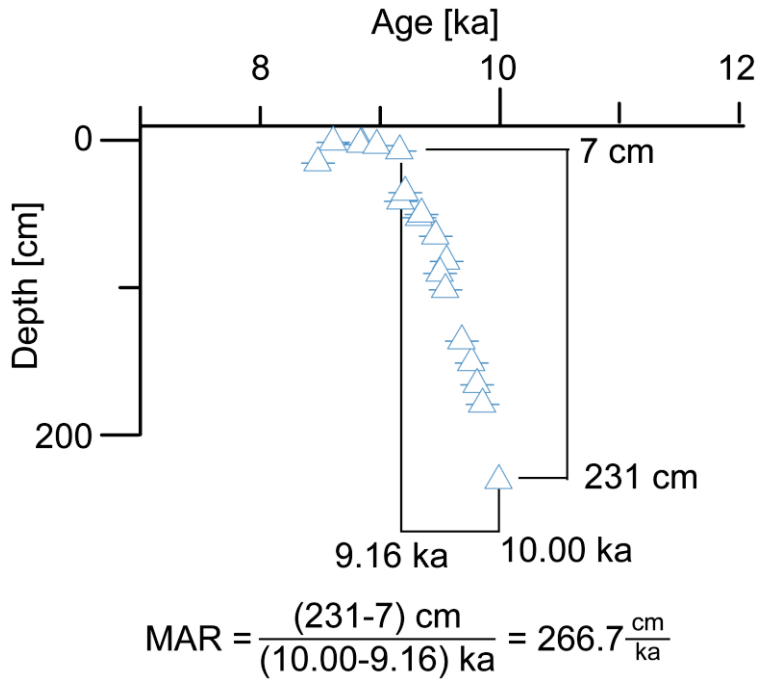

Fig. 3.2: Simplified example of Mound Aggregation Rate (MAR). The deepest and shallowest depth, as well as the oldest and youngest age of continuous coral growth, are subtracted and divided as shown in the calculation. The result shows the vertical MAR in [cm/ka].

The gained rate reflects the vertical accumulated amount of sediment around framework forming coral material in the selected period. MAR does not reflect coral growth directly, since it is not calculated from coral to coral, ignoring minor inversions within the core. In clusters, MAR represents an overall rate of mound aggregation.

3.4 Results

The here presented data originates from up to 7000 cm long cores and is used to reconstruct mound aggregations of the two drilled sites Dragon Mound and Brittlestar Ridge I. The given depths of coral samples and coral clusters is given in cm below seafloor (cmbsf=short cm). The presented data is found in the supplement (Table 3.2).

3.4.1 Mound aggregation of GeoB18116-2 on Dragon Mound

In total, 115 coral fragments from the coral bearing sediment core GeoB18116-2, were analysed. After applying the quality control, 93 fragments remain to be discussed. Only one coral was discarded due to its high ^{232}Th value exceeding the upper limit (Fig. 3.3b), the other 21 discarded samples showed U-series open system behaviour (Fig. 3.3a and Table 3.2 in supplement).

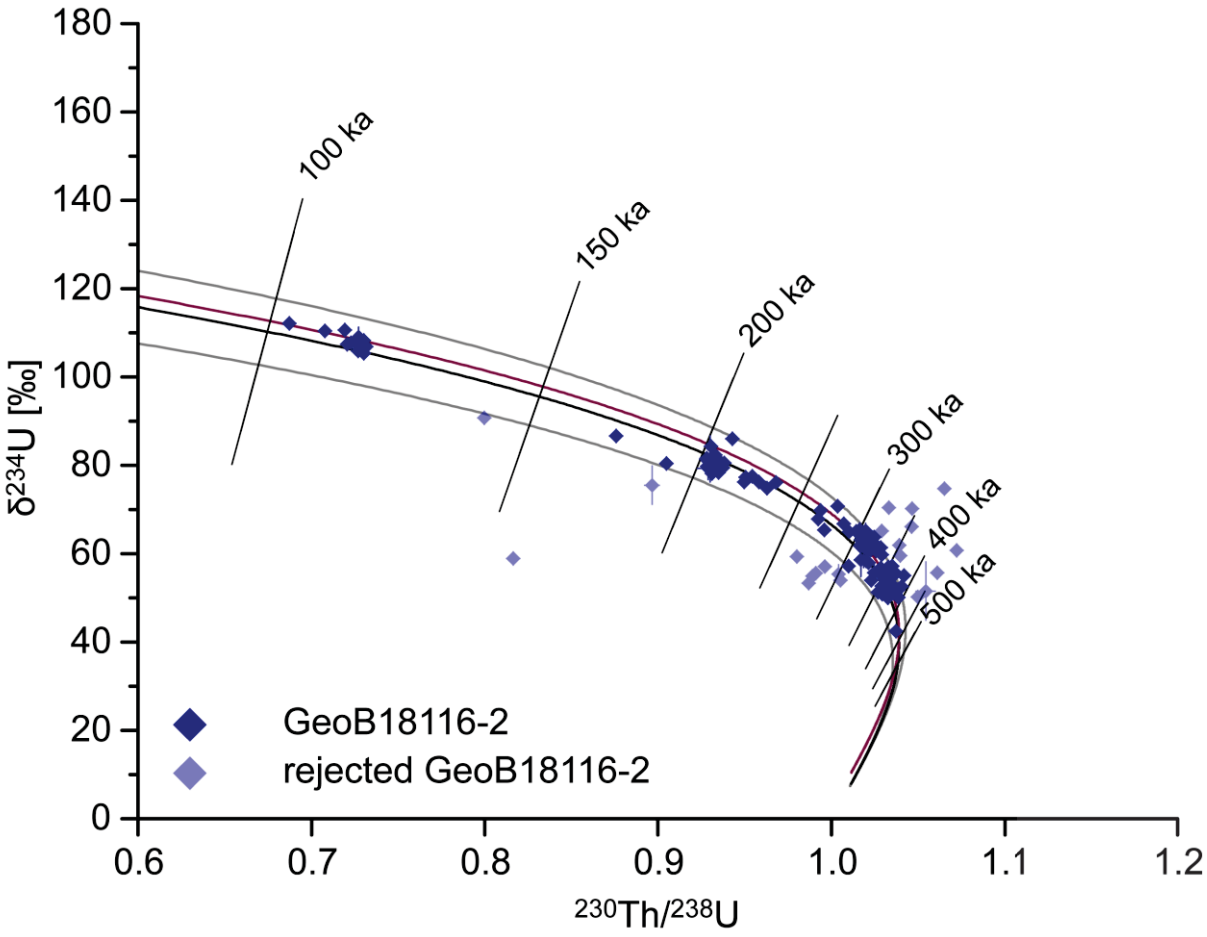

Fig. 3.3a: $\delta^{234}U$ seawater evolution curve for GeoB18116-2 over time. Black curve shows the standard (Atlantic) evolution from the present-day value of 146.8‰ back in time. Samples within the grey lines (±10‰ of the black line) are considered to show closed system behaviour. Note that values on the x-axis start at 0.6. Dark blue rhombus are pristine coral samples revealing closed system behaviour, transparent blue rhombus show open system behaviour and are discarded in further discussions. The red curve shows a modified Mediterranean evolution curve with an assumed modern-day value of ~148.3‰ (Chapter 6).

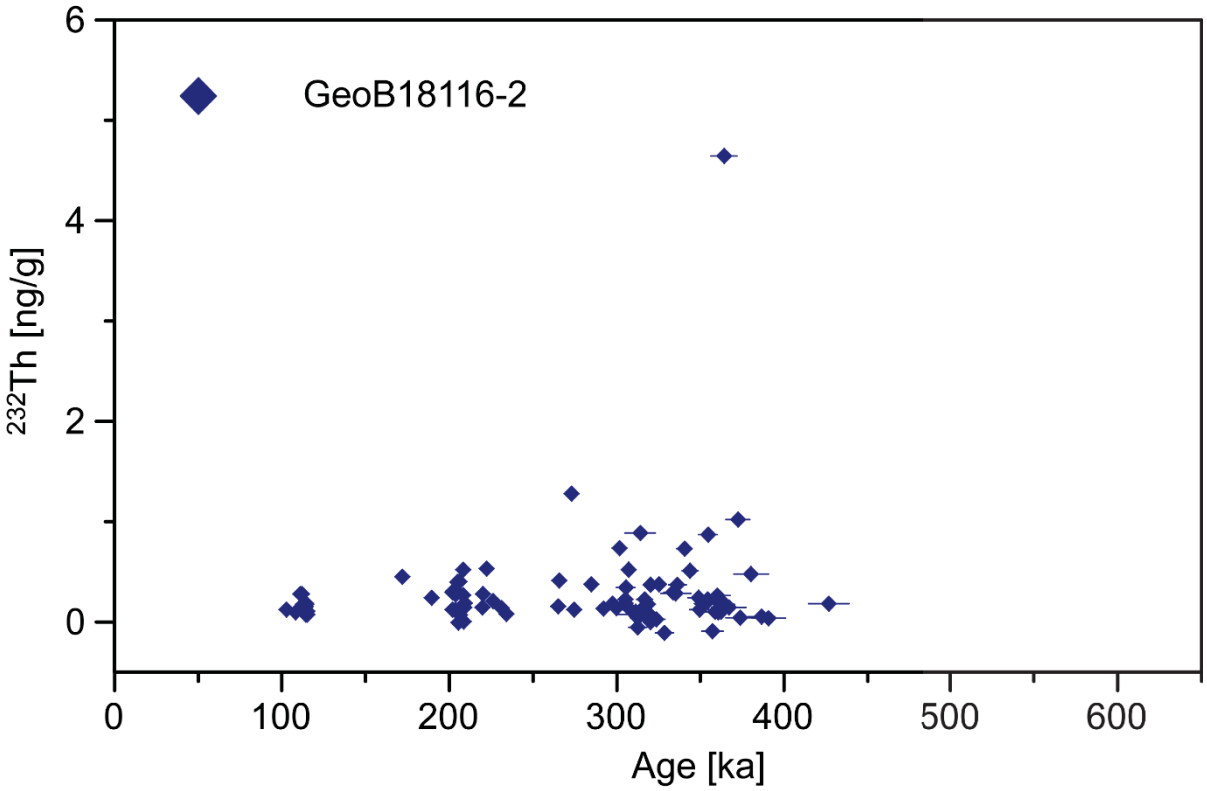

Fig. 3.3b: ^{232}Th values of CWC samples from core GeoB18116-2. For Samples older than 100 ka, an upper limit of 10 ng/g ^{232}Th as part of the quality control was proposed (see text).

GeoB18116-2 core on Dragon Mound is 7075 cm long, with a recovery of 96%. The dominant species is *M. oculata* with rare fragments of *L. pertusa* (*D. pertusum*). Since only the upper 61 m of the core are bearing corals, GeoB18116-2 is the second mound ever to be fully penetrated. The entire age-depth profile over 450 ka is split into three clusters (Fig. 3.4). The first cluster comprises of 56 coral fragments (n=56) and reveals a large scatter in age (420 to 260 ka; 6000 to 2500 cm). In the lower section of cluster 1 (6100 to 4000 cm), the observed age scatter is larger with up to 90 ka than observed in the upper section (3800 to 2500 cm) where age scatter, only ranging 35 ka, is lower. The overall MAR for Cluster 1 is 26 cm/ka.

Between the first and second cluster, missing coral occurrence spans circa 30 ka. The second cluster (n=23), spanning 240 to 200 ka (2300 to 1100 cm) with an overall MAR of 49 cm/ka, shows an age scattering in the lower section (n=8) coinciding with low MAR of 15 cm/ka, comparable to cluster 1. The remaining upper section of Cluster 2 (n=15; 210 to 200 ka), as well as the third and youngest cluster (n=14; 115-100 ka), appear to be in stratigraphic order and show MAR as high as 81 cm/ka and 83 cm/ka respectively. Between the second and third cluster, a possible hiatus of 85 ka is observed. Only one sample was dated at 171 ka during the second gap.

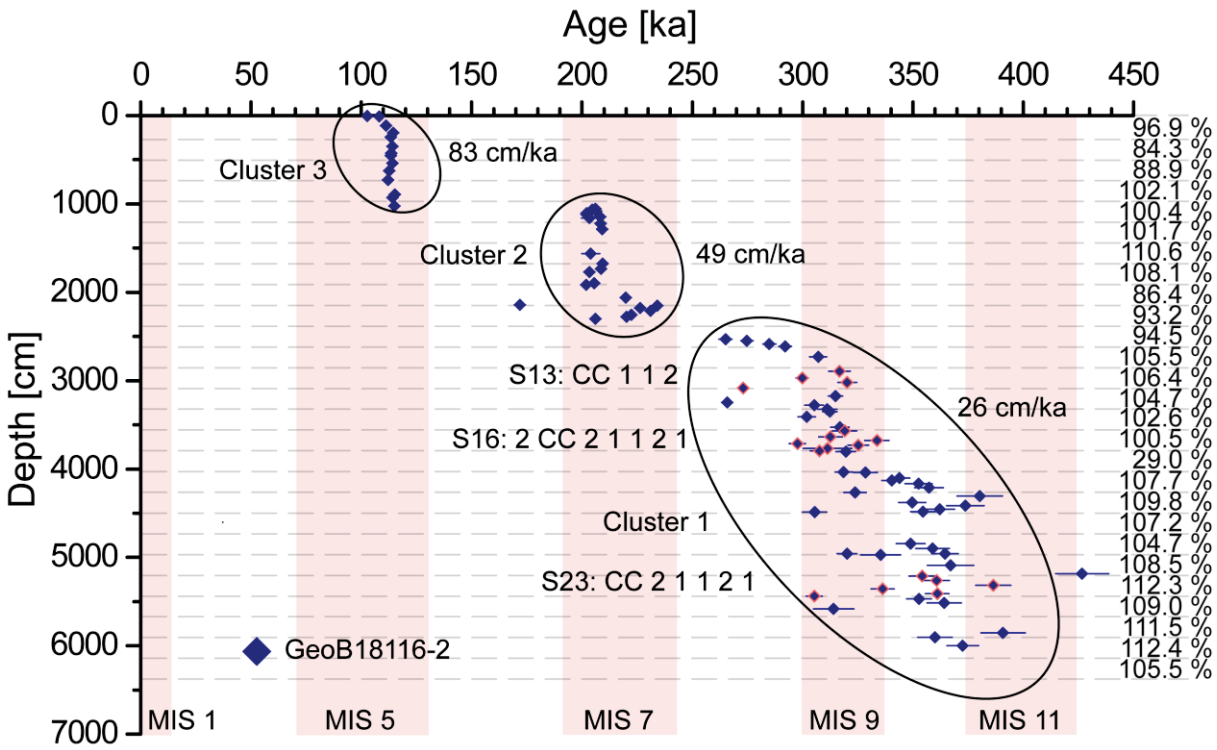

Fig. 3.4: GeoB18116-2 on Dragon Mound (dark blue rhombus). Red framed rhombus show coral ages from individual barrels as explained in Chapter 3.5.1. Samples, originating from one barrel of 2.5 m, e.g. segment S16, lack stratigraphic order with depth. Cluster 1, 2 and 3 show consecutive coral growth periods with calculated MAR [cm/ka]. Dashed vertical bars indicate individual core barrels. Values on the right side show the recovery of each core barrel (e.g. S13: 106.4%, S16: 100.5%, S23: 112%).

It should be noted, that coral ages within individual 235 cm drilled MeBo liners span as much as 80 ka, as shown for individual Segments in Fig. 3.4 (red framed rhombus) and 3.6 (black framed triangles). As shown in Fig. 2.10, the MeBo cores are split into three sections. From core top to core bottom, the barrel segments are labelled 1, 2 and CoreCatcher (CC). As seen in table 3.2, the distribution of age, depth and core number is not systematic in appearance. Potential disturbances, like sample displacement during drilling or sampling processes, can thus be ruled out.

3.4.2 Mound aggregation of GeoB18118-1 and GeoB18118-2 on Brittlestar Ridge I

Sixty-two CWC fragments from Gravity Core GeoB18118-1 were dated. Six samples were measured twice to reduce potential impurities on the sample, as seen by high ^{232}Th values and to achieve higher precision on $\delta^{234}U$. After applying the above-mentioned quality criteria, a total of 56 samples remain for the discussion. For the adjacent MeBo core GeoB18118-2, a total of 99 CWC were sampled and dated. Eleven samples have been replicated due to the reasons mentioned above. Numerous samples were discarded during quality control due to age-related diagenesis, such as skeleton corrosion and remaining contaminating surfaces, leading to U-series open system behaviour, which is shown through comparison with the closed system seawater evolution curve (Fig. 3.5a). A total of 53 samples remain after rigorous quality control, hence only 60%.

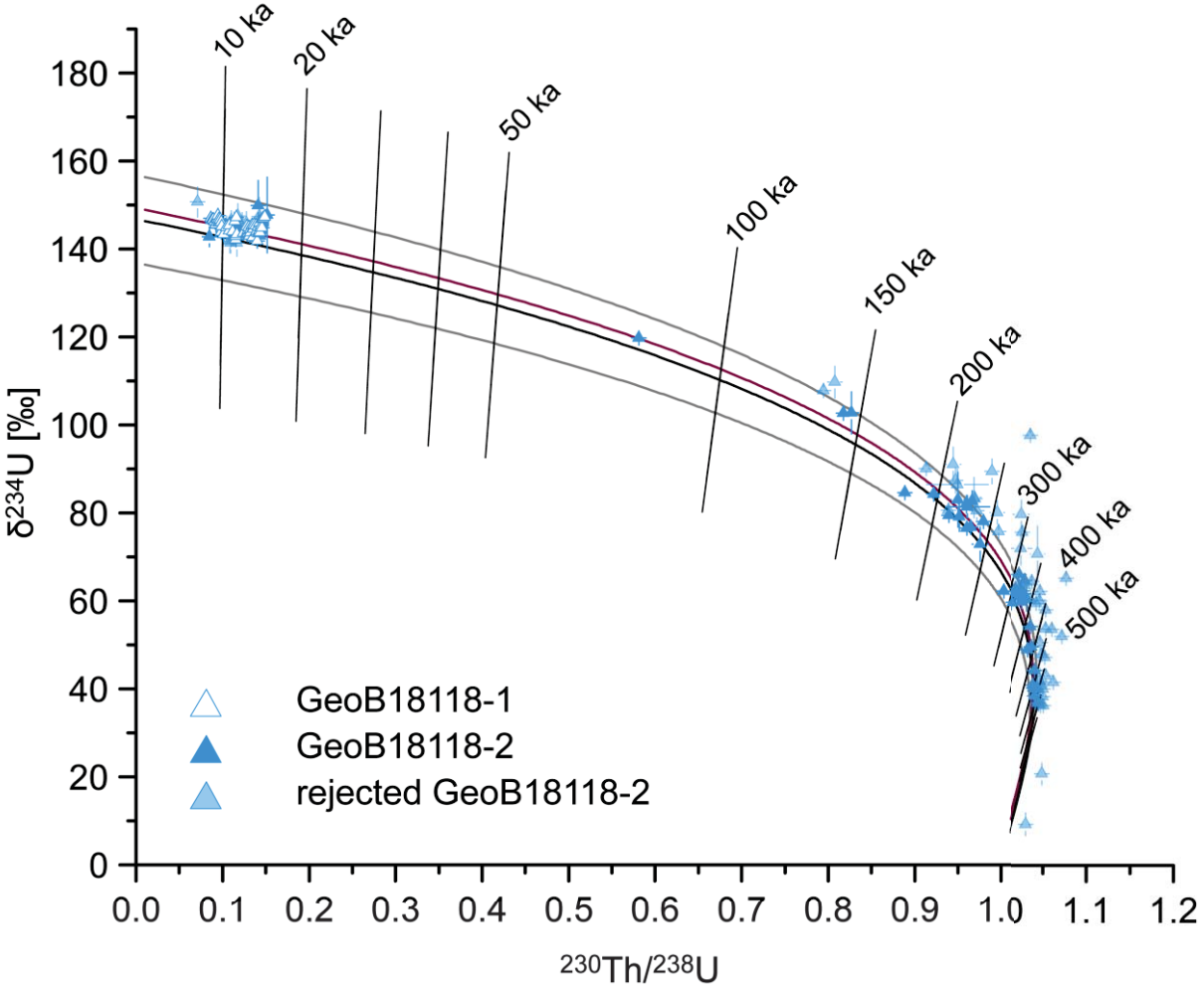

Fig. 3.5a: $\delta^{234}U$ seawater evolution curve for GeoB18118-1 (open light blue triangles) and GeoB18118-2 (light blue triangles) over time. Black curve shows the standard (Atlantic) evolution from the present-day value of 146.8‰ back in time. Samples within the grey lines (±10‰ of the black line) are considered to show closed system behaviour. Light blue triangles and open triangles are pristine coral samples revealing closed system behaviour, transparent light blue triangles show open system behaviour and are discarded in further discussions. The red curve shows a modified Mediterranean evolution curve with an assumed modern-day value of ~148.3‰ (Chapter 6).

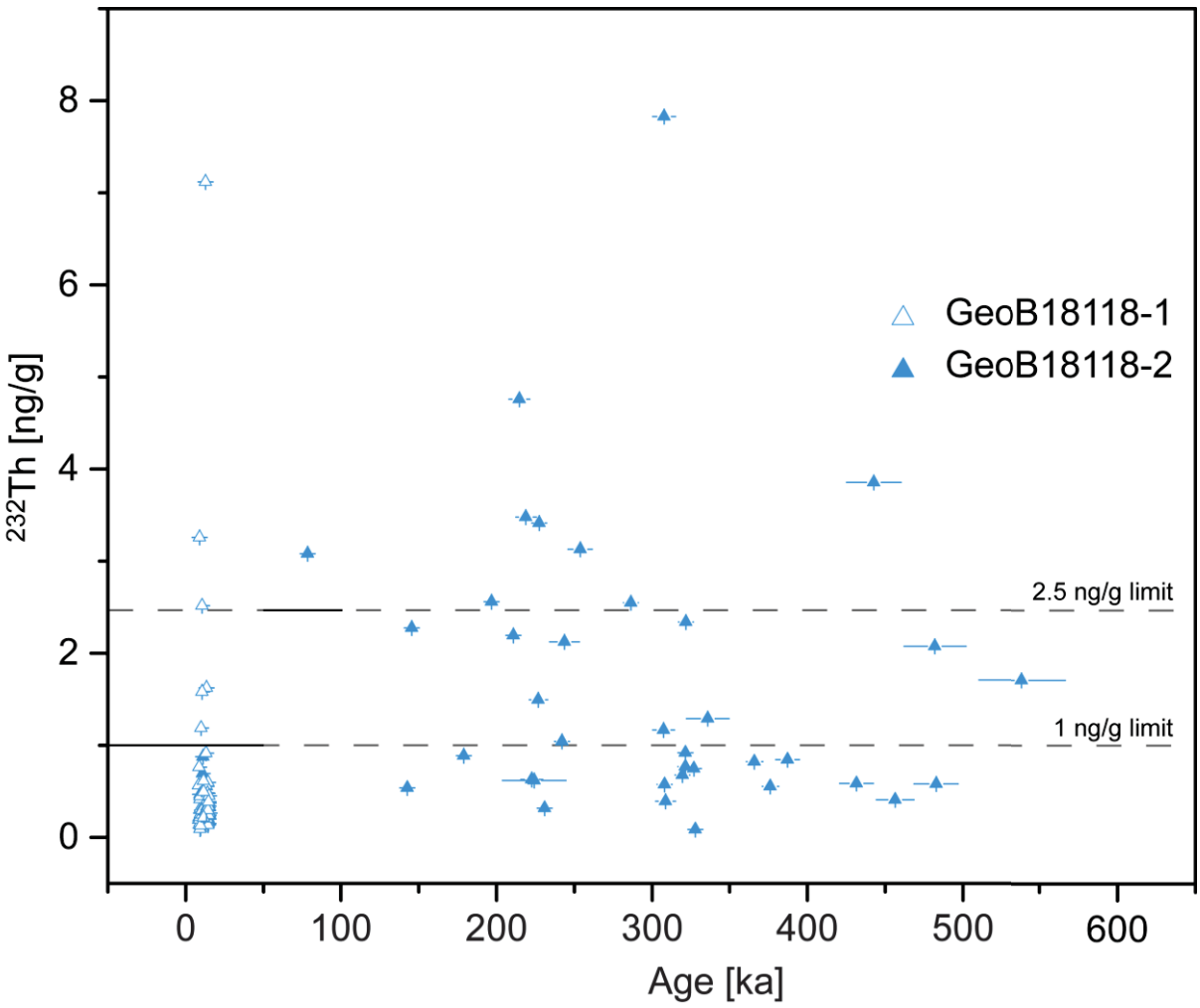

Fig. 3.5b: ^{232}Th values of CWC samples from core GeoB18118-1 (open light blue triangles) and GeoB18118-2 (light blue triangles). Upper thresholds of ^{232}Th concentrations were defined (see text): 1 ng/g (≤10 ka), 2.5 ng/g (≤100 ka) and 10 ng/g (≥100 ka). Solid lines mark limits for the particular time slices.

The dominant reef-building species on Brittlestar I (GeoB18118-1 and GeoB18118-2), are *L. pertusa* (*D. pertusum*) and *M. oculata*. With a recovery of 873 cm (72%), GeoB18118-1 revealed U-series ages ranging from 15.1 to 8.6 ka. No significant age inversions are observed in the age-depth profile (Fig. 3.6a open blue triangle). The only sample, which does not appear in stratigraphic order is at 11.6 ka in 580 cm depth. One sample of the same depth shows an age of 13.4 ka, which is in good agreement with the other samples. This inversion can happen during coring, sampling or analytical treatment and will not be further discussed. Other minor inversions are well within the measurement uncertainties or within possible processes during mound evolution. The here presented results (Fig. 3.6a) can be divided into three clusters. The first cluster, comprised of 31 samples, ranges from 15.1 to 12.5 ka and reveals an overall MAR of ~83 cm/ka, however, MAR as high as 213 cm/ka is observed between 14.7 to 13.4 ka followed by a subsequent slowdown in aggregation towards a possible hiatus during the Younger

Dryas event (YD). The second cluster (n= 8) ranges from the end of YD (11.7 ka) to 10.4 ka with a MAR of 50 cm/ka. The third and last cluster (n=17), spans from 9.8 to 8.4 ka with an overall MAR of 115 cm/ka. However, MAR as high as 210 cm/ka is observed until 9.1 ka, followed by a slowdown in MAR of 21 cm/ka. No coral was dated younger than 8.4 ka in core GeoB18118-1. The overall MAR, spanning from 15.1 to 8.6 ka, is as high as 130 cm/ka.

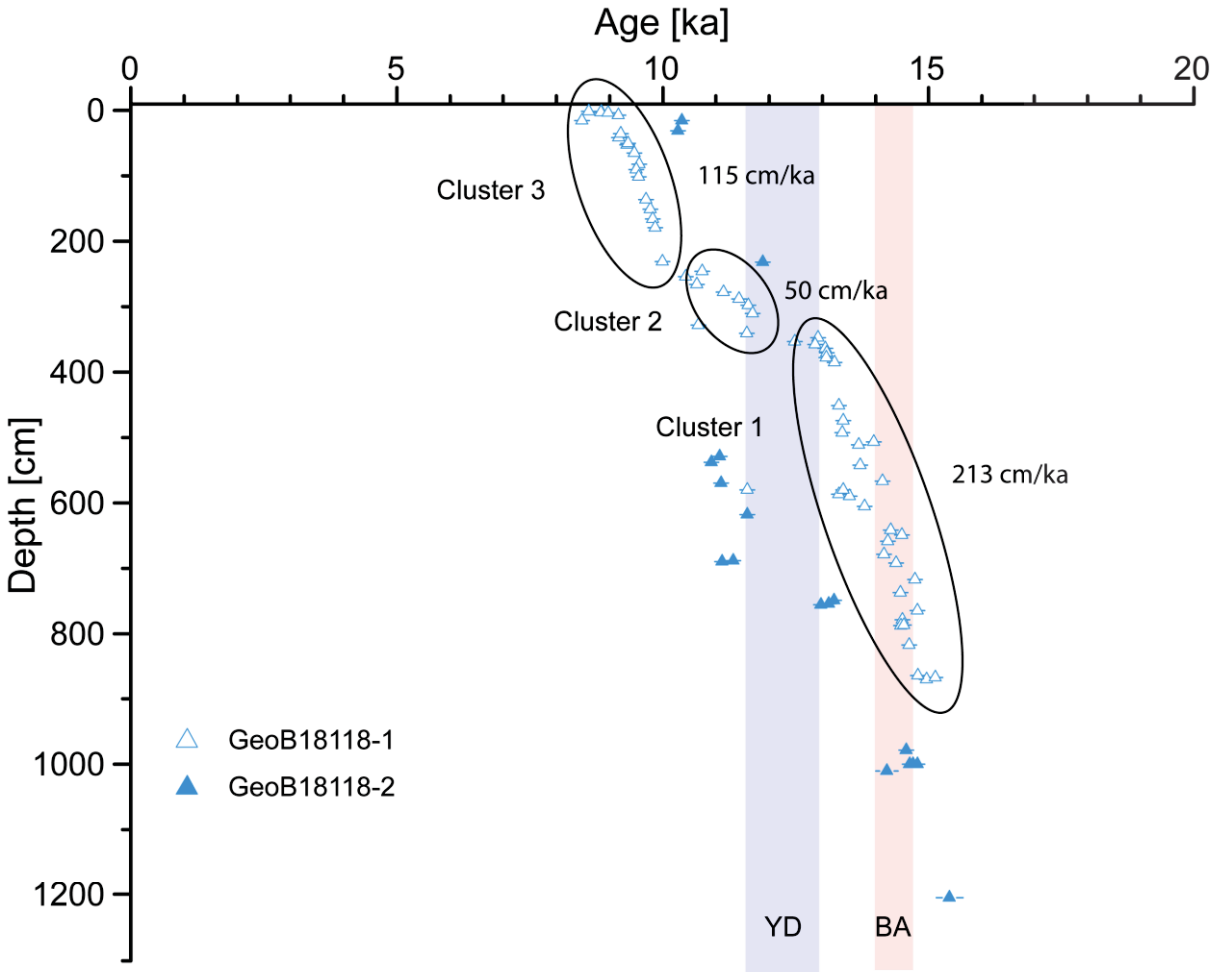

Fig. 3.6a: GeoB18118-1 (open light blue triangles) and GeoB18118-2 (light blue triangles) on Brittlestar I. Cluster 1, 2 and 3 show consecutive coral growth periods with calculated MAR [cm/ka]. The apparent temporal and spatial offset between GeoB18118-1 and GeoB18118-2 emerge due to two separate core drillings.

The 7075 cm long MeBo core GeoB18118-2 with a recovery of 73% reveals an age range spanning from 538 to 8.3 ka, evidencing four age clusters (Fig. 3.6b). The age clusters are separated by possible hiatuses, individually spanning up to 60 ka. The oldest cluster is comprised of 8 coral fragments ranging from 538 to 376 ka and covers a core depth of 1600 cm (7000 to 5400 cm). This cluster shows a large age scatter and several age inversions. Calculated MAR is as low as 10 cm/ka for this cluster. Followed by a gap in the coral record, spanning 1300 cm (40 ka) only one coral was dated at 365 ka (4150 cm). The recovery of core segments around this single coral is 37% (Fig. 3.6b). The second cluster (n= 12) ranges from 336 to 307 ka and reveals a similar MAR of 17 cm/ka. During a 76 ka lasting gap of consecutive coral occurrence (307–230 ka), two corals were dated at 286 ka and 242 ka.

The third cluster is comprised of 12 coral fragments and spans from 253 to 196 ka (3000 to 1686 cm). The recovery in this cluster is relatively high (72%), though in the lower section (up to 2000 cm) a larger scatter, e.g. 43 ka (253-210 ka) within 100 cm of the core can be observed. MAR shows a similar magnitude as the second cluster with 25 cm/ka. The last gap is observed from 196 to 15 ka. This gap has a high recovery of 67%, with two corals dated at 145 and 142 ka (1350-1450 cm) and a single coral at 78 ka (1301 cm). The fourth and last cluster, on the contrary, shows a low recovery of 31%. Nineteen coral fragments are dated from 15.4 to 8.3 ka spanning the upper 1200 cm. MAR is calculated with values as high as 168 cm/ka. Over a timespan of over 550 ka, only a few corals show significant age inversions, e.g. in the second cluster, the youngest coral with 286.5 ka (3900 cm) and a coral fragment in 3100 cm (336 ka, Fig. 3.6b), as well as one coral fragment in 232 cm (11.8 ka) in the fourth cluster (Fig. 3.6a). Regarding the down core age distribution, an increasing age spread over core depth is observed, e.g. the first (oldest) cluster shows a higher spread in ages than the younger clusters (third and fourth).

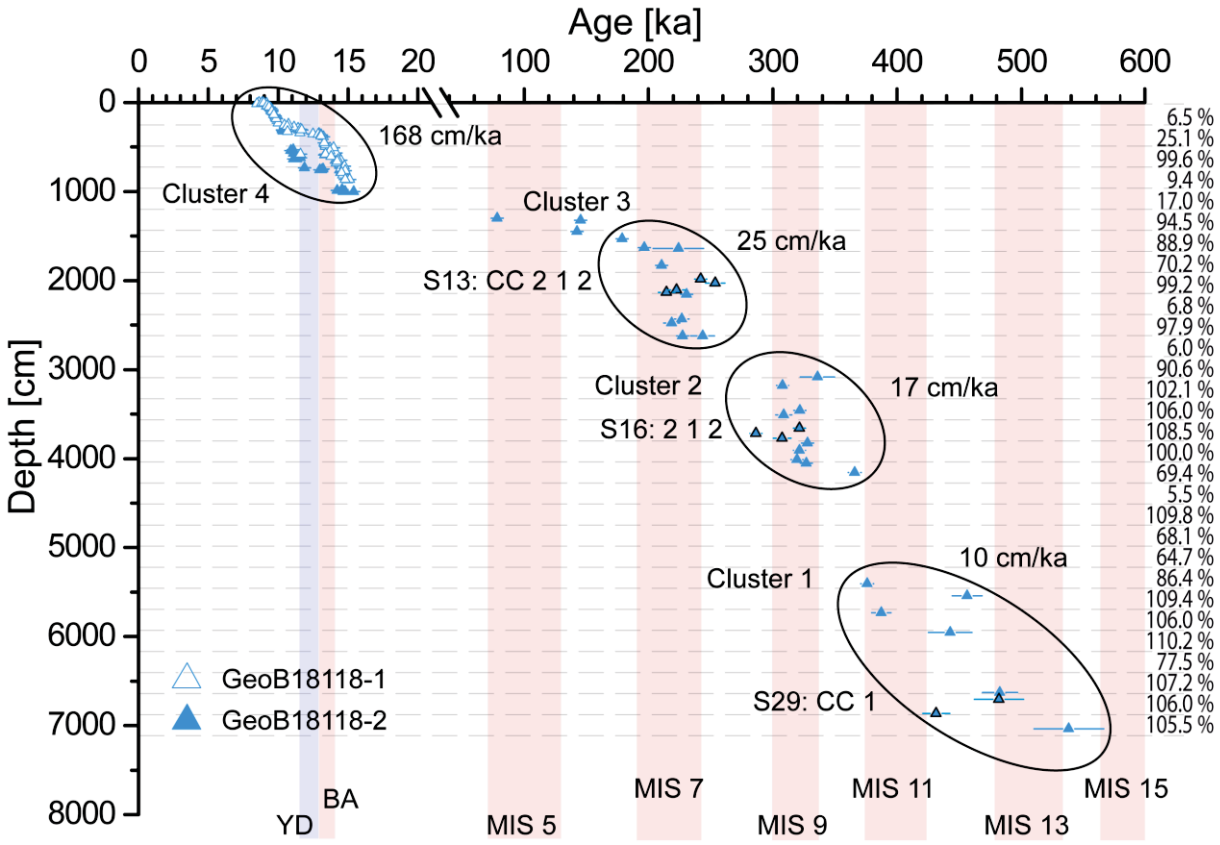

Fig. 3.6b: GeoB18118-1 (open light blue triangles) and GeoB18118-2 (light blue triangles) on Brittlestar I. Black framed triangles show coral ages from individual barrels as explained in Chapter 3.5.1. Samples, originating from one barrel of 2.5 m, e.g. segment S16, lack stratigraphic order with depth. Cluster 1, 2 and 3 show consecutive coral growth periods with calculated MAR [cm/ka]. Dashed vertical bars indicate individual core barrels. Values on the right side show the recovery of each core barrel (e.g. S13: 99.2%, S16: 108.5%, S29: 106%).

The three presented cores (GeoB18116-2, GeoB18118-1 and GeoB18118-2) reveal a discontinuous coral growth during predominantly interglacial periods. Stratigraphic order can be observed in all three cores, which coincide with high MAR of up to 80 and 170 cm/ka over the upper 1000 cm core depth respectively. With increasing depth, the two long MeBo cores exposed increasing scatter.

3.5 Discussion

During the following discussion, GeoB18118-1 and GeoB18118-2 will be referred to as Brittlestar I (BR I), since both originate from the same ridge structure separated by only 1 km. GeoB18116-2 is further referred to as Dragon Mound (DM).

3.5.1 Mound Evolution

The observed age-depth profiles of both sites clearly reflect the discontinuous nature of CWC growth as previously observed on other coral mounds (Freiwald et al. 2004, Roberts et al. 2006, Kano et al. 2007). The observed scatter within each growth phase and the vast spread of ages within individual barrels is visualised by three segments, shown exemplarily for DM (Fig. 3.4, red framed rhombus) and BR I (Fig. 3.6; black framed triangles). The age model of BR I reveals a similar, yet less distinct scatter than observed at the age model of DM. The extent of the observed differences in the patterns, might result from the number of dated corals per mound, inflicting a small bias (DM: n=93; BR I: n=53). Both mounds however, show similar features starting from a depth of circa 2000 cm downwards, which can commonly not be observed in shorter gravity cores (up to 15 m).

The U-series age scatter at depth, observed on DM and partly on BR I, could have been caused either by diagenetic alteration or by mound erosional processes ranging from minor age inversions to mass wasting events. The time of exposure and thus the time for diagenetic alteration increases with the sample age. Therefore, old samples are more prone to show altered coral skeletons. Diagenetic alterations, including the addition or removal of U and Th from the coral skeleton, lead to U-series open system behaviour as seen in Fig. 3.3a and Fig. 3.5a. The Alteration of the coral skeleton may cause sample ages to appear younger or older than their “real” age (e.g. Lomitschka and Mangini 1999, Cheng et al. 2000). However, low ^{232}Th levels, merely constant ^{238}U concentrations of 4±1.5 µg/g, the physical preservation of the fossil fragments, as well as the isotope ratios with the U-series closed system seawater evolution reveals only minor scattering in the DM data and no systematic offset in the BR I data.

The data is thus well within the expected U-series closed system boundaries and therefore, suggests that the observed scatter is not caused by the diagenetic alteration of coral skeletons or U-series open system behaviour. Alternatively, a sedimentological mound history needs to be invoked which can explain the origin of the age scatter with depth.

3.5.1.1 Mound Evolution Model: Dragon Mound

For the mound evolution of Dragon Mound, three main mound evolution processes are proposed: (i) mass wasting events, reflected by large age scatters and a uniform youngest age (timing of the event; Fig. 3.7b). (ii) Erosional processes, resulting in minor mixed-age layers (Fig. 3.7c) and lastly (iii) successive coral growth periods characterized by stratigraphic order and elevated MARs (Fig. 3.7d).

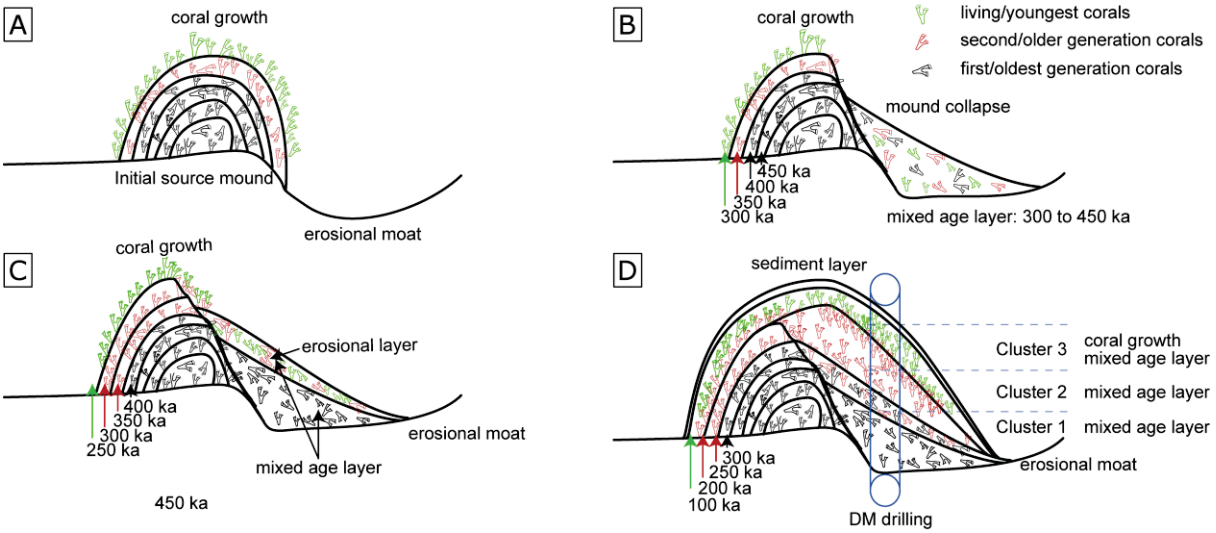

Fig. 3.7: Mound evolution scenario proposed for DM. (a) Initial mound built up with active coral growth. (b) Collapsed mound flank created mixed-age layers. (c) Active coral growth and further erosion create erosional layers with mixed-ages. (d) Active coral growth is diminished by enhanced sedimentation. The core, drilled at the indicated position, would reveal mixed-age samples in the lower part (Cluster 1 and 2) and stratigraphically ordered samples in the upper part (Cluster 3).

As seen on the multi-beam map of DM (Fig. 3.1c) and reported by e.g. Hebbeln et al. (2015), most mounds in the EMCP have very distinct erosional moats, most likely due to strong bottom currents and mound related turbulences (Comas et al. 1999). These moats may lead to instability at the mound basis (Fig. 3.7a) and thus lead to a collapse of the weakened mound slope (Fig. 3.7b). Landslides off the mounds flank could cause a stratigraphically disordered relocation of coral mound material as observed in the first cluster of DM (Fig. 3.7b). Since no age younger than 300 ka was dated in the first cluster (6100 to 3500 cm), however, multiple samples dated at 300 ka are distributed throughout Cluster 1 (e.g. 5500, 4500 and 3500 cm), a mass wasting event, centred around 300 ka is proposed to have caused the observed age scatter at the base of DM. The upper part of Cluster 1 (3500 to 2900 cm) revealed a similar age scatter, however to a smaller extent. Thus, the observed age scatter may as well reflect a relocation of coral fragments by either a minor landslide or gravitational redistribution. The first successive coral growth (290 to 260 ka) was observed at the top of Cluster 1 (2500 cm).

The lowest part of Cluster 2 (~2200 cm), similar to the upper Cluster 1, revealed minor age scatter and thus is proposed to reflect erosional processes, resulting in a mixed-age layer (Fig. 3.7c). The upper part of Cluster 2 and Cluster 3 (1900 to 0 cm) represent successive coral growth with stratigraphic order and high MARs (up to 80 cm/ka; Fig. 3.7d). A more detailed explanation of the mound evolution observed on DM is provided in the supplement.

3.5.1.2 Mound Evolution Model: Brittlestar Ridge I

Contrary to DM, no mass wasting events, here associated with core sections revealing large age scatter and a uniform young age limit, were identified in the age-depth profile of BR I. The core site, as shown in the multi-beam map of BR I (Fig. 3.1b), is located on the ridge top. Since BR I spans several km in length and several hundred meter in width, one would expect to find mass wasting like signatures in age-depth profiles along the flanks of the ridge, rather than on the top.

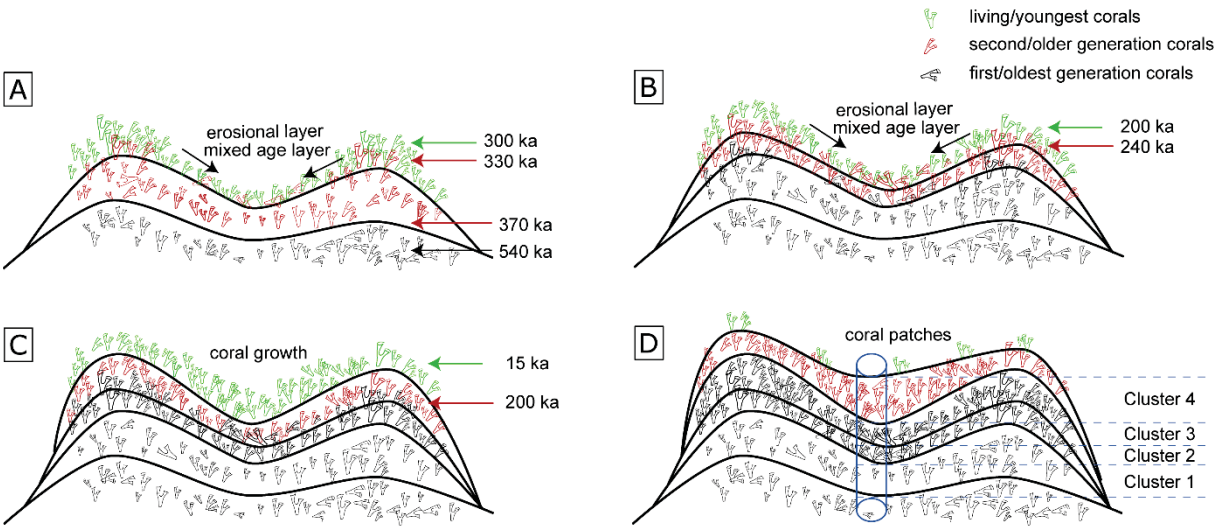

Fig. 3.8: Mound evolution scenario proposed for BR I. (a) Initial mound built up with active coral growth and minor erosion from higher topography. (b) Active growth on top of the former mixed-age layer with further minor erosion from higher topography. (c) Active coral growth after a long period of potentially unfavourable growth conditions (Hiatus). (d) Present-day patchy coral growth. The core, drilled at the indicated position, would reveal minor mixed-age samples in the lower part (Cluster 1, 2 and the lower Cluster 3) and stratigraphically ordered samples (the upper part of Cluster 3 and Cluster 4).

However, the mound evolution of BR I is potentially comprised of (ii) erosional processes, resulting in mixed-age layers and (iii) successive coral growth periods with elevated MARs. Cluster 1 and 2 revealed minor age scatter (Fig. 3.6b, S29; S16) and low MARs (17-10 cm/ka), potentially reflecting erosional processes, redistributing coral fragments rather than successive coral growth (Fig. 3.8a). Mixed-age layers (2500 to 2000 cm) followed by successive

coral growth (1900-0 cm) and MARs ranging between 25 and 168 cm/ka were observed in Cluster 3 (Fig. 3.8b) and Cluster 4 (Fig. 3.8c) respectively.

Erosional processes, like framework collapse, coral debris redistribution due to gravitational deposition and mass wasting events like mound collapses, have been identified to cause age reversals (e.g. Dorschel et al. 2005, Rüggeberg et al. 2007, Eisele et al. 2008, Frank et al. 2009). However, for the first time, detailed mound evolutions spanning several hundreds of thousands of years have been explored. For both mounds, although in relatively close proximity, potentially different types of mound evolution have been identified. On the one hand, BR I appears to be mostly in stratigraphic order, showing only minor erosional influences. DM, on the other hand, shows various mixed-age layers, potentially resulting from mass wasting events and erosional processes as proposed above. Although DM has been fully penetrated, the age scatter observed in the lower sections (6100 to 4500 cm) and the proposed mass wasting origin of the base cluster, suggests that parts of DM might be older than ~400 ka.

The observed differences in mound evolution processes however, may originate from the core location as well. The core location on DM, on a junction between two mound branches and merely 20 m above the seafloor, may be more exposed to coral fragment redistribution, than the core location of BR I on the ridge top (329 m) surrounded by steep flanks, which reach into depths of 400 to 500 m (Fig. 3.1). Therefore, multiple long drillings would be necessary to better assess the 4 dimensional mound evolutions of both mounds. The mound evolutions however, do not explain why coral occurrence is observed during some interglacial periods (for DM: MIS 9, MIS 7, MIS 5 and BR I: MIS 9, MIS 7, MIS 1) and is missing during other interglacial periods (for DM: MIS 1 and BR I: MIS 5). Thus, an oceanographic and atmospheric approach to constrain the drivers of CWC growth in the AS needs to be regarded (Chapter 3.5.3).

3.5.2 Mound Aggregation Rates in the EMCP

Given the proposed scenarios of mound evolution, the calculated MARs for DM need to be differentiated. Here, active aggregation rates represent the successive built-up of coral framework, supported by baffled sediment over a certain time period, i.e. centimetre per thousand years (cm/ka). If mass wasting events are responsible for the deposition of the older clusters of DM (6100 to 3500 cm), the calculated MARs do not represent an active aggregation rate, however a passive aggregation, since a mass wasting event would occur within a short time.

As stated by Frank et al. (2009), MARs of >30 cm/ka reflect densely populated coral mounds during ideal growth conditions, whereas MARs below 5 cm/ka reflect dormant coral reefs and mounds. On DM, Cluster 1 revealed calculated MAR of 26 cm/ka and thus would reflect a densely populated coral mound with successive coral growth over 100 ka (Fig. 3.4). However, the proposed nature of mound aggregation suggests otherwise. The first assumed real coral growth on DM, between 299 and 265 ka (MIS 8), with a calculated MAR of 12 cm/ka, represents less active to dormant coral growth. For Cluster 2 (240 to 200 ka) and Cluster 3 (120 to 100 ka), MARs of 49 cm/ka and 83 cm/ka reflect flourishing, densely populated coral mounds during ideal growth conditions. Similar high growth rates were reported e.g. in the East Atlantic and the Alboran Sea during the Holocene (Frank et al. 2009, Fink et al. 2013, Wefing et al. 2017, Wienberg et al. 2018).

Since BR I does not show major impacts of erosional processes, such as mass wasting events, the calculated MARs more likely represent active mound aggregation. Cluster 1 on BR I (530 to 380 ka), with an overall MAR of 10 cm/ka would thus be considered a less active growth period. However, multiple growth periods may be reflected in Cluster 1 over a 150 ka period, which is comprised of only 8 samples. Cluster 2 (360 to 290 ka) and Cluster 3 (250 to 200 ka) with overall MARs of 17 cm/ka and 25 cm/ka respectively, reflect enhanced coral growth under less ideal growth conditions. However, considering individual growth periods within these clusters, e.g. Cluster 2 (327 to 307 ka), MAR as high as 50 cm/ka can be observed, reflecting a densely populated coral mound. Cluster 4 (15 to 8 ka) however, reflects a flourishing coral mound with an overall MAR ranging between 126 to 168 cm/ka (GeoB18118-1 and GeoB18118-2 respectively). Multiple studies have reported coral growth in the AS during the last 15 ka, with MARs ranging between 100 to even 700 cm/ka (Fink et al. 2013, Stalder et al. 2018, Wang et al. 2019, Feenstra et al. 2020). The available data for the Alboran Sea (EMCP and WMCP) is concurrent for the most recent growth period (15 to ~6 ka).

Hemsing (2017) calculated average MARs (MAR_{av}) for CWC mounds located in the Atlantic Ocean and the Mediterranean Sea from published data. The Atlantic MAR_{av}, based on 53 cores with maximal ages ranging between 1 ka and 2.7 Ma, was calculated with 4.4 cm/ka, whereas for the Mediterranean Sea, the author calculated a MAR_{av} of 27.2 cm/ka, based on 8 cores with maximal ages between 5 and 520 ka. Hemsing (2017) included the here presented core GeoB18118-2 with a maximal age of 520 ka and a MAR_{av} of 13.1 cm/ka. Excluding GeoB18118-2 from the Mediterranean MAR_{av}, results in an overall Mediterranean MAR of 32.9 cm/ka, exclusively representing the coral growth period between 1.7 to 13.3 ka (Hemsing 2017). Thus, only the last 15 ka of coral growth on BR I can be directly compared with the Mediterranean MAR_{av}. For the last 15 ka, GeoB18118-1 and GeoB18118-2 reveal MAR_{av} as high as 126 and 168 cm/ka (Fig. 3.6a and 3.6b), which spectacularly exceed the Mediterranean MAR_{av} of 32.9 cm/ka (27.2 cm/ka; Hemsing 2017).

The overall mound MAR_{av} for GeoB18118-2, with ages between 538 to 490 ka at the bottom (6703 cm/ 7035 cm) and 8.3 ka at the top (15 cm), can be estimated to 13.7±0.4 cm/ka. If the proposed mound evolution of DM is disregarded and a successive mound aggregation is assumed for DM, an overall MAR_{av} of 14.9±0.6 cm/ka can be estimated, with a basal age between 426 and 390 ka and a penetrated mound height of 61 m. Both mounds thus reveal similar MAR_{av} of 14±1 cm/ka. However, this overall rate is the expression of rapid aggregation over short periods (e.g. MIS 5 on DM or MIS 1 on BR I), followed by long periods of dormant mound activities (e.g. MIS 8 or MIS 6 on DM) and possibly erosion, as discussed in detail for coral mound aggregations in the NE Atlantic (Frank et al. 2009). However, the presented mounds reveal higher MAR_{av} than observed in the Atlantic Ocean with MAR_{av} of 4.4 cm/ka (Hemsing 2017). Nevertheless, for a meaningful comparison of Atlantic and Mediterranean MAR_{av}, it is important to compare the same time interval in both locations, e.g. from 550 ka to present.

Furthermore Hemsing (2017) calculated basal ages, based on MAR_{av} for different mound heights in the Mediterranean Sea. According to the author, mounds of 40 m height and a MAR_{av} of 27.2 cm/ka would reveal a basal age of 147 ka, whereas a basal age of 551 ka was estimated for mounds of 150 m height using the same MAR_{av}. In a previous work, Krengel (2016), suggested a basal age of 1 MA ±0.3 for BR I, based on preliminary calculated MARs and a potential maximum height of 160 m (Hebbeln et al. 2015). BR I, is composed of an 80 m elevation above the surrounding seafloor, from which the upper 70 m (GeoB18118-2) revealed ages ranging between 538 to 490 ka and an additionally 80 m deep erosional moat, thus a maximal mound height of 160 m can be estimated. However, it is unknown to which extent

BR I is comprised of coral framework. Thus, based on the MAR_{av} of BR I (13.7±0.4 cm/ka), the basal age is re-estimated for a minimum height of 80 m and a maximal height of 160 m, resulting in a potential onset of mound formation between 595±20 ka and 1190±50 ka respectively. The onset of BR I would therefore coincide with the Mid-Pleistocene-Transition (MPT; 1250 to 700 ka) and thus the onset of the 100 ka cyclicity of glacial-interglacial cycles or shortly after.

3.5.3 Cold-water coral occurrence in the Alboran Sea

Several studies on CWC in the Alboran Sea have shown flourishing coral growth during the last 15 ka (Schröder-Ritzrau et al. 2005, Fink et al. 2013, Lo Iacono et al. 2014, Fink et al. 2015, Stalder et al. 2015, Stalder et al. 2018, Wang et al. 2019, Feenstra et al. 2020, Fentimen et al. 2020). Although Fentimen et al. (2020) provided individual ages older than 15 ka, no detailed CWC growth history beyond 15 ka was yet provided. The here presented MeBo cores thus present a unique data set, displaying discontinuous coral growth predominantly during each interglacial of the past 550 ka, seemingly paced by a 100 ka cyclicity. However, distinct local differences in coral occurrence are revealed in the age-depth profiles of DM and BR I (Fig. 3.4 and Fig. 3.6). DM shows enhanced coral presence in MIS 10, MIS 9, MIS 7 and MIS 5, with additional minor coral presence during MIS 11 and MIS 8 and yet a lack of corals younger than 100 ka (Fig. 3.4). For BR I, enhanced coral occurrence is observed during MIS 9, MIS 7 and the Holocene (MIS 1), with few coral fragments during MIS 13, MIS 12, MIS 11, MIS 8 and MIS 5 (Fig. 3.6). Although, Termination T1 and the Holocene mark the period of most flourishing CWC growth observed in the EMCP and WMCP (e.g. Fink et al. 2013, Stalder et al. 2018, Wang et al. 2019, this study), no coral on DM younger than MIS 5 was found yet. Hebbeln et al. (2015) and Hebbeln et al. (2019) presented multi-beam hydrographic maps of the EMCP, revealing a belt of shallow, elongated coral mounds in the southern EMCP (~230 m water depth), however, similar to DM, these mounds are partly buried. In close proximity to these mounds, the Moulaya River enters the Alboran Sea, transporting sediment from the Moroccan hinterland with an estimated sediment load of 12 Mt/a (Snoussi et al. 2002, Terhzaz et al. 2018). Enhanced fluviatile sediment discharge could possibly have caused the burial of these mounds. However if the shallow mound belt was buried within the same time interval, a coherent demise of coral occurrence around 100 ka should be observable on the buried mounds of the southern EMCP.

Hence, it is clear that the corals in the southern AS grew during each interglacial period of the past 550 ka, similarities and differences in growth history of both mounds are most possibly due to the water depth in which the corals have settled (DM: 236 m; BR I: 329 m), the

local food supply and oxygen level, the bottom water current dynamic and continental runoff of sediments from Morocco (e.g. Moulaya River), as shown by several studies for the Holocene on CWC and associated taxa in the Alboran Sea (Fink et al. 2013, Stalder et al. 2015, Stalder et al. 2018, Wang et al. 2019, Feenstra et al. 2020, Fentimen et al. 2020).

However, multiple studies focused their investigations on cores located on BR I (Fink et al. 2013, Stalder et al. 2018, Feenstra et al. 2020, Fentimen et al. 2020, this study). Ranging in depth between 319 and 434 m, all investigated cores with recoveries between 338 and 926 cm, revealed synchronised coral growth during MIS 1, as observed in the here presented cores (GeoB18118-1 and GeoB18118-2). However, one core (recovery 926 cm; Fentimen et al. 2020) additionally revealed coral fragments dated during MIS 9, MIS 8, MIS 7, MIS 5 and MIS 3. With the only exception of MIS 3, where no corals were found in this study, the observed coral occurrences by Fentimen et al. (2020) are concurrent with the combined U-series age record of BR I and DM (Fig. 3.10). Even though, the drilled MeBo cores seemingly reveal a rough outline of periods with flourishing and dormant coral growth, the combined age record is considered to be representative to some degree for the general occurrence of corals within the EMCP. Whereas a multi-core study on one mound would reveal stronger constraints on the exact timing of coral growth and hiatuses on the investigated mound, as indicated by the comparison of BR I cores from Fentimen et al. (2020) and this study. However, the presented U-series age record unravels the general timing of CWC occurrence in the EMCP over the past 550 ka. At present-day, the three known coral provinces in the AS reveal distinct differences in their coral occurrences. In the WMCP, no living corals are found at present day, whereas a merely patchy CWC occurrence in the EMCP was observed. However, flourishing CWC growth was observed on the Cabliers Mounds to the east of the EMCP (Hebbeln et al. 2009, Corbera et al. 2019). Although this reveals distinct regional differences in coral growth, most possibly caused by different environmental parameter, e.g. water depth, food- or sediment supply and bottom current strength as well as the position of the AS gyre system, concurrent coral occurrence, summarized in Fink et al. (2015), was observed over the last 15 ka throughout the AS. Thus it is argued, that the presented age constraints of coral occurrences on DM and BR I, encompassing major growth periods and diminished CWC occurrence in the EMCP, are representative not only for the EMCP, but also for the southern AS.

Thus, in the next section, the general coral occurrence and the observed 100 ka cyclicity of thriving coral growth is regarded in the context of oceanographic and atmospheric changes during glacial-interglacial cycles of the past 550 ka.

3.5.4 The impact of Mediterranean climate dynamics on cold-water coral occurrences in the Alboran Sea

Interglacial periods are marked by the extent of the Northern Hemisphere ice sheets limited to 60°N and are associated with high sea level as well as a similar ocean circulation as observed today (Rohling et al. 2014, Böhm et al. 2015). Humid and wet climatic conditions are known to have prevailed during the present and the last interglacial in the Mediterranean Region (Gasse 2000, Gasse and Roberts 2004, Smith et al. 2004). Reinforced Mediterranean Outflow volume, evoked by a combination of the deepened sill at the SoG and enhanced freshwater input into the Mediterranean Sea (Rohling et al. 2002, Gasse and Roberts 2004, Alhammoud et al. 2010, Rogerson et al. 2012), strengthened the Atlantic Jet (AJ) flowing into the Mediterranean Sea (AS). Strong winds and a southward drift of the AJ entailed coastal and offshore upwelling as well as a strong and stable AS gyre system and thus vertical mixing of up to 200-300 m within the AS gyre system (Heburn and La Violette 1990, Sarhan 2000). A reduced density gradient between inflowing Atlantic water and fresher Mediterranean water certainly favoured a deeper vertical mixing, potentially making organic matter more available for organisms like CWC, dwelling in intermediate depths. Although at present-day, the East Alboran Gyre (EAG), recirculates westwards over the location of BR I (Fig. 3.1; Viúdez and Tintoré 1995), neither the position nor the behaviour of the AS gyres are considered stable (Tintore et al. 1988, Heburn and La Violette 1990, Perkins et al. 1990).

The enhanced freshwater input via river run-off was proposed to have increased the flux of organic matter and terrigenous sediment into the Mediterranean Sea (Rossignol-Strick 1985, Tjallingii et al. 2008, Revel et al. 2010, Terhzaz et al. 2018). Enhanced coral growth in the AS has been correlated with increased fluvial input, as well as high surface productivity and internal waves (Fink et al. 2013, Wang et al. 2019, Feenstra et al. 2020). Based on the benthic foraminiferal assemblages and XRF Al-normalized elemental ratios in the EMCP, Fentimen et al. (2020) proposed wet continental conditions, as described above for the interglacial periods MIS 9 to MIS 1 and thus, as seen in the presented U-series age record favourable coral growth conditions in the AS must have prevailed (Fig. 3.10). Although the U-series record clearly shows enhanced CWC occurrence in the EMCP during the interglacials mid-MIS 11, MIS 9, MIS 7, mid-MIS 5 and ranging from Termination T1 (transition MIS 2/MIS 1) to the early Holocene, a clear decline of coral occurrence apparently coincides with sapropel layers occurring in the EMS (Fig. 3.9 and Fig. 3.10). Sapropel layers in the EMS are induced by enhanced freshwater input into the Mediterranean Sea, as seen for the past 150 ka by enhanced African monsoonal systems and thus increased Nile river discharge (Fig. 3.9; Revel et al. 2010, Ehrmann et al. 2016). Reduced salinity and thus reduced density in the surface

waters led to a slowdown of the Mediterranean overturning circulation and therefore a slowdown of LIW formation and consequently LIW velocities (Toucanne et al. 2012). CWC in the southern AS reportedly dwell in the LIW water mass and are dependent on strong bottom current velocities (e.g. Dorschel et al. 2007, Fink et al. 2015).

Furthermore, nutrient input, associated with river run-off, resulted in enhanced primary productivity in the entire Mediterranean Sea (Bárcena et al. 2001, Jimenez-Espejo et al. 2008, Rohling et al. 2015). In consequence, this lead to dysoxic or anoxic conditions and the deposition of organic-rich sapropel layers (S) in the EMS and Organic Rich Layers (ORL) in the WMS (Cacho et al. 2002, Rogerson et al. 2008, Rohling et al. 2015). Consistently, based on benthic foraminifera assemblages, eutrophic and less oxygenated conditions in the EMCP were proposed during interglacial periods of the last 300 ka (Fentimen et al. 2020).

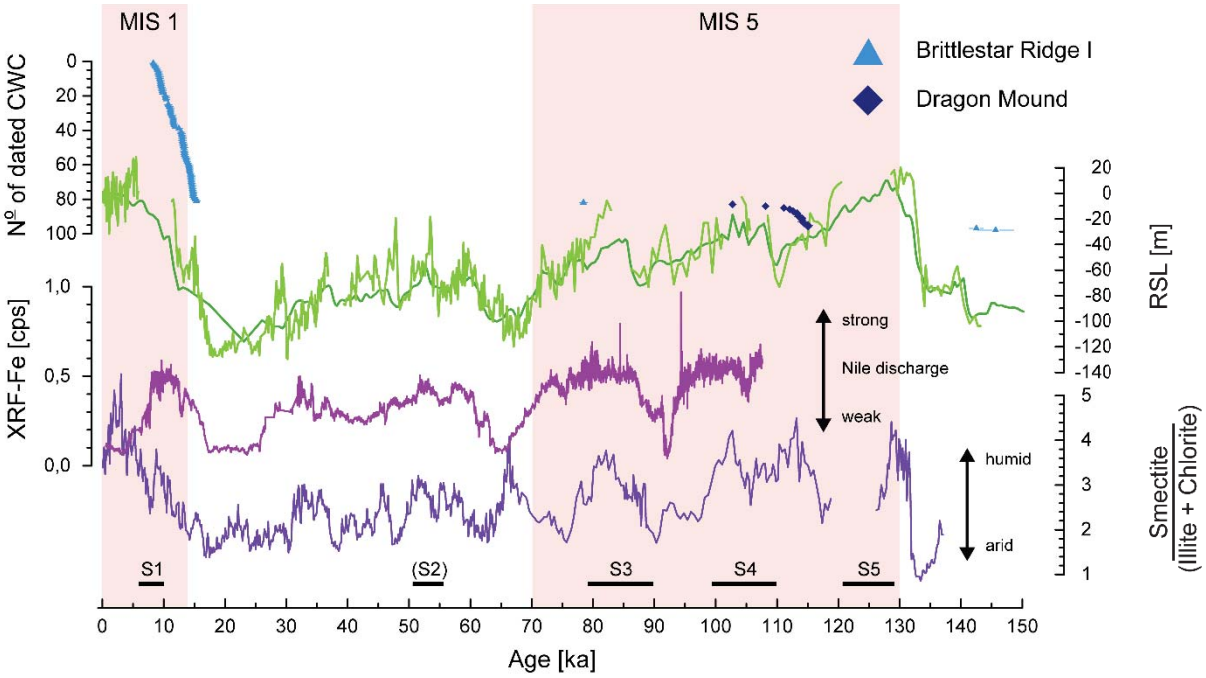

Fig. 3.9: Combined U-series record of the presented locations Dragon Mound and Brittlestar I through time. CWC samples are ordered by youngest to oldest ages. Nile River discharge (violet; Revel et al. 2010) and clay mineral assemblages (purple; Ehrmann et al. 2016) indicate humid conditions with enhanced freshwater input into the Mediterranean Sea. Two Relative Sea Level records (RSL, green; Rohling et al. 2014) indicate sea level variability over the last 150 ka. Black bars indicate sapropel layers (Ziegler et al. 2010, Konijnendijk et al. 2014, Rohling et al. 2015).

During the last interglacial period, a lack in CWC occurrence is observed during S5 (Fig 3.9, 129 to 121 ka; Ziegler et al. 2010), coinciding with warm and wet conditions and most possibly enhanced Nile River discharge (Revel et al. 2010, Blome et al. 2012, Ehrmann et al. 2016). Enhanced CWC growth (DM: 115 to 111 ka; MAR: 228 cm/ka) is observed after the end of sapropel conditions, marked by reduced rainfall in the EMS and thus reduced Nile River discharge as well as an increase in the MOW strength, which correlates with a strengthening in LIW formation and velocity (Bar-Matthews et al. 2003, Martrat et al. 2014, Bahr et al. 2015, Ehrmann et al. 2016). A prominent increase in the Mediterranean Relative Sea Level (RSL) of over 30 m, observed at 110 ka, suggests reinforced freshwater input into the EMS, reflected by humid conditions and enhanced Nile River discharge, as well as reduced MOW strength and thus reduced LIW formation (Blome et al. 2012, Rohling et al. 2014, Bahr et al. 2015, Ehrmann et al. 2016). Consequently, coinciding with this renewed onset of sapropel conditions (S4: 110 to 99 ka; Ziegler et al. 2010), a reduced or even diminished coral occurrence can be observed in the EMCP.

The most recent period of successive coral growth (T1 to mid-Holocene) reveals a flourishing abundance of CWC during different environmental conditions as observed for earlier interglacials (Fig. 3.9 and Fig. 3.10). T1 is globally marked by the onset of the warm Bølling-Allerød (B/A) interval (14.6 to 12.9 ka) and the meltwater puls 1A, leading to a fast sea level rise and thus the deepening of the SoG sill, which therefore induced a higher volume of fresher Atlantic Water into the Mediterranean Sea (Weaver et al. 2003, Sierro et al. 2005). Enhanced productivity in the AS was observed coinciding with the onset of the Mediterranean sea level rise (23–18 ka), with a clear decline in productivity during the B/A and a significant decrease at circa 9 ka (Bárcena et al. 2001, Cacho et al. 2002, Jimenez-Espejo et al. 2008, Fink et al. 2013).

Although enhanced productivity prevailed since the LGM, the onset of CWC growth in the AS reportedly started between 15.5-15 ka (Feenstra et al. 2020, this study). This temporal offset might be due to a generally lower sea level in the Mediterranean Sea and reduced Atlantic inflow, consequently a less stable gyre system would have prevailed. Several scenarios of the gyre system have been discussed, including the disappearing of the EAG during weak SoG exchange periods in winter (Tintore et al. 1988, Bormans and Garrett 1989, Heburn and La Violette 1990, Perkins et al. 1990). Prior to 16 ka, an eastwards displacement of the WAG due to prevailing westerlies and a low pressure system over the Mediterranean Sea was suggested (Grazzini and Pierre 1991). Thus, it is argued that, although high productivity prevailed in the AS, the gyre system was weak, displaced and potentially reduced to one gyre and hence, the

vertical mixing did not provide the CWC with sufficent organic matter in water depths of 230 to 330 m to sustain consecutive coral growth prior to 15.5 ka.

High MARs (up to ~600 cm/ka) and successive CWC growth were observed during the B/A, however, a consistent clear decline of CWC growth can be observed in the AS during the YD (Fink et al. 2013, Stalder et al. 2015, Stalder et al. 2018, Wang et al. 2019, Feenstra et al. 2020, this study). Compared to the B/A or the Early Holocene, the YD was colder and dryer, reflected in Mediterranean sea level of circa -20 m below present and a slow down of the deglacial rate of sea level increase from 20 mm/a to only 4 mm/a. During this time, enhanced and well ventilated LIW as well as a briefly reinforced primary productivity, was observed (Sierro et al. 1998, Bárcena et al. 2001, Toucanne et al. 2012, Rohling et al. 2014, Abdul et al. 2016). Although high productivity and well ventilated, strong LIW prevailed, which are excellent conditions for coral growth, Fink et al. (2015) proposed that dynamic local variations in the gyre system behaviour, e.g. reduced vertical mixing, might have caused the decline of CWCs during the YD. Flourishing growth conditions returned by the end of the YD reflected in high MARs (75 to 400 cm/ka) in the AS (e.g. Fink et al. 2013, Wang et al. 2019, this study).

In the AS, water column stratification and peak productivity rates resulted in ORL 1 (14.5–8.2 ka; Rogerson et al. 2008). The timing of ORL 1 clearly correlates with periods of flourishing CWC growth in AS (15.5 to 12.7 ka and 11.6-9.0 ka). However during the Early Holocene, water column stratification and peak productivity rates in the EMS resulted in the formation of sapropel S1 (10–6 ka; Rohling et al. 2015). Hence, poorly oxygenated bottom waters (LIW) were observed in the AS. Furthermore, a significant drop in productivity in the AS was observed at circa 9 ka, coinciding with a uniform cessation of successive CWC mound growth in the EMCP (Fink et al. 2013, Stalder et al. 2015, Stalder et al. 2018, Feenstra et al. 2020, Fentimen et al. 2020, this study). However, in the WMCP, MARs of up to 500-700 cm/ka were observed until 8 ka (Wang et al. 2019), potentially revealing local differences between the two coral provinces. Nevertheless, mound formation more or less ceased with the onset of the Mid Holocene. Although from the Angolan Margin, CWC reefs are known to thrive under dysoxic conditions, compensating the lack of oxygen with higher food intake (Hanz et al. 2019), the unfavourable conditions in the AS most possibly led to the demise of thriving CWC growth, as productivity in the AS clearly declined and oxygen depletion progressed throughout S1 (10-6 ka).

Thriving CWC growth during interglacial periods in the AS is arguably dependent on a combination of (i) the freshwater input into the Mediterranean Sea, which induces primary productivity and transports sediment, yet causes a slowdown of the Mediterranean overturning circulation and (ii) the strength and position of the AS gyre system, which provides food particles into coral dwelling depths.

During T1, freshwater input was crucial to trigger initial primary productivity, which then enhanced the exchange at the SoG. A stronger gyre system and a reduced density gradient between Atlantic and Mediterranean water masses induced enhanced vertical mixing, benefiting CWC in 330 m depth. However, sapropel conditions, with peak freshwater input into the Mediterranean Sea, lead most possibly to poorly oxygenated and sluggish bottom water currents and due to the stratification of the water column, to a reduced, shallower vertical mixing. Hence, a decline of CWC can be observed.

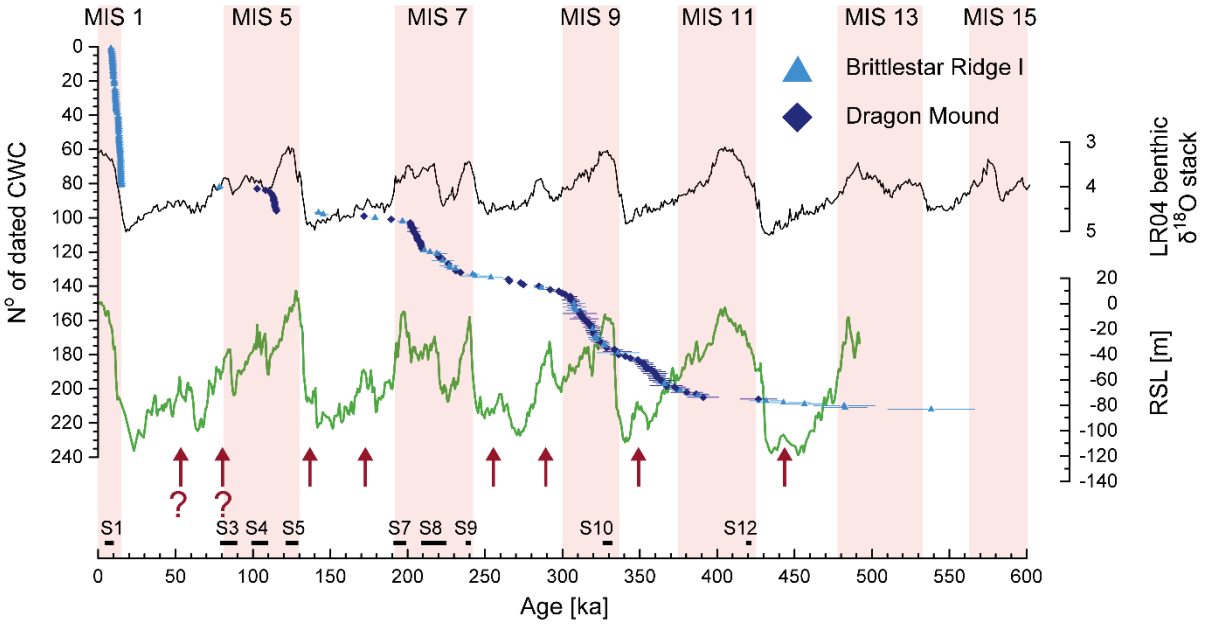

Fig. 3.10: Combined U-series record of the presented locations Dragon Mound and Brittlestar I through time. CWC samples are ordered by youngest to oldest ages. LR04 stack (black; Lisiecki and Raymo 2005) and the Relative Sea Level (RSL, green; Rohling et al. 2014) show global and Mediterranean sea level variability. RSL indicates Mediterranean freshwater input. Black bars indicate sapropel layers (Ziegler et al. 2010, Konijnendijk et al. 2014, Rohling et al. 2015). Red arrows indicate brief Mediterranean sea level rise during glacial periods co-occurring with coral occurrence. Marine Isotope Stages (MIS) are shown in transparent red shades.

Concurrently to MIS 5 and MIS 1 (Fig. 3.9), the combined U-series record (Fig. 3.10) reveals reduced CWC occurrence or even a lack of CWC during sapropel conditions of earlier interglacial periods. Coinciding with high Mediterranean sea level, prolonged warm, wet and sapropelic conditions were proposed for MIS 11c (420 to 398 ka; Emeis et al. 2000, Kandiano et al. 2012, Konijnendijk et al. 2014, Rohling et al. 2014). Applicable with S5 and S4, a distinct lack of CWC can be observed (420 to 390 ka), however, the available CWC record is scarce between 550 and 390 ka with only seven investigated coral fragments. During MIS 9 and MIS 7, low CWC occurrences are observed during analog warm conditions, leading to the formation of sapropel layers (S10 to S7, Fig. 3.10).

Hence, during all sapropel layers of the past 450 ka (Fig. 3.10), thriving growth conditions could not be maintained. Most possibly a combination of (i) a significant reduction of productivity in the AS (as seen during MIS 1), (ii) changes in the gyre system behaviour, e.g. shallower vertical mixing due to water column stratification and (iii) poorly oxygenated bottom waters lead to the demise of CWC during these peak warm periods. However, subsequent to sapropel conditions, flourishing CWC growth in the AS, observed during MIS 9. MIS 7, MIS 5 co-occurred with reduced freshwater input. Hence the reduced freshwater input, the Mediterranean overturning circulation reinvigorated and thus lead to the production of strengthened and well-ventilated water masses (e.g. LIW). Although these periods are associated with decreasing Mediterranean sea level as well as colder and more arid climate conditions, compared to the peak warm sapropelic periods, a sufficient level of productivity and vertical mixing in the AS must have prevailed to facilitate thriving CWC growth.

Contrary to interglacial periods and with the exception of MIS 10, CWC occurrences are sporadic during glacial periods (MIS 12 to MIS 6) and limited to low MARs. Glacial periods are characterized by a large global ice extent (e.g. Berger et al. 1999, Lisiecki and Raymo 2005) and consequently, up to −140 m lower sea level, leading to a reduced sill depth of the SoG. In the Northern Hemisphere, the ice sheet growth lead to changes in the Polar Front position (PF). During interglacial periods, the PF in the North Atlantic resided north of 50°N and migrated to a more southern position during glacial periods due to ice sheet build up, with a maximal southern displacement towards ~45-40°N during the LGM (Ruddiman and McIntyre 1981, Grousset et al. 1993, Robinson et al. 1995, Rohling et al. 1998, Kageyama et al. 2006). The glacial PF frequently induced cold, polar air outbreaks into the Mediterranean Region (Rohling et al. 1998, Hayes et al. 2005, Moreno et al. 2005, Tjallingii et al. 2008). In the Northeast Atlantic, glacial SST decreased dramatically as e.g. seen in the GoC and thus, via Atlantic inflowing water, resulted in strongly reduced SST in the Alboran Sea and the

Mediterranean Sea (Cacho et al. 2002, Martrat et al. 2004, Martrat et al. 2007, Martrat et al. 2014). The Atlantic Meridional Overturning Circulation (AMOC) is known to be sluggish during these times (Vidal et al. 1997, McManus et al. 2004) adding to the overall climate cooling of the East Atlantic and Mediterranean Region. The cool climate in the Mediterranean Region is associated with arid conditions on the African Continent and the Iberian Peninsula (e.g. Gasse 2000). Several studies on off- and on-mound cores in the AS showed that semi-arid/arid climate conditions are reflected by enhanced aeolian sediment input originating from the Sahara and reduced fluviatile sediment input and thus low river run-off (Moreno et al. 2005, Sierro et al. 2005, Fink et al. 2013, Feenstra et al. 2020, Fentimen et al. 2020). Reduced SST, as well as cool and arid climate, certainly led to a reduction of evaporation loss over the Mediterranean Sea. Thus, less inflowing water through the SoG was required to balance the water budget. Within the AS, this most likely led to a weakened Atlantic Jet and a weakened AS gyre system. During glacial periods a southern ITCZ position favoured low-pressure systems in the Mediterranean Region (COHMAP-Members 1988) and thus a less stable and possibly displaced AS gyre system, reducing vertical mixing and upwelling (Ausín et al. 2015). On the other hand, the overturning circulation in the Mediterranean Sea apparently stems from an increase of net evaporation towards the Eastern Mediterranean Basin, similar to modern day winter conditions (e.g. Hayes et al. 2005, Kuhlemann et al. 2008). Consequently, more saline surface waters lead to reinforced intermediate and deep water formation, e.g. the enhanced formation of LIW in the Eastern Mediterranean Basin (Toucanne et al. 2012).

Seemingly, the lack of sufficient freshwater input during cold and arid glacial periods does not provide sufficient nutrients and thus primary productivity for CWC to thrive in. Although glacial conditions in the Mediterranean Sea are marked by enhanced LIW velocities and thus strong bottom currents, which are important for CWC (White et al. 2005, Dorschel et al. 2007), the weakened AS gyre system and the resulting reduced and shallower vertical mixing, might further be responsible for the scarce occurrence of glacial CWC in the AS (Fig. 3.4; 3.6b and Fig. 3.10). However, glacial CWC occurrences in the AS coincide with interstadial periods, marked by dominant Mediterranean sea level increases of circa 20-30 m as seen throughout MIS 12 to MIS 6 (Fig 3.10, red arrows). Although the RSL reflects a Mediterranean wide sea level, CWC occurrences evidence that for brief intervals during each glacial period, conditions changed towards more favourable CWC growth conditions. Hence, these periods of rapid sea level rises in the Mediterranean Sea are most possibly invoked by enhanced freshwater input and thus most possibly provided increased primary productivity and sediment input.

However the brief interstadial periods did not provide sufficient conditions to support successive CWC growth, as reflected in the limited availability of CWC fragments and low glacial MARs, e.g. MIS 8 on DM or MIS 6 on BR I (Fig. 3.4 and Fig 3.6b). Although only one coral was dated during the last glacial period, one would expect similar CWC occurrence, as seen during MIS 6 or MIS 8, coinciding with the Mediterranean sea level rise at circa 70 and 50 ka (Fig. 3.10; red question marks). Concurrently, a few CWC fragments, ranging around 73±3 ka and 51±1 ka, were found on BR I (Fentimen et al. 2020).

The CWC occurrence in the AS is seemingly depended on sufficient primary productivity and the availability of food particles in coral dwelling depths. Food particles most possibly only reached CWC dwelling depths during an enhanced and strong AS gyre system and deep vertical mixing. One major driver of CWC growth thus appears to be the freshwater input into the Mediterranean Sea. Freshwater, not only influences the Mediterranean overturning circulation and the Mediterranean sea level, thus freshwater input indirectly also influences the AJ and the AS gyre system, freshwater further provides nutrients, inducing primary productivity and transports sediments, necessary to aggregate coral mounds and preserve the coral fragments pristinely over 550 ka, as presented in this study.

3.6 Conclusion

For the first time, CWC mounds in the Alboran Sea were drilled beyond the reach of gravity corer. Using the MeBo drilling rig, cores as long as 70 m were retrieved. Two MeBo cores and one gravity core from two different locations in the EMCP have been presented. The BR I core revealed coral occurrence over 70 m length with a basal age of 520 ka. However, with a high probability, coral occurrence on BR I is suspected beyond the drilled 70 m. The shallower DM was fully penetrated at 61 m and revealed a basal age of approximately 400±20 ka. After applying rigorous quality control methods, both mounds yield a total of 202 coral ages, which were used for individual and combined age-depth models, covering the past 550 ka. BR I showed a quasi-stratified age-depth model with minor age inversions and mixed-age layers, most likely resulting from erosion. In contrast, DM revealed a complex age-depth model with severe signs of erosion and potential mass wasting events, creating extended mixed-age layers. The presented age models are unparalleled in the number of dated coral fragments and therefore reveal detailed insight in the growth history of EMCP coral mounds. Based on the average MARs and the potential basal depth of BR I (80 to 160 m), a possible onset of coral growth in the Alboran Sea was calculated between 595 and 1190 ka and thus during the Mid Pleistocene Transition.

However, to test the mound evolution theory and to verify the onset of coral growth on BR I, additional long cores from both locations are required (Fig. 3.11). Additional long cores on BR I are only possible on the ridge top, due to its steep morphology. Although long cores from the flanks would be equally interesting, in Fig. 3.11 three ridge top positions are proposed. With the modern MeBo (200 m), new long cores could identify the basal mound age and therefore the onset of BR I, as well as the actual mound height, which could provide an overall Mound Aggregation Rate. For the elongated DM, three additional drill holes, as indicated by white open stars in Fig. 3.11, are suggested. The base of the presented core GeoB18116-2 most possibly consists of reworked coral fragments, originating from erosional processes. Hence, additional cores on DM might reflect a different, less disturbed and less inverted age model and coral fragments, potentially older than 400 ka.

The occurrence of CWC over the last 550 ka is observed predominantly during interglacial periods. However, peak climate warm periods, coinciding with sapropel layers, are barely represented in the presently available CWC record, which provides a first hint that these periods result in a limitation of coral growth. Furthermore, the flourishing coral growth co-occurring with the onset of T1 and brief coral occurrences during glacial periods (interstadials) constitute exceptions to this observation.

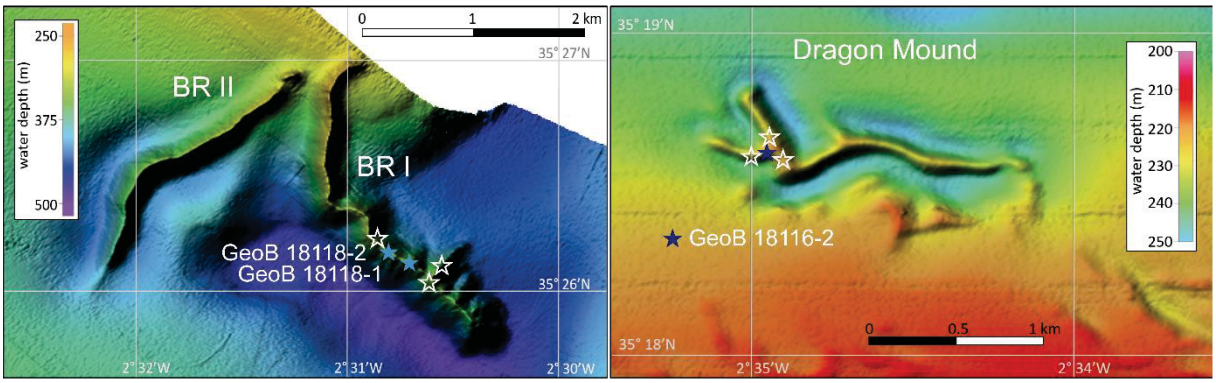

Fig. 3.11: Proposed MeBo drillings to verify the proposed mound evolution scenario. Full stars indicate core location introduced in this study. Open stars mark proposed new drillings.

Coral growth in the EMCP was tightly linked to freshwater input into the Mediterranean Sea. Enhanced freshwater input evoked primary productivity via the supply of nutrients and transported sediment, necessary for mound growth. Consequently to enhanced freshwater input, the Mediterranean sea level rose, the Atlantic inflow increased and thus strengthened the AS gyre system. Hence, enhanced vertical mixing into coral dwelling intermediate depths (230-300 m) made food available for the CWC. Three different "growth" scenarios, during which more favourable conditions for coral growth prevailed, were pointed out. (i) The most prominent mode was observed post-sapropelic conditions during interglacial periods. During declining Mediterranean sea levels and thus most possibly colder and drier climate, reduced freshwater input still provided sufficient nutrients and sediment to facilitate flourishing CWC growth. However, the thereof consequently reduced water column stratification enabled a more vigorous Mediterranean overturning circulation, resulting in well-ventilated bottom waters and a stronger AS gyre system. (ii) The second mode was observed during Termination T1 and thus during a period of a general warming climate and rising sea level. Enhanced freshwater input during the LGM triggered enhanced primary productivity prior to observed CWC growth. With rising Mediterranean sea level and thus a strong AS gyre system, CWC recolonized the AS. However, a clear decline during sapropel conditions was observed. (iii) The third and last mode could be identified during the interstadials of glacial periods, when intense but brief sea level rises occurred in the Mediterranean Sea, most possible induced by enhanced freshwater discharges. With vigorous LIW velocities, freshwater induced primary productivity and sediment input as well as a potentially favourable AS gyre system position. These brief intervals provided favourable conditions with active coral growth.

4 Cold-water corals as archives for past intermediate water temperatures in the Alboran Sea

4.1 Introduction

Over the last decades, several studies in the Mediterranean Region, contributed to a better understanding of the climate evolution during the Holocene and the last glacial period (e.g. Cacho et al. 1999, Bárcena et al. 2001, Martrat et al. 2004, Rogerson et al. 2004, Moreno et al. 2005, Voelker et al. 2006, Voelker et al. 2010, Martrat et al. 2014, Bahr et al. 2015, Toucanne et al. 2015, Kaboth et al. 2017, Català et al. 2019). Severe changes in oceanographic parameters have been linked to the positioning of the polar and subtropical fronts and the displacements of storm tracks (Rogerson et al. 2004, Voelker et al. 2010, Fletcher et al. 2013, Martrat et al. 2014, Singh et al. 2015, Toucanne et al. 2015), as well as the Atlantic Meridional Overturning Circulation (AMOC) (Thornalley et al. 2009, Colin et al. 2010, Repschläger et al. 2017). The majority of water in the Mediterranean Sea, inflowing or outflowing, traverses through the Alboran Sea (AS), which is an important connector between the Atlantic and the Mediterranean Sea. Therefore, the AS is very susceptible to changes in Atlantic Ocean inflow conditions (Català et al. 2019).

One approach to tackle this potential Atlantic-Mediterranean connection is the evolution of the Sea Surface Temperature (SST). Predominantly the Holocene and the last glacial period were investigated intensively by several authors (Cacho et al. 2001, Martrat et al. 2004, Martrat et al. 2014, Ausín et al. 2015, Jiménez-Amat and Zahn 2015, Català et al. 2019). However, these records differ in the used temperature proxies. Several studies applied the UK'37 index, measured on alkenones (Cacho et al. 2001, Martrat et al. 2004, Martrat et al. 2014, Ausín et al. 2015), which potentially reflects average annual temperatures. Other studies used the Mg/Ca ratio, measured in planktonic foraminifera, which reflects a more seasonal biased temperature signal (Jiménez-Amat and Zahn 2015, Català et al. 2019).

In recent years, a new thermometer has been established to determine mid-depth temperatures using the Li/Mg ratio of CWC. In the AS, CWC dwell in the Levantine Intermediate Water (LIW). LIW is fed by Atlantic Water, which is modified (MAW) throughout its pathway from the SoG to the Levantine Basin (East Mediterranean Basin), where it sinks to intermediate depths due to increased density (Chapter 2.2; Millot and Taupier-Letage 2005). While flowing westwards, through all Mediterranean Basins, LIW is a major component in most water mass formations and contributes up to 70% to the Mediterranean Outflow Water (MOW), leaving the Strait of Gibraltar (Millot and Taupier-Letage 2005, Millot 2009, Millot 2014).

For the first time the temperature of LIW is measured directly, using CWC from two mound provinces in the Alboran Sea, which today bath in LIW, but in the past may have been bathed in more Atlantic type water according to Wang et al. (2019). Given the importance of LIW in the Mediterranean Sea recirculation and its warmth and salt ejection into the Atlantic (MOW), unprecedented measures of LIW water mass temperature during the peak growth periods of CWC in the Alboran Sea are provided, spanning the past 550 ka. Furthermore, one may expect a tied link between SST and mid-depth water temperature due to the SST in the mid-depth water mass formation region. Moreover, the comparison of local SST (AS) and LIW bottom water temperature provides hints on the thermal water mass stratification in the AS, which however today, is less important if compared to the salinity induced stratification. Hence, similarities and differences in short- and long-term temperature variabilities can be explored, spanning the Holocene and previous glacial and interglacial periods.

4.2 Regional setting

The oceanography of the Alboran Sea is comprised of three distinct main water masses. Atlantic surface water, inflowing through the Strait of Gibraltar, is mixed rapidly with resident Mediterranean water and thus called MAW. Below MAW (0-200 m), LIW resides in water depths between 200 to 600 m. Underlying LIW is the WMDW (Millot and Taupier-Letage 2005, Català et al. 2019).

Generally, the Mediterranean Sea is considered oligotrophic, however, the Alboran Sea shows the highest marine productivity due to quasi-permanent areas of upwelling. Basin-wide gyre systems, like the West Alboran Gyre (WAG) and the East Alboran Gyre (EAG) and atmospheric circulation cause vertical mixing and wind-induced upwelling, transporting biogenic material both vertically and horizontally (Garcia-Gorriz and Carr 1999, Sarhan 2000, Baldacci et al. 2001, Dafner et al. 2003, d'Ortenzio and Ribera d'Alcalà 2009). Sediments found in the Alboran Sea are comprised of aeolian dust, transported from the Sahara (Stuut et al. 2009, Terhzaz et al. 2018) and fluvial input, originating primarily from the Iberian Peninsula and the Moroccan hinterland (Fabres et al. 2002, Terhzaz et al. 2018).

Over the last decades, several hundred CWC mounds were discovered along the Moroccan margin (Comas and Pinheiro 2007, Lo Iacono et al. 2014, Lo Iacono et al. 2018). Based on the geographical position from west to east three coral provinces, the West Melilla Coral Province (WMCP), the most prominent East Melilla Coral Province (EMCP) and the Cabliers Mounds were created. Today, coral occurrence is limited to the EMCP with isolated patches of corals and to the Cabliers Mounds with flourishing coral reefs (Hebbeln et al. 2009, Corbera et al. 2019). The EMCP, shown in Fig. 4.1a is comprised of three subsections. In the northern section (c), predominantly large coral ridges were found (Fig. 4.1c). The middle section is comprised of oval to arcuate coral mounds and in the southern section (Fig. 4.1d) mainly elongated, partly buried ridges were found (Hebbeln 2019).

4.3 Material and methods

4.3.1 Samples

In this study, the Li/Mg temperatures of five on-mound cores, collected in 2014 during MSM-36 "MoccoMeBo" cruise aboard the RV Maria S. Merian (Hebbeln et al. 2015), are presented. From the first location, a vast ridge structure called Brittlestar Ridge I, two cores GeoB18118-1 and GeoB18118-2 were investigated (Fig. 4.1c). The gravity core (GC) GeoB18118-1 (35°26.139'N, 2°30.765'W), is located in 332 m water depth. In close proximity to the GC, GeoB18118-2 (35°26.160'N, 2°30.810'W) was taken in 329 m water depth. The second location is in the south of the EMCP. In 236 m water depth the core GeoB18116-2 was taken from a partially buried mound, called Dragon Mound (35°18.642'N, 2°34.933'W; Fig 2.1; Hebbeln 2019). The corresponding age model to both locations was presented in Chapter 3. Two cores, originating from the WMCP, which have been published in Wang et al. (2019), were additionally investigated for Li/Mg temperature. GeoB18127-1 (35°28.96'N, 3°04.641'W) was taken in 365 m water depth with a recovery of 563 cm. GeoB18130-1 (35°28.099'N, 3°08.747'W) is located at 379 m depth and has a recovery of 148 cm. In total, 15 samples were investigated.

Additionally, two CTD stations were taken during the "MoccoMeBo" cruise (Fig. 4.1b; white stars). In close proximity to BR I and over a 12-hour tide cycle, 11 casts were conducted on the so-called Yoyo-CTD GeoB18122-1. Another single cast CTD, GeoB18110-1, was conducted some 10 km to the east of DM.

Table 4.1: Metadata of sampling stations (GC – Gravity Corer; MeBo – Bremen drill rig) visited during MSM36 in the Alboran Sea (EMCP – East Melilla Coral Province; WMCP – West Melilla Coral Province).

Station	Area	Gear	Latitude [°N]	Longitude [°W]	Water depth [m]	Recovery [cm]
GeoB18118-1	EMCP	GC	35°26.139	2°30.765	332	873
GeoB18118-2	EMCP	MeBo	35°26.160	2°30.810	329	5298
GeoB18116-2	EMCP	MeBo	35°18.642	2°34.933	236	7147
GeoB18127-1	WMCP	GC	35°28.960	3°04.641	365	563
GeoB18130-1	WMCP	GC	35°28.099	3°08.747	379	148

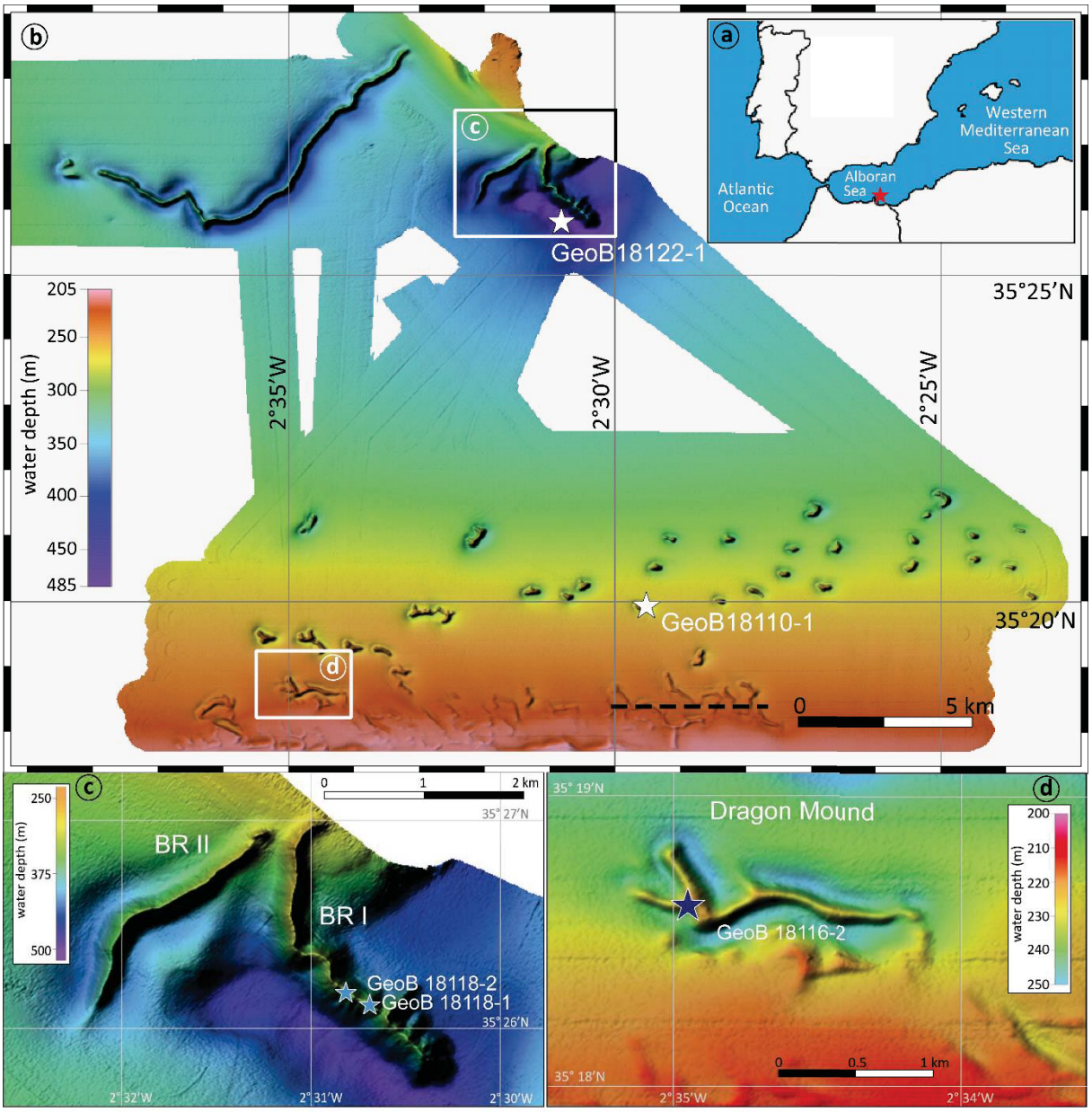

Fig. 4.1: (a) Overview map, including the location of EMCP in the Alboran Sea. (b) Multi-beam bathymetric map of the EMCP with a 25 m grid resolution. Box (c) and (d) show a close up of the core locations (GeoB18118-1, GeoB18118-2 and GeoB18116-2) and the mound topography. White stars indicate the locations of CTD stations (GeoB18122-1 and GeoB18110-1). (c) The topography of Brittlestar I (BR I) and on mound core locations GeoB18118-1 and GeoB18118-2. (d) The topography of Dragon Mound (DM) and on mound core location GeoB18116-2. Map is modified after (Hebbeln 2019).

4.3.2 Li/Mg chemistry

Coral fragment aliquot of each U-series sample was used for the Li/Mg analysis. After mechanical cleaning, the samples were dissolved in 10 ml 0.5M HNO_3. Assuming the coral skeleton is purely made of $CaCO_3$, the solution (500 µg/ml Ca) is further diluted with 0.5M HNO_3, to obtain a solution of 10 µg/ml Ca.

4.3.3 Analysis

All samples were measured on an iCap Q^{TM} ICP-MS with an upstream desolvating nebulizer system Apex HF (ESI) at the Institute of Environmental Physics, Heidelberg, Germany. The reliability of in-house measurements were confirmed by reconstructing the calibration curve of Montagna et al. (2014) using coral samples younger than 100 a (Lausecker 2015) and inter-laboratory measurements of sample aliquots at LSCE (Laboratoire des Sciences du Climat et de l'Environnement, Gif-sur-Yvette, France) (Krengel 2016). In-house standard ICECTD-20 PL501-6 C4 was used to monitor and correct the instrumental drift. The main factors of error of Li/Mg measurements are sample heterogeneity, analytical and calibration curve uncertainties, which amount to an error of 1 °C (Lausecker 2015).

4.3.4 Quality control

Coral samples were preselected by U-series dating quality control. In total 201 samples, which passed the U-series dating quality control, were analysed, 93 samples originate from Dragon Mound (DM) and 109 samples on Brittlestar Ridge I (BR I). A total of 193 samples (DM: 91; BR I: 102) remain after removing samples, exceeding a measurement uncertainty of 1 °C or showing unphysically negative temperatures. The 15 samples, originating from the WMCP (GeoB18127-1 and GeoB18130-1) were treated accordingly.

4.4 Results

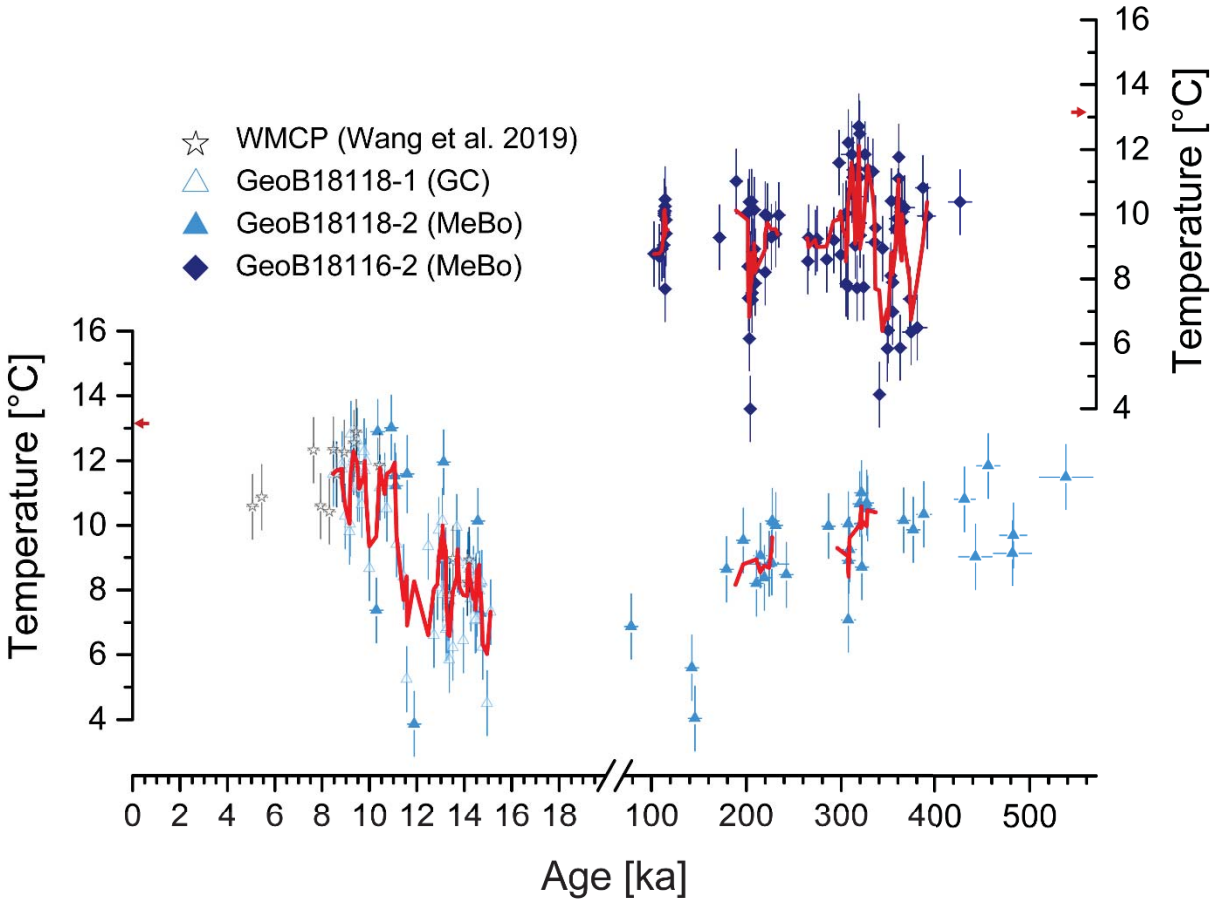

Fig. 4.2: Reconstructed Li/Mg temperature for the past 550 ka. The younger segment from 18 to 0 ka contains the cores GeoB18118-1 (BR I; open light blue triangles), GeoB18118-2 (BR I; light blue triangles) and the cores GeoB18127-1 and GeoB18130-1 (open black stars) from the WMCP (Wang et al. 2019). The Li/Mg temperature trend is indicated in red. The second section from 570 to 80 ka contains the cores GeoB18118-2 (BR I; light blue triangles) and GeoB18116-2 (DM; dark blue rhombus). The general temperature trend (3-point running mean) is indicated in red. Red arrows indicate modern day water temperature at core location.

The presented data is found in the supplement (Table 4.2).

4.4.1 Seawater temperature derived from Li/Mg on Dragon Mound

According to the strategy taken in Chapter 3.4, the results are considered in three clusters (Fig. 3.4 and 3.6). Cluster one, with n=55 samples, covers the period ranging from 400 to 250 ka. Temperatures in this cluster range between 12.7 and 4.4 °C. A predominantly decreasing temperature trend (12 to 4 °C) is observed between 400 and 350 ka with brief but intense warming phase of 7 °C between 373 to 354 ka. A second pronounced warming phase, lasting from 337 to 305 ka can also be observed with temperatures rising from 7 °C towards 11.4 °C within 12 ka (341-329 ka). These warm periods display small but frequent temperature variations between 11.6 and 9 °C. The youngest part of cluster one reveals temperatures as low as 8.5 °C. The second cluster (n=22; 230 to 200 ka) reveals a temperature range of 11 to 4 °C and a generally decreasing trend in temperature from 9.5 to 7 °C over this time interval. The third cluster (n=13) ranges from 115 to 102 ka and is characterized by reducing temperatures from 10.4 to 7.7 °C.

4.4.2 Seawater temperature derived from Li/Mg on Brittlestar Ridge I

Similar to DM, the proposed cluster scheme of chapter 3.4 is used. The first cluster (n=9; 538 to 366 ka) is characterized by relative stable temperatures between 11.8 and 8.9 °C. Cluster 2 with n=10 samples ranges in age from 327 to 307 ka and temperatures from 11.0 to 8.7 °C. This interval highlights a general cooling trend of ~2 °C (10.5 to 8.4 °C). The third cluster (n=8; 242 to 210 ka) varies between 10.3 and 8.20 °C, revealing another decreasing temperature trend of ~2 °C. Between the third and fourth cluster, 4 fragments were measured at 8.6, 4, 5.5 and 6.8 °C allocated to 178, 145, 142 and 78 ka respectively. The fourth cluster (n=70, 15.12 to 8.5 ka) ranges in temperature from 13 to 4.5 °C. A general warming trend, from ~4 °C (at 15 ka) towards 10 °C (at 13 ka) can be observed. During the YD event, only 3 fragments were measured, revealing temperatures as low as 5.2 and 3.8 °C. Starting from 11.4 ka towards 8.5 ka another general warming trend with a large scatter can be observed (12.7 to 8.6 °C).

4.4.3 Seawater temperature derived from Li/Mg on GeoB18127-1 and GeoB18130-1 in the WMCP

Samples from GeoB18127-1 (n=9), range in age between 14.1 to 5.3 ka. During the Bølling-Allerød (B-A) period, 3 samples reveal temperatures of 8.2, 8.9 and 7.8 °C (at 14.1, 13.5 and 13.4 ka). At the end of the Early Holocene, observed temperatures range between 10.4 and 12.5 °C (at 10.2 to 8.3 ka). The two youngest samples, at 7.6 and 5.3 ka during the Mid Holocene revealed temperatures of 12.3 and 10.9 °C.

For GeoB18130-1 n= 6 samples, ranging from 9.4 to 5.1 were investigated. During the Early Holocene, 4 samples average around 12.3±1 °C with temperatures from 12.9 to 11.9 °C. Two samples during the Mid Holocene show cooler temperatures of 10.6 °C at 7.9 and 5.1 ka.

4.5 Discussion

The reliability of CWC Li/Mg temperatures was previously tested on *L. pertusa (D. pertusum)*, originating from a Norwegian reef, ranging in age between 10.30-0.02 ka (Raddatz et al. 2016). With temperatures derived from faunal assemblages and Mg/Ca ratios of the foraminifera species *N. pachyderma (s),* a comparison of SST/sub-SST (100 m water depth) and the reconstructed Li/Mg bottom water temperature revealed a striking similarity (Raddatz et al. 2016).

4.5.1 Constraining the predominant water mass in coral dwelling depths

Considering today's oceanography (Chapter 2.2), the core locations are situated in the LIW, as indicated in Fig. 4.3. CTD data, taken in 2014 during the Mocco MeBo cruise (Hebbeln et al. 2015), provides temperatures and salinity data in close proximity to DM (GeoB110-1; Fig. 4.3a) and at the core location of BR I (GeoB18122-1; Fig. 4.3b). Both CTD casts, shown in Fig. 4.1, indicate surface water properties in January 2014 (winter) of circa 15 °C and 36.8 psu. At the depth of DM (236 m) and BRI (329-332 m) temperatures of 13.2 °C and salinity of 38.4 psu prevail. The measured SST value (Fig. 4.3) represents the annual minimum temperature and is in good agreement with published modern mean winter temperatures in the AS of 15.5 °C (Shaltout and Omstedt 2014). According to Shaltout and Omstedt (2014), the annual mean SST in the AS is 19.01±4.0 °C, which is 4 °C above the measured CTD value (Fig 4.4). A distinct difference, however, can be noticed in the thermocline (halocline) depths. At the shallower CTD location, close to DM, MAW can be identified into depths of circa 100 m and LIW at depths of 180-190 m, with a strongly expressed 80 m mixed water layer. At the CTD location on BR I, MAW can be identified down to depths of circa 130 m and LIW is recognized in 210 m water depth, separated by 80 m thick mixed layer. In summer, the depth gradient of

temperature in the AS further increases as highlighted in the annual mean temperature cross-section shown in Fig. 4.4.

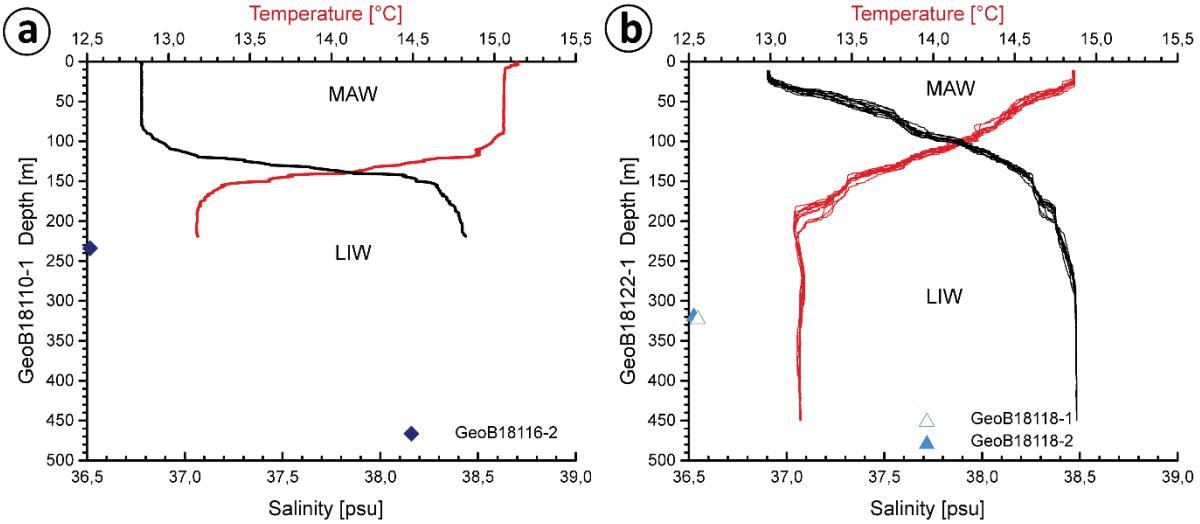

Fig. 4.3: Temperature and salinity depth profiles at the core sites GeoB18110-1 (a) and GeoB18122-1 (b). CTD station locations are shown in Fig. 4.1. Salinity (black) and Temperature (red) are shown vs depth. CTD data was taken in January 2014 during MSM36 (Hebbeln et al. 2015).

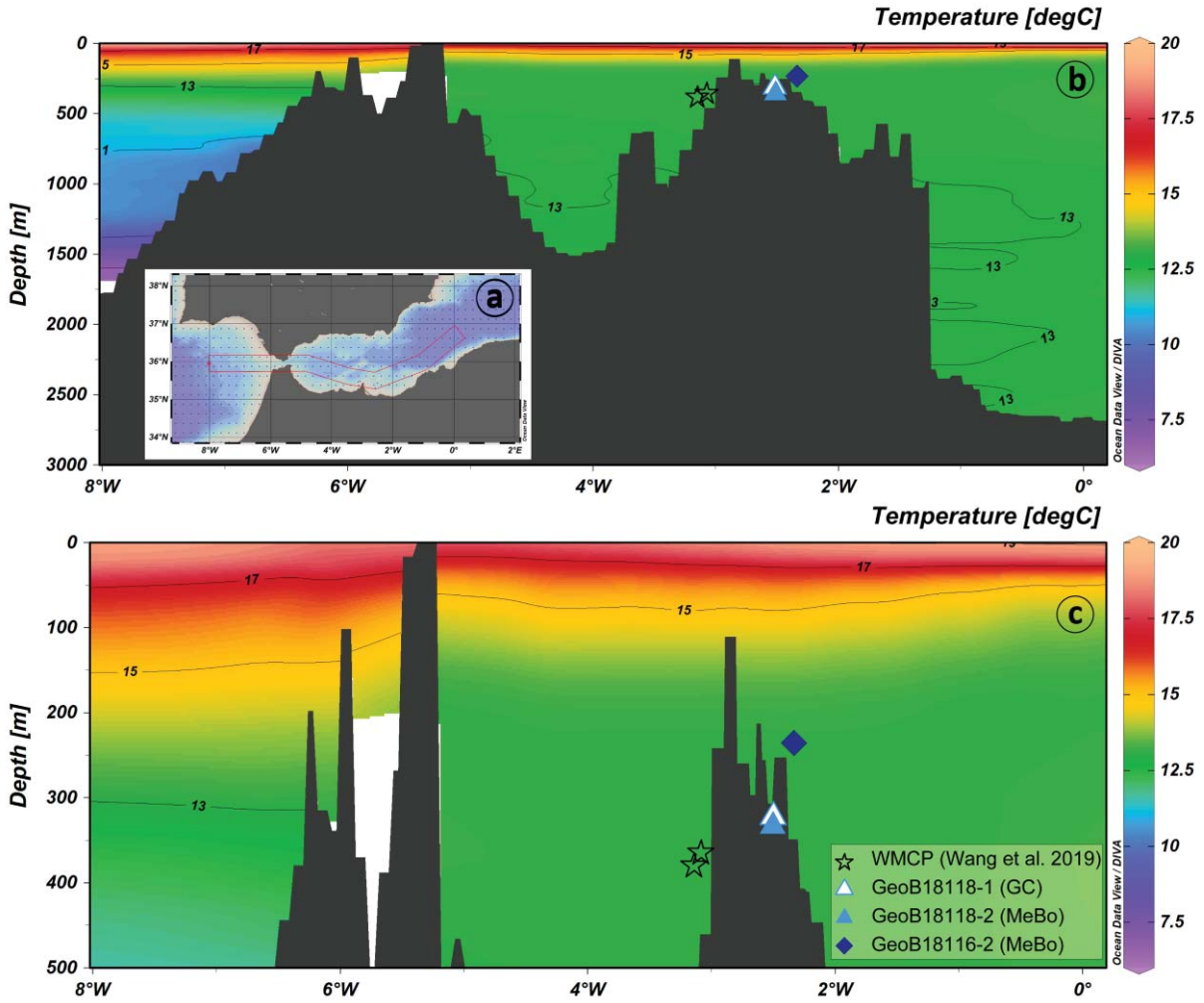

Fig. 4.4: Ocean Data View transect (Schlitzer 2018) using the WOA13 data set and spanning from the Gulf of Cádiz to the eastern end of the Alboran Sea (a). The deep section (b) reveals that temperatures below 12.5 °C are only found to the west of the SoG. The shallower section (c) shows the temperature gradient between surface water, exceeding 17 °C and LIW (~13 °C). Core locations are indicated by previously used symbols.

Based on the modern hydrography, both locations in the EMCP (BR I and DM) are influenced by LIW today. Assuming that the production and flow of LIW is a hydrological feature that existed also during previous interglacial periods (Chapter 2.2), changes in environmental conditions, such as temperature, would predominantly reflect variations of the LIW composition. However, during glacial periods with reduced sea levels of down to -140 m, DM (236 m water depth) did reside shallower within the water column and was possibly within the mixed layer, or even within MAW. Therefore, for interglacial periods, both EMCP core locations are combined into one temperature record, while for glacial periods, this seems not reasonable. Today, LIW in the Alboran Sea resides in water depths between 200 and 600 m,

with its core at 400 m (Millot 2009), thus a predominant LIW influence was assumed for the cores GeoB18127-1 (365 m) and GeoB18130-1 (379 m) (Wang et al. 2019).

However, $\delta^{13}C$ data suggests that on glacial–interglacial levels, a water mass change might have taken place (Wang et al. 2019). This indication comes from the epibenthic foraminifera species *Cibicidoides mundulus* and *Cibicidoides pachyderma,* which was used to trace past water column structure in the WMCP (Wang et al. 2019). Based on a change in $\delta^{13}C$ values and a coinciding increase in grain size during the Early Holocene, Wang et al. (2019) proposed dominant influence of MAW prior to the B/A ($\delta^{13}C$= 0.8-1.1‰), a gradual change with strong fluctuations from MAW to LIW influence between the B/A and the Mid Holocene (13.3-7.6 ka) and finally a LIW dominated influence ($\delta^{13}C$= 0.3–0.6‰) since the Mid-Holocene. Similar values were observed in the EMCP, at an off-mound sediment core south-west of BR I (Fink et al. 2013). The most enhanced mound aggregation in the WMCP (14.1–12.9 ka; 11.6–7.6 ka) with high MARs (113-176 cm/ka; 75-107 cm/ka) coincides with the timing of gradual changes in water mass dominance (13.3–7.6 ka). Thus Wang et al. (2019) proposed that the investigated WMCP coral mound resided within the interface between MAW and LIW and thus within a layer of strong hydrodynamics and high food availability.

This change in water mass dominance is somewhat contradicting to the observed nBWT evolution as presented over the last 16 ka (Fig 4.2 and Fig 4.5). If a change in water mass dominance occurred, one would expect warmer nBWT, more similar to observed SST prior to 13 ka and colder temperatures during a predominant LIW influence (Mid Holocene), as seen in the modern water column structure (Fig. 4.3 and Fig. 4.4c). However, consecutive warming of the prevailing water mass is observed (Fig. 4.5). Additionally, nBWT, derived from Mg/Ca data from benthic foraminifera on cores from the WMCP (Hebbeln et al. 2019), revealed a similar warming trend in nBWT evolution as observed here, in the Li/Mg CWC temperature. Thus, both nBWT reconstructions (EMCP: this study and WMCP: Hebbeln et al. 2019) can not confirm this change in water mass influence. The observed $\delta^{13}C$ range (0.8–1.1‰) prior to the B/A coincides with modern $\delta^{13}C$ values (0.9‰) observed within the AS and the WMS (Pierre 1999).

Within the WMS, periods of depleted $\delta^{13}C$ were reported to coincide with enhanced organic detritus input during warm interglacial intervals and thus coinciding with ORL and sapropel layers (Toucanne et al. 2015). The timing of the Organic Rich Layer 1 (ORL; 14.5–8.2 ka; Rogerson et al. 2008) and the sapropel S1 (10–6 ka; Rohling et al. 2015) agree with the timing of the depletion in $\delta^{13}C$ reported by Wang et al. (2019). Thus, enhanced productivity in the entire Mediterranean Sea and increased in-sediment organic matter mineralization could be

the driving force in the observed $\delta^{13}C$ depletion. However, a close proximity of the coral mounds to the MAW-LIW interface as proposed by Wang et al. (2019), creating internal waves and enhanced turbulence and thus supplying the corals with particulate material, like organic matter and sediments is still most likely (White et al. 2005, Mienis et al. 2007, Wang et al. 2019). Hence, during interglacial periods, it is argued, that both coral provinces (EMCP and WMCP) dwell within the same water mass (LIW) and therefore should reveal concurrent nBWT (Fig. 4.5).

Analog to the modern-day hydrography (Chapter 2.2), with approximately 90% of inflowing Atlantic Water involved in the formation of intermediate and deep water masses in the EMS and WMS (Millot and Taupier-Letage 2005), one would expect a prominent temperature influence of inflowing Atlantic water on e.g. LIW during past glacial and interglacial periods. To investigate such influence, high-resolution SST records in the AS over the past 16 ka are compared to the obtained Li/Mg nBWT record. A high-resolution Mg/Ca SST record derived from the foraminifera species *Globigerina bulloides*, is shown in Fig. 4.5 (Català et al. 2019). *G. bulloides* is reported to have its major growth season during spring in the Mediterranean Sea (Català et al. 2019), with modern spring mean temperatures of 18 °C (Shaltout and Omstedt 2014). Additionally SST records based on alkenone temperature reconstructions from the AS, spanning several climate cycles (Martrat et al. 2014) are used for comparison. The SST variability in the Alboran Sea is very susceptible to atmospheric and oceanic changes in the Atlantic Ocean (Cacho et al. 1999, Sierro et al. 2005, Frigola et al. 2008, Toucanne et al. 2012, Martrat et al. 2014, Català et al. 2019).

The presented Li/Mg data and SST records show the highest resolution during T1 and the Early-Holocene. Therefore, temperatures will be discussed from the most recent growth period (16 to 4 ka) to 550 ka.

4.5.2 Intermediate water mass temperature during the deglaciation and Holocene

The youngest investigated climate period ranges from the deglaciation to the end of the Mid Holocene (16 to 4 ka) and is represented by a total of n= 87 Li/Mg temperatures. The samples from the WMCP (n= 16; 14.1 to 5 ka) are complementary to the EMCP samples (15 to 8.5 ka) and extend the temperature record towards 5 ka. Both coral reefs are situated within the LIW water mass, which is represented by a constant temperature with depth. Hence, assuming both sites to reflect LIW over the time interval from 15-5 ka, one would expect a concurrent temperature with time. The data from both mounds perfectly match within an uncertainty of 1 °C, which thus most likely confirms a persistent presence of LIW through time at the coral sites (Fig. 4.5).

During the deglaciation, a major Northern Hemisphere ice sheet instability drove the cold event, called Heinrich Event 1 (H1). The release of freshwater into the North Atlantic and the southward transport of IRD is well attested (Heinrich 1988, Bard et al. 2000, Toucanne et al. 2010, Martrat et al. 2014). In addition, the North Atlantic overturning circulationwas reduced (Böhm et al. 2015), causing the Northern Hemisphere and in particular the northeast Atlantic to cool dramatically at the surface due to the lack of northward heat transport by the North Atlantic Current (Eynaud et al. 2009). Along the Iberian Margin, H1 is associated with reduced occurrence of temperate and humid pollen, reflecting cold and arid climate, an enhanced occurrence of the subpolar planktic foraminifera species *N. pachyderma (s)*, indicating predominant subpolar water (Cacho et al. 1999, Sierro et al. 2005, Voelker et al. 2006, Desprat et al. 2007, Martrat et al. 2014). Consequently, subpolar waters were penetrating into the GoC and into the Alboran Sea, resulting in a massive cooling of the sea surface by more than 8 °C compared to today (Martrat et al. 2007, Martrat et al. 2014). Reconstructed alkenone temperatures are about 11 °C compared to 19 °C at the early Holocene. The Mg/Ca temperature record shows a similar strong cooling during H1 if compared to the early Holocene, while strong differences between both methods appear across the YD cold reversal and throughout the Holocene. The damping of temperature changes observed in the Mg/Ca record was interpreted as the resilient capacity of *G. bulloides* to develop in changing growth seasons, which would have allowed to compensate for the large deglacial SST warming. The obvious difference has been consequently linked to a relatively mild upwelling season during the cold reversal of the YD and a cold upwelling in the AS today (Català et al. 2019). In the nBWT record, the end of the H1 is marked by two temperature values ranging from 4.5 and 7.3 °C (~15 ka). Those values are 8.5 to 6.5 °C colder than present, but the minimum temperatures during H1 remain unknown due to the lack of CWCs between 17 and 15 ka.

Hence, within the uncertainty, the apparent LIW temperature changes at the end of H1 match the ones of the surface layer.

Hence, the temperature difference between surface and LIW was similarly strong at the end of H1 compared to today. However, possible biases regarding growth season of corals and foraminifera remain unknown and actual measures during peak cooling of H1 are unknown. Nevertheless, an equally well-stratified water column in terms of temperature (and possibly salinity), compared to today, is observed. Therefore, the origin of LIW temperature changes are likely to be expected in the LIW formation region in the eastern Mediterranean, which is comparable to today.

Following on H1, as the PF moved northwards during the Bølling-Allerød (B/A) period, the influence of polar waters vanished, accompanied by an SST increase of 2-6 °C (Cacho et al. 1999, Martrat et al. 2014, Català et al. 2019). In contrast, CWC Li/Mg temperatures increase by only 2 °C during the B/A warming with a mean value of 8 °C, still 5 °C lower than present (Fig. 4.5). Hence, the temperature in the formation region of LIW must have remained colder for this time interval, which increased the thermal stratification of the water column in the AS.

The general warming trend towards the Early Holocene peak SST maximum of 18-19 °C approximately 10.5 ka ago, was briefly interrupted by the YD cold event (12.7-11.7 ka). The alkenone SST record of core ODP 976, nicely shows this event with a massive surface cooling of up to 7 °C compared to the Holocene thermal maximum. The CWC temperatures also demonstrate a dramatic cooling by 4 °C towards temperatures of as low as 4 °C between 12.5 to 11.5 ka (Fig. 4.5). Hence, once again CWC temperatures mirror the SST changes at the SoG, but now the amplitude is damped by a factor of two, compared to the surface, indicating a less dramatic colling in the LIW formation region. Note that the Mg/Ca SST does not show a YD cooling, which has been interpreted as a lack of adaption of the foraminifera species to its growing season, damping the cooling through mild autumn upwelling in the AS. The data conflicts with this interpretation, given the very low temperatures of LIW. To solve this disagreement, one may assume a different growing season between CWC and foraminifera, which is reasonable since corals feed on advected organic matter, possibly derived from surface or lateral sources. The excellent synchronicity of alkenone temperature and CWC Li/Mg temperature may imply a similar timing of alkenone production and CWC calcification. Note, that the origin of the YD cooling has been suggested as a consequence of a reoccurrence of a southward movement of the PF, reaching SoG latitudes, similar to H1 (Cacho et al. 2001). These findings are derived along the Iberian Margin, from a reduced occurrence of temperate

and humid pollen and enhanced occurrence of *N. pachyderma (s)*, reflecting cold, arid and most possibly subpolar conditions. Following upon the YD, all records demonstrate maximum temperatures comparable to today, considering the growing season, during the early Holocene at circa 10.5 ka. Enhanced freshwater injections into the Atlantic Ocean induced a strong stratification of the North Atlantic, south of Iceland, which was interpreted as a stable but weak subpolar gyre circulation (Thornalley et al. 2009). Nd-isotope data on thermocline ocean dwelling CWC from Rockall Bank confirmed a reinvigoration of the circulation, leading to a strong and stable subtropical gyre by circa 9 ka (Colin et al. 2010). Simultaneously a reduced heat transport from the subtropical gyre towards the North Atlantic was proposed for lower latitudes (Repschläger et al. 2017). However, the period of maximum SST coincides with a strong phase of stratification in the western Mediterranean Sea as well, associated with the last stage of ORL 1 (Català et al. 2019). Hence, a contribution of warmer subtropical waters flowing into the Mediterranean Sea or enhanced stratification of the AS was suspected to be accountable for the observed maximum in SST (Català et al. 2019).

The Early Holocene SST and LIW temperatures in the AS thus seem influenced by the dynamics of the Atlantic gyres and show a similar thermal gradient (ΔT= 3-6 °C) compared to today (ΔT= 2-5 °C). The end of the Early Holocene and the Mid Holocene (~9 to 4 ka) reveal a general cooling trend in Mg/Ca SST reconstruction, while alkenone SST remains constant (Fig 4.5). Diminishing meltwater flux in the North Atlantic caused the enforcement of the subpolar gyre, which likely extended towards the southeast (Thornalley et al. 2009, Colin et al. 2010), which promoted the transport of polar waters into the subtropical gyre, resulting in an increase in seasonality of the inflow, but also the general atmospheric circulation of the northeast Atlantic. CWC reveal a moderate temperature oscillation around a mean value of 11.5 °C, which is 1.5 °C lower than the present-day LIW temperature. The amplitude of 1.5 °C is within 2 sigma uncertainty of the reconstruction and thus not significant. Solely two temperature values that have been measured at ~10 ka ago, when temperatures suddenly drop by 4 °C for several centuries are significantly different. This event has no counterpart in other records and therefore stands out. Since no information on possible changes in the LIW formation region or dramatic changes of the Atlantic inflow is available, a reasonable explanation for those two temperature values, which certainly need to be confirmed, cannot be provided.

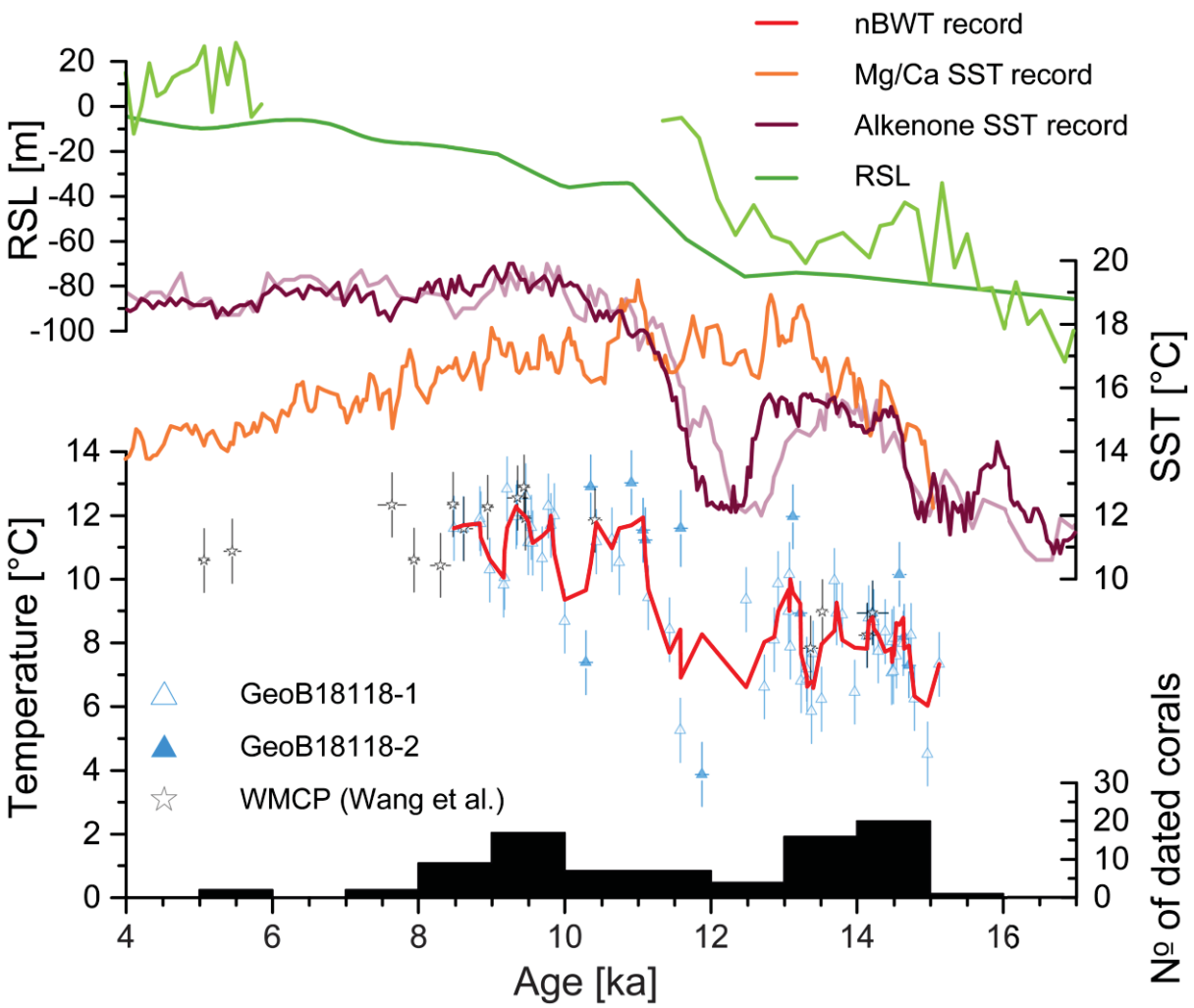

Fig. 4.5: Near Bottom Water Temperature (nBWT) derived from Li/Mg ratios from GeoB18118-1 (light blue open triangles), GeoB18118-2 (light blue triangles) and core locations in the WMCP (black open stars; Wang et al. 2019). Red line shows the combined 3-point running mean of Li/Mg derived temperatures during the Holocene. SST records derived Mg/Ca values on foraminifera (orange; Català et al. 2019) and alkenone values (purple; Martrat et al. 2014) are shown in the upper section. Note that the transparent purple record (MD95-2043) is located closer to the EMCP. The purple record (ODP-976) however, was conducted in a higher resolution but is closer to the WMCP. Relative Sea Levels are given at the top (green; Rohling et al. 2014). Bottom black boxes show the number of dated corals per 1 ka.

Lastly, corals grow over short periods, while the SST records, especially alkenone derived records, reflect an average over many growth seasons of surface-dwelling organisms (e.g. Laepple and Huybers 2013). Therefore, the increasing variability of LIW temperature and the very cold temperatures, observed prior to the B/A warming and throughout the YD, may in fact speak for an influx of either polar Atlantic waters, as seen briefly in the Gulf of Cádiz during H1 (Voelker et al. 2006) or a direct, regional influence of melt-water and river discharge on the LIW formation temperature. However, at present-day the mean annual Atlantic inflow at the SoG is estimated with 0.81±0.06 Sv (Soto-Navarro et al. 2010), whereas a combined freshwater inflow, comprised of groundwater -, river - and the Black Sea input was estimated

to comprise just 0.025 Sv (Bethoux and Gentili 1999, Ludwig et al. 2009, Ollivier et al. 2011, Rodellas et al. 2015; Border et al., in prep.). For the past 50 ka, SoG exchange was assessed to have ranged between 0.6 and 0.5 Sv during the glacial period (Rogerson et al. 2012, Simon 2017). No assessment of the enhanced freshwater input during periods of increased freshwater discharge is available, therefore a maximum of 0.075 Sv, triple of the modern value, is assumed. Since the inflow at the SoG is by far larger than the input of freshwater, it is argued, that the observed temperature variability in the CWC derived LIW record originates from the temperature variability of inflowing Atlantic Water, since the temperature of discharged freshwater would only show a minor influence on SST variability in the LIW formation region.

Cold temperatures as seen during H1 and YD are related to a positioning of the PF close to the SoG inducing southward transport of subpolar waters along the Iberian Margin into the Mediterranean Sea (Cacho et al. 2001, Voelker et al. 2006, Desprat et al. 2007). In contrast, maximum temperatures as today, and during the Early Holocene, are related to the northward displacement of the PF (Cacho et al. 2001, Voelker et al. 2006) and thus inducing warm subtropical water into the Mediterranean Sea.

4.5.3 Intermediate water mass temperature development over the past 550 ka

The interglacial MIS 5 revealed SST temperatures, based on alkenones, between 18–23 °C, with the warmest period between 127 ka and 121 ka (Martrat et al. 2014). Coinciding with the SST maximum, organic-rich layers (132-129 ka) and sapropelic layers (S5: 127-121 ka) are observed (Martrat et al. 2014). Since no corals were dated prior and during the peak MIS 5 (127–121 ka), direct measures of the water column thermal structure are not available.

Subsequently, SST decreased from 23 to 18 °C (121–114 ka), followed by a brief but distinctive cold event with SST as low as 12.5 °C (111±1 ka). During this period (115-102 ka; Fig. 4.6), ten CWC samples were dated (Fig. 4.6) and yield nBWT between 9.0 to 10.4 °C ($nBWT_{av}$= 9.7 °C). Therefore, the temperature gradient amounts to circa 7 °C between the surface and LIW, which is surprisingly similar to the observed temperature gradient (5.5–7.5 °C) in the early Holocene and deglaciation. The LIW temperature is thus similar to the B/A period during this period of Mediterranean and Northern Hemisphere cooling and ice sheet growth (Fig. 4.6). High resolution terrestrial and marine proxy records off the Iberian Margin revealed a reduction of tree pollen and an increase in the subpolar foraminifera species *N. pachyderma (s)*, indicating cold, dry and subpolar conditions along the Iberian Margin during the glacial inception, which were interpreted as similar to Heinrich Events (Pailler and Bard 2002, Sánchez Goñi et al. 2005, Tzedakis 2005). Equivalent to H1 and to some extent similar to the YD, both periods have been linked to a southern position of the PF (Cacho et al. 2001, Voelker et al. 2006). During such phases, CWC seem to vanish in the WMCP and EMCP.

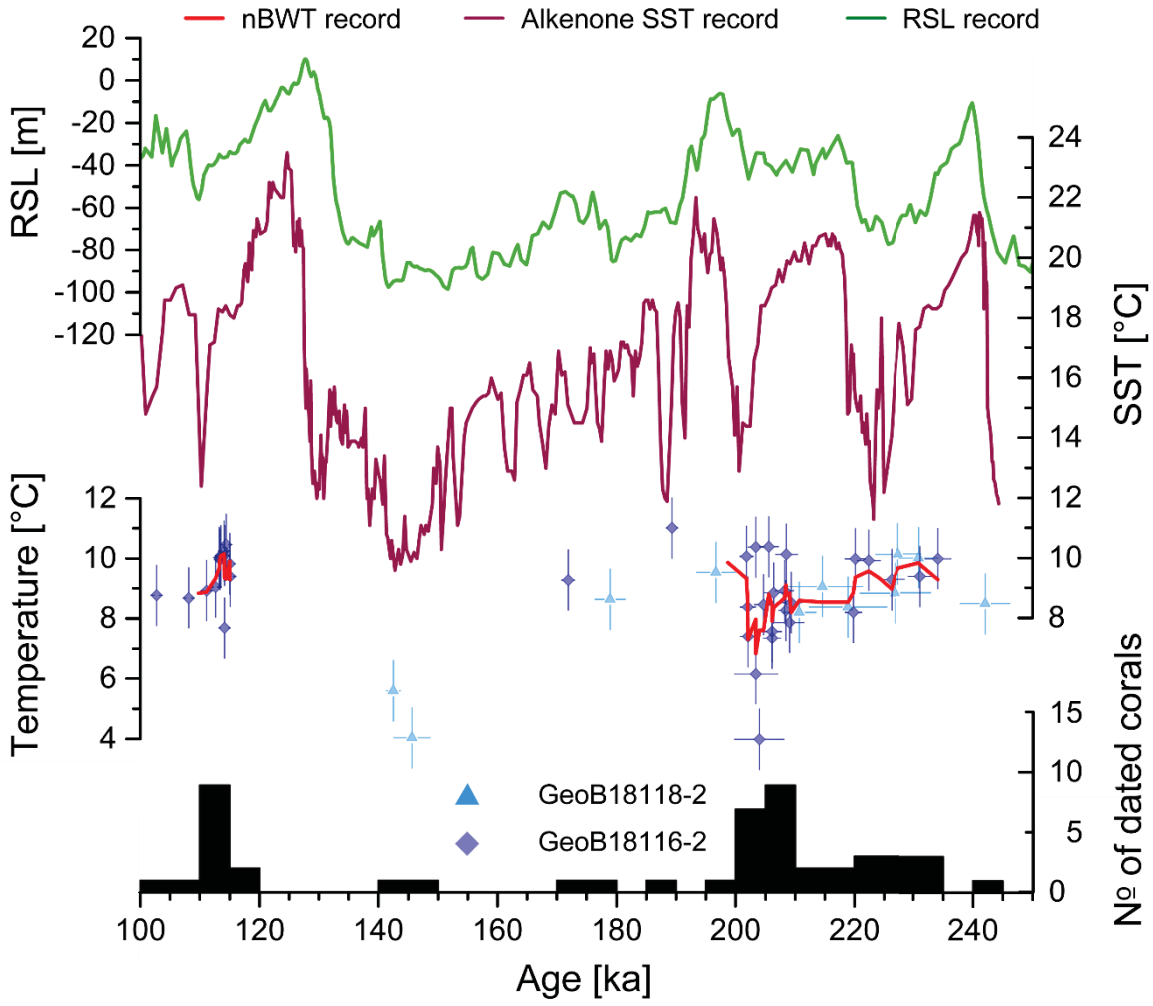

Fig. 4.6: Near Bottom Water Temperature (nBWT) derived from Li/Mg ratios between 100 and 250 ka. GeoB18118-2 (light blue triangles) and GeoB18116-2 (dark blue rhombus) are displayed. Red line shows the combined 3-point running mean record during this period. The dark red record shows an SST record derived from alkenones (Martrat et al. 2004). Green record shows Relative Sea Level (RSL; Rohling et al. 2014). Bottom black boxes show the number of dated corals per 5 ka.

During MIS 6, SST reconstruction reveals a general decrease from 180 ka towards 150 ka from 18 °C to a minimum of 10 °C, which is reached at 140 ka, when the global ice volume was highest and the sea level reached a minimum. For this entire time span solely four CWC are available, which however cover the initial warmer phase at 180 to 170 ka with a nBWT of 9±1 °C and the coldest time to 145 ka with a nBWT of 5±1 °C (Fig. 4.6). Similar low temperatures of circa 4 °C were observed only at the end of H1 (~15 ka) and the YD (~12 ka), when SST values also reached a minimum at ~10 °C (Fig. 4.5). Consequently, the nBWT again mimics the SST trend with a warm period offset of up to 8 °C and a minimum offset during the coldest period of ~5 °C. Note, that between 180 to 170 ka, corals of both mounds show once again similar temperatures at sea levels of -80 to -60 m, indicative of both sites bathing

in the same water mass (here most likely LIW). The gradient between SST and nBWT thus reveals the previously observed values ranging between 8±1 to 5±1 °C.

Further back in time, the SST record, of MIS 7 from 245 to 190 ka, varies strongly and systematically through time. The temperature spans over 10 °C with highest values over 20 °C and lowest values being close to glacial minimum values of 10 °C. Three prolonged warm SST maxima (245 ka, 215 ka and 195 ka) and three shorter glacial type periods (stadials) are identified (221 ka, 200 ka and 190 ka; Fig. 4.6; Martrat et al. 2004). However, the observed glacial type periods in SST are not reflected in the Mediterranean RSL (Rohling et al. 2014). In contrast to this SST record, the reconstructed nBWT shows overall little variability and ranges from 8 to 10.5 °C between 245 to 190 ka. Several corals have been dated synchronous to the observed SST minima, but do not show major cooling. Hence, the nBWT does no longer seem to follow the reconstructed SST values. During the second cold period around 211 ka, the CWC temperatures reveal a dramatic excursion to near glacial values of 4 °C in two corals, while others remain at the mean value of 10 °C. Hence, there is an indication of short cold spells recorded also in the nBWT and therefore possibly in the LIW, but the record is less well constrained in its timing as the SST record (Fig 4.6). During this time, temperate and humid tree pollen indicate a gradual decrease towards cold and arid climate from 210 to 200 ka, however, the maximum of the cold period is expected at 198-196 ka (Martrat et al. 2004, Tzedakis et al. 2004, Desprat et al. 2006, Desprat et al. 2007). In contrast, the dated CWC, which show a glacial type temperature would date this event to 210±5 ka. Given the individual character of each coral, the possibility of short age reversals in the coral bearing sediments does not further allow to constrain the timing of the one cold spell recorded. Overall multiple CWC were dated spanning MIS 7, but age errors increase to partly as large as ±4 ka. Therefore, these corals may not cover the short glacial type stadials recorded in the SST record. On the other hand, the few corals indicating the possibility of a basin-wide cold spell through a decrease of the nBWT to near glacial values, infer a moderately earlier timing of these events around 210 ka.

The third short glacial type cold spell in the SST record is once again not represented in the nBWT record. Therefore, regarding MIS 7, it can be concluded, that the nBWT and therefore most likely the LIW was generally in a colder state with temperatures of solely 8 to 10 °C on average. Additionally, the close coupling of SST and nBWT observed in more recent interglacials is not traced, which either reflects the decreasing precision of U-series ages or a mechanism of LIW formation that decouples the SST of Atlantic inflow from the SST at the LIW production site. For the latter process, a reasonable explanation has not yet been found,

but one may speculate that a stronger west-east temperature gradient must have existed throughout the Mediterranean Sea with average colder temperatures in the East as compared to today increasing the thermal gradient of MAW and LIW to up to 10 °C, while during cold spells (glacial type stadials) the temperature gradient almost vanished, except for the one at 210 ka.

The AS-SST reconstruction only covers the past 245 ka, thus for the further discussion, other sources of SST values are necessary to refer to. For the discussion of SST and nBWT beyond 240 ka, an alkenone SST record from the GoC is used, which is closely related to the SST variability within the AS (Fig. 4.8; Martrat et al. 2007). However, for the period of overlap between both records, during peak warm climate the GoC SST is estimated 1-2 °C lower as the AS SST, while during peak glacial (low sea level) the SST is also up to 2 °C colder than the one in the AS. Additionally, the RSL from the Mediterranean Sea (Rohling et al. 2014) is used to guide through the general climate trend (Martrat et al. 2004, Martrat et al. 2007).

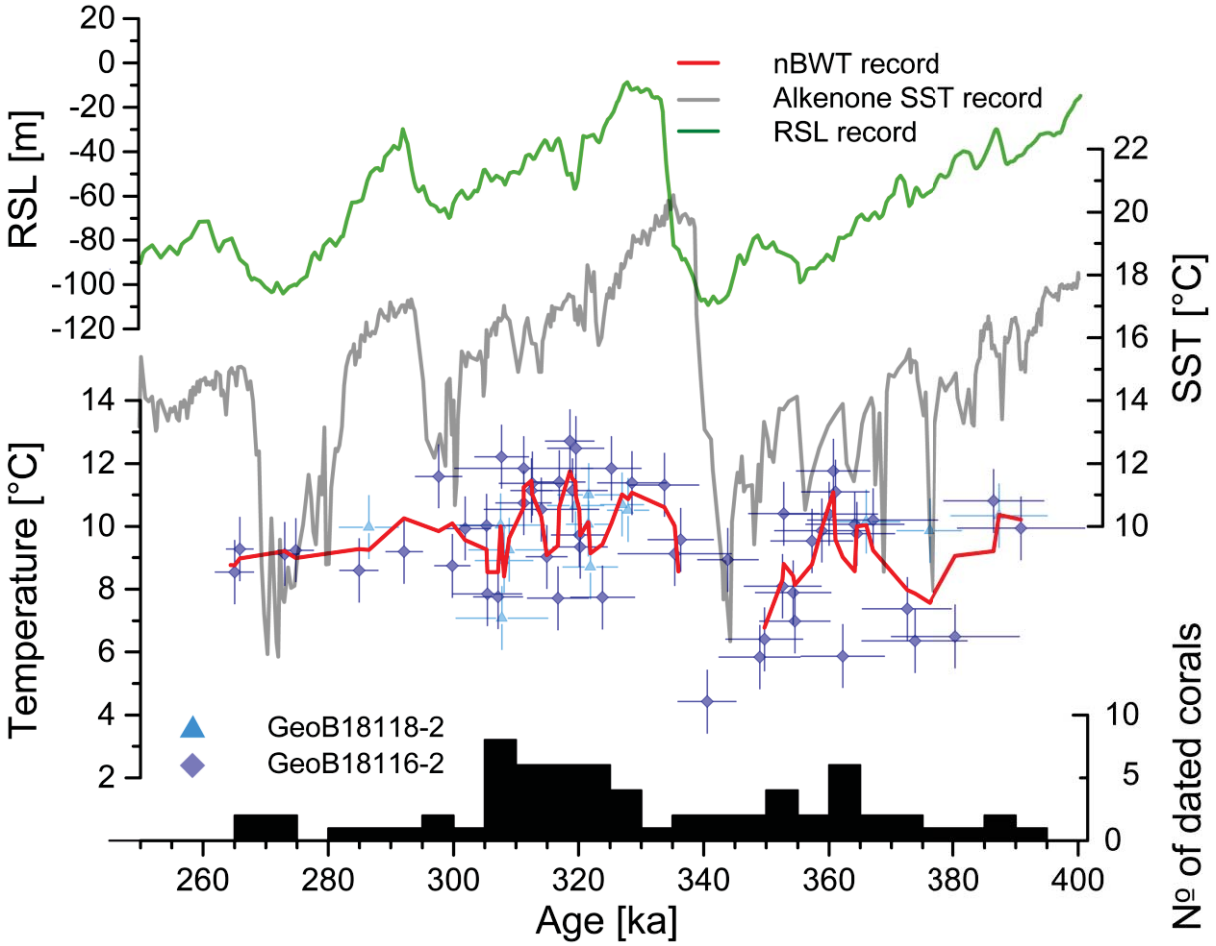

Fig. 4.7: Near Bottom Water Temperature (nBWT) derived from Li/Mg ratios between 250 and 400 ka. GeoB18118-2 (light blue triangles) and GeoB18116-2 (dark blue rhombus) are displayed. Red line shows the combined 3-point running mean record during this period. Gulf of Cádiz SST reconstruction derived from alkenones (grey record; Martrat et al. 2007). Green record shows Relative Sea Level (RSL; Rohling et al. 2014). Bottom black boxes show the number of dated corals per 5 ka.

Regarding the time span from 400 to 250 ka, the record covers MIS 10, MIS 9 and MIS 8. The GoC SST record nicely follows the global climate trend as given in the sea level reconstruction, with SST ranging from up to 20 °C during the warm climate of MIS 9 to as low as 6 °C during peak ice extent and lowest sea level of MIS 10 and MIS 8 (Fig 4.7). In particular, during the peak glaciations, SST of the GoC appears more variable with prominent cooling events of down to 6 °C at 345±5 ka and 270±5 ka. Overall, the glacial-interglacial variability of GoC SST follows a saw tooth shape with rapid warming during terminations and slow cooling during glacial inceptions as expected from the global climate trends. The nBWT reconstruction, which is based on individual dated corals now reveals substantially larger errors for the individual coral ages, which thus limits the possibility to distinguish the timing of nBWT changes. As during previous interglacials, corals are not representing the peak warm period with highest sea level, hence the period equivalent to present-day climate.

Overall, nBWT and thus LIW temperatures span similar ranges compared to previous glacial-interglacial cycles with values ranging from up to 12 °C during the late MIS 9 to values as low as 4 °C during peak glaciation (MIS 10). Both mounds deliver however identical values through time, which certainly highlights the existence of a LIW type water mass, which is well stratified underneath the Atlantic inflow. Since the observed range of nBWT and SST (note that GoC SST is during peak values up to 2 °C lower than the one in the AS) are similar and somewhat synchronous (considering the large uncertainty in CWC ages), thus one can certainly assume that the coupling between Atlantic inflow (SST) and temperature at the LIW formation site is similar to the past 140 ka.

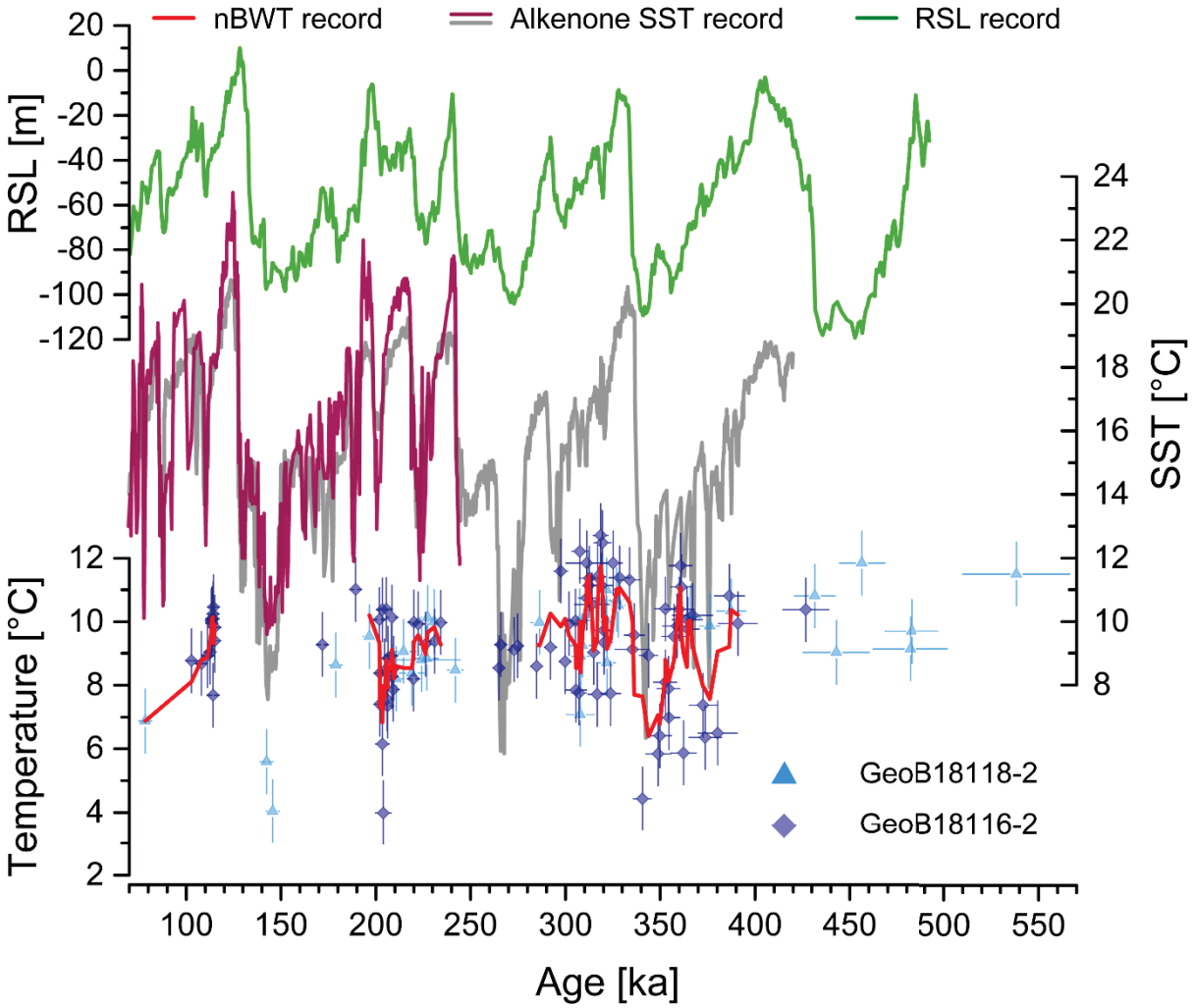

Fig. 4.8: Near Bottom Water Temperature (nBWT) derived from Li/Mg ratios between 70 and 560 ka. GeoB18118-2 (light blue triangles) and GeoB18116-2 (dark blue rhombus) are displayed. Red line shows the combined 3-point running mean record during this period. The dark red record shows an alkenone derived SST record (Martrat et al. 2004). Gulf of Cádiz SST reconstruction derived from alkenones (grey record; Martrat et al. 2007). Patterns of both long-term SST records generally match, thus the GoC SST can be substituted for the AS SST record exceeding 250 ka. Green record shows Relative Sea Level (RSL; Rohling et al. 2014).

The final time segment, between 550 and 420 ka, covers MIS 13 (492 to 478 ka) and MIS 12 (478 to 424 ka) with solely 7 CWC samples (Fig. 4.8). The CWC derived nBWT once again span ranges, similar to the ones of previous interglacials with an average of roughly 10±2 °C. No indication of glacial LIW temperatures are found and corals did certainly not occur during peak sea level and thus expected warmest SST and nBWT. Thus the oldest studied CWC confirm the average value of nBWT but do not yet provide an opportunity to study temporal changes of LIW formation temperatures.

Overall, it can be concluded, that CWC derived peak glacial nBWT values are a rare or potentially even absent case in the AS, due to the lack of CWC occurrence. However, three times during MIS 10, MIS 6 and during a cold spell within MIS 7, spectacular low values of as low as 4 °C are reconstructed. Such values are similar to present-day temperatures observed south of Iceland or within the Norwegian Sea at similar shallow depth but do not exist in the Mediterranean Sea. Since CWC dwell in a water temperature range between 4–14 °C (Freiwald et al. 2009, Roberts 2009) and glacial LIW temperatures of 4 °C were observed, it is unlikely that LIW temperatures dropped below the comfort zone of CWC (<4 °C) within these short glacial peaks. Hence, a temperature-driven demise of CWC during peak glacial periods is unlikely.

The water, bathing both coral locations and thus at 100 m depth distance, shows a persitent thermal stratification with the surface layer and a persistent thermal gradient of at least 3 °C. Therefore, the water bathing the CWC likely originated in the eastern Mediterranean Sea forming a LIW type water mass during the past 7 glacial-interglacial cycles. This water mass must have been substantially colder during peak glacial periods. On the other hand, equally rare CWC occurrences are found during peak sea level, i.e. peak climate warm phases (MIS 5, MIS 11, MIS 13) when SST values in the AS reach values as high as 20 °C. During such peak interglacials, nBWT values are expected to reach 13 °C as today. In fact, such high values are solely observed today, during the early Holocene and during MIS 9. Assuming, that the LIW temperature reconstructions are accurate within a precision of 1 to 2 °C, the modern temperature of the LIW seems a rare case in the evolution of the Mediterranean Sea over the past 550 ka. The observed interglacial temperature values suggest a significantly lower mean value of 10±2 °C for the interior of the Mediterranean Sea. This implies that the Atlantic inflow must have been on average colder, presuming a tied coupling of AS-SST and LIW temperature or alternatively that the formation of the LIW was related to stronger winter cooling in the eastern Mediterranean and possibly a less important salt injection from loss of evaporation.

In any case, the temperature reconstruction demonstrates a strong coupling of AS-SST and underlying water, with a persistent temperature stratification over the past 550 ka. This implies that the Mediterranean Sea interior water mass formation responds to the changes in the Atlantic, driven by the latitudinal displacement of PF and AF. These changes are linked to changes in atmospheric circulation and freshwater runoff into the Mediterranean Sea, affecting the nutrient cycle, regional upwelling and thus the conditions the corals live in, as discussed in the previous chapter.

4.6 Conclusion

Near bottom water temperatures, recorded by Li/Mg ratios in CWC from the Alboran Sea were used to trace the thermal history over 7 entire climate cycles. nBWT from the shallow DM (236 m) and the deeper BR I (329 m) are consistent over the interglacial periods of the past 550 ka and thus reveal a coherent, predominant water mass, most possibly LIW.

The last deglaciation and the Holocene are studied at an unprecedented temporal resolution and revealed a temperature evolution of LIW from cold conditions at the end of Heinrich Event 1 to similar as present warm conditions at the early Holocene. The LIW temperature closely follows the temporal evolution of the AS-SST based on alkenone-SST reconstructions. Mg/Ca SST reconstructions, which are thought to reflect a seasonal upwelling signal, do not show a YD cold reversal which was thought to reflect upwelling of warmer LIW. The Li/Mg temperatures contradict this theory since a strong cooling of the LIW is observed during the YD, with values far below the alkenone SST reconstructions. Temperature reconstructions demonstrate the existence of a persistent thermal gradient in the upper water column of the AS, with MAW at the surface and LIW underneath, but with variable thermal depth gradients.

The Holocene with an unprecedented fine temporal resolution revealed a distinct difference in the temperature gradient between two SST reconstructions, based on Mg/Ca from foraminifera and alkenones and the nBWT reconstruction. The Mg/Ca SST record suggests a gradual decrease in temperature-driven stratification between MAW and LIW, whereas the alkenone derived SST record suggests a persistent strong temperature gradient. Since the season of calcification cannot influence this observed difference in the evolution of the temperature gradient, a small annual variability in LIW temperatures over the past 15 ka within the AS is suggested.

The nBWT reconstruction of LIW, over the last 550 ka, revealed an overall temperature range from 6 to 13 °C during interglacial periods (MIS 9 to MIS 1) and the glacial periods MIS 12 and MIS 8. Cold, glacial-like LIW temperatures (< 6 °C) are limited to short time intervals, as seen during MIS 10 (350 ka), MIS 7 (200 ka), MIS 6 (145 ka) and during the termination 1 (H1 and YD). The observed temperature range over the last 550 ka suggests that the modern-day temperature of LIW (13.2 °C) at the core locations within the EMCP (BR I and DM) is almost unprecedented. The Li/Mg data implies significantly colder water mass temperatures than today, with an average of 9.4±4 °C over the last 550 ka. Within the Alboran Sea, modern-day temperatures do not fall below 12 °C, even at water depths of 3000 m. Close to modern-day temperatures were solely reached around 320 ka (12.5±1 °C) and at 9.4±1 ka (12.5±1 °C).

Values, most possibly exceeding modern-day temperatures would be expected for the warmest period during MIS 11 (390-430 ka) and during MIS 5 (127–121 ka), however, so far no CWC were found during these periods.

During glacial periods, where CWC occurrence is restricted, nBWT of both locations show coherent temperatures of 9.5±1 °C at MIS 10 (370 ka), MIS 8 (285 ka) and MIS 6 (180 ka), during reduced Mediterranean sea levels between -40 to -80 m. Although glacial data with co-occurring corals from both locations is scarce, it is assumed that up to a Mediterranean sea level reduction of -80 m the same water mass is predominant. However, comparisons during full glacial conditions, with temperatures of 6-4 °C, are not possible.

Based on terrestrial and marine records along the Iberian Margin, within the GoC and the AS, a clear correlation of (i) cooling events in SST, cold and arid climate in the Mediterranean Region and sub-polar planktic foraminifera species during interglacial periods and (ii) the coincident reduction and demise of CWC occurrence in the AS could be established. Glacial periods in the Mediterranean Region are associated with cold and arid conditions and a southern position of the PF towards ~45-40°N (Ruddiman and McIntyre 1981, Grousset et al. 1993, Robinson et al. 1995, Rohling et al. 1998, Kageyama et al. 2006) as well as a general lack of CWC occurrence as shown in Chapter 3.

5 The "*Gibraltar seesaw pattern*": Implications of atmospheric-oceanic interplay on CWC growth in the Alboran Sea and the Gulf of Cádiz

The research cruise MSM 36 „MoccoMeBo" in 2014 was motivated by previously observed, distinct differences in the temporal evolution of CWC mounds in the Gulf of Cádiz and the Alboran Sea recorded for the past climate cycle (e.g. Wienberg et al. 2009, Wienberg et al. 2010, Fink et al. 2013). The abbreviation "CWC" stands here for the most important reef forming species *L. pertusa (D. pertusum)* and *M. oculata*. Other local species may behave differently. For example, other *Dendrophyllia* corals are known to occur during the Holocene in the GoC. During the last glacial period, flourishing CWC growth was observed in the GoC, followed by a complete demise of CWC activity circa 10 ka ago (Wienberg et al. 2009, Wienberg et al. 2010). Contrasting to this finding, CWC started to colonize the AS around ~14 ka (Fink et al. 2013) and populate reefs until present in some regions of the AS. Productivity was identified as the most important factor steering the observed timing of CWC growth on both sides of the SoG (Wienberg et al. 2010, Fink et al. 2013), but the mechanisms of the distinct timing remain unknown. This surprising finding was identified as the "*(most likely climate-driven) Gibraltar-seesaw pattern*" (Hebbeln et al. 2015) from which three work hypotheses were formulated by Dierk Hebbeln and his coworker (Hebbeln et al. 2015):

"(1) The Gibraltar-seesaw pattern describing the LGM-Holocene development of CWC along the Moroccan margins on both sites of the Strait of Gibraltar is a long-lasting productivity-driven feature spanning at least the last glacial-interglacial cycle.
(2) The long-term development of the Moroccan CWC mounds is characterized by a major change in growth patterns as proposed by several mound development models.
(3) The initiation of the Moroccan coral mounds on both sides of the Strait of Gibraltar is triggered by major large-scale paleo-environmental change(s)."

Although the available U-series age data does not permit to judge on hypothesis (2), comparing the overall maximum Mound Aggregation Rates (MARs) on both sides of the SoG, similar maximum MARs, ranging between 122-66 cm/ka (GoC; Hemsing 2017) and 168-126 cm/ka (AS; this study) can be observed. However, the mound formation patterns differentiate severely. Whereas, in the GoC, thousands of mainly small mounds were found, with a mean height of 18 m (Hebbeln et al. 2019), multiple steep ridges of up to 150 m height and hundreds of elongated and arcuate mounds of up to 40 m height were found in the AS (Hebbeln 2019). To address the above work hypotheses (1) and (3), the published U-series age data from the GoC (Wienberg et al. 2009, Wienberg et al. 2010, Frank et al. 2011, Dubois-Dauphin et al. 2016, Krengel 2016, Hemsing 2017) and AS (Fink et al. 2013, Fink et al. 2015, Wang et al. 2019,

Feenstra et al. 2020, Fentimen et al. 2020, this study) have been compiled, spanning over the past 550 ka, i.e. 7 climate cycles.

Moreover, Li/Mg temperature reconstructions from both sides of the SoG may point out changes of physical properties and stratification of the water column, i.e large scale paleo-environmental changes. Note, that U-series age data from the GoC, conducted prior to 2016, was measured on different mass spectrometer generations (ICP-QMS, MC-ICPMS, TIMS) and thus shows significant differences in the quality of the age measurements.

5.1 Favourable CWC growth conditions during interglacial and glacial periods in the AS and GoC over the past 550 ka

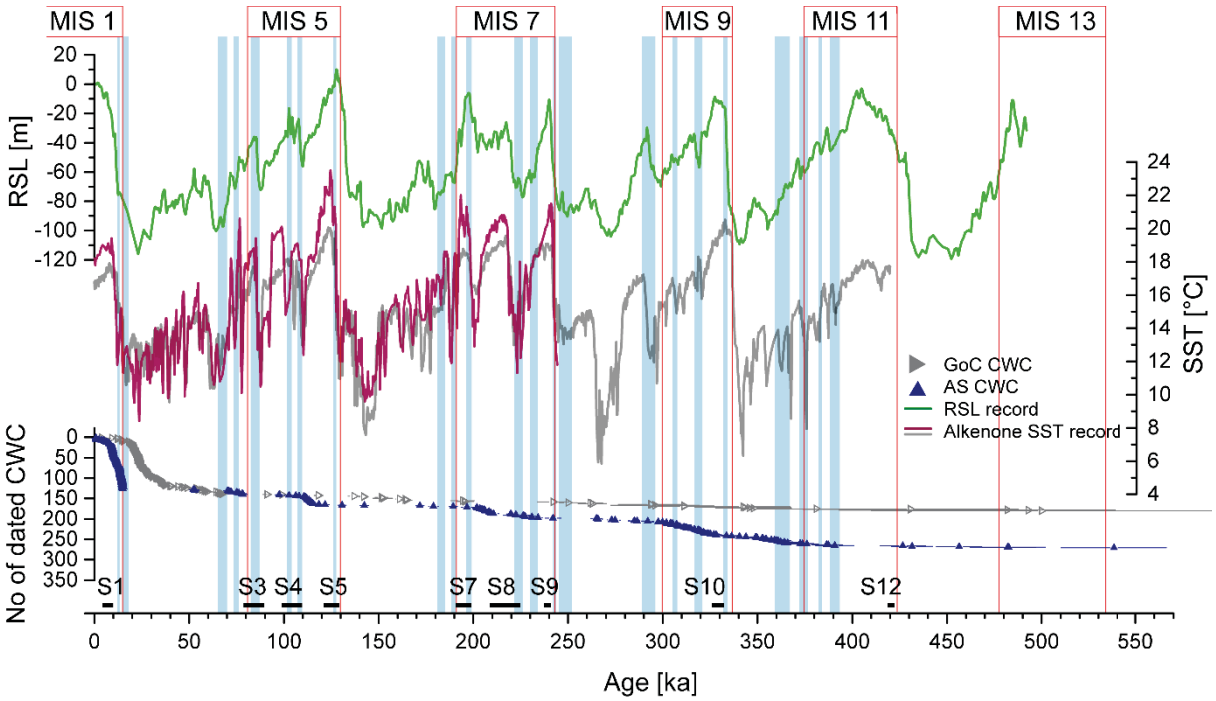

Fig. 5.1: Compiled U-series records from the Alboran Sea and the GoC over 550 ka. Blue triangles mark AS CWC, whereas grey triangles represent the GoC CWC record. The dark red record shows an alkenone derived AS SST record (Martrat et al. 2004). GoC SST reconstruction (grey record) is derived from alkenones as well (Martrat et al. 2007). Patterns of both long-term SST records generally match over time, thus the GoC SST is used as substitute for the AS SST record exceeding 250 ka. The green record shows Relative Sea Level (RSL; Rohling et al. 2014). Sapropel layers are shown at the bottom (Ziegler et al. 2010, Konijnendijk et al. 2014, Rohling et al. 2015). Blue vertical bars show cold stadial conditions at the Iberian Margin, coinciding with Greenland Stadials (GS) and Heinrich Events (H) (Desprat et al. 2007). Red vertical bars indicate interglacial Marine Isotope Stages (MIS).

The compiled U-series age data from the GoC and the AS over the past 150 ka (Fig. 5.1), strongly indicates a Gibraltar-seesaw pattern of predominantly glacial CWC in the GoC and interglacial CWC in the AS, as formulated in hypothesis (1). Furthermore, the observed CWC growth pattern over the past 550 ka provides a good foundation to speculate, that the Gibraltar-seesaw pattern is very likely for earlier glacial-interglacial cycles as well. However, it remains best resolved during the last glacial-interglacial cycles up until 250 ka, due to the significant differences in the quality of the age measurements older than 250 ka in the GoC. Thus, further investigation may be necessary to strengthen the argument on a long-term scale.

Hence, the productivity-driven nature of the Gibraltar-seesaw pattern (1) is discussed in the following, focussing on atmospheric and oceanographic changes on a regional scale, surrounding the SoG. Glacial-interglacial cycles are expressed in the form of dramatic SST changes and sea level fluctuations due to the global ice volume changes (Fig. 5.1). Regional changes in precipitation and a north-south oscillation of the PF and AF are known as well (Fig. 5.2 and 5.3; Eynaud et al. 2009, Denton et al. 2010, Clark et al. 2012).

Glacial periods are globally marked by large ice sheet build-ups and a southern position of the PF between 45°N and 40°N (Grousset et al. 1993, Robinson et al. 1995, Rohling et al. 1998, Kageyama et al. 2006, Eynaud et al. 2009). Due to polar air residing at temperate latitudes, cold polar air outbreaks were frequently induced into the western Mediterranean Region, potentially triggering enhanced cyclogenesis within the Western and the Central Mediterranean Basin, creating a meridional geostrophic circulation (Rohling et al. 1998, Hayes et al. 2005, Kuhlemann et al. 2008), possibly distributing aeolian dust over the Mediterranean Region and into the GoC (Fig. 5.2). The environmental conditions around the western Mediterranean Region were of predominantly cold, semi-arid to arid climate, with low river run-off and low fluvial sediment input, yet enhanced Saharan dust input (Martrat et al. 2004, Sierro et al. 2005, Fink et al. 2013, Terhzaz et al. 2018, Feenstra et al. 2020).

During glacial periods, when SST in the AS and GoC ranged between 8 to 15 °C (Fig. 5.1; Martrat et al. 2004, Martrat et al. 2007), minor glacial CWC occurrences in the AS revealed coralline Li/Mg nBWT between 4 to 6 °C over the past 550 ka (340 ka, 200 ka, 140 ka, 15 ka, 12 ka; Chapter 4, this study). In the GoC, however, flourishing glacial coral growth over the past 70 ka revealed coralline Li/Mg temperatures ranging between 0 to 6 °C (Hemsing 2017). Thus, during glacial periods, a temperature-driven demise of the investigated CWC species in the AS is highly unlikely.

Hence, reduced productivity and reduced, shallow vertical mixing represent unfavourable conditions for sustained coral growth within the AS. Thus, only minor CWC occurrences were observed during most glacial periods (MIS 12 to MIS 2), however, dominant CWC growth during MIS 10 was observed. The AS CWC occurrences during glacial periods in the AS coincide with brief increases of the Mediterranean sea level (Rohling et al. 2014), as well as rapidly increasing SST. These interstadial conditions were observed in the AS SST as well as GoC SST records and are most likely associated with a brief retreat of the PF to a more northern position (Martrat et al. 2004, Martrat et al. 2007). Hence, a brief return to more interglacial-like conditions, providing freshwater input and thus more productivity and vertical mixing than during full glacial periods is suggested. However, due to the scarcity of

the GoC CWC record beyond 70 ka, it remains uncertain if CWC growth in the GoC was reduced during these interstadial interceptions.

During glacial periods, the reduced freshwater input into the Mediterranean Sea and therefore reduced Nile River discharge resulted in the formation of more dense LIW with higher flow speed (Revel et al. 2010, Toucanne et al. 2012). Consequently, in the GoC, denser MOW was recognized in greater depths with higher velocities (Voelker et al. 2006, Bahr et al. 2014, Bahr et al. 2015, Kaboth et al. 2016, Kaboth et al. 2017). It has been shown, that MOW strength and density positively influences the strength and the position of the Azores Current within the GoC via the β-plume effect (Xu et al. 2007, Volkov and Fu 2011, Kaboth-Bahr et al. 2018) and thus most possibly enhancing eddy energy within the GoC. Furthermore, the glacial Azores Front, associated with enhanced productivity, resided within the GoC (~35°N; Alves and Colin de Verdière 1999, Rogerson et al. 2004).

Hence, strong offshore winds and aeolian dust input from the arid Mediterranean Region and enhanced productivity due to local upwelling in the GoC represent favourable conditions for glacial CWC growth within the GoC (Wienberg et al. 2010). Consequently, CWC occurrences were found during the glacial periods MIS 6 and MIS 4 -2. Although the amount of CWC in the GoC, measured with insufficient quality, is scarce, CWC most possibly grew during MIS 12, MIS 10 and MIS 8.

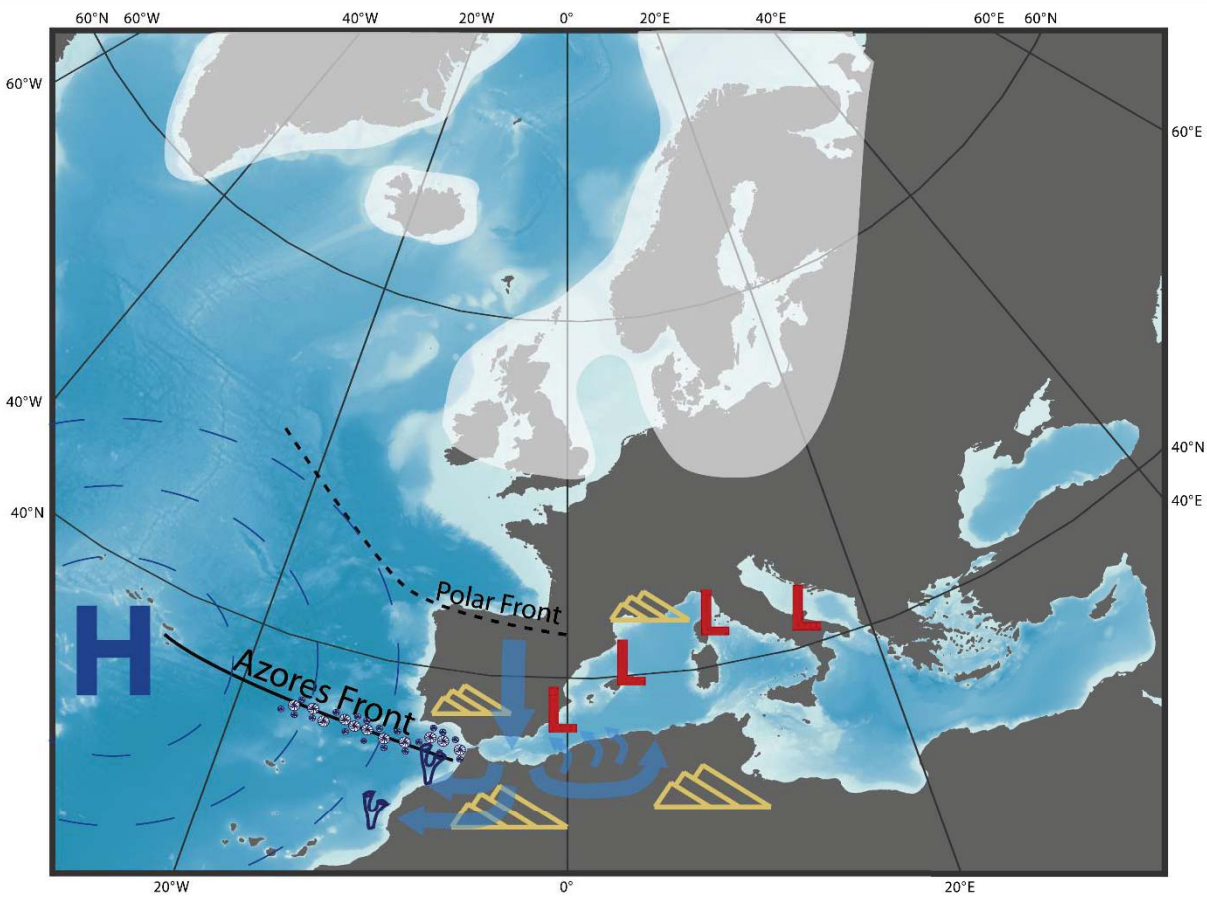

Fig. 5.2: Sketch of the postulated atmospheric and oceanographic parameters during glacial periods. Major ice sheets reside as south as circa 50°N (indicated by white area). Southerly Polar Front position induces polar air outbreaks into the western Mediterranean Sea (blue arrows). Enhanced cyclonic systems and an arid and cold climate (yellow dunes) causing enhanced aeolian Sahara dust input into the Mediterranean Sea and most likely into the GoC. A more northern position of the Azores Front provides enhanced productivity in the GoC, marked by small particles. Flourishing CWC growth in the Gulf of Cádiz is indicated by the coral symbol.

Globally, interglacial periods are marked by rising temperatures, enhanced precipitation, the retreat of ice sheets and glaciers as well as a northern position of the PF (Fig. 5.3; Eynaud et al. 2009, Denton et al. 2010, Clark et al. 2012). During warm climate periods, the Mediterranean Region is considered temperate/warm and humid, reflected in pollen records, warm SST, enhanced freshwater input as seen in African Monsoon activity and Nile River discharge (Martrat et al. 2004, Desprat et al. 2007, Revel et al. 2010, Ehrmann et al. 2016). A strong evaporation loss due to warm temperatures leads to a massive eastward salt increase and strong winter overturning, which thus, results in a stronger Atlantic inflow and Mediterranean outflow via the SoG. Although, enhanced freshwater input into the Mediterranean Sea leads to reduced density-driven LIW formation and thus reduced overturning velocity, rising sea levels and thus higher sill depths strengthen the overturning

volume (Rogerson et al. 2012, Simon 2017). During periods of peak freshwater input, water column stratification increased and thus caused further slow down in LIW velocity, resulting in a decrease of the outflow velocity and less dense MOW (Toucanne et al. 2012, Bahr et al. 2014, Kaboth et al. 2017). Consequently to these climatic changes in the Mediterranean Region and thus during all warm stages since 300 ka, while beyond dating is not sufficiently precise anymore to constrain the age of corals to a particular cold- or warm climate stage, the CWC in the GoC clearly vanished (Fig. 5.1). The significant decrease in aeolian dust input and the decrease in upwelling induced productivity, most possibly represent unfavourable growth conditions in the GoC (Wienberg et al. 2010). In the Mediterranean Sea however, enhanced freshwater input, transporting nutrients and sediment, lead basin-wide to high primary productivity and locally to vigorous vertical mixing, transporting food particles into coral dwelling depths, as seen in the AS (Heburn and La Violette 1990, Sarhan 2000, Bárcena et al. 2001, Jimenez-Espejo et al. 2008, Fink et al. 2013, Rohling et al. 2015). Thus, the most abundant warm climate CWC occurrence in the AS can be observed during interglacial periods MIS 9, MIS 7, MIS 5 and from Termination T1 throughout MIS 1 (14 to 0 ka; Fig. 5.1).

However, peak climate warm periods are barely represented in the presently available AS CWC record, which provides a first hint that these periods result in a limitation of coral growth. One may suspect that temperatures rose above critical values for *L. pe*rtusa (*D. pertusum*) and *M. oculata*, i.e. 14 °C (Roberts et al. 2006, Freiwald et al. 2009) or that further increased primary productivity lead to a deoxygenation of the bottom waters through the remineralization of organic matter (e.g. Fink et al. 2013). Indications for de-oxygenation are the sapropel events in the Mediterranean Sea, when organic matter is preserved in the sediment due to the lack of bottom water oxygen. In fact, CWC growth is very limited during such periods of low oxygen (Fig. 5.1). However, the compilation is solely well resolved for the last known sapropel S1, when a general decline of AS CWC is observed. During earlier climate states and partly more intense organic sediment preservation events the data is not sufficiently well resolved to prove a major change of CWC activity during these events.

Therefore, it is assumed, that the production hypothesis emitted by Wienberg et al. (2010) and Frank et al. (2011) holds for several climate cycles and that warm climate stages represent solely weak upwelling activity in the GoC. In addition, the GoC CWC grew under the influence of different water masses as compared to the AS. The AS CWC habitats are clearly dominated by the presence of LIW (e.g. Fink et al. 2013, Wang et al. 2019, this study), while in the GoC, multiple predominant water masses like the MOW, the Eastern Atlantic Central

Waters (EACW) and the East Antarctic Intermediate Water (EAAIW) reside in coral dwelling depths between 600 to 1000 m water depths, as explained in more detail in Hemsing (2017).

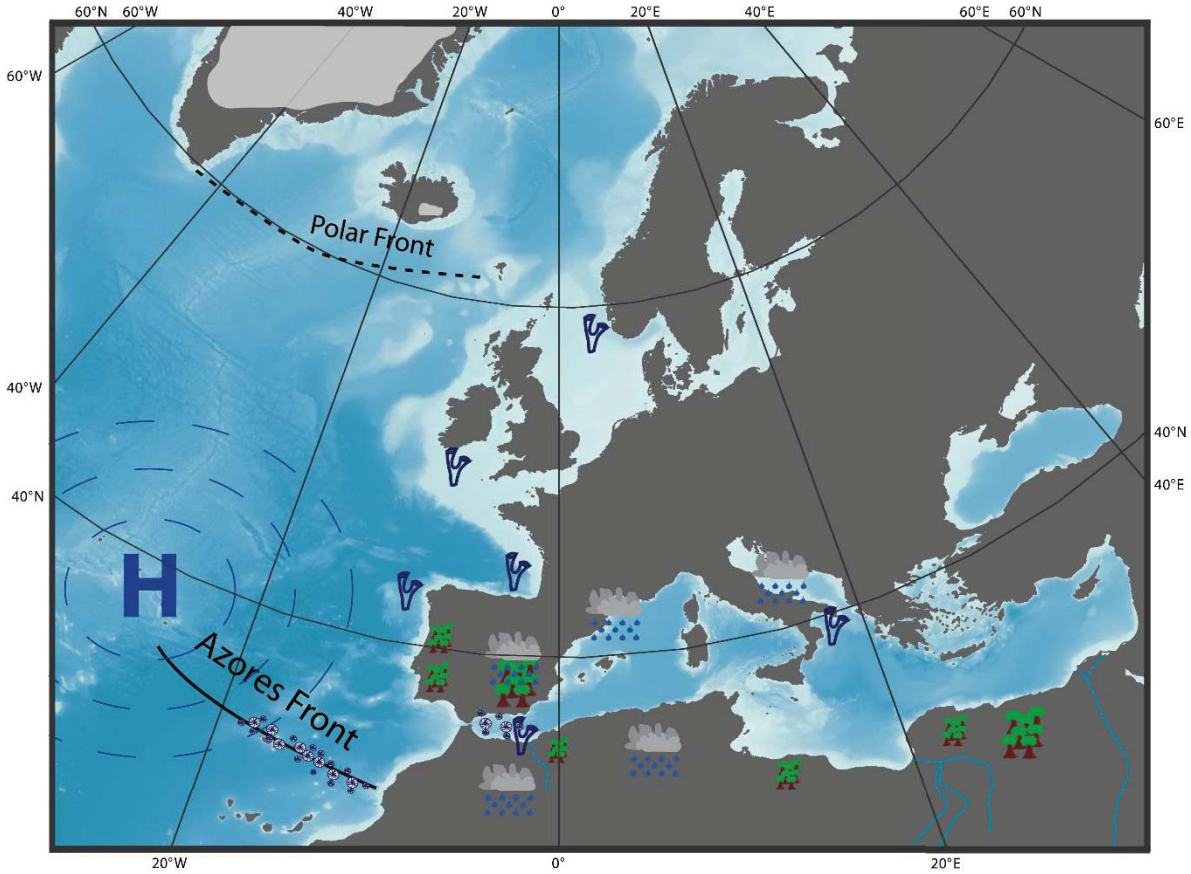

Fig. 5.3: Sketch of the postulated atmospheric and oceanographic parameters during interglacial periods. Ice sheets (indicated by white areas) and the Polar Front reside at circa 60 °N or at higher latitudes. Predominant warm and wet climate in the Mediterranean Region is indicated by vegetation and clouds. Enhanced freshwater input, transporting sediment and biogenic material is indicated by rivers, areas with high productivity are indicated by small particles. Flourishing CWC growth during interglacial periods in the Eastern North Atlantic and the Mediterranean Sea are indicated by coral symbols.

Favourable AS CWC growth conditions apparently declined during cold stadials within warm climate periods, when AS CWC habitats show a minor activity or even absent CWC developments, documented in the stadials of MIS 5 and most likely during stadials of earlier warm climate periods (e.g. MIS 9 and MIS 7; Fig. 5.1). Cold stadials are marked by significant decreases in the AS and GoC SST records as well as a decline of warm and humid pollen along the Iberian Margin (Martrat et al. 2004, Desprat et al. 2007, Martrat et al. 2007) and can most possibly be associated with a southward advance of the PF. Thus, regarding the minor AS CWC growth activity, cold stadials appear to reflect a counter situation to the observed AS

CWC occurrence during warm interstadials during cold climate periods. However, a brief onset of GoC CWC growth during cold stadials cannot be clearly identified due to the scarcity of dated GoC CWC. Although, to some extent GoC CWC growth was observed coinciding with cold stadials over the past 300 ka (MIS 9, MIS 7 and MIS 5), the amount and quality of dated CWC from these glacial periods remains tenuous.

The observed Gibraltar-seesaw pattern appears concomitant with glacial-interglacial atmospheric and oceanographic changes. Thus, the observed seesaw coral growth pattern is proposed to be driven by the dynamic frontal system of the PF. Although productivity, as hypothesized (1), is one main driver of CWC growth as evidenced by multiple studies (White et al. 2005, Mienis et al. 2007, Taviani et al. 2016, Hanz et al. 2019, Wang et al. 2019), the Gibraltar-seesaw pattern seemingly is driven by the south-north oscillation of the PF, controlling the oceanic and climatic conditions of the Mediterranean Region and thus provides the necessary productivity in either location to facilitate sustainable CWC growth. However, distinct deviations from a strict glacial-interglacial seesaw pattern are evidenced by minor CWC growth activities during stadial and interstadial periods in the AS and presumably in the GoC. Further investigation on GoC CWC growth activities may be necessary to conclude on a concurrent GoC growth pattern during these periods.
Lastly, a closer look on the CWC ages from both, the AS and GoC, spanning the past 50 ka (Fig. 5.4) reveals abundant CWC and active reef forming throughout most of MIS 3 and a further increase of CWC abundance during the LGM. However, with the onset of termination T1, a significant decrease of CWC activity is observed at circa 19 ka. During H1 (18.0-14.6 ka), concurrently with reduced surface productivity in the GoC, a southern PF position as south as the SoG was observed (Colmenero-Hidalgo et al. 2004, Voelker et al. 2006, Wienberg et al. 2010). The climatic and environmental changes during H1 are accompanied with a lack of dated corals in the GoC and thus a potential demise of CWC in the GoC (~18–15 ka) during H1 (Fig. 5.4). Subsequent to H1, during the onset of the interglacial MIS 1, only minor CWC occurrences were found in the GoC until circa 12 ka, where CWC activities in the GoC ceased by the end of the YD cold event. In the AS however, the onset of CWC growth (~15 ka) coincides with the end of H1. During the subsequent warming period (B/A), an increase in AS CWC abundance with high MARs of up to 160 cm/ka were found throughout most of the Early and Mid-Holocene, however during the YD cold event, AS CWC occurrences diminished severely (Fig. 5.4).

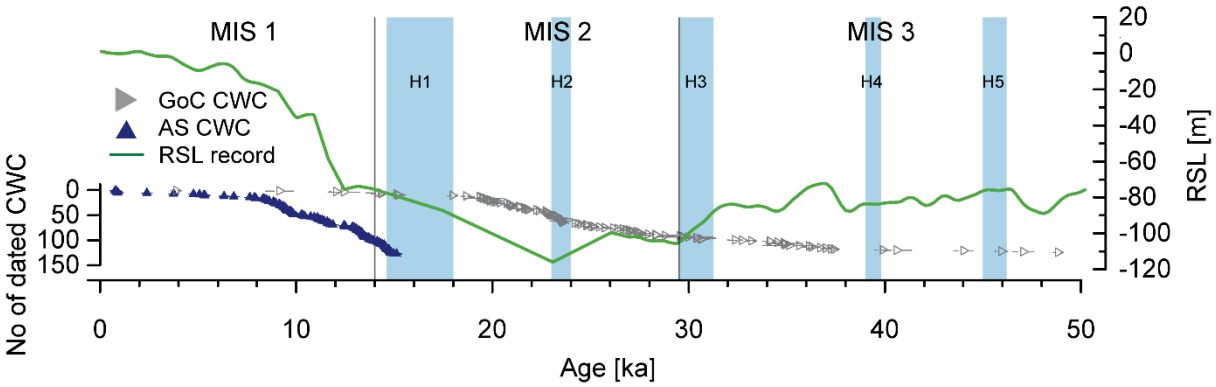

Fig. 5.4: CWC growth of the past 50 ka in the GoC (grey triangles) and the AS (blue triangles). Seemingly, H1 with a PF position at SoG latitudes restrict productivity during glacial periods in the GoC and thus coral growth. Mediterranean sea level is shown in green (RSL; Rohling et al. 2014). Blue vertical bars show Heinrich Events (H).

The observed lack of CWC during H1 gives rise to speculations, that strong H events accompanied by a PF position at SoG latitudes pose unfavourable growth conditions for GoC CWC. Regarding the GoC CWC activities over the past 50 ka, reduced activities seemingly coincide with H2 and H3. However, the GoC record is too scarce to judge CWC activities on H4 and H5. Thus, further investigation of GoC CWC activities during H events need to be conducted. Conclusively, the question remains, where CWC in the Mediterranean Region found refuge during short periods of unfavourable conditions on both sides of the SoG. In the Eastern Mediterranean Region, flourishing CWC occurrences during the YD cold event and individual glacial corals, found east of the Strait of Sicily in the Ionian Sea, the Adriatic Sea and the Eastern Mediterranean Sea might provide an indication of a potential glacial refuge for the Mediterranean Region (Taviani et al. 2005, McCulloch et al. 2010, Fink et al. 2015).

If the origin of the observed coral – climate relationship is driven by the position of the polar front, one might expect that the origin of the CWC growth Gibraltar-seesaw pattern might be related to the initiation of this frontal dynamic system. During 1250 and 700 ka, the so-called "mid-Pleistocene transition" (MPT), the global climate changed significantly. A reduction in the North Atlantic SST, as well as an increase of aridity and the monsoon intensity in Africa, was observed (Clark et al. 2006). Furthermore, global climate variability changed from the dominant 41 ka orbital cyclicity to a 100 ka orbital cyclicity (Hays et al. 1976, Pisias and Moore Jr 1981, Clark et al. 2006). As seen in e.g. the benthic $\delta^{18}O$ stack LR04 (Lisiecki and Raymo 2005), over the past 800-700 ka, the 100 ka orbital cyclicity determined the pace of glacial-interglacial cycles. Prior to MIS 22 (900 ka), mild glacial and lukewarm interglacial periods were observed, however, the onset of full glacial-interglacial conditions are reported for MIS 22 (Elderfield et al. 2012). Hence, the position of the PF is determined by the size of North Hemisphere ice sheets, an onset of coral growth during the MPT or shortly after is highly possible.

However, hypothesis (3), regarding "*the initiation of the Moroccan coral mounds on both sides of the Strait of Gibraltar*" is, based on the available long-term data, difficult to asses. Two mounds from the GoC have been fully penetrated (Wulle Mound and MeBo Mound; Hebbeln et al. 2015, Krengel 2016), revealing basal ages of 350±20 ka (Wulle) and 450±50 ka (MeBo). However, corals from multiple studies in the GoC revealed mound surface ages ranging between 4 and 345 ka (Frank et al. 2009, Wienberg et al. 2009, Wienberg et al. 2010, Frank et al. 2011, Krengel 2016, Hemsing 2017). Since several thousand exposed and buried coral mounds have been found in the GoC (Hebbeln et al. 2019), finding the oldest mound, representing the onset of CWC growth in the GoC, may prove difficult.

For the AS however, three large ridges, namely Brittlestar Ridge I, II and III may provide an answer for the onset of mound initiation in the AS. The oldest sample on BR I was dated at 538±28 ka, however BR I was not fully penetrated in a depth of 70 m. Dependent on the actual mound height between 80 to 160 m and based on the calculated overall $MAR_{BR\ I}$, BR I may reveal a basal age of 595±20 ka (base at 80 m) or 1190±50 ka (base at 160 m). The onset of BR I thus would lie well within the MPT or shortly after.

5.2 Conclusion

The compiled U-series age data from the GoC and the AS strongly indicates a Gibraltar-seesaw pattern, spanning over at least the last glacial-interglacial cycles (MIS 6 to MIS 1) and most likely over earlier glacial-interglacial cycles up to 550 ka. The Gibraltar-seesaw pattern was associated with glacial-interglacial atmospheric and oceanographic changes, most possibly driven by the dynamic frontal system of the PF. The south-north oscillation of the PF, during glacial-interglacial cycles potentially affects the oceanic and climatic conditions of the Mediterranean Region and is thus proposed to trigger the necessary primary productivity in either location to facilitate sustainable CWC growth. However, distinct deviations from a strict glacial-interglacial seesaw pattern are evidenced by minor CWC growth activities during stadial and interstadial periods in the AS and presumably in the GoC. However, further investigation of GoC CWC growth activities may be necessary to conclude on a concurrent GoC growth pattern during these periods. Concurrently with the H1 event, when the PF supposedly resided at SoG latitudes, CWC in the GoC vanish for over two millennia. At the end of H1, which is associated with the retreat of the PF to a more northern position, minor CWC growth briefly returned to the GoC, whereas at the same time in the AS, the onset of flourishing CWC growth was observed.

If the origin of the observed coral – climate relationship is driven by the position of the polar front, the potential onset of CWC growth in the Mediterranean Region might have started during the MPT (1250-700 ka). During the MPT, (i) climate variability changed from a 41 ka orbital cyclicity to a 100 ka orbital cyclicity and (ii) mild glacial to lukewarm interglacial conditions changed to full glacial-interglacial conditions. Hence, the position of the PF is determined by the size of North Hemisphere ice sheets and the south-north oscillation is driven by the glacial-interglacial cyclicity. An onset of CWC in the Mediterranean Region during the MPT coincides with the calculated maximum basal age of BR I, ranging between 595±20 and 1190±50 ka.

6 New constraints on the evolution and potential drivers of seawater $\delta^{234}U$ over the last 400 ka

Over the past decade, several studies have pointed out temporal and spatial changes of the natural $^{234}U/^{238}U$ ratio in the world oceans. This is a stunning observation since U is a conservative element with a residence time of 380.000 years in the oceans. The detection of small ‰-variations in the $^{234}U/^{238}U$ activity ratio became feasible, thanks to ever-increasing analytical precision of mass-spectrometric U-isotope measurements. Regional isotopic differences came to light, in particular in semi-enclosed ocean basins (Andersen et al. 2010). First evidence were found for small but measurable changes of the world ocean U–isotopic composition through climate change. Cold-water corals (CWC) provide a unique, well-preserved archive to study the oceans $^{234}U/^{238}U$ ratio. In a recent study, it was proposed that isotopic differences, evidenced between the equatorial Pacific and Atlantic, are related to ocean circulation (Chen et al. 2016). Through the study of Mediterranean Sea CWC (AS), the novel findings further contribute to the history of seawater $^{234}U/^{238}U$ variations. Moreover, a unique U-series database from numerous Atlantic coral provinces is compiled here, for a better constraint of the global patterns over the past climate cycles.

6.1 Introduction

In the oceans, the concentration of the salt like element Uranium is controlled by its sources and sinks and its chemical behaviour. Due to the weathering of continental crusts, U is released into meteoric waters as U(VI)-ion. In absence of oxygen, U is reduced to its oxygenation state U(IV), in which it remains particle reactive and mostly insoluble. Consequently, the major U sources to the ocean are rivers, groundwater and direct transport of particles via aeolian dust. Most of the discharged U is stored in the oxygen-depleted (and reducing) sediments of coastal zones, which thus act as strong sinks of U (even to the ocean), but can act as a source if sediments are oxygenated (e.g. Ivanovich and Harmon 1992, Dunk et al. 2002). Other sources, such as hydrothermal vents and the weathering of marine crusts are however, not well constrained, thus overall large uncertainties remain in the global U budget (Dunk et al. 2002).

Further sinks are suboxic and anoxic sediments and the precipitation of biogenic carbonates (Dunk et al. 2002). Via the sources, U with different activity ratios of $^{234}U/^{238}U$ (AR_U) is released into the ocean. Since solely small deviations from the secular radioactive equilibrium occur in the ocean the ‰-deviation from radioactive equilibrium in $\delta^{234}U$ is commonly used, e.g. $\delta^{234}U = (AR_U-1)*1000$. Due to the alpha recoil process, ^{234}U can be weathered more easily from mineral surfaces. Hence the AR_U is elevated in meteoric waters if compared to the

secondary equilibrium. This is nicely demonstrated in the AR_U of 38 most important rivers, contributing freshwater to the world ocean. The river AR_U varies between 1.070 to 2.030, i.e. in $\delta^{234}U$ notation, between 70 and 1030‰ (Dunk et al. 2002).

Differences in the host rock and the weathering process determine the sources U concentration and $\delta^{234}U$ (Kronfeld and Vogel 1991, Palmer and Edmond 1993, Dunk et al. 2002). Physical weathering, like the mechanical breakdown of rocks via vegetation or ice, exposes fresh surfaces and thus increases the surface area, predominantly releasing ^{234}U from damaged crystal lattice and through alpha recoil. Rivers influenced by predominantly physical weathering show high $\delta^{234}U$ of up to 1000‰. On the other hand, with predominantly chemical weathering, lower values as low as 100‰ are found in rivers (Kronfeld and Vogel 1991, Dunk et al. 2002, Henderson 2002). Robinson et al. (2004) could demonstrate in the runoff from New Zealand mountains that climate changes can influence the relative rate of physical and chemical weathering and thus the relative release of excess ^{234}U to the ocean. Based on the compilation of 38 rivers, Dunk et al. (2002) estimated a global mean river input of $\delta^{234}U$ = 170 to 260‰ and a mean groundwater input of $\delta^{234}U$ = 200 to 2000‰. Note, the giant uncertainty of the groundwater isotopic composition, which related to the few existing measures of direct groundwater discharge to the ocean. A further possible source of excess ^{234}U are pore waters in marine sediments, which according to Ku (1965) may contribute as much as 50% to the oceanic excess of ^{234}U.

Due to the constant flux of enriched ^{234}U waters towards the ocean and due to the long residence time of U in the ocean (~380 ka) modern seawater carries an elevated $\delta^{234}U$ value of 146.8±0.6‰, which is ~15% above the secondary equilibrium (Andersen et al. 2010). Assuming a steady-state isotopic composition of the world ocean, the constant input of excess ^{234}U counteracts the decay of excess ^{234}U and thus prevents a return to the secular equilibrium. Whether or not the U cycle is in steady-state is not known, but strong evidence of near steady-state is provided by the long-term stability of the world ocean $^{234}U/^{238}U$ isotopic ratio (Henderson 2002) and the small deviations observed in different ocean basins (<1‰) (Andersen et al. 2010). Consequently, detecting deviation from the present state of U cycling requires either very high precision or archives closely related to regional sources (or sinks, assuming isotopic fractionation during the removal process).

The removal of U via anoxic sediments (e.g. sapropel layers in the Mediterranean Sea) or biogenic carbonates (e.g. corals) does however not significantly fractionate the isotopes ^{234}U and ^{238}U and therefore does not have a measurable influence on seawater $\delta^{234}U$ (Henderson 2002). Amongst other biogenic carbonates, corals capture the $\delta^{234}U$ from seawater during growth in their skeleton. The initial U isotope ratio, at the time of skeleton formation, is crucial for U-series dating. This is because the seawater evolution is used as one quality control criteria to determine U-series open or closed system behaviour in age data. Mostly a constant $^{234}U/^{238}U$ ratio identical to modern seawater $\delta^{234}U$ is assumed. Especially corals older than 100 ka, show initial $\delta^{234}U_i$, which deviate significantly from the modern value and are usually considered diagenetically altered, thus unreliable. Consequently, such ages may be discarded. As pointed out by Henderson (2002), this rejection approach suggests a constant seawater $\delta^{234}U$ throughout the last one million year of the Pleistocene. However, assuming a one-box model for the $\delta^{234}U$ distribution in the ocean, Henderson (2002) proposed a 15‰ variation in $\delta^{234}U$ from its present-day value over the past 360 ka to be within reasonable ranges. Additionally, a maximum of riverine input variation of 65‰ over a period of 100 ka was suggested to ensure the limited seawater variation of 15‰ (Henderson 2002). Over the last 800 ka, Henderson (2002) published samples with predominantly lower $\delta^{234}U$ than modern seawater, the author thus proposed, that the rate of physical weathering over the past 800 ka was not higher than present-day.

A more recent study (Chen et al. 2016) presented well-constrained $\delta^{234}U$ records from the equatorial Atlantic and Pacific over the last 30 ka. The Atlantic and Pacific record clearly showed a low glacial $\delta^{234}U$ seawater value of ~144‰, which rapidly increased within the Equatorial Atlantic to 150‰ during the Heinrich Event 1 (H1, 18.0-14.6 ka). Based on the timing of this increase, the authors pinpointed the variation in $\delta^{234}U$ towards external sources with excess ^{234}U, like the retreat of Northern Hemisphere ice sheets. The lack of homogenisation in the global oceans was related to reduced North Atlantic overturning circulation and thus global ocean mixing (Chen et al. 2016).

The Atlantic Meridional Overturning Circulation (AMOC) was proposed to have three states of operation (Böhm et al. 2015). Over the last 125 ka, the warm mode, mainly active between MIS 5 (125 to ~70 ka) and MIS 1 (~10 ka) was characterized by strong deep water formation and thus a homogenous seawater $\delta^{234}U$ in the ocean. This is similar today, with U being very well homogenous throughout the world ocean. Following the warm mode, a near shutdown of the North Atlantic Deep Water (NADW) formation and circulation is proposed as the “off mode”. The warm mode gradually changed into the off mode between 70 to 20 ka and was

present between 20 and 15 ka. An isolated circulation of the upper Atlantic (~2 km) dominated this cold climate state, which was at least active during termination TII (prior to 125 ka) and H1 (18.0–14.6 ka). Periods of ice sheet instability (H2, H3, etc.) are suspected to cause such weak or absent deep ventilation.

CWC, used in this study originate from a depth within the upper 2 km. During these periods, the isolated upper Atlantic is more sensitive to changes in excess ^{234}U due to the reduced volume (at least 50%) of water participating in active mixing and overturning. However, the origin of the excess ^{234}U and the driving force of this glacial to interglacial variation is still unknown but is suspected in the Nordic Sea related to freshwater release. Since the Mediterranean Sea is closely linked to the subtropical and polar Atlantic surface inflow and runoff from ice sheets, records from this semi-enclosed basin may help find a prominent region of excess ^{234}U release. On the other hand, ever more constrained seawater $\delta^{234}U$ records over glacial-interglacial cycle will help improve the criteria for U-series quality control and open system behaviours to augment the quality and precision of chronologies. Lastly, variability in the relative rate of physical and chemical weathering could be seen by higher than present-day $\delta^{234}U$ values. CWC have been shown to be valuable archives to study the oceanic $\delta^{234}U$ ratio. Here, over 1.500 pristine coral ages from the Atlantic (n=1.288) and the Mediterranean Sea (n=322), spanning from 400 ka to present-day, were compiled. In the first part, similarities and difference between the Mediterranean and the Atlantic are discussed with a close focus on the last 15 ka. The second part of this study concentrates on the overall variation of the combined records spanning 400 ka.

6.2 Regional setting

The regional setting of the Alboran Sea and the EMCP are introduced in Chapter 3.2.

6.3 Material and methods

The here investigated and presented coral samples were introduced in the previous Chapter 3. Sample origins and quality control have been discussed in the same chapter. Published data used in Chapter 6.4.3 were treated the same, as far as additional data was available. Samples exceeding an analytical uncertainty of $2\sigma > 5‰$ were removed from discussion (Table 3.2)

6.4 Results

6.4.1 $\delta^{234}U$ from coral ages located on Dragon Mound (GeoB18116-2)

The oldest samples found on DM (426±12 ka) revealed $\delta^{234}U$ of 141.7±5.4‰. Exceeding $2\sigma > 5‰$, this sample is not displayed in Fig. 6.1. The second oldest sample, dated within MIS 11 (390.8±10 ka) revealed a high $\delta^{234}U$ of 151.2±5.1‰ and is displayed in Fig. 6.1. During MIS 10 (n=19), the $\delta^{234}U$ values average around 148.2±3.6‰ with minimum and maximum values of 139‰ and 156‰, showing a high variability in the data. The subsequently following MIS 9 is represented with 25 samples, which show values again ranging between 135.5‰ and 156‰. The average of 149.2±3.5‰ is comparable within uncertainty to the previous ones. With n= 5 samples during MIS 8 a similar mean value of 148.5±2.0‰ as observed during MIS 10 and MIS 9, although minimum and maximum values are less variable and enclosed in the previous ranges with 141‰ to 154‰. MIS 7 is represented by n= 22 samples and averages around 144.4±2.1‰ with an overall range in values from 139 to 155‰. With only n=2 samples, MIS 6 shows $\delta^{234}U$ values between 137 and 141‰. The youngest coral occurrence (n=14) during MIS 5 ranges from 145 to 151.4‰ with an average of 148.5±1.3‰.

6.4.2 $\delta^{234}U$ from coral ages located on Brittlestar Ridge I (GeoB18118-1 and GeoB18118-2)

The oldest sample found in BR I reveals severe measurement errors in age (538.2±28 ka) and $\delta^{234}U$ value 169.1±13.6‰. For MIS 13, n=2 samples were measured with $\delta^{234}U$ of 156±6.4‰ and 150±8.5‰. The samples, older than MIS 12 exceed an analytical uncertainty of $2\sigma > 5$‰ and are thus not displayed in Fig. 6.1. Coral occurrence on BR I is observed in all subsequent MIS to a minor amount (Fig. 5.1). MIS 12 is represented by n=1 (432±10 ka) and a $\delta^{234}U$ of 150‰ with errors as high as 4.9‰. MIS 11 and MIS 10 are represented by n=2 and n=1 samples respectively, ranging around 148.6±3.7‰, 141±2.5‰ and 152.6±2.7‰. MIS 9 is strongly represented with n=9 samples, ranging between 142 and 158‰. Samples show generally high values, resulting in an average $\delta^{234}U$ value of 152.4±2.4‰. The glacial MIS 8 (n=1) shows a low value of 139.9±2.1‰. MIS 7 (n=6) reveals a general declining trend in $\delta^{234}U$ values from 155 to 144‰ (average: 148.8±2.1‰) towards the subsequent MIS 6 (n=2). With one value as low as 140.3±1.1‰ at the start of MIS 6, a general inclining trend is observed towards the end of MIS 6 with values at 153.7±0.6‰. One value at 149.5±1‰ was measured for the end of MIS 5 (n=1). The youngest cluster of coral occurrence during MIS 1 is represented with n=80 samples. During Termination 1, at 15.1 ka, $\delta^{234}U$ values are as high as 153.7±1‰ and decline towards 147.6‰ at 14.2 ka. With minor variations ranging between 148 and 151‰ values decline towards 12.7 ka and the beginning of the Younger Dryas event (YD: 12.7 to 11.7 ka). During the YD only three samples were found between 148 and 149‰. Between 11.7 to 9.8 ka, $\delta^{234}U$ values appear relatively stable, ranging from 147 and 150‰ with an average of 148.9±0.6‰. The last segment towards 8.5 ka reveals higher values with an average of 150.3±0.7‰, ranging from 149.3 to 151.6‰. The youngest measured coral in this record has high errors in $\delta^{234}U$ with 146.2±2.3‰ at 8.3 ka.

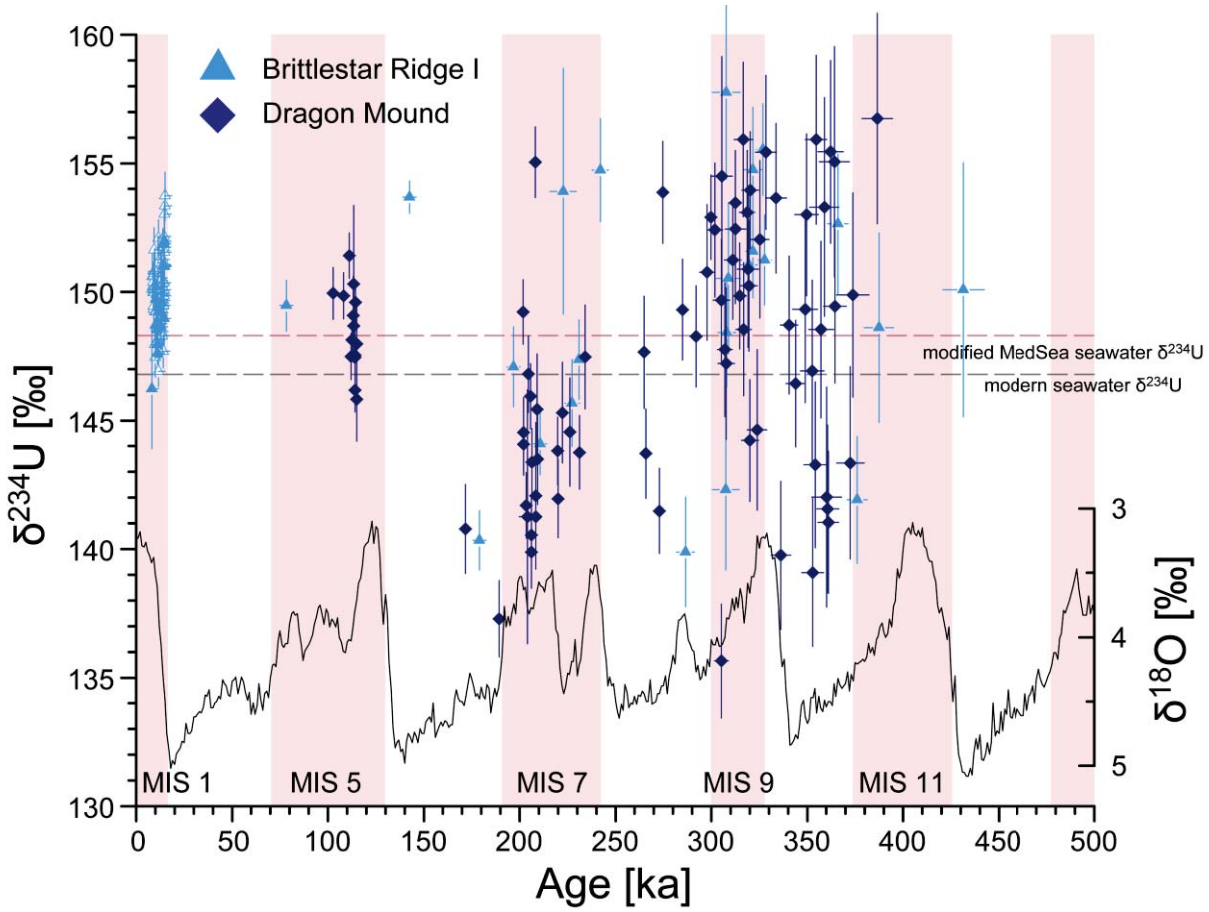

Fig. 6.1: All $\delta^{234}U$ values originating from Brittestar Ridge I and Dragon Mound in the EMCP, Mediterranean Sea. The black dotted line represents the modern seawater $\delta^{234}U$, whereas the red dotted line represents the modified Mediterranean Sea seawater $\delta^{234}U$ as explained in Chapter 6.5.1. The global $\delta^{18}O$ stack LR04 (Lisiecki and Raymo 2005) indicates global climate variations over time.

In the EMCP, both locations show coeval $\delta^{234}U$ values and an overall variation of ~148±7‰ throughout the last 400 ka. The limited glacial data (n= ~20) indicates generally low $\delta^{234}U$ of ~141‰, whereas interglacial data (n= >250) show predominantly higher $\delta^{234}U$ between 145 and 153‰. MIS 9 and MIS 5 show significantly higher values of 150 to 153‰ compared to the modern global ocean mean value of seawater (146.8‰), which however is similar to the early B/A deglacial value, observed 15 ka ago.

6.4.3 The Mediterranean and the Atlantic $\delta^{234}U$ records

CWC should show a uniform $\delta^{234}U$ driven by the isotopic composition of the Atlantic and thus the global ocean, due to the relatively short residence time of circa 50-100 of water in the Mediterranean Sea (Millot and Taupier-Letage 2005). The inflowing AW is mixed rapidly with Mediterranean water masses like the Levantine Intermediate Water (LIW) and thus called the Modified Atlantic Water (MAW) (Millot and Taupier-Letage 2005, Català et al. 2019). Given the rapid overturning and mixing of discharged freshwater throughout the Mediterranean Sea, it is assumed, that Mediterranean Sea water may have a homogenous isotopic composition. This composition may however moderately differ from the global ocean, or Atlantic, due to regional runoff of ^{234}U enriched freshwater. With this assumption, one may combine in first order all available measurements of the U-isotopic composition from CWC of the entire Mediterranean Sea, which dwelled in intermediate or deep water masses. This allows establishing a $\delta^{234}U(t)$ Mediterranean Record. The above-presented data is here combined with published and unpublished data from the entire Mediterranean Sea (Schröder-Ritzrau et al. 2005, McCulloch et al. 2010, Wang et al. 2019, Feenstra et al. 2020, Fentimen et al. 2020, this study). The resulting Mediterranean $\delta^{234}U$ -Record (MUR) spans over 400 ka and is comprised of 322 $\delta^{234}U$ values. This record will be compared to an Atlantic $\delta^{234}U$ -Record (AUR), established on numerous published and unpublished values from the Heidelberg U-series CWC age database, including presently 1288 $\delta^{234}U$ values (Adkins 1998, Cheng et al. 2000, Frank et al. 2004, Frank et al. 2005, Lindberg and Mienert 2005, Schröder-Ritzrau et al. 2005, Eltgroth et al. 2006, Robinson et al. 2006, Robinson et al. 2007, de Haas et al. 2008, Frank et al. 2009, Mangini et al. 2010, Wienberg et al. 2010, Eisele et al. 2011, Frank et al. 2011, Montero-Serrano et al. 2011, Copard et al. 2012, Douarin et al. 2013, Raddatz et al. 2014, Chen et al. 2015, Glogowski et al. 2015, Matos et al. 2015, Chen et al. 2016, Dubois-Dauphin et al. 2016, Raddatz et al. 2016, Rüggeberg et al. 2016, Victorero et al. 2016, Matos et al. 2017, Wefing et al. 2017, Bonneau et al. 2018, Wienberg et al. 2018, Elliot et al. 2019). In general, used unpublished data is part of ongoing research and therefore only available on request (Heidelberg U-series CWC age database, Prof. Norbert Frank). Both the MUR and AUR still contain large time gaps, but general patterns are appearing. Note that inter-laboratory differences are minimal as all data have been adjusted to Cheng et al. (2000) half-lives and most of the data (n= 873) has been measured in Heidelberg on the MC-ICP-MS infrastructure.

For the period between 400 and 125 ka, the MUR and AUR records are combined (5 ka bins) due to the low amount of samples (n=158). The combined $\delta^{234}U$ record reveals a general declining trend from 400 ka ($\delta^{234}U_{av}$: ~152‰) towards 130 ka ($\delta^{234}U_{av}$: ~147‰). The interglacial periods MIS 11 and MIS 9 ($\delta^{234}U_{av}$: ~152 to 150‰) reveal generally higher $\delta^{234}U$ values than the glacial periods MIS 10 and MIS 8 ($\delta^{234}U_{av}$: ~149-148‰; Fig. 6.2). However, MIS 7 and MIS 6 reveal similar values of $\delta^{234}U_{av}$: ~147.5‰.

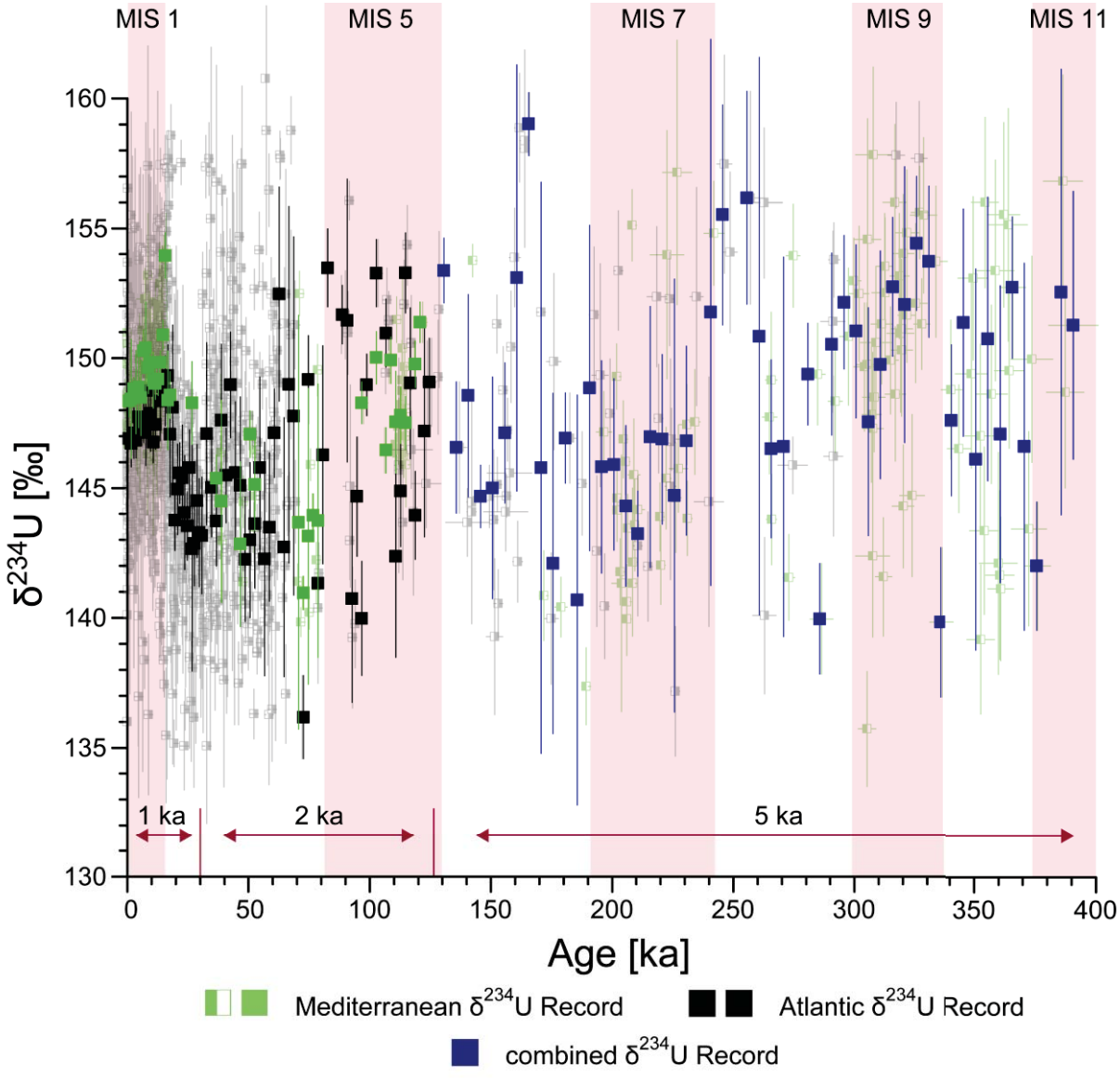

Fig. 6.2: All available $\delta^{234}U$ values (transparent, half-filled squares) for the Mediterranean Sea (green) and the Atlantic (black). Both records are binned separately in 1 ka (0-30 ka), 2 ka (30-125 ka) and shown in green (Mediterranean Sea) and black (Atlantic). The combined record (blue) is binned in 5 ka from 125 to 400 ka. Light red shades indicate interglacial periods.

With limited data availability during the penultimate interglacial period and the early LGM, for MUR and AUR, each data set was merged in 2 ka bins from 125 ka to 30 ka. Both records have the highest resolution between 30 and 0 ka. AUR, with an average of 48 $\delta^{234}U$ values per 1 ka and MUR, with up to 30 $\delta^{234}U$ values per 1 ka (Fig. 6.2). Both records were each merged in 1 ka bins during this period.

During MIS 5, the AUR (n=57) reveals large variations, ranging between 136 and 153‰ ($\delta^{234}U_{av}$: ~147‰). Between the onset of MIS 4 and the beginning of MIS 2, the AUR reveals a prominent decrease in $\delta^{234}U$ from 147.7‰ (63 ka) to 143‰ (51 ka; Fig. 6.2 and Fig. 6.3, black line). Followed by a well-resolved increase of 3.8‰, $\delta^{234}U$ briefly reaches the highest values of 146.8‰ (modern-day value) during MIS 3. Towards 28 ka, $\delta^{234}U$ values gradually decrease with 0.2‰/ka to 143.5‰. During the LGM, up until 20 ka, $\delta^{234}U$ slowly increases with 0.2‰/ka. Between 20 ka and 15 ka, values as high as 148.7‰ can be observed. During the last 15 ka, $\delta^{234}U$ values gradually decrease towards the modern value of 146.8‰, however, during a brief period within the Early Holocene (8±2 ka), the AUR reveals a higher variability in $\delta^{234}U$ around 147.5‰.

During MIS 5, the MUR (n=35) revealed similar values of $\delta^{234}U_{av}$: ~147‰ compared to AUR, however, a smaller variation ranging between 140 and 151‰ can be observed. The last glacial period (MIS 4 to MIS 2) is represented by only n=12 samples in the MUR. Values range between 142 to 147‰ with an overall lower $\delta^{234}U_{av}$: of 145.0‰. During the deglaciation and the Holocene, a rapid increase from glacial low values towards 148‰ (17.5 ka) and towards 150‰ (14.5 ka), with a brief significant increase at 15.5 ka (n=2) with maximum values of 153.8‰, can be observed. During the last 15 ka, $\delta^{234}U$ values range between 149-150‰ (6.5 ka) and decrease towards 1 ka (n=17) with values around 148.2‰.

6.5 Discussion

6.5.1 The Mediterranean offset

Derived from the Mediterranean coral data, the modern Mediterranean $\delta^{234}U$ value (~148.3±0.5‰) is elevated by ~1.7‰ compared to the modern Atlantic $\delta^{234}U$ of 146.8‰ and has been higher throughout the Termination T1, the Holocene and potentially the penultimate interglacial period. This unprecedented observation contradicts the general assumption, that modern $\delta^{234}U$ is homogeneously distributed throughout the world's oceans with differences, no larger than 0.4‰ (Andersen et al. 2010) and that the Mediterranean Seawater mirrors the global ocean (Delanghe et al. 2002). Moreover, it requires an adjustment of the evaluation of U-series dating of marine Mediterranean samples. In Fig. 3.5a and 3.6a (Chapter 3) and Fig. 6.1 (this chapter) an adjusted Mediterranean Seawater Evolution curve and modern value have been added.

Comparing both, the Atlantic and Mediterranean Sea record, it is evident that over the last 16 ka, the AUR represents the baseline for $\delta^{234}U$ values in the Mediterranean Sea. However, within the Mediterranean Sea, sources of higher $\delta^{234}U$ values imprint a constant offset in $\delta^{234}U$. The offset to the Atlantic can be observed in corals spanning from the Alboran Sea (AS) in the western basin (Krengel 2016, Wang et al. 2019, Feenstra et al. 2020, Fentimen et al. 2020, this study) to corals from the Ionian Sea (IoS) in the eastern basin (this study). Both locations dwell directly (AS) or are indirectly influenced (IoS) by the intermediate water mass LIW. This suggests a basin-wide elevated value of $\delta^{234}U$. The inflowing Atlantic Water is instantly mixed with Mediterranean water masses (Català et al. 2019) and thus a measurable offset should be imprinted after entering through the SoG as well.

According to Dunk et al. (2002), three sources, with a significant amount of U can supply the oceans. (i) River run-off, with worldwide $\delta^{234}U$ values ranging between 70 to 1030‰ is the biggest source, followed by (ii) direct groundwater discharge and (iii) aeolian crustal dust (Dunk et al. 2002). At present-day, there are no studies published, concerning either source, providing an answer for the constantly elevated $\delta^{234}U$ value in the Mediterranean Sea, however, results from ongoing work in assessing groundwater discharge into the Mediterranean Sea show discharges with dissolved $\delta^{234}U$ values as high as 1200‰ (Border et al., in prep). During glacial periods, with arid and dry climate, river run-off and groundwater discharge were probably severely reduced. Yet enhanced glacial Saharan dust fluxes were recognised by several studies (Moreno et al. 2002, Larrasoaña et al. 2003, Moreno et al. 2005, Català et al. 2019). During the LGM, both, the AUR and MUR records show similar low $\delta^{234}U$ values (Fig. 6.3). Due to the limited data availability and elevated errors, a distinct difference,

as seen during the Holocene or the lack of difference between both records cannot be demonstrated. However, one would assume that, with the lack of high $\delta^{234}U$ sources flowing into the Mediterranean Sea, both records would mirror each other in terms of $\delta^{234}U$.

During T1 and the early Holocene, with enhanced meltwater production and run-off via rivers and groundwater discharge into the Atlantic and the Mediterranean Sea, both records show increasing $\delta^{234}U$ values, with the climax at 16 to 14 ka and highest values of up to 148.7‰ (AUR) and 151.2‰ (MUR) (Chen et al. 2016, this study). The observed offset in the MUR might be due to the semi-enclosed geology of the Mediterranean Sea, as seen in studies from the semi-enclosed deep Arctic Ocean, which reported present-day $\delta^{234}U$= 147.3±0.1‰ (Andersen et al. 2010). Surrounded by land in a warming and wetter climate with enhanced meltwater production, rivers like the Ebro, Rhône, Po, Tiber, Drin, Evros, Nile and Moulaya, as well as direct groundwater discharges potentially supplied a large amount of freshwater with enhanced $\delta^{234}U$ due to intense physical weathering during the previous glacial period (Chen et al. 2016). Another potential source of enhanced $\delta^{234}U$ to the Mediterranean Sea is the connection to the Black Sea via the Marmara Sea.

During glacial periods with low sea level of up to -120 m, both, the Black Sea and the Marmara Sea, were disconnected from the Mediterranean Sea due to low sea levels and shallow sill depths (Aksu et al. 2002, Major et al. 2002, Eriş et al. 2011, Soulet et al. 2011). Amongst rivers, the Fennoscandian and Alpine ice sheets are known sources of meltwater flowing into the Black Sea (e.g. Major et al. 2002), potentially bearing high dissolved $\delta^{234}U$ as suggested and shown by Henderson et al. (2006) and (Chen et al. 2016). Several studies have discussed late-glacial overspills from the semi-freshwater Black Sea "Lake" into the Marmara Sea and further into the Mediterranean Sea (Major et al. 2002, Soulet et al. 2011). Although, the frequency and amount of glacial overspill are still controversially debated. With rising sea level, the Mediterranean Sea reconnected with the Marmara Sea (~12.8 to 10.5 ka) and with the Black Sea (~9.5-8.5 ka) (Aksu et al. 2002, Kaminski et al. 2002, Major et al. 2002, Yanko-Hombach 2003, Soulet et al. 2010, Eriş et al. 2011). The timing of frequent water mass exchange, respectively a reconnection of the Black Sea to the Mediterranean Sea coincides with a renewed increase in $\delta^{234}U$ in the MUR (Fig. 6.3; 10-7 ka).

The decreasing difference in the MUR offset from 2‰ to 1.5‰, as seen in Fig. 6.3 and stated in Chapter 6.4.3, may have multiple reasons. (i) Since 0.5‰ decrease lies within the measurement error of the samples, it might simply be an over-interpretation of the data. However a decrease in the offset is plausible, due to (ii) higher sea level and thus more

exchange through the SoG, (iii) reduced river run-off and groundwater discharges today, compared to the B/A and Early Holocene. (iv) With higher physical weathering during glacial periods and reduced physical weathering at present-day, higher dissolved $\delta^{234}U$ would have been discharged into the Mediterranean Sea with the onset of meltwater releases. (vi) Lastly, Chen et al. (2016) have proposed, that the reduction of AMOC has caused a rise of $\delta^{234}U$ in the North to Equatorial Atlantic. Hence, the North Atlantic feeds the Mediterranean Sea, the latter received a significant excess amount of ^{234}U during the deglaciation, which vanished only upon the restart of deep convection, circa 15 ka ago.

The exact source and intensity of increased $\delta^{234}U$ input remains yet unknown. However, potential candidates are rivers, submerged groundwater and large water bodies (e.g. glacial drainage of inactive aquifers and small basins like the Black Sea), connected to the Mediterranean Sea.

6.5.2 $\delta^{234}U$ variability over time

Over the last 125 ka, high variability in $\delta^{234}U$, ranging from 143 to 151‰ can be observed in the presented records (Fig. 6.2). During MIS 5, samples from both records show an average of $\delta^{234}U$= 148.5±1‰. Henderson (2002) suggested that during the last 800 ka, the rate of physical weathering over an extended period was never higher than at the present. This assumption was based on the lack of samples showing seawater $\delta^{234}U$ above modern values or more precisely, the rejection of data above modern values as a possible subject of sample alteration. However, both records imply a higher rate of physical weathering during MIS 5 with $\delta^{234}U$ exceeding modern-day seawater.

The subsequent MIS 4 to MIS 2 show glacial low values of ~143‰ at 51 and 27 ka, as reported by Chen et al. (2016) for the last glacial period around 25 ka. However, during MIS 3 significantly elevated $\delta^{234}U$ are observed, with close to modern-day values of ~146.7‰. At the end of the LGM, a stepwise increase of $\delta^{234}U$ is observed from 28 ka (143‰) towards ~20 ka (145‰) and a maximum at 14.6 ka (~148‰). As stated previously by Chen et al. (2016), the observed increases do neither coincide with global sea-level rise and the subsequent potential re-dissolution of high $\delta^{234}U$ bearing shelf- or mangrove sediments nor the re-oxygenation of organic layers in deep-sea sediments.

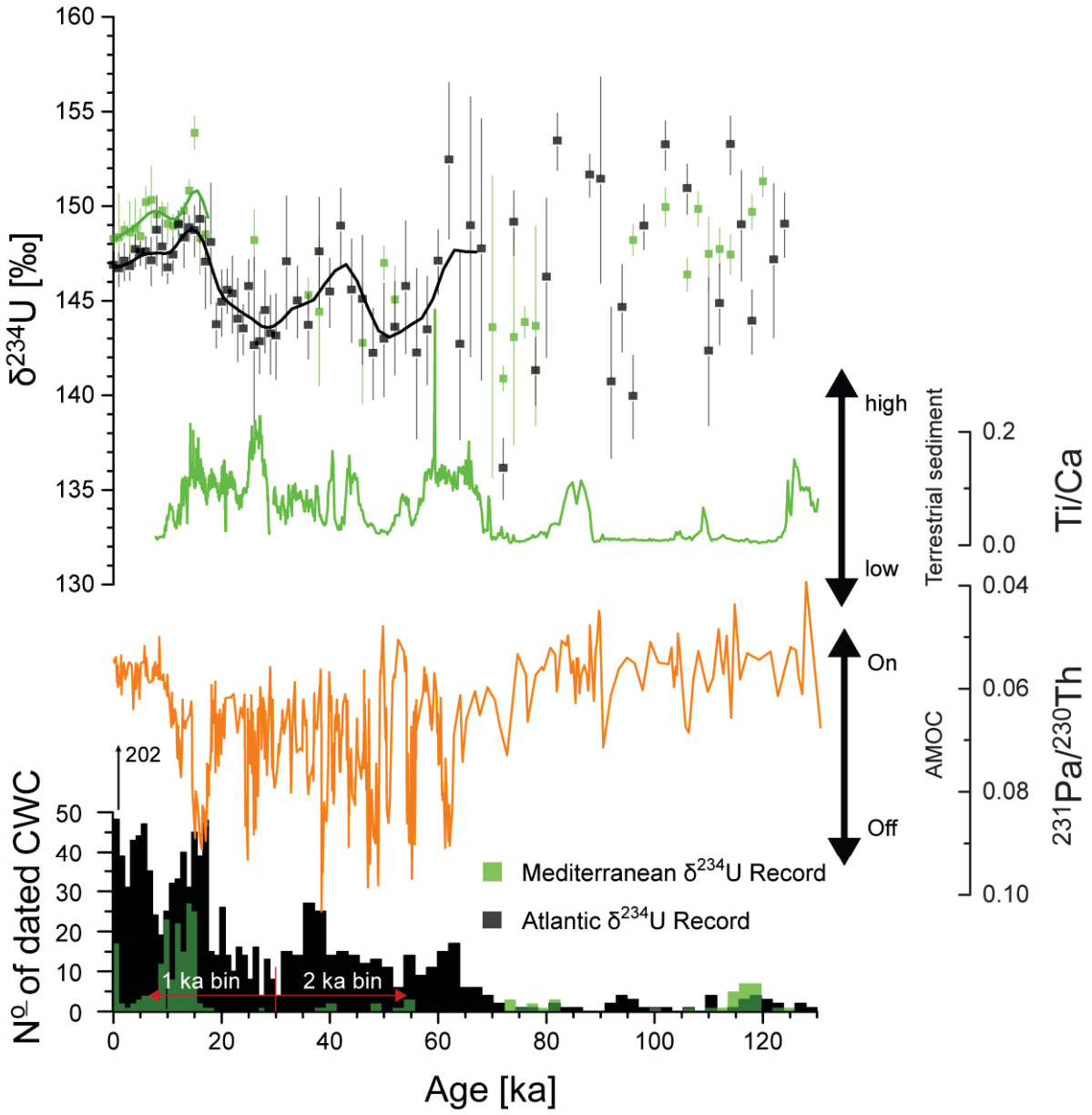

Fig. 6.3: The Mediterranean $\delta^{234}U$ record (MUR, dark green) revealed a distinct offset of ~2‰ compared to the Atlantic $\delta^{234}U$ record (AUR, black). Ti/Ca in sediment cores indicates variability in the terrigenous influence of subglacial meltwater activity (light green). Pa/Th values represent the strength of the AMOC. Bottom columns show the number of CWC used to comprise the Mediterranean Sea record (dark green) and the Atlantic record (black).

The influence of changing riverine U flux into the oceans has been discussed by Dunk et al. (2002) and Henderson (2002). The authors concluded that changes in seawater $\delta^{234}U$ most likely reflect changes in the average river $\delta^{234}U$ rather than a change in riverine U concentration. Over the last 400 ka, the compiled data confirms a broadly constant U concentration ([U]= 2-5 µg/g; Supplement, Table 3.2), as previously observed in CWC and other marine organisms (Broecker 1971, Robinson et al. 2006, Frank et al. 2011, Wefing et al. 2017). Chen et al. (2016) proposed subglacial meltwater releases as one potential source of high $\delta^{234}U$ values. Enhanced rates of physical weathering during glacial conditions produce predominately high $\delta^{234}U$ values as observed in an Antarctic lake, thought to be hydrologically connected to nearby ice sheets with $\delta^{234}U$ of up to 4000‰ (Henderson et al. 2006, Mikucki et al. 2015). This implies, a terrigenous source with high $\delta^{234}U$ values is necessary to increase glacial $\delta^{234}U$ in the Atlantic significantly, as seen in MIS 3.

During glacial periods, multiple large ice sheets covered the Northern Hemisphere. Subglacial meltwater releases via glacial drainage networks could have supplied the seawater with excess ^{234}U. One of these networks, the "Fleuve Manche", connected the southern North Sea basin with the Bay of Biscay via the English Channel and delivered terrigenous sediment into the Atlantic during each glacial period of the last 350 ka (Toucanne et al. 2010). Enhanced fluviatile distribution, with up to 20 g/cm^{2}ka, can be observed between 65-55 ka, at ~40 ka, ~25 ka and 15 ka. Over the last 65 ka, enhanced terrigenous sediment input into the Bay of Biscay coincides with high seawater $\delta^{234}U$. However, at ~25 ka, when enhanced input is observed in the Bay of Biscay, seawater $\delta^{234}U$ remains low. Regarding the last 350 ka of "Fleuve Manche" discharge, the combined records of AUR and MUR do not correlate with the terrigenous input record from the Bay of Biscay (Fig. 6.4). This, however, might be due to the record being binned in 5 ka and thus short term variations are averaged out, as seen in a direct comparison of Fig. 6.3 and 6.4, during MIS 5 to MIS 2.

Another potential driver of the observed $\delta^{234}U$ evolution is ocean mixing in the Atlantic (Chen et al. 2016). The off and cold mode of the AMOC, were respectively characterized by the near shutdown of the NADW formation and an isolated upper circulation (Böhm et al. 2015). The switch from warm towards off and cold mode co-occurred with rapid changes in seawater $\delta^{234}U$ (Fig. 6.3; Böhm et al. 2015). Although the AMOC signal is less clear due to high variability in the AMOC record and cannot account for the increase in $\delta^{234}U$ (Chen et al. 2016), the AMOC still can play a role in respect of the active volume redistributing $\delta^{234}U$ throughout the worlds ocean.

6.5.3 The combined Mediterranean and Atlantic $\delta^{234}U$ record

The $\delta^{234}U$ value over the last 120 ka varies by circa 146.8±5 ‰. The observed close correlation of AUR and MUR with a maximal deviation between both records of ~±3‰ allows, that both records can be combined into one long-term record, spanning over 400 ka. Applying the observed 5‰ variation in $\delta^{234}U$ during the last 120 ka to the combined record (Fig. 6.3), over 90% of the data lies well within this range. However, older samples show a larger scatter in $\delta^{234}U$, potentially due to a reduction in measurement precision caused by minor contaminations or diageneses processes.

Previous studies, conducted on 67 U-rich sediments samples from the Bahamas, suggested a 15‰ variation of seawater $\delta^{234}U$ over the last 800 ka, more specifically over the last 360 ka (Henderson 2002). The here compiled record, comprised of over 1.600 accurate U-series ages, is well constrained over the first 125 ka with 11.6 samples/ka, however, less constrained with 0.6 samples/ka until 400 ka. Nevertheless, a climate-related tendency of high $\delta^{234}U$ during interglacial periods (MIS 11, MIS 9, MIS 5 and MIS 1) and low $\delta^{234}U$ during glacial periods (MIS 10, MIS 8, MIS 4 and MIS 2) can be observed.

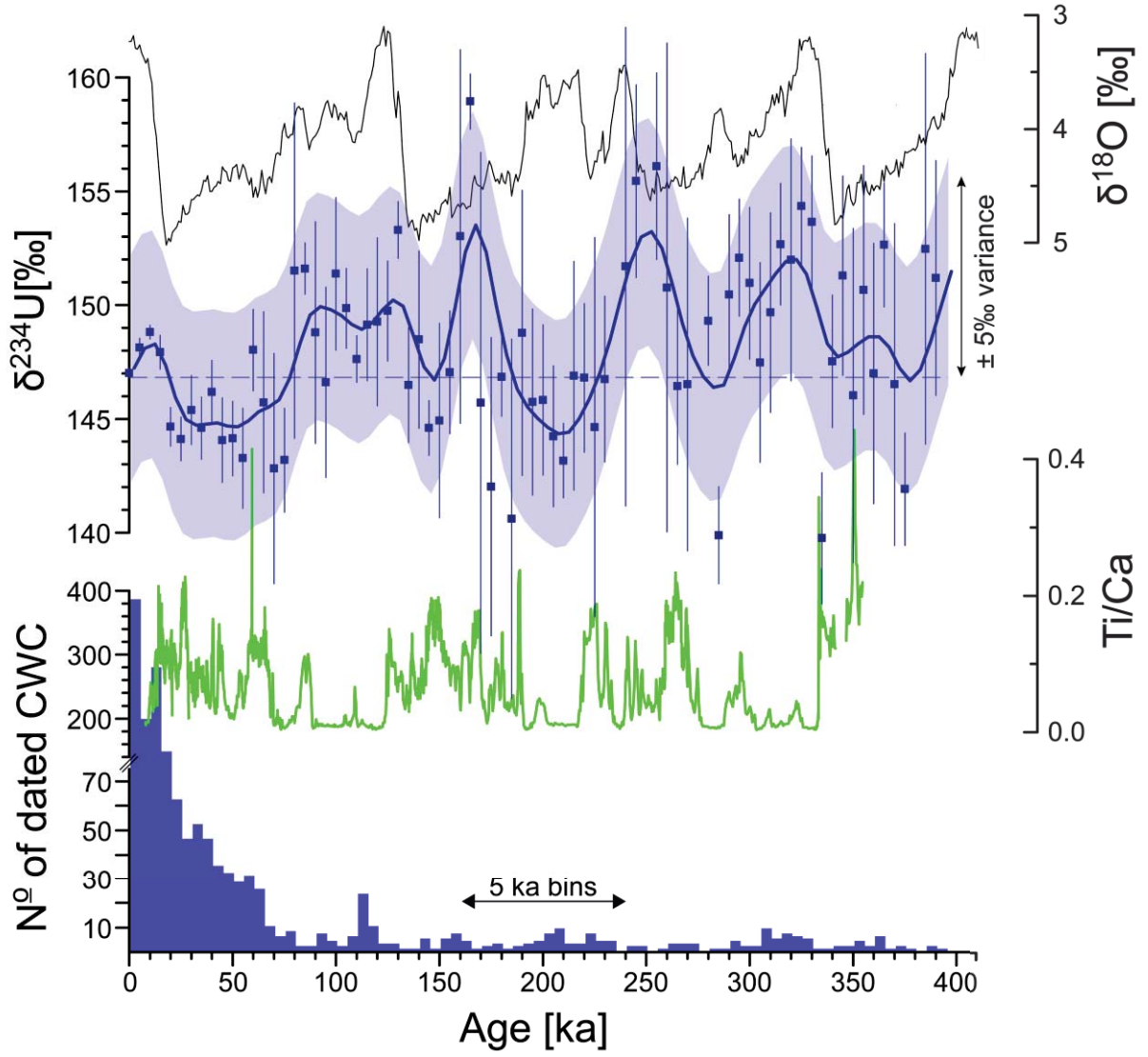

Fig. 6.4: Top: Global $\delta^{18}O$ stack LR04 (Lisiecki and Raymo 2005). The combined 5 ka binned Mediterranean and Atlantic record (blue) over 400 ka reveals generally higher $\delta^{234}U$ than observed in modern seawater $\delta^{234}U$ (blue dashed line). Times of increased terrigenous input during glacial periods is shown by Ti/Ca of the "Fleuve Manche" from the Bay of Biscay. Bottom: Number of used CWC (5 ka bins).

The tendency is less clear in some stages: MIS 8, revealed decreasing $\delta^{234}U$ as would be expected for glacial periods, however, mid-MIS 8 (280 ka) a significant increase of 6 ‰ from 146 to 153‰ is observed. Coinciding with major discharges from "Fleuve Manche" (Fig 6.3 and 6.4; Toucanne et al. 2010), the increase suggests early subglacial meltwater activities, as seen during the last 30 ka. For MIS 7, MIS 6 the observed tendency is almost reversed, MIS 7 reveals predominantly low $\delta^{234}U$ (~Ø 145‰) compared with other interglacial periods (i.e. MIS 9 and MIS 5). MIS 6 reveals predominantly high $\delta^{234}U$ values with (~Ø 150‰) and roughly coincides with terrigenous input from the ice sheets (Fig. 6.3). MIS 3 with predominantly glacial features shows a clear increase in $\delta^{234}U$ towards modern values. The increase can be explained with the enhanced terrigenous input from Northern Hemisphere ice sheets as shown by (Toucanne et al. 2010).

For a more constrained long-term record and a more precise assessment of glacial-interglacial variability, a higher data resolution is urgently required. The presented record already limits the range of variability over the last 400 ka from 15‰ (Henderson 2002) to a mere 8‰. However, the included data is carried together from several publications. E.g. the oldest used data set is over 20 years old, the samples were measured by on various instruments like TIMS, ICP-MS and MC-ICP-MS, using various methods. The partial lack of supplied data prevents uniform quality control. Additionally, with only 0.6 samples/ka regional biases or the impact of diageneses can not be ruled out strictly.

6.6 Conclusion

The presented $\delta^{234}U$ values, ranging from the last 15 ka to present-day, with values from 151.2 to 148.3±0.5‰ contradict the long presumed homogenous distribution of U isotopes in the oceans water with a modern $\delta^{234}U$ value of 146.8±0.4‰ (Andersen et al. 2010). The Atlantic- Mediterranean Sea offset is so far only observed during interglacial periods MIS 5 and MIS 1 and is not quantifiable, given the low amount of samples with additionally high uncertainties during the LGM, which suggests that sources like rivers, groundwater and the Black Sea, with potentially increased $\delta^{234}U$, cause the observed offset in the Mediterranean Sea. According to (Dunk et al. 2002), rivers and groundwater discharges supply the oceans with large amounts of excess ^{234}U. Aeolian dust, revealing an overall low excess ^{234}U signal, is predominantly supplied to the Mediterranean Sea during glacial periods and most possibly only shows minor impact to the $\delta^{234}U$ MUR.

Over the past 125 ka, seawater $\delta^{234}U$ revealed predominantly high values during MIS 5, MIS 3 and MIS 1 and predominantly low values during MIS 4 and MIS 2. Increasing $\delta^{234}U$ values have been correlated with subglacial meltwater activities of the Northern Hemisphere ice sheets. The “Fleuve Manche” is one potential source, supplying the Atlantic Ocean with terrigenous sediments and excess ^{234}U during these periods. The Mediterranean and Atlantic U-records show close correlation with a small Mediterranean offset of maximum 3‰. With an overall variation of circa 5‰ during the past 125 ka, both records were combined into one record spanning over several glacial-interglacial cycles (400 ka). Previous studies suggested an overall variation in $\delta^{234}U$ of 15‰ over the last 360 ka, with over 1.600 data points the variation was constrained to a mere 8‰.

The rate of physical weathering, responsible for high excess ^{234}U and thus higher $\delta^{234}U$ was believed to have never exceeded modern rates. However, the combined record demonstrated that the average seawater $\delta^{234}U$ during MIS 5 was increased by at least 2‰ und thus the rate of physical weathering must have been higher than today. Other periods show even higher $\delta^{234}U$, suggesting higher physical weathering rates, e.g. MIS 9, MIS 8 and MIS 6. However, the precision of the combined record is limited by the amount of available data between 125 and 400 ka.

7 Conclusion and outlook

Using the Bremen drill rig MeBo, for the first time, CWC mounds in the Alboran Sea were successfully drilled beyond the reach of gravity corer. Based on two 70 m long coral bearing cores from two different mounds in the EMCP, a vast number of dated coral fragments (n=202) revealed discontinuous coral growth over 550 ka during predominantly interglacial periods. The BR I core revealed coral occurrence over 70 m length with a basal age of 520 ka. However, with a high probability coral occurrence on BR I is suspected beyond the drilled 70 m. The shallower DM was fully penetrated at 61 m and revealed a basal age of approximately 400±20 ka. However, the age-depth profiles of both mounds revealed complex mound histories with severe signs of erosion and potential mass wasting events, creating extended mixed-age layers. The presented, complex long-term mound evolutions are so far unprecedented. In order to further investigate the newly observed mound evolution on DM, several long cores along DM would be necessary.

Based on the assumption that BR I has a minimum mound height of 80 m and a maximum mound height of 160 m, the calculated overall mound aggregation rate of BR I revealed a potential onset of coral growth in the Alboran Sea between 595 and 1190 ka and thus during the Mid Pleistocene Transition. Several hundred exposed and buried coral mounds were reported in the AS. Within the EMCP three different types of coral mound morphologies were found. DM in the southern EMCP belongs to a belt of partly buried coral ridges. Since coral growth on DM started approximately 400 ka ago and stopped 100 ka ago, investigating other mounds of the southern EMCP could reveal a similar mound history of onset and cessation of coral occurrence. In the northern EMCP, at least two more large coral ridges like BR I have been found (BR II and BR III). Using the new MeBo 200, capable of drilling 200 m long cores, could potentially fully penetrate through these three large structures and reveal a conclusive timing of the CWC growth onset.

Changing climatic conditions in the Mediterranean Region over full glacial-interglacial cycles and the combined CWC growth record revealed a tight link to freshwater input into the Mediterranean Sea. Enhanced freshwater input evoked primary productivity via the supply of nutrients and the transport of sediments, necessary for flourishing coral and mound growth. The strengthened AS gyre system, fortified by enhanced freshwater input, enabled enhanced vertical mixing into intermediate, coral dwelling depths (230-330 m) and made food available for the corals.

Using the Li/Mg temperature proxy, a reconstruction of the nBWT over 550 ka was conducted. nBWT of the shallow DM (236 m) and the deeper BR I (329 m) are consistent over the interglacial periods of the past 550 ka and thus reveal a coherent, predominant water mass, most possibly LIW. During glacial periods, when Mediterranean sea level reduction ranges between -40 to -80 m, nBWT of both locations show coherent temperatures, suggesting predominant LIW in both locations during these low stand sea levels.

During interglacial periods, based on terrestrial and marine records along the Iberian Margin, within the GoC and the AS, a clear correlation of (i) cooling events in SST, cold and arid climate in the Mediterranean Region and sub-polar planktic foraminifera species and (ii) the coincident reduction and demise of CWC occurrence in the AS could be established. Glacial periods in the Mediterranean Region are associated with cold and arid conditions, a southern position of the PF towards ~45°N-40°N and a general lack of CWC occurrence. Thus it is argued, that the lack of CWC during cooling events occurring in interglacial periods is evoked by unfavourable climatic conditions, ultimately caused by a southward shift of the PF or a southward extension of the polar vortex, as seen by multiple authors during Heinrich Events and Greenland Stadials.

Comparing the available data of several long MeBo cores from the GoC and the AS confirmed the existence of the so-called “Gibraltar-seesaw pattern” over the last 150 ka and most possibly during earlier glacial-interglacial cycles as well. The Gibraltar-seesaw pattern, observed in discontinuous CWC growth during predominantly interglacial periods in the AS and during predominantly glacial periods in the GoC, seemingly depends on the north-south oscillation of the PF. A northern position of the PF results in warm and wet climate in the Mediterranean Region with enhanced freshwater input, transporting nutrients and sediment, hence, facilitating CWC growth in the AS. A southern position of the PF induces cold and arid climate in the Mediterranean Region, enhancing productivity in the GoC and thus facilitating CWC growth in the GoC. However, distinct deviations from a strict glacial-interglacial seesaw pattern were observed during stadial and interstadial periods. If the origin of the observed coral – climate relationship is driven by the position of the polar front, the potential onset of CWC growth in the Mediterranean Region might coincide with the MPT, where a dominant change in the orbital cyclicity and major ice sheet build up occurred. Using multiple on- and off- mound cores from both basins to conduct a multi-proxy analysis of foraminiferal assemblages, productivity and temperature proxies could result in a better understanding of the climatic variability affecting coral growth on both sides of the SoG.

Contradicting the long presumed homogenous distribution of U isotopes in the oceans, a Mediterranean offset (~3.5-1.5‰) from the Atlantic was observed during MIS 5 and MIS 1, with values ranging between 151.2 to 148.3‰. During interglacial periods, the amount of freshwater from sources with increased $\delta^{234}U$, e.g. rivers, groundwater and the Black Sea, most possibly control the observed offset in the Mediterranean Sea. However, during glacial periods, when freshwater inflow was reduced, the input of aeolian dust, carrying an overall low excess ^{234}U signal is thus proposed to show only minor impact to the $\delta^{234}U$ offset.

Comparing the Mediterranean and the Atlantic record, consistent predominant high $\delta^{234}U$ values were observed during the interglacial periods MIS 5, MIS 3 and MIS 1, whereas predominantly low values were observed during the glacial periods MIS 4 and MIS 2. Increasing $\delta^{234}U$ have been correlated with subglacial meltwater activities of the Northern Hemisphere ice sheets. The “Fleuve Manche” is one potential source, supplying the Atlantic Ocean with terrigenous sediments and excess ^{234}U during these periods. The Mediterranean and Atlantic $\delta^{234}U$-records show close correlation, with a small Mediterranean offset of maximum 3‰. Over the past 125 ka, an overall variation of circa 5‰ in $\delta^{234}U$ was observed in the presented records, thus both records were combined into one record spanning over several glacial-interglacial cycles (400 ka). With over 1.600 data points, the variation was strongly constrained to a mere 8‰ over the past 400 ka.

Furthermore, the rate of physical weathering, responsible for high excess ^{234}U and thus higher $\delta^{234}U$ was believed to have never exceeded modern rates. However, the combined record demonstrated that the average seawater $\delta^{234}U$ during MIS 5 was increased by at least 2‰ und thus the rate of physical weathering must have been higher than today. Other periods show even higher $\delta^{234}U$, suggesting higher physical weathering rates, e.g. MIS 9, MIS 8 and MIS 6. However, the precision of the combined record is limited by the amount of available data between 125 and 400 ka. With sufficient data coverage and higher resolution, this interval could be more constrained and contradicting periods like MIS 7 and MIS 6 could be better resolved. The presented record is a mere start in providing global-scale information on continental weathering rates and could lead to a more precise U-series geochronology of marine organisms of the last 400 ka.

Published and submitted publications of the author

Fentimen et al.: The influence of climatic variability on the long-term growth history of a Mediterranean cold-water coral mound (Melilla Mound Field) (submitted)

Feenstra et al.: Palaeo-environmental variability and the proliferation of cold-water coral growth at the onset of the last deglaciation in the Western Mediterranean (EastMelilla Mound Field, Alboran Sea) (submitted)

Stinnesbeck et al.: New evidence for an early settlement of the Yucatán Peninsula, Mexico: The Chan Hol 3 woman and her meaning for the Peopling of the Americas (accepted in PLOS One, 2020)

Wienberg, C., et al. (2018). "The giant Mauritanian cold-water coral mound province: Oxygen control on coral mound formation." Quaternary Science Reviews **185**: 135-152.

Frank et al. (2016): The Climate History of the Mid-Depth Atlantic Deep Water Coral Reefs - future needs for IODP? (Abstract and talk at IODP 2016)

Hebbeln et al. (2015): MoccoMeBo - Climate-driven development of Moroccan cold-water coral mounds revealed by MeBo-drilling: Atlantic vs. Mediterranean settings - Cruise MSM36 –2014 – Malaga (Spain) Las Palmas (Spain). MARIA S. MERIAN-Berichte, MSM36, 47 pp.[DFG-Senatskommission für Ozeanographie]

Supplementary material

Table 3.2: U-series dating results from all investigated cores GeoB18118-1, GeoB18118-2 and GeoB18116-2.

"AR" corresponds to activity ratio, "Depth" corresponds to depth in core, "QC" corresponds to Quality Control with reliable (R) and not reliable (nR) samples.

Lab.No.	Sample Name	^{238}U (µg/g)	2σ (µg/g)	^{232}Th (ng/g)	2σ (ng/g)	^{230}Th/^{238}U AR	2σ AR	^{230}Th/^{232}Th AR	2σ AR	δ^{234}U (‰)	2σ (‰)	Age uncor. (ka)	2σ (ka)	U/Th Age (ka)	2σ (ka)	$\delta^{234}U_i$ (‰)	2σ (‰)	Depth (cm)	QC
8063	GeoB18118-1 0-86 1 cm	3.1919	0.0001	0.7643	0.0015	0.0877	0.0003	1115	4	146.58	0.60	8.67	0.03	8.61	0.04	150.19	0.62	1	R
8096	GeoB18118-1 0-86 2.5 cm	3.3807	0.0001	0.2147	0.0004	0.0894	0.0002	4319	14	146.66	0.67	8.85	0.03	8.84	0.03	150.37	0.68	2.5	R
8102	GeoB18118-1 0-86 3 cm	3.9966	0.0002	0.1910	0.0006	0.0907	0.0003	5828	27	146.40	0.79	8.99	0.03	8.98	0.03	150.16	0.81	3	R
8076	GeoB18118-1 0-86 7 cm	3.7716	0.0001	0.4680	0.0005	0.0927	0.0002	2279	5	145.50	0.48	9.20	0.02	9.16	0.02	149.32	0.50	7	R
8069	GeoB18118-1 0-86 15 cm	3.0245	0.0003	0.5621	0.0015	0.0863	0.0004	1413	7	147.03	0.90	8.53	0.04	8.48	0.04	150.59	0.92	15	R
8367	GeoB18118-1 0-86 35 cm	3.1206	0.0001	0.4464	0.0013	0.0933	0.0003	1985	9	146.76	0.53	9.25	0.04	9.21	0.04	150.63	0.54	35	R
8065	GeoB18118-1 0-86 41 cm	2.8554	0.0001	0.1570	0.0003	0.0926	0.0002	5141	17	145.62	0.61	9.19	0.03	9.17	0.03	149.45	0.63	41	R
8369	GeoB18118-1 0-86 50 cm	3.1322	0.0002	0.2228	0.0007	0.0945	0.0003	4048	20	147.68	0.85	9.37	0.04	9.35	0.04	151.64	0.87	50	R
8368	GeoB18118-1 0-86 52 cm	3.8395	0.0003	0.0915	0.0003	0.0942	0.0003	12027	55	146.87	0.72	9.34	0.03	9.33	0.03	150.80	0.74	52	R
8067	GeoB18118-1 0-86 65 cm	3.2602	0.0002	0.4157	0.0011	0.0957	0.0003	2287	10	146.75	0.59	9.50	0.03	9.47	0.04	150.73	0.60	65	R
8066	GeoB18118-1 0-86 82 cm	3.1162	0.0002	0.4639	0.0010	0.0966	0.0003	1979	7	146.08	0.82	9.60	0.03	9.56	0.03	150.08	0.85	82	R
8098	GeoB18118-1 86-186 4 cm	3.1151	0.0001	0.1004	0.0003	0.0957	0.0003	9109	37	146.01	0.74	9.51	0.03	9.50	0.03	149.98	0.76	90	R
8370	GeoB18118-1 86-186 15 cm	3.3914	0.0003	0.2514	0.0006	0.0963	0.0003	3955	15	145.98	0.60	9.56	0.03	9.55	0.03	149.97	0.61	101	R
8371	GeoB18118-1 86-186 50 cm	3.2506	0.0002	0.1266	0.0004	0.0976	0.0003	7640	37	146.72	0.88	9.70	0.03	9.69	0.04	150.79	0.90	136	R
8064	GeoB18118-1 86-186 65 cm	3.2511	0.0002	0.3158	0.0007	0.0985	0.0003	3082	10	146.10	0.72	9.80	0.03	9.77	0.03	150.19	0.74	151	R
8077	GeoB18118-1 86-186 80 cm	3.3893	0.0001	0.2631	0.0007	0.0986	0.0003	3864	16	143.92	0.56	9.83	0.03	9.81	0.03	147.97	0.57	166	R
8100	GeoB18118-1 86-186 93 cm	2.7291	0.0001	0.2461	0.0006	0.0992	0.0004	3370	14	145.11	0.72	9.88	0.04	9.86	0.04	149.21	0.74	179	R
8372	GeoB18118-1 186-286 60 cm	2.7832	0.0001	0.2450	0.0004	0.1078	0.0002	3737	10	145.41	0.54	10.77	0.03	10.75	0.03	149.89	0.56	246	R
8373	GeoB18118-1 186-286 68 cm	3.2099	0.0002	0.2984	0.0009	0.1048	0.0004	3438	16	144.90	1.09	10.46	0.04	10.43	0.04	149.24	1.13	254	R
8099	GeoB18118-1 186-286 92 cm	3.8277	0.0001	0.3356	0.0007	0.1114	0.0003	3898	13	143.94	0.56	11.17	0.03	11.15	0.03	148.55	0.58	278	R
8062	GeoB18118-1 286-386 2 cm	3.1966	0.0002	0.3002	0.0007	0.1144	0.0004	3709	15	146.33	1.00	11.46	0.04	11.43	0.04	151.14	1.04	288	R
10157	GeoB18118-1 286-386 12 cm	3.6157	0.0001	0.2153	0.0003	0.1156	0.0002	5975	13	142.92	0.48	11.62	0.02	11.61	0.02	147.68	0.50	298	R
10158	GeoB18118-1 286-386 24 cm	4.2780	0.0001	0.6149	0.0007	0.1167	0.0002	2475	5	143.31	0.39	11.73	0.02	11.69	0.03	148.13	0.40	310	R
8071	GeoB18118-1 286-386 55 cm	3.0706	0.0001	0.4745	0.0012	0.1155	0.0004	2278	9	142.18	0.57	11.62	0.04	11.58	0.04	146.91	0.59	341	R
8376	GeoB18118-1 286-386 61 cm	3.4453	0.0002	0.2526	0.0006	0.1281	0.0004	5329	21	143.52	0.68	12.94	0.04	12.92	0.05	148.85	0.70	347	R
8377	GeoB18118-1 286-386 67 cm	3.5440	0.0002	0.2807	0.0006	0.1240	0.0003	4768	16	143.61	0.72	12.50	0.03	12.48	0.04	148.77	0.75	353	R
8378	GeoB18118-1 286-386 72 cm	2.3862	0.0002	0.2194	0.0006	0.1278	0.0004	4247	18	145.16	0.90	12.89	0.05	12.87	0.05	150.54	0.94	358	R
8379	GeoB18118-1 286-386 78 cm	2.8906	0.0001	0.2377	0.0007	0.1295	0.0004	4813	20	144.29	0.74	13.08	0.04	13.06	0.04	149.71	0.77	364	R
8380	GeoB18118-1 286-386 84 cm	3.4490	0.0002	0.5649	0.0013	0.1300	0.0005	2422	11	144.98	1.10	13.13	0.05	13.09	0.06	150.44	1.14	370	R
8381	GeoB18118-1 286-386 92 cm	3.8385	0.0002	0.2850	0.0008	0.1295	0.0004	5330	23	143.69	0.63	13.09	0.05	13.07	0.05	149.09	0.65	378	R

Lab.No.	Sample Name	^{238}U (µg/g)	2σ (µg/g)	^{232}Th (ng/g)	2σ (ng/g)	^{230}Th/^{238}U AR	2σ AR	^{230}Th/^{232}Th AR	2σ AR	δ^{234}U (‰)	2σ (‰)	Age uncor. (ka)	2σ (ka)	U/Th Age (ka)	2σ (ka)	$\delta^{234}U_i$ (‰)	2σ (‰)	Depth (cm)	QC
8097	GeoB18118-1 286-386 99 cm	2.6938	0.0001	0.9145	0.0021	0.1315	0.0003	1188	4	143.01	0.66	13.32	0.04	13.23	0.06	148.46	0.68	385	R
8104	GeoB18118-1 386-487 65 cm	3.1972	0.0001	0.5542	0.0013	0.1320	0.0004	2333	9	144.30	0.75	13.35	0.04	13.31	0.05	149.83	0.77	451	R
8095	GeoB18118-1 386-487 88 cm	3.1575	0.0001	0.2539	0.0006	0.1326	0.0004	5053	19	143.79	0.70	13.42	0.04	13.40	0.04	149.34	0.73	474	R
8093	GeoB18118-1 487-587 6 cm	3.0130	0.0001	0.4865	0.0010	0.1326	0.0004	2520	10	143.91	0.83	13.42	0.05	13.37	0.05	149.45	0.86	493	R
8382	GeoB18118-1 487-587 20 cm	2.6168	0.0002	0.4789	0.0011	0.1383	0.0005	2307	10	145.40	1.17	14.01	0.05	13.97	0.06	151.25	1.22	507	R
8070	GeoB18118-1 487-587 24 cm	2.5147	0.0001	0.2218	0.0006	0.1352	0.0004	4669	19	142.66	0.65	13.71	0.05	13.69	0.05	148.29	0.68	511	R
8383	GeoB18118-1 487-587 55 cm	3.5036	0.0002	0.2059	0.0006	0.1356	0.0005	7038	31	144.61	0.82	13.73	0.05	13.72	0.05	150.32	0.85	542	R
8094	GeoB18118-1 487-587 80 cm	2.8553	0.0001	0.2338	0.0005	0.1394	0.0004	5224	18	143.81	0.68	14.15	0.04	14.13	0.04	149.67	0.71	567	R
8384/1	GeoB18118-1 487-587 93 cm	3.5535	0.0002	0.4935	0.0013	0.1161	0.0004	2554	11	147.19	0.69	11.63	0.05	11.59	0.05	152.09	0.71	580	R
8384	GeoB18118-1 487-587 93 cm	3.4964	0.0001	0.2419	0.0004	0.1326	0.0003	5900	16	144.48	0.55	13.41	0.03	13.39	0.03	150.06	0.57	580	R
8072	GeoB18118-1 587-687 03 cm	3.3573	0.0001	0.2438	0.0004	0.1338	0.0004	5622	21	145.40	0.60	13.53	0.05	13.51	0.05	151.06	0.62	590	R
8385	GeoB18118-1 587-687 18 cm	3.8334	0.0006	0.3356	0.0013	0.1365	0.0006	4766	27	145.48	1.10	13.82	0.06	13.80	0.06	151.26	1.15	605	R
8386	GeoB18118-1 587-687 55 cm	2.8505	0.0002	0.2288	0.0006	0.1410	0.0004	5368	20	145.10	0.98	14.31	0.04	14.29	0.05	151.08	1.02	642	R
8075	GeoB18118-1 587-687 62 cm	3.0716	0.0001	0.2882	0.0006	0.1428	0.0004	4633	16	144.06	0.45	14.52	0.04	14.49	0.05	150.09	0.47	649	R
8387	GeoB18118-1 587-687 72 cm	3.2274	0.0002	0.3183	0.0008	0.1401	0.0004	4333	17	141.86	0.62	14.25	0.05	14.23	0.05	147.68	0.64	659	R
8103	GeoB18118-1 587-687 92 cm	3.6620	0.0002	0.2129	0.0005	0.1396	0.0003	7362	25	144.03	0.57	14.17	0.04	14.16	0.04	149.91	0.60	679	R
8080	GeoB18118-1 687-787 5 cm	3.2533	0.0001	0.1347	0.0004	0.1416	0.0004	10399	41	143.53	0.58	14.39	0.05	14.38	0.04	149.48	0.61	692	R
8388	GeoB18118-1 687-787 30 cm	2.7784	0.0001	0.3369	0.0013	0.1453	0.0007	3647	22	145.36	1.08	14.77	0.08	14.74	0.08	151.54	1.13	717	R
8101	GeoB18118-1 687-787 50 cm	2.8455	0.0001	0.5980	0.0012	0.1431	0.0004	2086	7	145.66	0.71	14.53	0.04	14.47	0.05	151.74	0.74	737	R
8389	GeoB18118-1 687-787 78 cm	2.5033	0.0002	0.2397	0.0008	0.1456	0.0005	4625	23	144.82	1.01	14.81	0.06	14.79	0.06	151.00	1.06	765	R
8068	GeoB18118-1 687-787 92 cm	3.6927	0.0002	0.3762	0.0011	0.1429	0.0004	4267	18	144.32	0.53	14.53	0.05	14.50	0.05	150.36	0.55	779	R
8390	GeoB18118-1 687-787 100 cm	3.2818	0.0002	0.2940	0.0008	0.1431	0.0005	4867	20	143.82	1.04	14.56	0.05	14.54	0.05	149.85	1.08	787	R
8074	GeoB18118-1 787-873 1 cm	3.2796	0.0001	0.2386	0.0006	0.1428	0.0004	5990	22	146.06	1.12	14.50	0.05	14.48	0.05	152.16	1.17	788	R
8079	GeoB18118-1 787-873 30cm	2.7784	0.0001	0.1507	0.0003	0.1441	0.0004	8121	24	144.92	0.66	14.64	0.04	14.63	0.04	151.04	0.69	817	R
10160	GeoB18118-1 787-873 77 cm	3.6481	0.0001	0.3847	0.0005	0.1459	0.0003	4217	11	146.76	0.45	14.82	0.04	14.80	0.04	153.03	0.47	864	R
8392	GeoB18118-1 787-873 80 cm	3.2318	0.0002	0.4506	0.0009	0.1491	0.0005	3265	13	147.30	0.88	15.16	0.06	15.12	0.06	153.73	0.92	867	R
8091	GeoB18118-1 787-873 83 cm	2.7916	0.0001	0.2651	0.0005	0.1475	0.0004	4746	15	147.00	0.56	14.98	0.04	14.96	0.04	153.35	0.59	870	R
10159	GeoB18118-1 286-386 42 cm	3.4150	0.0001	2.5163	0.0025	0.1086	0.0003	449	1	145.64	0.38	10.85	0.03	10.67	0.10	150.10	0.39	328	nR
8061	GeoB18118-1 386-487 1 cm	3.0354	0.0002	7.1176	0.0212	0.1317	0.0004	171	1	144.87	0.54	13.31	0.05	12.73	0.30	150.18	0.57	387	nR
7626	GeoB18118-2 P02 31 cm	3.1149	0.0001	0.1695	0.0003	0.1033	0.0002	5814	16	145.42	0.53	10.30	0.02	10.29	0.02	149.71	0.54	310	R
7622	GeoB18118-2 P02 CC Top	3.3618	0.0001	0.1678	0.0003	0.1039	0.0002	6377	17	144.43	0.43	10.37	0.02	10.36	0.02	148.72	0.44	320	R
7617	GeoB18118-2 P03 24 cm	2.7843	0.0001	0.1375	0.0002	0.1106	0.0003	6892	20	143.39	0.46	11.08	0.03	11.07	0.03	147.94	0.47	529	R
7614	GeoB18118-2 P03 33 cm	3.1542	0.0001	0.6926	0.0008	0.1095	0.0003	1541	4	144.02	0.61	10.97	0.03	10.91	0.04	148.53	0.63	538	R
7616	GeoB18118-2 P03 65 cm	3.6882	0.0001	0.2453	0.0003	0.1109	0.0002	5139	12	143.05	0.40	11.12	0.02	11.10	0.02	147.61	0.41	570	R
7615	GeoB18118-2 P03 113 cm	3.0024	0.0001	0.2582	0.0003	0.1156	0.0002	4150	10	143.96	0.42	11.61	0.02	11.59	0.03	148.75	0.43	618	R
10161	GeoB18118-2 P03 130 cm	3.1809	0.0001	0.8781	0.0029	0.1116	0.0003	1234	5	144.76	0.36	11.18	0.03	11.11	0.04	149.38	0.37	635	R
7613	GeoB18118-2 P03 130 cm	3.1058	0.0001	0.2552	0.0004	0.1132	0.0003	4253	14	144.03	0.54	11.35	0.04	11.33	0.04	148.72	0.55	635	R
7619	GeoB18118-2 P03 232 cm	3.2577	0.0001	0.4831	0.0006	0.1185	0.0002	2454	6	144.30	0.39	11.92	0.02	11.88	0.03	149.22	0.41	732	R

Lab.No.	Sample Name	^{238}U (µg/g)	2σ (µg/g)	^{232}Th (ng/g)	2σ (ng/g)	$^{230}Th/^{238}U$ AR	2σ AR	$^{230}Th/^{232}Th$ AR	2σ AR	$\delta^{234}U$ (‰)	2σ (‰)	Age uncor. (ka)	2σ (ka)	U/Th Age (ka)	2σ (ka)	$\delta^{234}U_i$ (‰)	2σ (‰)	Depth (cm)	QC
7610	GeoB18118-2 P04 9 cm	4.5274	0.0002	0.3590	0.0011	0.1309	0.0004	5089	22	144.11	0.57	13.24	0.05	13.22	0.04	149.60	0.59	749	R
7608	GeoB18118-2 P04 CC2	2.6437	0.0001	0.2076	0.0004	0.1300	0.0004	5110	17	143.76	0.53	13.14	0.04	13.12	0.04	149.19	0.55	754	R
10162	GeoB18118-2 P04 CC1	2.8595	0.0001	0.2303	0.0004	0.1286	0.0003	4880	14	143.29	0.45	12.99	0.03	12.97	0.03	148.65	0.47	756	R
7609	GeoB18118-2 P05 3 cm	3.1191	0.0001	0.2113	0.0012	0.1433	0.0007	6514	47	142.96	1.00	14.59	0.08	14.57	0.08	148.97	1.05	978	R
7089	GeoB18118-2 P05 10 cm	2.7291	0.0037	0.3414	0.0031	0.1410	0.0018	3486	54	149.86	5.75	14.24	0.22	14.21	0.21	156.00	5.98	985	R
8364	GeoB18118-2 P05 CC1	3.5141	0.0002	0.3734	0.0009	0.1444	0.0004	4129	16	145.70	0.64	14.67	0.05	14.64	0.05	151.86	0.67	1000	R
7611	GeoB18118-2 P05 CC2	3.4127	0.0001	0.3789	0.0006	0.1450	0.0003	4033	11	145.78	0.60	14.73	0.04	14.71	0.04	151.96	0.63	1000	R
10163	GeoB18118-2 P05 CC3	2.8234	0.0001	0.1979	0.0003	0.1455	0.0003	6373	18	144.81	0.58	14.81	0.04	14.79	0.04	150.99	0.60	1000	R
6995	GeoB18118-2 P05 CC4	3.3356	0.0126	0.2626	0.0024	0.1515	0.0020	5909	91	147.76	8.58	15.41	0.25	15.39	0.25	154.33	8.97	1000	R
7857	GeoB18118-2 P06 91 cm	3.8949	0.0001	3.0806	0.0066	0.5813	0.0014	2242	7	119.74	0.79	78.65	0.29	78.45	0.29	149.47	0.99	1301	R
7086	GeoB18118-2 P06 111 cm	2.6636	0.0063	2.2723	0.0226	0.8266	0.0075	3009	40	102.74	4.80	145.86	2.95	145.65	2.99	155.07	7.36	1321	R
7094	GeoB18118-2 P06 200 cm	3.3101	0.0001	0.5380	0.0022	0.8173	0.0033	15459	89	102.73	0.26	142.55	1.12	142.51	1.14	153.68	0.63	1450	R
7084	GeoB18118-2 P07 84 cm	3.8745	0.0002	0.8875	0.0060	0.8889	0.0051	11904	106	84.63	0.35	179.01	2.47	178.95	2.52	140.35	1.15	1529	R
7102	GeoB18118-2 P07 186 cm	3.1731	0.0001	2.5612	0.0151	0.9222	0.0054	3499	29	84.35	0.46	196.92	3.12	196.72	3.20	147.08	1.55	1631	R
7078	GeoB18118-2 P07 CC B	3.2411	0.0043	0.6165	0.0139	0.9610	0.0255	15656	546	81.42	2.54	224.23	19.88	224.18	20.36	153.42	10.05	1640	R
7097	GeoB18118-2 P08 CC1	3.4631	0.0001	2.1909	0.0082	0.9397	0.0041	4555	26	79.43	0.24	210.89	2.71	210.73	2.74	144.09	1.20	1830	R
7087	GeoB18118-2 P09 66 cm	3.2447	0.0001	1.0452	0.0053	0.9796	0.0048	9327	65	78.07	0.43	242.13	4.16	242.05	4.13	154.73	2.00	1981	R
7072	GeoB18118-2 P09 115 cm	3.0891	0.0043	3.1314	0.0190	0.9951	0.0078	3027	30	80.15	2.60	254.08	8.05	253.83	7.87	164.23	6.46	2030	R
7068	GeoB18118-2 P09 188 cm	3.7339	0.0066	0.6293	0.0069	0.9597	0.0094	17556	256	82.01	1.97	222.77	7.10	222.72	6.94	153.91	4.78	2103	R
7080	GeoB18118-2 P09 CC1	3.0248	0.0061	4.7573	0.0240	0.9497	0.0073	1879	17	83.03	6.25	215.02	6.55	214.63	6.68	152.30	11.81	2133	R
7069	GeoB18118-2 P10 CC B	3.0051	0.0001	0.3148	0.0017	0.9646	0.0041	28250	195	76.73	0.38	230.93	3.27	230.91	3.27	147.37	1.54	2157	R
7088	GeoB18118-2 P11 45 cm	3.9697	0.0067	1.4944	0.0074	0.9661	0.0074	7969	72	82.72	2.29	227.00	5.83	226.91	5.98	157.08	5.10	2460	R
7081	GeoB18118-2 P11 91 cm	3.9802	0.0089	3.4777	0.0357	0.9515	0.0086	3388	46	79.18	3.39	219.15	6.70	218.93	6.49	147.01	6.84	2476	R
6997	GeoB18118-2 P12 CC	3.5014	0.0125	2.1223	0.0178	0.9756	0.0091	4962	59	72.87	3.88	243.79	9.10	243.64	9.61	145.08	8.67	2621	R
7093	GeoB18118-2 P12 CC T	3.6698	0.0001	3.4142	0.0167	0.9602	0.0050	3170	23	76.60	0.31	227.65	3.76	227.41	3.83	145.67	1.68	2622	R
6998	GeoB18118-2 P13 CC	3.3912	0.0088	1.2896	0.0039	1.0312	0.0055	8300	46	60.66	2.96	336.11	13.79	336.01	13.73	156.79	9.77	3085	R
7070	GeoB18118-2 P13 177 cm	3.5331	0.0001	0.5741	0.0015	1.0176	0.0028	19191	74	62.14	0.36	308.12	4.61	308.08	4.58	148.43	2.10	3177	R
7098	GeoB18118-2 P15 99 cm	3.2324	0.0001	7.8297	0.0301	1.0227	0.0047	1295	8	66.11	0.38	308.36	7.30	307.76	7.30	157.76	3.38	3424	R
7862	GeoB18118-2 P15 132 cm	3.1112	0.0001	2.3389	0.0045	1.0291	0.0023	4166	12	64.78	0.49	322.05	4.38	321.86	4.33	160.89	2.31	3457	R
7073	GeoB18118-2 P15 186 cm	3.4903	0.0001	0.3941	0.0031	1.0190	0.0039	27691	242	62.87	0.46	308.91	6.11	308.88	6.41	150.53	2.94	3511	R
7878	GeoB18118-2 P16 99 cm	2.9688	0.0001	0.9167	0.0017	1.0243	0.0019	10120	27	61.09	0.41	321.66	3.34	321.58	3.52	151.59	1.82	3659	R
7082	GeoB18118-2 P16 159 cm	3.0542	0.0001	2.5462	0.0084	1.0030	0.0036	3696	18	62.25	0.47	286.72	4.92	286.51	4.71	139.89	2.14	3719	R
7099	GeoB18118-2 P16 20 cm	3.8025	0.0001	1.1687	0.0051	1.0142	0.0043	10134	62	59.67	0.54	307.60	7.01	307.52	7.06	142.30	3.12	3770	R
7865	GeoB18118-2 P17 30 cm	3.4723	0.0001	0.0848	0.0002	1.0261	0.0017	127816	333	59.87	0.41	327.89	3.35	327.88	3.28	151.24	1.75	3824	R
7866	GeoB18118-2 P17 110 cm	3.2978	0.0001	0.7674	0.0019	1.0259	0.0027	13415	49	62.36	0.46	321.67	4.93	321.61	4.89	154.76	2.42	3905	R
8148	GeoB18118-2 P17 215 cm	3.3918	0.0002	0.6757	0.0015	1.0233	0.0023	15660	50	61.22	0.77	319.58	4.53	319.53	4.46	151.05	2.69	4010	R
7864	GeoB18118-2 P18 24 cm	4.4006	0.0001	0.7477	0.0013	1.0280	0.0017	18399	44	61.73	0.39	326.98	3.44	326.94	3.39	155.53	1.78	4054	R
7887	GeoB18118-2 P18 127 cm	2.8798	0.0001	0.8227	0.0015	1.0357	0.0019	11054	29	54.26	0.52	366.02	5.40	365.95	5.33	152.64	2.73	4157	R
7891	GeoB18118-2 P23 CC1	3.3862	0.0001	0.5535	0.0010	1.0324	0.0017	19327	46	49.02	0.45	376.17	5.69	376.13	5.21	141.92	2.47	5405	R
7877	GeoB18118-2 P24 100 cm	3.3349	0.0001	0.4081	0.0007	1.0399	0.0017	25919	61	40.37	0.57	456.47	12.07	456.44	11.99	146.68	5.38	5540	R
7867	GeoB18118-2 P25 57 cm	2.7116	0.0001	0.8423	0.0016	1.0370	0.0022	10162	29	49.73	0.61	387.44	7.62	387.36	7.64	148.61	3.69	5732	R

Lab.No.	Sample Name	^{238}U (µg/g)	2σ (µg/g)	^{232}Th (ng/g)	2σ (ng/g)	$^{230}Th/^{238}U$ AR	2σ AR	$^{230}Th/^{232}Th$ AR	2σ AR	$\delta^{234}U$ (‰)	2σ (‰)	Age uncor. (ka)	2σ (ka)	U/Th Age (ka)	2σ (ka)	$\delta^{234}U_i$ (‰)	2σ (‰)	Depth (cm)	QC
7882	GeoB18118-2 P26 44 cm	3.8562	0.0001	3.8537	0.0115	1.0384	0.0030	3167	13	41.02	0.36	443.04	17.00	442.79	17.53	143.38	7.21	5954	R
7855	GeoB18118-2 P28 CC1	3.7554	0.0001	0.5833	0.0010	1.0432	0.0018	20460	51	40.09	0.35	482.79	15.05	482.75	14.10	156.89	6.40	6630	R
7884	GeoB18118-2 P29 88 cm	3.9056	0.0001	2.0777	0.0045	1.0410	0.0024	5975	19	38.50	0.36	482.17	19.22	482.04	19.84	150.38	8.55	6703	R
7885	GeoB18118-2 P29 CC1	2.8677	0.0001	0.5847	0.0012	1.0407	0.0020	15543	43	44.32	0.56	431.59	10.58	431.54	10.76	150.08	4.94	6865	R
7872	GeoB18118-2 P30 185 cm	3.3591	0.0001	1.7113	0.0030	1.0444	0.0019	6245	16	36.93	0.46	538.36	28.89	538.23	28.06	169.07	13.57	7035	R
8365	GeoB18118-2 P06 91 cm	2.7688	0.0001	0.6295	0.0018	0.7947	0.0021	10636	41	107.85	0.85	133.56	0.71	133.51	0.71	157.29	1.27	1301	nR
7076	GeoB18118-2 P06 141 cm	3.2647	0.0050	1.0487	0.0057	0.8075	0.0065	7764	75	109.78	3.59	137.20	2.40	137.12	2.35	161.74	5.40	1391	nR
7074	GeoB18118-2 P08 8 cm	3.2166	0.0051	2.0642	0.0609	0.9496	0.0356	4570	218	86.49	3.52	212.44	24.23	212.28	27.08	157.59	13.66	1758	nR
7124	GeoB18118-2 P08 50 cm	2.8525	0.0050	8.8954	0.0436	0.9471	0.0061	939	7	87.41	2.93	210.19	4.51	209.41	4.56	157.98	5.68	1800	nR
7085	GeoB18118-2 P08 95 cm	3.5882	0.0089	3.1819	0.0254	0.9444	0.0090	3307	40	91.10	3.87	205.97	6.33	205.75	6.02	162.96	7.46	1845	nR
7075	GeoB18118-2 P09 21 cm	2.9886	0.0054	2.9639	0.0183	0.9684	0.0072	3016	29	83.53	4.56	228.03	6.63	227.78	6.55	159.01	9.16	2021	nR
7092	GeoB18118-2 P09 150 cm	2.6257	0.0001	3.9699	0.0123	0.9694	0.0030	1968	9	83.20	0.42	229.09	2.29	228.71	2.34	158.80	1.32	2150	nR
7083	GeoB18118-2 P13 110 cm	2.7507	0.0040	1.1686	0.0089	1.0251	0.0126	7508	108	72.07	3.84	300.87	20.78	300.77	20.38	168.63	13.24	3110	nR
7100	GeoB18118-2 P14 162 cm	3.1225	0.0001	0.8683	0.0043	1.0376	0.0049	11454	78	64.52	0.39	339.04	10.30	338.97	10.42	168.18	5.06	3412	nR
7863	GeoB18118-2 P15 CC1	3.5200	0.0008	0.7918	0.0014	1.0294	0.0019	13914	35	63.69	0.50	324.99	3.73	324.93	3.85	159.55	2.14	3557	nR
7868	GeoB18118-2 P19 CC1	3.0347	0.0001	7.0281	0.0195	1.0468	0.0029	1376	5	50.62	0.56	420.10	13.48	419.53	13.30	165.68	6.49	4266	nR
8321	GeoB18116-2 P01 3 cm	3.5779	0.0003	0.1243	0.0005	0.6874	0.0018	59509	273	112.15	0.74	102.77	0.46	102.76	0.46	149.94	1.01	3	R
8143	GeoB18116-2 P01 10 cm	3.3877	0.0003	0.0952	0.0003	0.7077	0.0017	77045	312	110.39	0.64	108.14	0.46	108.13	0.46	149.85	0.89	10	R
8322	GeoB18116-2 P01 111 cm	3.5696	0.0002	0.2790	0.0007	0.7194	0.0015	27695	90	110.60	0.63	111.14	0.41	111.12	0.41	151.41	0.89	111	R
8086	GeoB18116-2 P01-2 193 cm	2.4111	0.0001	0.1769	0.0004	0.7301	0.0015	30341	95	108.25	0.59	114.46	0.43	114.44	0.43	149.59	0.84	193	R
8323	GeoB18116-2 P01 CC 2 cm	3.0345	0.0001	0.0905	0.0004	0.7260	0.0025	74026	415	107.91	0.64	113.42	0.67	113.41	0.68	148.68	0.92	244	R
8324	GeoB18116-2 P02 198 cm	3.5239	0.0002	0.1549	0.0003	0.7279	0.0015	50305	148	106.87	0.53	114.13	0.44	114.12	0.42	147.55	0.75	348	R
8285	GeoB18116-2 P02 155 cm	3.2865	0.0010	0.1469	0.0016	0.7273	0.0017	49644	547	109.05	2.21	113.54	0.63	113.52	0.66	150.30	3.06	425	R
8286	GeoB18116-2 P02 182 cm	3.4189	0.0001	0.1073	0.0006	0.7258	0.0020	70618	419	108.24	1.09	113.29	0.56	113.29	0.59	149.09	1.52	452	R
8083	GeoB18116-2 P03 36 cm	3.0523	0.0001	0.0762	0.0003	0.7271	0.0016	88763	399	105.89	0.60	114.11	0.44	114.10	0.47	146.18	0.85	541	R
8325	GeoB18116-2 P03 119 cm	3.0534	0.0001	0.1755	0.0004	0.7230	0.0015	38253	116	107.75	0.50	112.63	0.41	112.61	0.40	148.14	0.71	624	R
8326	GeoB18116-2 P03 CC 6 cm	3.3643	0.0002	0.2811	0.0008	0.7207	0.0022	26189	110	107.45	0.63	112.10	0.59	112.07	0.58	147.49	0.90	730	R
8287	GeoB18116-2 P04 154 cm	3.3740	0.0002	0.1102	0.0006	0.7315	0.0017	68299	405	106.88	1.23	115.12	0.51	115.11	0.52	147.97	1.71	894	R
8327	GeoB18116-2 P04 190 cm	3.2531	0.0004	0.1907	0.0008	0.7280	0.0027	37606	211	106.79	1.47	114.18	0.78	114.16	0.76	147.46	2.06	930	R
8328	GeoB18116-2 P05 48 cm	3.1825	0.0002	0.0731	0.0003	0.7302	0.0027	96691	523	105.34	1.16	115.07	0.75	115.06	0.76	145.82	1.63	1023	R
8358	GeoB18116-2 P05 78.5 cm	3.3907	0.0001	0.1070	0.0004	0.9314	0.0021	90207	366	78.49	0.74	206.16	1.43	206.15	1.44	140.55	1.44	1054	R
8360	GeoB18116-2 P05 90 cm	3.3806	0.0002	0.3990	0.0016	0.9331	0.0022	24161	114	82.32	0.76	204.69	1.48	204.67	1.46	146.80	1.48	1065	R
8359	GeoB18116-2 P05 105 cm	3.1647	0.0001	0.0703	0.0003	0.9334	0.0023	128360	651	80.00	0.65	206.42	1.54	206.42	1.56	143.38	1.32	1080	R
8361	GeoB18116-2 P05 128.5 cm	3.4715	0.0002	0.1221	0.0005	0.9278	0.0019	80694	356	81.39	0.62	202.06	1.21	202.05	1.25	144.08	1.21	1104	R
8362	GeoB18116-2 P05 144 cm	3.7602	0.0002	0.3043	0.0007	0.9282	0.0020	35077	113	81.64	0.71	202.13	1.28	202.10	1.27	144.53	1.36	1120	R
8363	GeoB18116-2 P05 171 cm	2.4360	0.0001	0.5219	0.0012	0.9427	0.0023	13372	45	86.07	0.67	208.27	1.54	208.22	1.54	155.04	1.38	1146	R
8329	GeoB18116-2 P05 184 cm	3.0870	0.0007	0.1198	0.0010	0.9301	0.0024	72933	618	81.43	5.21	203.43	3.70	203.42	3.61	144.70	9.37	1160	R
8140	GeoB18116-2 P06 12 cm	3.4438	0.0001	0.2690	0.0006	0.9348	0.0016	36529	101	78.38	0.68	208.44	1.17	208.42	1.13	141.26	1.30	1222	R

Lab.Nr.	Sample Name	^{238}U (µg/g)	2σ (µg/g)	^{232}Th (ng/g)	2σ (ng/g)	$^{230}Th/^{238}U$ AR	2σ AR	$^{230}Th/^{232}Th$ AR	2σ AR	$\delta^{234}U$ (‰)	2σ (‰)	Age uncor. (ka)	2σ (ka)	U/Th Age (ka)	2σ (ka)	$\delta^{234}U_i$ (‰)	2σ (‰)	Depth (cm)	QC
8330	GeoB18116-2 P06 75 cm	3.3724	0.0002	0.1465	0.0005	0.9381	0.0035	65673	334	80.54	1.07	209.10	2.38	209.09	2.39	145.43	2.17	1285	R
8332	GeoB18116-2 P07 119 cm	3.2213	0.0005	0.2766	0.0020	0.9289	0.0062	32923	326	79.36	2.61	204.01	4.19	203.99	4.14	141.25	4.94	1564	R
8131	GeoB18116-2 P07 CC 15 cm	3.5165	0.0002	0.1889	0.0006	0.9373	0.0024	53326	230	79.42	0.90	209.34	1.72	209.32	1.72	143.50	1.78	1676	R
8288	GeoB18116-2 P08 53 cm	2.6841	0.0003	0.0034	0.0001	0.9354	0.0023	2277150	42639	78.80	1.53	208.53	1.80	208.53	1.81	142.07	2.85	1733	R
8289	GeoB18116-2 P08 88 cm	3.1722	0.0002	0.3180	0.0008	0.9283	0.0020	28339	92	79.74	0.65	203.45	1.28	203.43	1.32	141.70	1.27	1768	R
8290	GeoB18116-2 P08 216 cm	2.9356	0.0002	-0.0040	0.0000	0.9338	0.0023	-2107874	-22999	81.63	0.62	205.59	1.48	205.59	1.54	145.94	1.27	1896	R
8291	GeoB18116-2 P08 CC 16 cm	3.3620	0.0002	0.2967	0.0008	0.9306	0.0017	32308	106	84.35	0.66	201.87	1.12	201.85	1.09	149.22	1.26	1914	R
8333	GeoB18116-2 P09 143 cm	3.7626	0.0001	0.1477	0.0006	0.9504	0.0018	73472	326	77.27	0.64	219.80	1.36	219.79	1.38	143.82	1.32	2058	R
8125	GeoB18116-2 P09 CC 9 cm	3.2939	0.0001	0.4525	0.0015	0.8759	0.0022	19439	82	86.61	1.03	171.89	1.06	171.86	1.08	140.78	1.73	2142	R
8292	GeoB18116-2 P10 2 cm	3.0513	0.0002	0.0783	0.0004	0.9679	0.0024	115394	672	76.08	0.93	234.18	2.14	234.17	2.16	147.47	2.01	2152	R
8393	GeoB18116-2 P10 29 cm	3.7620	0.0002	0.2100	0.0007	0.9581	0.0026	52413	234	76.25	1.01	226.30	2.18	226.29	2.16	144.55	2.11	2179	R
8394	GeoB18116-2 P10 58 cm	3.4780	0.0001	0.1388	0.0004	0.9627	0.0022	73693	254	74.81	0.63	231.13	1.85	231.12	1.91	143.76	1.44	2209	R
8395	GeoB18116-2 P10 105 cm	3.3528	0.0002	0.5298	0.0013	0.9543	0.0024	18439	66	77.50	0.96	222.44	1.93	222.40	1.92	145.30	1.96	2255	R
8396	GeoB18116-2 P10 126 cm	3.6931	0.0001	0.2816	0.0007	0.9497	0.0022	38005	131	76.21	0.73	220.13	1.69	220.11	1.68	141.96	1.52	2276	R
8397	GeoB18116-2 P10 151 cm	3.4737	0.0001	0.4056	0.0009	0.9309	0.0024	24328	84	78.13	0.70	206.12	1.59	206.09	1.61	139.89	1.41	2301	R
8399	GeoB18116-2 P11 144 cm	3.1084	0.0001	0.1539	0.0006	0.9938	0.0027	61281	287	69.81	0.83	265.03	3.06	265.02	3.05	147.65	2.18	2529	R
8129	GeoB18116-2 P11 164 cm	3.3845	0.0002	0.1257	0.0005	1.0036	0.0023	82522	378	70.77	0.72	274.79	2.69	274.78	2.83	153.87	1.99	2549	R
8334	GeoB18116-2 P11 200 cm	4.3004	0.0002	0.3753	0.0012	1.0070	0.0021	35068	136	66.74	0.67	284.91	3.04	284.89	3.01	149.31	1.96	2585	R
8146	GeoB18116-2 P11 CC 11 cm	3.4363	0.0002	0.1350	0.0005	1.0103	0.0019	78498	315	64.94	0.67	292.13	2.90	292.12	2.93	148.27	1.96	2614	R
8142	GeoB18116-2 P12 112 cm	3.1399	0.0002	0.5239	0.0020	1.0168	0.0022	18635	84	62.03	0.85	307.15	3.97	307.11	3.89	147.75	2.60	2732	R
8335	GeoB18116-2 P13 39 cm	3.2315	0.0002	0.2249	0.0009	1.0247	0.0027	44779	212	63.71	0.86	316.70	4.93	316.68	4.86	155.93	3.01	2894	R
8087	GeoB18116-2 P13 113 cm	3.7576	0.0001	0.1374	0.0005	1.0164	0.0018	84588	334	65.52	0.48	299.83	2.77	299.82	2.78	152.90	1.65	2968	R
8293	GeoB18116-2 P13 163 cm	3.4278	0.0002	0.0021	0.0000	1.0250	0.0024	5066757	46714	62.28	0.52	320.23	4.44	320.23	4.31	153.96	2.28	3018	R
8132	GeoB18116-2 P13 CC 7 cm	4.0224	0.0002	1.2790	0.0025	0.9958	0.0019	9562	26	65.40	0.63	273.08	2.45	273.00	2.38	141.48	1.65	3082	R
8085	GeoB18116-2 P14 82 cm	3.7028	0.0001	0.1213	0.0004	1.0210	0.0017	95070	363	61.53	0.63	314.91	3.24	314.90	3.26	149.84	2.06	3172	R
8141	GeoB18116-2 P14 155 cm	3.0717	0.0002	0.4118	0.0008	0.9922	0.0017	22594	61	67.80	0.71	265.87	2.06	265.83	2.12	143.71	1.74	3245	R
8090	GeoB18116-2 P14 190 cm	3.7108	0.0001	0.1896	0.0006	1.0171	0.0025	60668	236	63.16	0.65	305.28	4.16	305.27	4.25	149.68	2.36	3280	R
8294	GeoB18116-2 P14 CC 16 cm	3.8167	0.0002	0.1046	0.0006	1.0203	0.0026	113824	718	62.76	0.56	311.20	4.35	311.20	4.39	151.23	2.31	3324	R
8295	GeoB18116-2 P15 26 cm	3.3090	0.0001	0.0408	0.0003	1.0219	0.0018	253553	1930	63.46	0.60	312.44	3.24	312.44	3.28	153.46	2.04	3351	R
8296	GeoB18116-2 P15 86 cm	3.0360	0.0004	0.7361	0.0017	1.0171	0.0025	12845	43	64.93	0.83	301.94	3.99	301.88	4.01	152.40	2.60	3411	R
8137	GeoB18116-2 P15 200 cm	3.0252	0.0004	0.0971	0.0004	1.0210	0.0021	96871	422	60.66	0.78	316.89	4.11	316.89	4.13	148.54	2.59	3525	R
8297	GeoB18116-2 P16 8 cm	2.8670	0.0001	0.0315	0.0003	1.0230	0.0030	284623	3207	61.24	0.77	319.03	5.50	319.02	5.53	150.88	3.03	3568	R
8298	GeoB18116-2 P16 76 cm	3.2697	0.0002	-0.0558	0.0147	1.0214	0.0030	-182775	-48177	63.00	0.73	312.62	5.20	312.62	5.32	152.44	2.90	3636	R
8299	GeoB18116-2 P16 118 cm	3.3915	0.0002	0.2932	0.0009	1.0290	0.0026	36112	140	59.83	0.65	333.70	5.38	333.68	5.50	153.64	2.92	3678	R
8300	GeoB18116-2 P16 151 cm	3.0567	0.0002	0.1846	0.0005	1.0142	0.0023	51012	179	65.01	0.92	297.64	3.68	297.63	3.67	150.76	2.64	3711	R
8301	GeoB18116-2 P16 170 cm	3.4608	0.0002	0.3763	0.0011	1.0257	0.0023	28702	104	60.64	0.91	325.24	4.79	325.21	4.76	152.05	3.06	3730	R
8302	GeoB18116-2 P16 206 cm	3.0131	0.0002	0.0764	0.0005	1.0187	0.0033	122334	881	61.46	4.53	311.23	10.90	311.22	11.03	148.12	11.86	3766	R
8303	GeoB18116-2 P16 CC 14 cm	3.4346	0.0002	0.1283	0.0005	1.0168	0.0024	82766	363	61.70	0.98	307.70	4.31	307.69	4.28	147.21	2.94	3792	R
8277	GeoB18116-2 P17 9 cm	3.2722	0.0001	0.0738	0.0004	1.0228	0.0024	138377	902	60.89	0.68	319.55	4.53	319.54	4.46	150.23	2.54	3804	R
8084	GeoB18116-2 P18 2 cm	3.7244	0.0001	0.1766	0.0007	1.0240	0.0021	65782	302	62.22	0.70	318.59	3.88	318.58	3.89	153.09	2.40	4032	R
8272	GeoB18116-2 P18 7 cm	3.0508	0.0001	-0.1098	0.0014	1.0284	0.0027	-87218	-1107	61.42	0.71	328.50	5.47	328.51	5.44	155.43	3.00	4037	R

Lab.No.	Sample Name	^{238}U (µg/g)	2σ (µg/g)	^{232}Th (ng/g)	2σ (ng/g)	$^{230}Th/^{238}U$ AR	2σ AR	$^{230}Th/^{232}Th$ AR	2σ AR	$\delta^{234}U$ (‰)	2σ (‰)	Age uncor. (ka)	2σ (ka)	U/Th Age (ka)	2σ (ka)	$\delta^{234}U_i$ (‰)	2σ (‰)	Depth (cm)	QC
8127	GeoB18116-2 P18 71 cm	3.8353	0.0002	0.5128	0.0011	1.0282	0.0020	23477	67	55.41	0.55	343.89	4.67	343.86	4.80	146.44	2.47	4101	R
8273	GeoB18116-2 P18 100 cm	2.8904	0.0001	0.7310	0.0015	1.0284	0.0020	12409	35	56.80	0.71	340.59	4.70	340.53	4.62	148.71	2.69	4130	R
8274	GeoB18116-2 P18 134 cm	2.8849	0.0001	0.1822	0.0008	1.0304	0.0023	49803	254	54.24	0.91	352.61	6.15	352.59	6.12	146.92	3.54	4164	R
8275	GeoB18116-2 P18 181 cm	2.7246	0.0001	-0.0915	0.0026	1.0322	0.0023	-93807	-2714	54.11	0.76	357.25	6.34	357.26	6.50	148.53	3.44	4211	R
8276	GeoB18116-2 P18 CC 15 cm	2.8123	0.0001	0.0264	0.0003	1.0215	0.0025	332461	3575	57.92	0.93	323.83	5.33	323.82	5.11	144.64	3.13	4263	R
8267	GeoB18116-2 P19 41 cm	2.3946	0.0001	0.4812	0.0013	1.0418	0.0030	15845	63	55.06	1.00	380.36	10.19	380.31	10.29	161.32	5.52	4306	R
8268	GeoB18116-2 P19 115 cm	3.2184	0.0001	0.1211	0.0005	1.0327	0.0026	83721	411	56.95	0.63	349.68	6.38	349.67	6.12	153.00	3.15	4380	R
8269	GeoB18116-2 P19 150 cm	3.7922	0.0003	0.0411	0.0005	1.0357	0.0028	291465	3619	52.12	0.59	373.76	8.25	373.75	8.49	149.88	3.97	4415	R
8081	GeoB18116-2 P19 188 cm	3.9817	0.0002	0.1035	0.0006	1.0364	0.0024	121519	760	55.84	0.74	362.23	6.73	362.22	6.61	155.44	3.56	4453	R
8270	GeoB18116-2 P19 221 cm	3.5335	0.0002	0.8716	0.0018	1.0352	0.0021	12819	37	57.24	0.80	354.64	5.58	354.58	5.60	155.92	3.29	4480	R
8271	GeoB18116-2 P19 CC 1.5 cm	3.4419	0.0009	0.3464	0.0009	1.0197	0.0029	30976	122	65.17	1.68	305.46	5.74	305.43	5.47	154.50	4.65	4487	R
8260	GeoB18116-2 P21 109 cm	3.1802	0.0003	0.2444	0.0007	1.0308	0.0025	40715	148	55.70	0.89	348.95	6.44	348.93	6.46	149.32	3.63	4844	R
8261	GeoB18116-2 P21 163 cm	3.6490	0.0002	0.1008	0.0018	1.0347	0.0027	114232	2106	55.59	0.98	358.90	7.55	358.90	7.55	153.30	4.25	4898	R
8262	GeoB18116-2 P21 CC 3 cm	3.6660	0.0002	0.3735	0.0011	1.0200	0.0024	30628	113	58.36	0.61	320.13	4.41	320.10	4.46	144.23	2.37	4957	R
8144	GeoB18116-2 P21 224 cm	3.4211	0.0001	0.1767	0.0006	1.0340	0.0021	61077	251	53.35	0.57	364.49	5.82	364.47	5.98	149.44	2.99	4959	R
8257	GeoB18116-2 P22 3 cm	3.4525	0.0003	0.2862	0.0008	1.0245	0.0034	37599	165	55.66	2.24	335.37	9.12	335.35	9.00	143.59	6.84	4973	R
8139	GeoB18116-2 P22 120 cm	2.7867	0.0007	0.1447	0.0005	1.0343	0.0026	60670	241	52.85	2.06	367.05	10.49	367.03	10.45	149.12	7.29	5090	R
8133	GeoB18116-2 P22 212 cm	3.1865	0.0002	0.1813	0.0006	1.0372	0.0023	55357	218	42.43	0.72	426.73	11.94	426.71	12.05	141.71	5.39	5182	R
8254	GeoB18116-2 P23 7 cm	3.8676	0.0002	0.2240	0.0007	1.0291	0.0022	54035	204	52.64	0.78	354.30	5.96	354.28	6.01	143.28	3.22	5212	R
8138	GeoB18116-2 P23 55 cm	2.8123	0.0002	0.0977	0.0003	1.0296	0.0020	90174	354	51.08	0.81	360.70	5.81	360.69	5.86	141.57	3.25	5260	R
8255	GeoB18116-2 P23 110 cm	2.9597	0.0001	0.0536	0.0003	1.0404	0.0022	174784	1071	52.57	0.69	386.50	7.83	386.50	7.95	156.74	4.08	5315	R
8256	GeoB18116-2 P23 152 cm	3.1559	0.0001	0.3711	0.0010	1.0229	0.0023	26452	93	54.02	0.77	336.35	5.22	336.32	5.22	139.76	2.87	5357	R
8136	GeoB18116-2 P23 204 cm	3.4945	0.0001	0.2057	0.0006	1.0294	0.0018	53352	184	50.84	0.64	361.04	5.30	361.03	5.35	141.03	2.77	5409	R
8145	GeoB18116-2 P23 CC 14 cm	2.7234	0.0001	0.2264	0.0006	1.0097	0.0022	37103	131	57.24	0.72	305.29	3.75	305.27	3.66	135.65	2.22	5439	R
8082	GeoB18116-2 P24 29 cm	3.1616	0.0001	0.1783	0.0006	1.0268	0.0022	55533	230	51.32	0.67	352.81	5.86	352.80	5.65	139.09	2.87	5469	R
8250	GeoB18116-2 P24 73 cm	3.1899	0.0001	4.6430	0.0101	1.0367	0.0026	2165	7	55.40	1.03	364.50	7.78	364.14	7.83	155.05	4.48	5513	R
8251	GeoB18116-2 P24 141 cm	3.1865	0.0001	0.8871	0.0024	1.0169	0.0026	11087	41	58.64	3.81	314.11	9.27	314.04	9.13	142.45	9.97	5581	R
8249	GeoB18116-2 P25 177 cm	2.7893	0.0001	0.0365	0.0003	1.0385	0.0028	240967	2080	50.09	0.94	390.87	10.64	390.87	10.12	151.19	5.17	5852	R
8089	GeoB18116-2 P25 227 cm	3.4856	0.0002	0.2621	0.0012	1.0297	0.0027	41774	217	51.34	1.06	360.05	7.84	360.03	7.74	142.02	4.27	5902	R
8244	GeoB18116-2 P26 88 cm	3.3858	0.0001	1.0237	0.0020	1.0325	0.0022	10375	31	50.02	0.82	372.61	7.12	372.53	7.17	143.35	3.74	5998	R
8147	GeoB18116-2 noDepth	3.2210	0.0004	0.2407	0.0005	0.9047	0.0013	36945	96	80.40	0.85	189.36	0.84	189.34	0.82	137.29	1.48	X	R
8331	GeoB18116-2 P06-2 175 cm	0.1320	-0.3876			332752.8818		-114372				Out of range	noValue		0.00	noValue	noValue	1385	nR
8135	GeoB18116-2 P08-2 176 cm	4.0140	0.0005	0.4867	0.0040	0.8965	0.0042	22482	214	75.53	4.33	187.59	3.37	187.56	3.20	128.34	7.44	1856	nR
8398	GeoB18116-2 P10-1 191 cm	3.4652	0.0001	0.6453	0.0018	0.7997	0.0018	13111	48	90.77	0.96	139.98	0.70	139.93	0.68	134.81	1.46	2341	nR
8088	GeoB18116-2 P13-2 125 cm	4.9771	0.0003	0.3641	0.0007	1.0465	0.0020	43573	120	70.20	0.67	342.46	4.63	342.44	4.71	184.79	3.02	2980	nR
8263	GeoB18116-2 P20-1 12 cm	2.8906	0.0002	0.0269	0.0004	1.0330	0.0022	339526	5139	70.46	0.76	316.44	4.02	316.44	4.02	172.33	2.70	4512	nR
8264	GeoB18116-2 P20-1 94 cm	2.9009	0.0001	0.2059	0.0008	1.0611	0.0024	45657	198	55.70	0.81	458.14	16.40	458.12	16.93	203.32	10.16	4594	nR
8134	GeoB18116-2 P20-1 118 cm	3.3781	0.0006	0.4068	0.0045	1.0543	0.0056	26439	325	51.53	6.63	451.97	noValue	451.94	124.84	184.83	69.42	4618	nR
8124	GeoB18116-2 P20-2 124 cm	2.8404	0.0001	0.1517	0.0005	1.0721	0.0025	61200	261	60.80	0.96	485.08	21.40	485.06	22.14	239.50	15.46	4624	nR
8265	GeoB18116-2 P20-2 174 cm	3.4240	0.0001	0.1957	0.0008	1.0463	0.0027	55873	266	66.14	0.62	353.74	6.62	353.72	6.61	179.74	3.76	4674	nR

Lab.No.	Sample Name	^{238}U (µg/g)	2σ (µg/g)	^{232}Th (ng/g)	2σ (ng/g)	$^{230}Th/^{238}U$ AR	2σ AR	$^{230}Th/^{232}Th$ AR	2σ AR	$\delta^{234}U$ (‰)	2σ (‰)	Age uncor. (ka)	2σ (ka)	U/Th Age (ka)	2σ (ka)	$\delta^{234}U_i$ (‰)	2σ (‰)	Depth (cm)	QC
8266	GeoB18116-2 P20-2 208 cm	2.3539	0.0001	0.1638	0.0007	1.0651	0.0020	46764	226	74.77	1.11	373.00	6.57	372.98	6.51	214.56	5.08	4708	nR
8126	GeoB18116-2 P20 CC 11 cm	3.5047	0.0001	0.1819	0.0006	1.0289	0.0023	60414	241	65.16	0.65	320.76	4.36	320.75	4.37	161.31	2.56	4746	nR
8130	GeoB18116-2 P21-1 37 cm	3.0484	0.0001	0.3204	0.0008	1.0396	0.0019	30234	92	59.55	0.92	358.30	5.70	358.27	5.66	163.93	3.65	4772	nR
8259	GeoB18116-2 P21-1 51 cm	2.9955	0.0003	0.6309	0.0020	1.0391	0.0025	14966	60	61.93	1.17	349.71	6.91	349.66	6.60	166.36	4.41	4786	nR
8258	GeoB18116-2 P22-1 83 cm	2.1100	0.0002	0.0426	0.0004	1.0041	0.0027	150955	1349	55.32	2.23	300.19	5.95	300.19	6.02	129.23	5.65	5053	nR
8252	GeoB18116-2 P24-2 115 cm	3.3820	0.0001	3.5110	0.0079	0.9910	0.0024	2896	9	55.58	0.80	281.65	3.27	281.38	3.28	123.11	2.11	5665	nR
8253	GeoB18116-2 P24CC 15 cm	3.7216	0.0002	2.3342	0.0048	0.9868	0.0024	4781	15	53.35	0.76	279.62	3.24	279.46	3.18	117.54	1.97	5674	nR
8246	GeoB18116-2 P25-1 47 cm	3.0614	0.0001	5.1226	0.0109	0.9891	0.0022	1797	6	54.94	0.98	280.09	3.20	279.67	3.17	121.11	2.42	5722	nR
8247	GeoB18116-2 P25-1 91 cm	3.3841	0.0001	1.8022	0.0056	0.9963	0.0027	5688	23	57.14	0.95	285.98	3.90	285.85	3.84	128.18	2.55	5766	nR
8248	GeoB18116-2 P25-1 103 cm	3.0432	0.0002	0.4726	0.0016	1.0053	0.0024	19680	83	53.96	1.16	304.67	4.28	304.64	4.36	127.63	3.16	5778	nR
8128	GeoB18116-2 P25-2 122 cm	3.0330	0.0001	0.6389	0.0013	0.9801	0.0019	14216	40	59.40	1.04	263.42	2.50	263.37	2.53	125.04	2.37	5797	nR
8243	GeoB18116-2 P26-1 70 cm	3.3087	0.0002	2.0154	0.0041	1.0497	0.0025	5239	16	50.26	0.85	436.49	14.04	436.34	14.36	172.49	7.58	5980	nR
8245	GeoB18116-2 P26-2 192 cm	2.7156	0.0001	17.2623	0.0333	0.8165	0.0018	390	1	58.93	1.02	157.13	0.84	155.45	1.16	91.44	1.60	6102	nR

Table 4.2: Li/Mg temperature proxy results from three EMCP cores: GeoB18118-1, GeoB18118-2 and GeoB18116-2. Two cores from the WMCP are included as well: GeoB18127-1 and GeoB18130-1. “T (Mon)”= Temperature after Montagna et al. 2014; “T (Cun)”= Temperature after Cuny-G et al. 2019. Concentrations of Li and Mg correspond to concentrations in sample solution.

Lab.Nr.	Sample Name	[Li] (pg/ml)	σ (pg/ml)	[Mg] (ng/ml)	σ (ng/ml)	Li/Mg uncor. (mg/g)	σ (mg/g)	Li/Mg uncor. (mmol/mol)	σ (mmol/mol)	Li/Mg cor. (mmol/mol)	σ (mmol/mol)	T (Mon) [°C]	int. 2σ [°C]	T (Cun) [°C]	int. 2σ [°C]	ext. 2σ [°C]	Age (ka)	2σ (ka)
8069	GeoB18118-1 0-86 15 cm	17.75	0.27	20.46	0.12	0.87	0.01	3.04	0.05	3.05	0.05	11.72	0.58	11.58	0.46	1.0	8.48	0.04
8063	GeoB18118-1 0-86 1 cm	16.13	0.17	18.59	0.05	0.87	0.01	3.04	0.03	3.05	0.03	11.71	0.53	11.58	0.38	1.0	8.61	0.04
8096	GeoB18118-1 0-86 2.5 cm	15.54	0.19	18.14	0.07	0.86	0.01	3.00	0.04	3.00	0.04	12.01	0.55	11.89	0.41	1.0	8.84	0.03
8092	GeoB18118-1 0-86 2 cm	16.19	0.19	18.76	0.01	0.86	0.01	3.02	0.04	3.03	0.04	11.86	0.54	11.73	0.40	1.0	8.85	0.12
8102	GeoB18118-1 0-86 3 cm	15.96	0.18	17.29	0.01	0.92	0.01	3.23	0.04	3.23	0.04	10.50	0.49	10.28	0.38	1.0	8.98	0.03
8076	GeoB18118-1 0-86 7 cm	14.63	0.11	15.55	0.05	0.94	0.01	3.30	0.03	3.31	0.03	10.05	0.44	9.81	0.33	1.0	9.16	0.02
8065	GeoB18118-1 0-86 41 cm	16.14	0.29	17.33	0.06	0.93	0.02	3.26	0.06	3.27	0.06	10.27	0.56	10.04	0.48	1.0	9.17	0.03
8367	GeoB18118-1 0-86 35 cm	13.01	0.21	15.67	0.01	0.83	0.01	2.91	0.05	2.88	0.05	12.89	0.62	12.82	0.48	1.0	9.21	0.04
8368	GeoB18118-1 0-86 52 cm	13.57	0.19	15.70	0.01	0.86	0.01	3.03	0.04	3.00	0.04	12.07	0.57	11.95	0.43	1.0	9.33	0.03
8369	GeoB18118-1 0-86 50 cm	15.10	0.19	17.57	0.02	0.86	0.01	3.01	0.04	2.98	0.04	12.18	0.56	12.07	0.41	1.0	9.35	0.04
8067	GeoB18118-1 0-86 65 cm	14.91	0.29	18.01	0.08	0.83	0.02	2.90	0.06	2.91	0.06	12.68	0.66	12.60	0.54	1.0	9.47	0.04
8098	GeoB18118-1 86-186 4 cm	17.58	0.18	19.82	0.08	0.89	0.01	3.11	0.03	3.11	0.03	11.30	0.51	11.13	0.38	1.0	9.50	0.03
8370	GeoB18118-1 86-186 15 cm	16.12	0.23	18.37	0.02	0.88	0.01	3.07	0.04	3.04	0.04	11.75	0.56	11.61	0.44	1.0	9.55	0.03
8066	GeoB18118-1 0-86 82 cm	16.64	0.21	18.79	0.08	0.89	0.01	3.10	0.04	3.11	0.04	11.29	0.54	11.12	0.41	1.0	9.56	0.03
8371	GeoB18118-1 86-186 50 cm	16.19	0.24	17.63	0.00	0.92	0.01	3.22	0.05	3.18	0.05	10.83	0.53	10.63	0.43	1.0	9.69	0.04
8064	GeoB18118-1 86-186 65 cm	14.98	0.13	17.84	0.05	0.84	0.01	2.94	0.03	2.95	0.03	12.38	0.54	12.28	0.37	1.0	9.77	0.03
8077	GeoB18118-1 86-186 80 cm	15.45	0.21	17.89	0.11	0.86	0.01	3.02	0.04	3.03	0.04	11.81	0.57	11.68	0.44	1.0	9.81	0.03
8100	GeoB18118-1 86-186 93 cm	15.47	0.13	18.14	0.03	0.85	0.01	2.99	0.02	2.99	0.02	12.10	0.52	11.98	0.36	1.0	9.86	0.04
8078	GeoB18118-1 186-286 45 cm	19.19	0.18	19.35	0.09	0.99	0.01	3.47	0.04	3.48	0.04	8.99	0.42	8.67	0.34	1.0	10.00	0.07
8373	GeoB18118-1 186-286 68 cm	14.77	0.14	16.49	0.00	0.90	0.01	3.14	0.03	3.11	0.03	11.33	0.50	11.16	0.36	1.0	10.43	0.04
8375	GeoB18118-1 186-286 80 cm	14.63	0.19	16.37	0.01	0.89	0.01	3.13	0.04	3.10	0.04	11.39	0.54	11.23	0.41	1.0	10.65	0.07
8372	GeoB18118-1 186-286 60 cm	16.33	0.23	17.69	0.00	0.92	0.01	3.23	0.05	3.20	0.05	10.72	0.53	10.51	0.42	1.0	10.75	0.03
8099	GeoB18118-1 186-286 92 cm	18.08	0.13	18.83	0.01	0.96	0.01	3.36	0.02	3.37	0.02	9.68	0.42	9.41	0.31	1.0	11.15	0.03
8062	GeoB18118-1 286-386 2 cm	17.78	0.20	17.71	0.04	1.00	0.01	3.52	0.04	3.53	0.04	8.74	0.43	8.40	0.35	1.0	11.43	0.04
8071	GeoB18118-1 286-386 55 cm	19.55	0.11	16.83	0.05	1.16	0.01	4.07	0.03	4.08	0.03	5.77	0.27	5.24	0.25	1.0	11.58	0.04
8377	GeoB18118-1 286-386 67 cm	15.91	0.20	16.33	0.02	0.97	0.01	3.41	0.04	3.38	0.04	9.62	0.47	9.34	0.38	1.0	12.48	0.04
8061	GeoB18118-1 386-487 1 cm	19.32	0.26	17.71	0.04	1.09	0.01	3.82	0.05	3.83	0.05	7.05	0.40	6.60	0.37	1.0	12.73	0.30
8378	GeoB18118-1 286-386 72 cm	16.77	0.16	16.24	0.03	1.03	0.01	3.61	0.03	3.58	0.03	8.44	0.40	8.09	0.32	1.0	12.87	0.05
8376	GeoB18118-1 286-386 61 cm	14.82	0.15	15.57	0.01	0.95	0.01	3.33	0.03	3.30	0.03	10.09	0.46	9.85	0.35	1.0	12.92	0.05
8379	GeoB18118-1 286-386 78 cm	17.92	0.28	18.08	0.02	0.99	0.02	3.47	0.05	3.43	0.05	9.27	0.49	8.98	0.42	1.0	13.06	0.04
8381	GeoB18118-1 286-386 92 cm	15.32	0.11	16.30	0.03	0.94	0.01	3.29	0.03	3.26	0.02	10.36	0.45	10.14	0.32	1.0	13.07	0.05
8380	GeoB18118-1 286-386 84 cm	17.65	0.23	16.92	0.01	1.04	0.01	3.65	0.05	3.62	0.05	8.23	0.43	7.86	0.37	1.0	13.09	0.06
8097	GeoB18118-1 286-386 99 cm	21.47	0.35	19.82	0.05	1.08	0.02	3.79	0.06	3.80	0.06	7.23	0.45	6.79	0.42	1.0	13.23	0.06
8104	GeoB18118-1 386-487 65 cm	18.20	0.20	17.09	0.01	1.06	0.01	3.73	0.04	3.73	0.04	7.58	0.38	7.17	0.33	1.0	13.31	0.05
8073	GeoB18118-1 487-587 100 cm	20.89	0.24	19.36	0.09	1.08	0.01	3.78	0.05	3.79	0.05	7.27	0.39	6.84	0.35	1.0	13.31	0.07
8093	GeoB18118-1 487-587 6 cm	21.77	0.14	19.23	0.07	1.13	0.01	3.96	0.03	3.97	0.03	6.32	0.30	5.83	0.27	1.0	13.37	0.05
8384	GeoB18118-1 487-587 93 cm	25.94	0.28	16.18	0.04	1.60	0.02	5.61	0.06	5.55	0.06	-0.54	0.22	-1.47	0.29	1.0	13.39	0.03
8095	GeoB18118-1 386-487 88 cm	18.65	0.31	17.92	0.06	1.04	0.02	3.64	0.06	3.65	0.06	8.04	0.47	7.66	0.43	1.0	13.40	0.04
8072	GeoB18118-1 587-687 3 cm	16.67	0.31	15.01	0.07	1.11	0.02	3.89	0.07	3.90	0.07	6.69	0.47	6.22	0.47	1.0	13.51	0.05
8070	GeoB18118-1 487-587 24 cm	14.83	0.06	15.40	0.02	0.96	0.00	3.37	0.01	3.28	0.01	10.18	0.42	9.94	0.29	1.0	13.69	0.05
8383	GeoB18118-1 487-587 55 cm	16.43	0.13	16.55	0.01	0.99	0.01	3.48	0.03	3.44	0.03	9.23	0.41	8.93	0.31	1.0	13.72	0.05
8385	GeoB18118-1 587-687 18 cm	16.66	0.22	16.72	0.01	1.00	0.01	3.49	0.05	3.45	0.05	9.17	0.46	8.87	0.38	1.0	13.80	0.06
8382	GeoB18118-1 487-587 20 cm	20.37	0.21	18.30	0.03	1.11	0.01	3.90	0.04	3.86	0.04	6.90	0.35	6.44	0.32	1.0	13.97	0.06

Lab.Nr.	Sample Name	[Li] (pg/ml)	σ (pg/ml)	[Mg] (ng/ml)	σ (ng/ml)	Li/Mg uncor. (mg/g)	σ (mg/g)	Li/Mg uncor. (mmol/mol)	σ (mmol/mol)	Li/Mg cor. (mmol/mol)	σ (mmol/mol)	T (Mon) [°C]	int. 2σ [°C]	T (Cun) [°C]	int. 2σ [°C]	ext. 2σ [°C]	Age (ka)	2σ (ka)
8094	GeoB18118-1 487-587 80 cm	20.39	0.38	20.09	0.03	1.01	0.02	3.55	0.07	3.56	0.07	8.55	0.52	8.21	0.47	1.0	14.13	0.04
8103	GeoB18118-1 587-687 92 cm	16.58	0.33	16.77	0.00	0.99	0.02	3.46	0.07	3.47	0.07	9.09	0.55	8.78	0.50	1.0	14.16	0.04
8387	GeoB18118-1 587-687 72 cm	17.07	0.13	16.97	0.01	1.01	0.01	3.52	0.03	3.49	0.03	8.97	0.40	8.65	0.30	1.0	14.23	0.05
8386	GeoB18118-1 587-687 55 cm	18.94	0.31	18.05	0.04	1.05	0.02	3.67	0.06	3.64	0.06	8.11	0.47	7.73	0.43	1.0	14.29	0.05
8080	GeoB18118-1 687-787 5 cm	18.14	0.24	18.01	0.01	1.01	0.01	3.53	0.05	3.54	0.05	8.68	0.44	8.34	0.38	1.0	14.38	0.04
8101	GeoB18118-1 687-787 50 cm	18.91	0.13	17.67	0.02	1.07	0.01	3.75	0.03	3.75	0.03	7.47	0.34	7.05	0.27	1.0	14.47	0.05
8074	GeoB18118-1 787-873 1 cm	19.58	0.20	19.17	0.14	1.02	0.01	3.58	0.04	3.59	0.04	8.38	0.43	8.03	0.36	1.0	14.48	0.05
8075	GeoB18118-1 587-687 62 cm	18.61	0.23	17.44	0.05	1.07	0.01	3.74	0.05	3.75	0.05	7.50	0.40	7.08	0.36	1.0	14.49	0.05
8068	GeoB18118-1 687-787 92 cm	16.91	0.19	16.63	0.09	1.02	0.01	3.56	0.04	3.57	0.04	8.48	0.43	8.13	0.36	1.0	14.50	0.05
8390	GeoB18118-1 687-787 100 cm	18.68	0.22	17.35	0.00	1.08	0.01	3.77	0.04	3.66	0.04	7.96	0.40	7.58	0.35	1.0	14.54	0.05
8079	GeoB18118-1 787-873 30 cm	19.93	0.15	19.46	0.05	1.02	0.01	3.59	0.03	3.60	0.03	8.33	0.38	7.97	0.29	1.0	14.63	0.04
8388	GeoB18118-1 687-787 30 cm	17.64	0.26	17.19	0.00	1.03	0.02	3.59	0.05	3.56	0.05	8.57	0.46	8.23	0.41	1.0	14.74	0.08
8389	GeoB18118-1 687-787 78 cm	18.62	0.22	16.56	0.02	1.12	0.01	3.94	0.05	3.90	0.05	6.70	0.36	6.24	0.33	1.0	14.79	0.06
8091	GeoB18118-1 787-873 83 cm	21.10	0.13	17.53	0.03	1.20	0.01	4.21	0.03	4.22	0.03	5.07	0.25	4.50	0.24	1.0	14.96	0.04
8392	GeoB18118-1 787-873 80 cm	18.24	0.14	16.74	0.02	1.09	0.01	3.82	0.03	3.71	0.03	7.72	0.35	7.32	0.28	1.0	15.12	0.06
7626	GeoB18118-2 P02 31 cm	22.42	0.24	23.58	0.59	0.95	0.03	3.33	0.09	3.70	0.10	7.77	0.64	7.37	0.63	1.00	10.29	0.02
7622	GeoB18118-2 P02 CC Top	17.32	0.15	23.47	0.65	0.74	0.02	2.58	0.07	2.87	0.08	12.94	0.79	12.88	0.71	1.00	10.36	0.02
7614	GeoB18118-2 P03 33 cm	17.44	0.35	23.79	0.73	0.73	0.03	2.57	0.09	2.85	0.10	13.07	0.92	13.02	0.86	1.00	10.91	0.04
7617	GeoB18118-2 P03 24 cm	17.31	0.17	22.04	0.63	0.79	0.02	2.75	0.08	3.05	0.09	11.67	0.78	11.53	0.73	1.00	11.07	0.03
7616	GeoB18118-2 P03 65 cm	14.78	0.23	18.55	0.73	0.80	0.03	2.79	0.12	3.10	0.13	11.38	0.99	11.22	0.97	1.00	11.10	0.02
7615	GeoB18118-2 P03 113 cm	16.19	0.29	20.66	1.03	0.78	0.04	2.74	0.15	3.05	0.16	11.72	1.18	11.58	1.19	1.19	11.59	0.03
7619	GeoB18118-2 P03 232 cm	22.91	0.33	20.50	0.63	1.12	0.04	3.91	0.13	4.35	0.15	4.47	0.71	3.86	0.76	1.00	11.88	0.03
7608	GeoB18118-2 P04 CC	20.18	0.30	26.19	0.59	0.77	0.02	2.70	0.07	3.00	0.08	12.07	0.74	11.95	0.66	1.00	13.12	0.04
7610	GeoB18118-2 P04 9 cm	17.43	0.20	19.69	0.66	0.89	0.03	3.10	0.11	3.44	0.12	9.22	0.81	8.92	0.81	1.00	13.22	0.04
7089	GeoB18118-2 P05 10 cm	22.46	0.28	19.22	0.08	1.17	0.02	4.09	0.05	3.44	0.05	9.23	0.46	8.93	0.39	1.00	14.21	0.21
7609	GeoB18118-2 P05 3 cm	19.68	0.28	23.50	0.63	0.84	0.03	2.93	0.09	3.26	0.10	10.36	0.75	10.14	0.72	1.00	14.57	0.08
8364	GeoB18118-2 P05 CC	16.42	0.21	15.98	0.02	1.03	0.01	3.60	0.05	3.56	0.05	8.54	0.44	8.20	0.38	1.00	14.64	0.05
7611	GeoB18118-2 P05 CC	20.48	0.29	21.44	0.58	0.96	0.03	3.34	0.10	3.71	0.11	7.68	0.70	7.28	0.70	1.00	14.71	0.04
7857	GeoB18118-2 P06 91 cm	18.96	0.24	19.76	0.05	0.96	0.01	3.36	0.04	3.78	0.05	7.30	0.40	6.87	0.36	1.00	78.45	0.29
7094	GeoB18118-2 P06 200 cm	23.59	0.37	17.31	0.03	1.36	0.02	4.77	0.07	4.01	0.06	6.10	0.41	5.60	0.40	1.00	142.51	1.14
7086	GeoB18118-2 P06 111 cm	27.28	0.24	18.63	0.04	1.46	0.01	5.13	0.05	4.31	0.04	4.63	0.26	4.03	0.27	1.00	145.65	2.99
7084	GeoB18118-2 P07 84 cm	20.76	0.23	17.53	0.03	1.18	0.01	4.15	0.05	3.49	0.04	8.96	0.43	8.64	0.35	1.00	178.95	2.52
7102	GeoB18118-2 P07 186 cm	19.43	0.24	17.08	0.01	1.14	0.01	3.98	0.05	3.35	0.04	9.79	0.47	9.53	0.38	1.00	196.72	3.20
7097	GeoB18118-2 P08 CC	18.83	0.26	15.58	0.01	1.21	0.02	4.23	0.06	3.56	0.05	8.55	0.45	8.20	0.38	1.00	210.73	2.74
7080	GeoB18118-2 P09 CC	22.75	0.35	19.59	0.05	1.16	0.02	4.07	0.06	3.42	0.05	9.36	0.50	9.06	0.43	1.00	214.63	6.68
7081	GeoB18118-2 P11 91 cm	20.34	0.55	16.97	0.00	1.20	0.03	4.20	0.11	3.53	0.10	8.71	0.66	8.38	0.64	1.00	218.93	6.49
7078	GeoB18118-2 P07 CC Bottom	21.65	0.28	18.54	0.04	1.17	0.02	4.09	0.05	3.46	0.04	9.11	0.46	8.80	0.38	1.00	224.18	20.36
7088	GeoB18118-2 P11 45 cm	18.78	0.23	16.00	0.05	1.17	0.01	4.11	0.05	3.45	0.04	9.15	0.45	8.85	0.37	1.00	226.91	5.98
7093	GeoB18118-2 P12 CC Top	19.95	0.30	18.04	0.00	1.11	0.02	3.87	0.06	3.26	0.05	10.36	0.52	10.13	0.43	1.00	227.41	3.83
7069	GeoB18118-2 P10 CC Bottom	20.87	0.42	18.88	0.14	1.11	0.02	3.87	0.08	3.28	0.07	10.23	0.60	10.00	0.54	1.00	230.91	3.27
7087	GeoB18118-2 P09 66 cm	21.77	0.16	18.23	0.04	1.19	0.01	4.18	0.03	3.51	0.03	8.80	0.39	8.47	0.30	1.00	242.05	4.13
7082	GeoB18118-2 P16 159 cm	20.42	0.26	18.33	0.02	1.11	0.01	3.90	0.05	3.28	0.04	10.21	0.49	9.97	0.39	1.00	286.51	4.71
7099	GeoB18118-2 P16 20 cm	19.67	0.17	17.70	0.00	1.11	0.01	3.89	0.03	3.27	0.03	10.27	0.45	10.03	0.33	1.00	307.52	7.06
7098	GeoB18118-2 P15 99 cm	25.35	0.37	19.92	0.05	1.27	0.02	4.46	0.07	3.75	0.05	7.49	0.43	7.08	0.39	1.00	307.76	7.30
7070	GeoB18118-2 P13 177 cm	19.87	0.27	17.10	0.06	1.16	0.02	4.07	0.06	3.44	0.05	9.21	0.47	8.91	0.40	1.00	308.08	4.58
7073	GeoB18118-2 P15 186 cm	21.34	0.21	18.65	0.03	1.14	0.01	4.01	0.04	3.39	0.03	9.53	0.44	9.25	0.34	1.00	308.88	6.41
8148	GeoB18118-2 P17-2 215 cm	15.29	0.15	18.72	0.00	0.82	0.01	2.86	0.03	3.18	0.03	10.85	0.49	10.66	0.36	1.00	319.53	4.46
7878	GeoB18118-2 P16 99 cm	15.13	0.24	18.25	0.01	0.83	0.01	2.90	0.05	3.27	0.05	10.29	0.53	10.06	0.44	1.00	321.58	3.52
7866	GeoB18118-2 P17 110 cm	14.57	0.31	18.69	0.02	0.78	0.02	2.73	0.06	3.13	0.07	11.17	0.63	11.00	0.55	1.00	321.61	4.89
7862	GeoB18118-2 P15 132 cm	16.43	0.24	18.62	0.09	0.88	0.01	3.09	0.05	3.48	0.05	9.02	0.49	8.70	0.42	1.00	321.86	4.33
7864	GeoB18118-2 P18 24 cm	14.11	0.20	17.86	0.05	0.79	0.01	2.77	0.04	3.17	0.05	10.89	0.53	10.70	0.43	1.00	326.94	3.39

Lab.Nr.	Sample Name	[Li] (pg/ml)	σ (pg/ml)	[Mg] (ng/ml)	σ (ng/ml)	Li/Mg uncor. (mg/g)	σ (mg/g)	Li/Mg uncor. (mmol/mol)	σ (mmol/mol)	Li/Mg cor. (mmol/mol)	σ (mmol/mol)	T (Mon) [°C]	int. 2σ [°C]	T (Cun) [°C]	int. 2σ [°C]	ext. 2σ [°C]	Age (ka)	2σ (ka)
7865	GeoB18118-2 P17 30 cm	15.18	0.07	18.71	0.01	0.81	0.00	2.84	0.01	3.20	0.01	10.72	0.45	10.52	0.30	1.00	327.88	3.28
7887	GeoB18118-2 P18 127 cm	15.10	0.08	18.60	0.02	0.81	0.00	2.84	0.02	3.25	0.02	10.37	0.44	10.15	0.30	1.00	365.95	5.33
7891	GeoB18118-2 P23 CC	14.98	0.33	18.22	0.04	0.82	0.02	2.88	0.06	3.30	0.07	10.10	0.61	9.86	0.55	1.00	376.13	5.21
7867	GeoB18118-2 P25 57 cm	15.37	0.16	18.78	0.06	0.82	0.01	2.87	0.03	3.23	0.03	10.55	0.48	10.34	0.36	1.00	387.36	7.64
7885	GeoB18118-2 P29 CC	13.74	0.20	17.45	0.02	0.79	0.01	2.76	0.04	3.16	0.05	10.99	0.54	10.81	0.42	1.00	431.54	10.76
7882	GeoB18118-2 P26 44 cm	14.31	0.16	16.76	0.02	0.85	0.01	2.99	0.03	3.43	0.04	9.33	0.44	9.03	0.35	1.00	442.79	17.53
7877	GeoB18118-2 P24 100 cm	15.05	0.25	20.07	0.06	0.75	0.01	2.63	0.04	3.01	0.05	11.96	0.59	11.84	0.47	1.00	456.44	11.99
7884	GeoB18118-2 P29 88 cm	15.60	0.15	18.38	0.05	0.85	0.01	2.97	0.03	3.41	0.03	9.43	0.44	9.15	0.34	1.00	482.04	19.84
7855	GeoB18118-2 P28 CC	14.71	0.27	17.45	0.04	0.84	0.02	2.95	0.06	3.32	0.06	9.95	0.56	9.69	0.49	1.00	482.75	14.10
7872	GeoB18118-2 P30 185 cm	14.11	0.13	18.19	0.02	0.78	0.01	2.72	0.02	3.06	0.03	11.64	0.51	11.49	0.36	1.00	538.23	28.06
8321	GeoB18116-2 P01-1 3 cm	17.05	0.18	16.78	0.04	1.02	0.01	3.56	0.04	3.47	0.04	9.08	0.43	8.77	0.35	1.00	102.76	0.46
8143	GeoB18116-2 P01-1 10 cm	16.48	0.18	18.42	0.01	0.89	0.01	3.13	0.03	3.48	0.04	9.00	0.43	8.68	0.35	1.00	108.13	0.46
8322	GeoB18116-2 P01-1 111 cm	15.77	0.10	15.64	0.01	1.01	0.01	3.53	0.02	3.44	0.02	9.23	0.40	8.93	0.29	1.00	111.12	0.41
8325	GeoB18116-2 P03-1 119 cm	17.86	0.10	17.80	0.00	1.00	0.01	3.51	0.02	3.42	0.02	9.34	0.40	9.04	0.29	1.00	112.61	0.40
8286	GeoB18116-2 P2-2 62 cm	15.98	0.15	16.55	0.01	0.97	0.01	3.38	0.03	3.27	0.03	10.26	0.46	10.02	0.34	1.00	113.29	0.59
8323	GeoB18116-2 P01-CC 2 cm	17.49	0.08	18.18	0.02	0.96	0.00	3.37	0.02	3.28	0.02	10.20	0.43	9.96	0.29	1.00	113.41	0.68
8285	GeoB18116-2 P2-2 35 cm	16.49	0.12	17.13	0.01	0.96	0.01	3.37	0.02	3.26	0.02	10.32	0.44	10.09	0.32	1.00	113.52	0.66
8083	GeoB18116-2 P03-1 36 cm	17.45	0.14	18.88	0.06	0.92	0.01	3.24	0.03	3.24	0.03	10.46	0.46	10.24	0.34	1.00	114.10	0.47
8324	GeoB18116-2 P02-1 78 cm	17.87	0.14	18.69	0.01	0.96	0.01	3.35	0.03	3.26	0.02	10.32	0.45	10.10	0.32	1.00	114.12	0.42
8327	GeoB18116-2 P04-2 190 cm	18.98	0.13	17.77	0.03	1.07	0.01	3.74	0.03	3.64	0.02	8.06	0.36	7.68	0.28	1.00	114.16	0.76
8086	GeoB18116-2 P01-2 73 cm	16.28	0.13	17.80	0.00	0.91	0.01	3.20	0.03	3.21	0.03	10.67	0.47	10.46	0.33	1.00	114.44	0.43
8328	GeoB18116-2 P05-1 48 cm	17.40	0.15	17.97	0.02	0.97	0.01	3.39	0.03	3.30	0.03	10.07	0.45	9.82	0.33	1.00	115.06	0.76
8287	GeoB18116-2 P04-2 154 cm	16.20	0.08	16.30	0.00	0.99	0.01	3.48	0.02	3.37	0.02	9.67	0.41	9.40	0.29	1.00	115.11	0.52
8125	GeoB18116-2 P09 CC 9 cm	17.38	0.17	17.21	0.03	1.01	0.01	3.54	0.03	3.39	0.03	9.56	0.44	9.28	0.34	1.00	171.86	1.08
8147	GeoB18116-2 no Depth	15.52	0.10	19.31	0.01	0.80	0.01	2.81	0.02	3.13	0.02	11.18	0.48	11.01	0.32	1.00	189.34	0.82
8291	GeoB18116-2 P08 CC 16 cm	18.39	0.19	19.09	0.03	0.96	0.01	3.37	0.04	3.27	0.03	10.30	0.47	10.07	0.36	1.00	201.85	1.09
8361	GeoB18116-2 P05-2 8-9 cm	15.97	0.15	15.69	0.00	1.02	0.01	3.57	0.03	3.53	0.03	8.72	0.41	8.39	0.32	1.00	202.05	1.25
8362	GeoB18116-2 P05-2 25 cm	16.39	0.24	15.38	0.02	1.07	0.02	3.73	0.06	3.69	0.06	7.79	0.44	7.40	0.40	1.00	202.10	1.27
8329	GeoB18116-2 P05-2 65 cm	20.03	0.13	17.48	0.03	1.15	0.01	4.01	0.03	3.91	0.03	6.63	0.30	6.16	0.26	1.00	203.42	3.61
8289	GeoB18116-2 P08-1 88 cm	16.39	0.05	17.25	0.01	0.95	0.00	3.33	0.01	3.22	0.01	10.59	0.44	10.37	0.29	1.00	203.43	1.32
8332	GeoB18116-2 P07-1 119 cm	20.08	0.17	15.85	0.02	1.27	0.01	4.44	0.04	4.32	0.04	4.58	0.26	3.98	0.26	1.00	203.99	4.14
8360	GeoB18116-2 P05-1 90 cm	15.87	0.18	15.63	0.02	1.01	0.01	3.55	0.04	3.52	0.04	8.79	0.43	8.46	0.35	1.00	204.67	1.46
8290	GeoB18116-2 P08-2 216 cm	16.96	0.13	17.86	0.02	0.95	0.01	3.33	0.03	3.22	0.03	10.60	0.46	10.39	0.33	1.00	205.59	1.54
8397	GeoB18116-2 P10-1 151 cm	16.48	0.31	15.29	0.01	1.08	0.02	3.77	0.07	3.67	0.07	7.94	0.50	7.56	0.47	1.00	206.09	1.61
8358	GeoB18116-2 P05-1 78.5 cm	16.61	0.18	15.55	0.01	1.07	0.01	3.74	0.04	3.70	0.04	7.74	0.39	7.34	0.33	1.00	206.15	1.44
8359	GeoB18116-2 P05-1 105 cm	15.75	0.23	15.80	0.01	1.00	0.01	3.49	0.05	3.45	0.05	9.16	0.48	8.85	0.41	1.00	206.42	1.56
8363	GeoB18116-2 P05-2 51 cm	16.29	0.20	16.40	0.00	0.99	0.01	3.48	0.04	3.44	0.04	9.23	0.46	8.93	0.37	1.00	208.22	1.54
8140	GeoB18116-2 P06-1 12 cm	20.26	0.22	22.21	0.00	0.91	0.01	3.19	0.03	3.55	0.04	8.61	0.42	8.27	0.34	1.00	208.42	1.13
8288	GeoB18116-2 P08-1 53 cm	18.28	0.12	19.03	0.02	0.96	0.01	3.36	0.02	3.26	0.02	10.36	0.44	10.14	0.31	1.00	208.53	1.81
8330	GeoB18116-2 P06-1 75 cm	17.57	0.11	16.59	0.01	1.06	0.01	3.71	0.02	3.61	0.02	8.23	0.36	7.87	0.28	1.00	209.09	2.39
8131	GeoB18116-2 P07 CC 15 cm	16.93	0.14	18.79	0.01	0.90	0.01	3.16	0.03	3.51	0.03	8.85	0.40	8.53	0.30	1.00	209.32	1.72
8333	GeoB18116-2 P09-2 143 cm	16.83	0.12	16.14	0.01	1.04	0.01	3.65	0.03	3.56	0.03	8.55	0.38	8.20	0.29	1.00	219.79	1.38
8396	GeoB18116-2 P10-1 126 cm	14.74	0.16	15.29	0.01	0.96	0.01	3.38	0.04	3.28	0.03	10.22	0.47	9.99	0.36	1.00	220.11	1.68
8395	GeoB18116-2 P10-1 105 cm	15.18	0.24	15.71	0.01	0.97	0.02	3.38	0.05	3.29	0.05	10.17	0.53	9.93	0.44	1.00	222.40	1.92
8393	GeoB18116-2 P10-1 29 cm	15.32	0.20	15.39	0.00	1.00	0.01	3.49	0.05	3.38	0.04	9.57	0.47	9.29	0.38	1.00	226.29	2.16
8394	GeoB18116-2 P10-1 58 cm	16.59	0.17	16.74	0.00	0.99	0.01	3.47	0.03	3.37	0.03	9.66	0.44	9.38	0.34	1.00	231.12	1.91
8292	GeoB18116-2 P10-1 2 cm	13.89	0.10	14.36	0.03	0.97	0.01	3.39	0.03	3.28	0.03	10.21	0.45	9.97	0.32	1.00	234.17	2.16
8399	GeoB18116-2 P11-2 144 cm	17.97	0.17	17.44	0.01	1.03	0.01	3.61	0.03	3.50	0.03	8.87	0.41	8.54	0.32	1.00	265.02	3.05
8141	GeoB18116-2 P14-2 155 cm	17.09	0.19	19.63	0.02	0.87	0.01	3.05	0.03	3.39	0.04	9.56	0.45	9.28	0.36	1.00	265.83	2.12
8132	GeoB18116-2 P13 CC 7 cm	15.94	0.14	18.18	0.02	0.88	0.01	3.07	0.03	3.41	0.03	9.41	0.42	9.12	0.32	1.00	273.00	2.38
8129	GeoB18116-2 P11-2 164 cm	15.99	0.17	18.34	0.01	0.87	0.01	3.05	0.03	3.39	0.04	9.52	0.44	9.24	0.35	1.00	274.78	2.83

Lab.Nr.	Sample Name	[Li] (pg/ml)	σ (pg/ml)	[Mg] (ng/ml)	σ (ng/ml)	Li/Mg uncor. (mg/g)	σ (mg/g)	Li/Mg uncor. (mmol/mol)	σ (mmol/mol)	Li/Mg cor. (mmol/mol)	σ (mmol/mol)	T (Mon) [°C]	int. 2σ [°C]	T (Cun) [°C]	int. 2σ [°C]	ext. 2σ [°C]	Age (ka)	2σ (ka)
8334	GeoB18116-2 P11-2 200 cm	17.20	0.10	16.80	0.01	1.02	0.01	3.59	0.02	3.49	0.02	8.92	0.38	8.60	0.28	1.00	284.89	3.01
8146	GeoB18116-2 P11 CC 11 cm	15.66	0.13	17.92	0.01	0.87	0.01	3.06	0.03	3.40	0.03	9.48	0.42	9.20	0.32	1.00	292.12	2.93
8300	GeoB18116-2 P16-2 151 cm	15.49	0.10	17.24	0.02	0.90	0.01	3.15	0.02	3.05	0.02	11.73	0.50	11.59	0.33	1.00	297.63	3.67
8087	GeoB18116-2 P13-1 113 cm	15.82	0.13	15.98	0.00	0.99	0.01	3.47	0.03	3.47	0.03	9.05	0.41	8.74	0.31	1.00	299.82	2.78
8296	GeoB18116-2 P15-1 86 cm	17.28	0.05	17.83	0.03	0.97	0.00	3.40	0.01	3.29	0.01	10.17	0.42	9.93	0.28	1.00	301.88	4.01
8090	GeoB18116-2 P14-2 190 cm	14.28	0.14	15.29	0.01	0.93	0.01	3.27	0.03	3.27	0.03	10.25	0.47	10.02	0.35	1.00	305.27	4.25
8271	GeoB18116-2 P19 CC 1 cm	16.15	0.10	14.97	0.02	1.08	0.01	3.78	0.02	3.62	0.02	8.22	0.36	7.85	0.28	1.00	305.43	5.47
8142	GeoB18116-2 P12-1 112 cm	22.01	0.10	23.56	0.01	0.93	0.00	3.27	0.02	3.63	0.02	8.12	0.35	7.75	0.26	1.00	307.11	3.89
8303	GeoB18116-2 P16 CC 14 cm	14.54	0.13	16.66	0.00	0.87	0.01	3.06	0.03	2.96	0.03	12.31	0.53	12.21	0.37	1.00	307.69	4.28
8294	GeoB18116-2 P14 CC 16 cm	15.60	0.13	16.70	0.01	0.93	0.01	3.27	0.03	3.17	0.03	10.93	0.48	10.74	0.34	1.00	311.20	4.39
8302	GeoB18116-2 P16-2 206 cm	16.89	0.12	19.03	0.02	0.89	0.01	3.11	0.02	3.01	0.02	11.97	0.51	11.85	0.34	1.00	311.22	11.03
8295	GeoB18116-2 P15-1 26 cm	15.10	0.12	16.46	0.02	0.92	0.01	3.21	0.03	3.11	0.02	11.30	0.49	11.14	0.34	1.00	312.44	3.28
8298	GeoB18116-2 P16-1 76 cm	16.30	0.14	17.95	0.05	0.91	0.01	3.18	0.03	3.08	0.03	11.52	0.51	11.36	0.36	1.00	312.62	5.32
8251	GeoB18116-2 P24-2 21 cm	14.76	0.20	17.52	0.03	0.84	0.01	2.95	0.04	3.20	0.04	10.74	0.52	10.54	0.42	1.00	314.04	9.13
8085	GeoB18116-2 P14-1 82 cm	17.88	0.21	18.30	0.00	0.98	0.01	3.42	0.04	3.43	0.04	9.32	0.45	9.03	0.37	1.00	314.90	3.26
8335	GeoB18116-2 P13-1 39 cm	17.75	0.14	16.53	0.00	1.07	0.01	3.76	0.03	3.64	0.03	8.09	0.37	7.71	0.30	1.00	316.68	4.86
8137	GeoB18116-2 P15-2 200 cm	15.36	0.19	19.45	0.02	0.79	0.01	2.76	0.03	3.07	0.04	11.55	0.53	11.40	0.40	1.00	316.89	4.13
8084	GeoB18116-2 P18-1 2 cm	16.01	0.16	19.41	0.01	0.83	0.01	2.89	0.03	2.89	0.03	12.78	0.56	12.71	0.39	1.00	318.58	3.89
8297	GeoB18116-2 P16-1 8 cm	15.54	0.09	16.94	0.04	0.92	0.01	3.21	0.02	3.11	0.02	11.30	0.48	11.14	0.32	1.00	319.02	5.53
8277	GeoB18116-2 P17-1 9 cm	13.61	0.13	15.79	0.02	0.86	0.01	3.02	0.03	2.92	0.03	12.56	0.55	12.48	0.38	1.00	319.54	4.46
8262	GeoB18116-2 P21 CC 3 cm	14.53	0.15	14.69	0.02	0.99	0.01	3.46	0.04	3.32	0.03	9.98	0.46	9.73	0.35	1.00	320.10	4.46
8293	GeoB18116-2 P13-2 163 cm	16.67	0.13	16.74	0.02	1.00	0.01	3.49	0.03	3.38	0.03	9.62	0.42	9.35	0.31	1.00	320.23	4.31
8276	GeoB18116-2 P18 CC 15 cm	18.21	0.17	16.98	0.04	1.07	0.01	3.76	0.04	3.64	0.04	8.11	0.39	7.74	0.32	1.00	323.82	5.11
8301	GeoB18116-2 P16-2 170 cm	14.15	0.12	15.93	0.01	0.89	0.01	3.11	0.03	3.01	0.03	11.97	0.52	11.84	0.36	1.00	325.21	4.76
8272	GeoB18116-2 P18-1 7 cm	15.72	0.14	17.14	0.05	0.92	0.01	3.21	0.03	3.08	0.03	11.53	0.51	11.38	0.36	1.00	328.51	5.44
8299	GeoB18116-2 P16-1 118 cm	14.83	0.16	16.30	0.03	0.91	0.01	3.19	0.03	3.08	0.03	11.47	0.52	11.32	0.38	1.00	333.68	5.50
8257	GeoB18116-2 P22-1 3 cm	16.19	0.11	15.91	0.04	1.02	0.01	3.56	0.03	3.41	0.02	9.41	0.41	9.12	0.30	1.00	335.35	9.00
8256	GeoB18116-2 P23-2 152 cm	17.98	0.19	18.04	0.04	1.00	0.01	3.49	0.04	3.34	0.04	9.83	0.46	9.57	0.36	1.00	336.32	5.22
8273	GeoB18116-2 P18-1 100 cm	19.44	0.15	15.39	0.03	1.26	0.01	4.42	0.04	4.23	0.03	5.00	0.26	4.42	0.26	1.00	340.53	4.62
8127	GeoB18116-2 P18-1 71 cm	14.70	0.09	16.62	0.01	0.88	0.01	3.10	0.02	3.44	0.02	9.23	0.40	8.93	0.29	1.00	343.86	4.80
8260	GeoB18116-2 P21-1 109 cm	19.84	0.14	17.06	0.03	1.16	0.01	4.07	0.03	3.97	0.03	6.33	0.30	5.84	0.26	1.00	348.93	6.46
8268	GeoB18116-2 P19-1 115 cm	17.34	0.20	15.04	0.03	1.15	0.01	4.04	0.05	3.87	0.05	6.86	0.37	6.41	0.34	1.00	349.67	6.12
8274	GeoB18116-2 P18-2 134 cm	17.95	0.20	16.83	0.04	1.07	0.01	3.74	0.04	3.58	0.04	8.45	0.42	8.09	0.35	1.00	352.59	6.12
8082	GeoB18116-2 P24-1 29 cm	15.44	0.10	16.82	0.03	0.92	0.01	3.21	0.02	3.22	0.02	10.61	0.45	10.40	0.31	1.00	352.80	5.65
8254	GeoB18116-2 P23-1 7 cm	17.62	0.23	16.66	0.00	1.06	0.01	3.70	0.05	3.61	0.05	8.26	0.43	7.89	0.37	1.00	354.28	6.01
8270	GeoB18116-2 P19-2 221 cm	17.14	0.14	15.27	0.03	1.12	0.01	3.93	0.03	3.76	0.03	7.40	0.35	6.98	0.29	1.00	354.58	5.60
8275	GeoB18116-2 P18-2 181 cm	16.08	0.12	16.11	0.03	1.00	0.01	3.50	0.03	3.35	0.03	9.80	0.43	9.53	0.32	1.00	357.26	6.50
8261	GeoB18116-2 P21-2 163 cm	17.23	0.20	17.53	0.04	0.98	0.01	3.44	0.04	3.30	0.04	10.11	0.48	9.87	0.38	1.00	358.90	7.55
8089	GeoB18116-2 P25-2 227 cm	15.89	0.14	17.31	0.05	0.92	0.01	3.21	0.03	3.22	0.03	10.60	0.47	10.39	0.35	1.00	360.03	7.74
8138	GeoB18116-2 P23-1 55 cm	14.77	0.16	19.02	0.01	0.78	0.01	2.72	0.03	3.02	0.03	11.89	0.53	11.77	0.38	1.00	360.69	5.86
8136	GeoB18116-2 P23-2 204 cm	14.71	0.13	18.38	0.01	0.80	0.01	2.80	0.02	3.11	0.03	11.27	0.49	11.10	0.35	1.00	361.03	5.35
8081	GeoB18116-2 P19-2 188 cm	20.94	0.26	18.56	0.03	1.13	0.01	3.95	0.05	3.96	0.05	6.36	0.36	5.87	0.34	1.00	362.22	6.61
8250	GeoB18116-2 P24-1 73 cm	14.98	0.17	17.40	0.00	0.86	0.01	3.02	0.03	3.27	0.04	10.30	0.48	10.07	0.37	1.00	364.14	7.83
8144	GeoB18116-2 P21-2 224 cm	15.41	0.14	18.09	0.00	0.85	0.01	2.98	0.03	3.31	0.03	10.01	0.45	9.76	0.33	1.00	364.47	5.98
8139	GeoB18116-2 P22-1 120 cm	16.35	0.14	19.59	0.01	0.83	0.01	2.92	0.02	3.25	0.03	10.42	0.46	10.20	0.33	1.00	367.03	10.45
8244	GeoB18116-2 P26-1 88 cm	19.34	0.19	20.35	0.01	0.95	0.01	3.33	0.03	3.70	0.04	7.76	0.37	7.37	0.31	1.00	372.53	7.17
8269	GeoB18116-2 P19-2 150 cm	16.99	0.24	14.70	0.03	1.16	0.02	4.05	0.06	3.87	0.05	6.81	0.40	6.35	0.38	1.00	373.75	8.49
8267	GeoB18116-2 P19-1 41 cm	20.73	0.13	18.37	0.01	1.13	0.01	3.95	0.02	3.85	0.02	6.94	0.31	6.50	0.26	1.00	380.31	10.29
8255	GeoB18116-2 P23-1 110 cm	14.93	0.20	15.86	0.04	0.94	0.01	3.30	0.05	3.16	0.04	10.99	0.53	10.81	0.42	1.00	386.50	7.95
8249	GeoB18116-2 P25-2 177 cm	16.64	0.10	19.21	0.00	0.87	0.01	3.03	0.02	3.29	0.02	10.18	0.43	9.94	0.30	1.00	390.87	10.12
8133	GeoB18116-2 P22-2 212 cm	16.22	0.18	19.59	0.01	0.83	0.01	2.90	0.03	3.22	0.04	10.59	0.49	10.37	0.37	1.00	426.71	12.05

Lab.Nr.	Sample Name	[Li] (pg/ml)	σ (pg/ml)	[Mg] (ng/ml)	σ (ng/ml)	Li/Mg uncor. (mg/g)	σ (mg/g)	Li/Mg uncor. (mmol/mol)	σ (mmol/mol)	Li/Mg cor. (mmol/mol)	σ (mmol/mol)	T (Mon) [°C]	int. 2σ [°C]	T (Cun) [°C]	int. 2σ [°C]	ext. 2σ [°C]	Age (ka)	2σ (ka)
7734	GeoB18127-1 0-2 cm	13.01	0.20	16.71	0.06	0.78	0.01	2.73	0.04	3.15	0.05	11.05	0.56	10.86	0.45	1.00	5.45	0.12
7736	GeoB18127-1 51-53 cm	13.44	0.31	18.46	0.05	0.73	0.02	2.55	0.06	2.94	0.07	12.41	0.69	12.32	0.59	1.00	7.64	0.19
7738	GeoB18127-78-79 cm	16.90	0.24	21.26	0.06	0.79	0.01	2.78	0.04	3.21	0.05	10.63	0.53	10.42	0.43	1.00	8.30	0.14
7740	GeoB18127-1 157-160 cm	15.35	0.21	20.36	0.07	0.75	0.01	2.64	0.04	3.05	0.04	11.71	0.56	11.57	0.43	1.00	8.62	0.12
7742	GeoB18127-1 250-253 cm	13.35	0.14	18.52	0.04	0.72	0.01	2.53	0.03	2.92	0.03	12.62	0.56	12.54	0.39	1.00	9.36	0.14
7744	GeoB18127-1 335-338 cm	15.97	0.29	21.44	0.10	0.74	0.01	2.61	0.05	3.01	0.06	11.96	0.62	11.84	0.51	1.00	10.42	0.09
7746	GeoB18127-1 402-406 cm	18.16	0.33	20.27	0.00	0.90	0.02	3.14	0.06	3.62	0.07	8.19	0.50	7.82	0.46	1.00	13.36	0.10
7748	GeoB18127-1 475-481 cm	15.53	0.35	18.27	0.05	0.85	0.02	2.98	0.07	3.44	0.08	9.26	0.60	8.96	0.56	1.00	13.52	0.08
7749	GeoB18127-1 490-491 cm	18.74	0.20	21.32	0.07	0.88	0.01	3.08	0.04	3.55	0.04	8.57	0.42	8.23	0.35	1.00	14.14	0.11
7751	GeoB18130-1 8-10 cm	15.76	0.21	19.97	0.02	0.79	0.01	2.76	0.04	3.19	0.04	10.78	0.52	10.58	0.41	1.00	5.07	0.03
7752	GeoB18130-1 33-34 cm	14.65	0.21	18.58	0.10	0.79	0.01	2.76	0.04	3.19	0.05	10.79	0.54	10.59	0.43	1.00	7.94	0.05
7753	GeoB18130-1 60-62 cm	14.66	0.24	20.14	0.08	0.73	0.01	2.55	0.04	2.94	0.05	12.43	0.61	12.33	0.48	1.00	8.47	0.06
7755	GeoB18130-1 105-106 cm	14.34	0.13	19.61	0.07	0.73	0.01	2.56	0.03	2.95	0.03	12.34	0.54	12.25	0.38	1.00	8.94	0.03
7759	GeoB18130-1 145-148 cm	12.65	0.32	17.82	0.10	0.71	0.02	2.49	0.07	2.87	0.08	12.94	0.75	12.88	0.66	1.00	9.44	0.05
7757	GeoB18130-1 127-128 cm	13.03	0.09	17.55	0.09	0.74	0.01	2.60	0.02	3.00	0.03	12.02	0.52	11.90	0.36	1.00	9.46	0.05

Supplement Text A:

Mound Evolution: Dragon Mound:

On DM, three different stages of mound formation can be identified. The lower part of cluster one (6100 to 3800 cm) reflects a large scatter of coral ages of up to 90 ka within an individual core barrel (Fig. 3.4; S23: red framed rhombus). The oldest coral of section S23 is dated at 390 ka (5200 cm) whereas the youngest age is dated at 305 ka (5400 cm). A similar range in age scatter from 390 to 300 ka can be observed in depths of 4300 cm as well. The distribution of ages, overall spanning 100 ka on 2000 cm core length, indicates that this part of the mound does not reflect actual coral growth but coral rubble and fragments, potentially deposited at the core location after a mass wasting event of a coral mound (e.g. mound collapse). The core location on DM between a northward-directed coral mound and a west/north-west directed extending foothill (Fig. 3.1c) suggests that, since no information on DM other than the presented age-depth profile is available to date, either side could be the source of the coral rubble and fragments. However, between the mound base (6100 cm) and 3800 cm, no age younger than 300 ka was dated, thus marking the potential time of deposition (Fig. 3.7b). To deposit ages ranging from 426 to 300 ka over 2000 cm height almost simultaneously, the source mound(s) needed to be of a certain height and thus potentially older than the presented mound base of circa 380 ka (Fig. 3.7a and Fig. 3.7b).

The second part of cluster one ranges from 3800 to 2700 cm and reveals ages between 333 to 265 ka. Although, compared to the lower part (6100 to 3800 cm), individual core barrels (Fig. 3.4; S16 and S13) reveal smaller age scatters of 40 to 50 ka, a similar formation with minor mass wasting events, as observed in the lower part is expected. At this point of the mound evolution, the area, covered today by the 6000 cm high mound, was a much small, 2000 cm high mound or coral rubble field on the seafloor. However, the second part (3800 to 2700 cm) does not show ages older than 333 ka which might be due to the stratigraphy of the source mound, ideally it would have older corals on the bottom and younger corals on top (Fig. 3.7c). Thus, a second mass wasting event or at least major redistribution processes of coral fragments may have caused the observed mound evolution. At the top of the second part (~2600 to 2500 cm), first evidence of successive coral growth appears with coral ages in stratigraphic order.

In the second cluster (Fig. 3.4), two different stages of mound evolution can be observed. Between 2301 and 2058 cm, coral ages reveal similar patterns as observed in the core sections below, with individual core barrels revealing age scatters of up to 50 ka (S10: 243 to 200 ka).

Starting at 1914 cm depth up to 1053 cm, only minor age differences of some 6 ka per barrel are observed, possibly reflecting successive coral growth over 1000 cm from 210 to 201 ka (Fig. 3.7d). It should be noted, that the lowest sampled coral (1023 cm) from the third and youngest cluster originates from the same core barrel as the upper corals from the second cluster (1160-1060 cm) and is in stratigraphic order. This implies that the age gap between 201 and 115 ka must be a hiatus, with little (or no) coral occurrence on site. However, a single coral was dated at 171 ka and originates from the CC of a barrel circa 1100 cm deeper (171 ka/2142 cm). The third and last cluster is stratigraphically in order with coral ages ranging from 115 to 102 ka over the upper 1000 cm of the core. This cluster thus reflects successive coral growth on Dragon Mound (Fig. 3.7d) at a rate (115 cm/ka) similar to active mound aggregation rates observed during the Holocene (e.g. Frank et al. 2009, Fink et al. 2013)

List of figures

List of tables

List of abbreviations

MED	Mediterranean Sea
EMS	Eastern Mediterranean Sea
WMS	Western Mediterranean Sea
EMB	Eastern Mediterranean Basin
CMB	Central Mediterranean Basin
WMB	Western Mediterranean Basin
AS	Alboran Sea
EAB	East Alboran Basin
WAB	West Alboran Basin
GoL	Gulf of Lions
GoC	Gulf of Cádiz
SoG	Strait of Gibraltar
SoS	Strait of Sicily
AMOC	Atlantic Meridional Overturning Circulation
NACW	North Atlantic Central Water
AW	Atlantic Water
AJ	Atlantic Jet
SAW	Surface Atlantic Water
MAW	Modified Atlantic Water
WAG	West Alboran Gyre
EAG	East Alboran Gyre
AOF	Almeria Oran Front
AC	Agerian Current
AeDW	Aegean Deep Water
AdDW	Adriatic Deep Water
TDW	Tyrrhenian Dense Water
WIW	Winter Intermediate Water
WMDW	West Mediterranean Deep Water
LIW	Levantine Intermediate Water
MOW	Mediterranean Outflow Water
AzF	Azores Front
AzC	Azores Current
PF	Polar Front
FRE	Freshwater Release Event
CWC	Cold-Water Corals
CMP	Coral Mound Provinces
EMCP	East Mediterranean Coral Province
WMCP	West Mediterranean Coral Province
BR I	Brittlestar Ridge I
DM	Dragon Mound
ROV	Remotely Operated Vehicles
GC	Gravity Core
MeBo	MeeresbodenBohrgerät (drilling device)
CC	CoreCatcher
CTD	Conductivity Temperature Depth (Probe and sample gear)
COC	Centre of Calcification
MAR	Mound aggregation Rate
MUR	Mediterranean $\delta^{234}U$ –Record

AUR	Atlantic $\delta^{234}U$ -Record
SST	Sea Surface Temperature
BWT	Bottom Water Temperature
nBWT	near Bottom Water Temperature
RSL	Relative Sea Level
MIS	Marine Isotope Stage
MPT	Mid Pleistocene Transition
LGM	Last Glacial Maximum
T1	Termination 1
HE	Heinrich Event
B/A	Bølling-Allerød
YD	Younger Dryas
ORL	Organic Rich Layer
S	Sapropel
U	Uranium
Th	Thorium
Sr	Strontium
Ca	Calcium
Mg	Magnesium
Ti	Titanium
Ma	Million annum; million years
ka	kilo annum / 1000 years
cmbsf	cm below seafloor; depth in core
Mt/a	Megaton per year
°C	degree Celsius (Temperature)
MC-ICP-MS	Multi Collector-Inductively Coupled Plasma-Mass Spectrometer
ICP-Q-MS	Inductively Coupled Plasma Quadrupole - Mass Spectrometer
TIMS	Thermal Ionization Mass Spectrometer

Bibliography

Abdul, N., et al. (2016). "Younger Dryas sea level and meltwater pulse 1B recorded in Barbados reef crest coral Acropora palmata." Paleoceanography **31**(2): 330-344.

Addamo, A. M., et al. (2016). "Merging scleractinian genera: the overwhelming genetic similarity between solitary Desmophyllum and colonial Lophelia." BMC evolutionary biology **16**(1): 108.

Adkins, J., et al. (2004). "Growth rates of the deep-sea scleractinia Desmophyllum cristagalli and Enallopsammia rostrata." Earth and Planetary Science Letters **227**(3-4): 481-490.

Adkins, J. F. (1998). "Deep-Sea Coral Evidence for Rapid Change in Ventilation of the Deep North Atlantic 15,400 Years Ago." Science **280**(5364): 725-728.

Adkins, J. F., et al. (2003). "Stable isotopes in deep-sea corals and a new mechanism for “vital effects”." Geochimica et Cosmochimica Acta **67**(6): 1129-1143.

Adkins, J. F., et al. (2002). "Radiocarbon dating of deep-sea corals." Radiocarbon **44**(2): 567-580.

Aksu, A. E., et al. (2002). "Persistent Holocene outflow from the Black Sea to the Eastern Mediterranean contradicts Noah's Flood hypothesis." GSA Today **12**(5): 4-10.

Alhammoud, B., et al. (2010). "Sensitivity of Mediterranean thermohaline circulation to gateway depth: A model investigation." Paleoceanography **25**(2).

Allison, N., et al. (2007). "Palaeoenvironmental records from fossil corals: the effects of submarine diagenesis on temperature and climate estimates." Geochimica et Cosmochimica Acta **71**(19): 4693-4703.

Alves, M. L. and A. Colin de Verdière (1999). "Instability dynamics of a subtropical jet and applications to the Azores Front Current System: eddy-driven mean flow." Journal of Physical Oceanography **29**(5): 837-864.

Anagnostou, E., et al. (2011). "Seawater nutrient and carbonate ion concentrations recorded as P/Ca, Ba/Ca, and U/Ca in the deep-sea coral Desmophyllum dianthus." Geochimica et Cosmochimica Acta **75**(9): 2529-2543.

Andersen, M. B., et al. (2010). "Precise determination of the open ocean234U/238U composition." Geochemistry, Geophysics, Geosystems **11**(12): n/a-n/a.

Anderson, E. C. and W. Libby (1951). "World-wide distribution of natural radiocarbon." Physical Review **81**(1): 64.

Arps, J. (2017). "Towards e-Precision of U-Series Age Determinations of Secondary Carbonates." PhD thesis - Heidelberg University: 144.

Astraldi, M., et al. (2001). "Dense water dynamics along the Strait of Sicily (Mediterranean Sea)." Journal of Physical Oceanography **31**(12): 3457-3475.

Ausín, B., et al. (2015). "Atmospheric patterns driving Holocene productivity in the Alboran Sea (Western Mediterranean): a multiproxy approach." The Holocene **25**(4): 583-595.

Bahr, A., et al. (2014). "Deciphering bottom current velocity and paleoclimate signals from contourite deposits in the Gulf of Cádiz during the last 140 kyr: An inorganic geochemical approach." Geochemistry, Geophysics, Geosystems **15**(8): 3145-3160.

Bahr, A., et al. (2015). "Persistent monsoonal forcing of Mediterranean Outflow Water dynamics during the late Pleistocene." Geology **43**(11): 951-954.

Baldacci, A., et al. (2001). "A study of the Alboran sea mesoscale system by means of empirical orthogonal function decomposition of satellite data." Journal of Marine Systems **29**(1-4): 293-311.

Bar-Matthews, M., et al. (2003). "Sea–land oxygen isotopic relationships from planktonic foraminifera and speleothems in the Eastern Mediterranean region and their implication for paleorainfall during interglacial intervals." Geochimica et Cosmochimica Acta **67**(17): 3181-3199.

Bárcena, M. A., et al. (2001). "Paleoproductivity variations related to climatic conditions in the Alboran Sea (western Mediterranean) during the last glacial–interglacial transition: the diatom record." Palaeogeography, Palaeoclimatology, Palaeoecology **167**(3-4): 337-357.

Bard, E., et al. (2000). "Hydrological impact of Heinrich events in the subtropical northeast Atlantic." Science **289**(5483): 1321-1324.

Barnes, J., et al. (1956). "Ratio of ionium to uranium in coral limestone." Science **124**(3213): 175-176.

Beck, J. W., et al. (1992). "Sea-surface temperature from coral skeletal strontium/calcium ratios." Science **257**(5070): 644-647.

Benzohra, M. and C. Millot (1995). "Characteristics and circulation of the surface and intermediate water masses off Algeria." Deep Sea Research Part I: Oceanographic Research Papers **42**(10): 1803-1830.

Berger, A., et al. (1999). "Modelling northern hemisphere ice volume over the last 3 Ma." Quaternary Science Reviews **18**(1): 1-11.

Bethoux, J. and B. Gentili (1999). "Functioning of the Mediterranean Sea: past and present changes related to freshwater input and climate changes." Journal of Marine Systems **20**(1-4): 33-47.

Bethoux, J., et al. (1999). "The Mediterranean Sea: a miniature ocean for climatic and environmental studies and a key for the climatic functioning of the North Atlantic." Progress in Oceanography **44**(1-3): 131-146.

Blome, M. W., et al. (2012). "The environmental context for the origins of modern human diversity: A synthesis of regional variability in African climate 150,000–30,000 years ago." Journal of human evolution **62**(5): 563-592.

Böhm, E., et al. (2015). "Strong and deep Atlantic meridional overturning circulation during the last glacial cycle." Nature **517**(7532): 73-76.

Bonneau, L., et al. (2018). "Imprint of Holocene Climate Variability on Cold-Water Coral Reef Growth at the SW Rockall Trough Margin, NE Atlantic." Geochemistry, Geophysics, Geosystems **19**(8): 2437-2452.

Bormans, M. and C. Garrett (1989). "A simple criterion for gyre formation by the surface outflow from a strait, with application to the Alboran Sea." Journal of Geophysical Research: Oceans **94**(C9): 12637-12644.

Bradley, R. S. (2015). Paleoclimatology: Reconstructing Climates of the Quaternary, Elsevier Science**:** 1-11.

Broecker, W. S. (1971). "A Kinetic Model for the Chemical Composition of Sea Water 1." Quaternary Research **1**(2): 188-207.

Bryan, S. P. and T. M. Marchitto (2008). "Mg/Ca–temperature proxy in benthic foraminifera: New calibrations from the Florida Straits and a hypothesis regarding Mg/Li." Paleoceanography and Paleoclimatology **23**(2).

Budillon, G., et al. (2010). "Hydrographic characteristics of water masses and circulation in the Northern Ionian Sea." Deep Sea Research Part II: Topical Studies in Oceanography **57**(5-6): 441-457.

Büscher, J. V., et al. (2017). "Interactive Effects of Ocean Acidification and Warming on Growth, Fitness and Survival of the Cold-Water Coral Lophelia pertusa under Different Food Availabilities." Frontiers in Marine Science **4**.

Cacho, I., et al. (2002). "Response of the Western Mediterranean Sea to rapid climatic variability during the last 50,000 years: a molecular biomarker approach." Journal of Marine Systems **33-34**: 253-272.

Cacho, I., et al. (2001). "Variability of the western Mediterranean Sea surface temperature during the last 25,000 years and its connection with the Northern Hemisphere climatic changes." Paleoceanography **16**(1): 40-52.

Cacho, I., et al. (1999). "Dansgaard-Oeschger and Heinrich event imprints in Alboran Sea paleotemperatures." Paleoceanography **14**(6): 698-705.

Cacho, I., et al. (2002). "Reconstructing Alboran Sea hydrography during the last organic rich layer formation." Geochim. Cosmochim. Acta **66**(A115).

Cairns, S. D. (2007). "Deep-water corals: An overview with special reference to diversity and distribution of deep-water Scleractinian corals." Bulletin of Marine Science **81**(3): 311-322.

Case, D. H., et al. (2010). "Environmental and biological controls on Mg and Li in deep-sea scleractinian corals." Earth and Planetary Science Letters **300**(3-4): 215-225.

Català, A., et al. (2019). "Holocene hydrography evolution in the Alboran Sea: a multi-record and multi-proxy comparison." Climate of the Past **15**(3): 927-942.

Chabaux, F., et al. (2003). "U-Th-Ra fractionation during weathering and river transport." Reviews in Mineralogy and geochemistry **52**(1): 533-576.

Chen, T., et al. (2016). "Ocean mixing and ice-sheet control of seawater 234U/238U during the last deglaciation." Science **354**(6312): 626-629.

Chen, T., et al. (2015). "Synchronous centennial abrupt events in the ocean and atmosphere during the last deglaciation." Science **349**(6255): 1537-1541.

Cheng, H., et al. (2000). "U-Th dating of deep-sea corals." Geochimica et Cosmochimica Acta **64**(14): 2401-2416.

Cheng, H., et al. (2000). "The half-lives of uranium-234 and thorium-230." Chemical Geology **169**(1-2): 17-33.

Cheng, H., et al. (2013). "Improvements in 230Th dating, 230Th and 234U half-life values, and U–Th isotopic measurements by multi-collector inductively coupled plasma mass spectrometry." Earth and Planetary Science Letters **371-372**: 82-91.

Clark, P. U., et al. (2006). "The middle Pleistocene transition: characteristics, mechanisms, and implications for long-term changes in atmospheric pCO2." Quaternary Science Reviews **25**(23-24): 3150-3184.

Clark, P. U., et al. (2012). "Global climate evolution during the last deglaciation." Proceedings of the National Academy of Sciences **109**(19): E1134-E1142.

COHMAP-Members (1988). "Climatic changes of the last 18,000 years: observations and model simulations." Science: 1043-1052.

Colin, C., et al. (2010). "Neodymium isotopic composition of deep-sea corals from the NE Atlantic: implications for past hydrological changes during the Holocene." Quaternary Science Reviews **29**(19-20): 2509-2517.

Colmenero-Hidalgo, E., et al. (2004). "Ocean surface water response to short-term climate changes revealed by coccolithophores from the Gulf of Cadiz (NE Atlantic) and Alboran Sea (W Mediterranean)." Palaeogeography, Palaeoclimatology, Palaeoecology **205**(3-4): 317-336.

Comas, M., et al. (2009). "TTR-17 Leg 1 Scientific Party, 2009 Deep-Water Coral Mounds in the Alboran Sea: The Melilla Mound Field Revisited." Geo-Marine Research on the Mediterranean and European-Atlantic Margins **220**: 8-9.

Comas, M. and L. M. Pinheiro (2007). Discovery of carbonate mounds in the Alboran Sea: the Melilla mound field. 1st International Conference of the Moroccan Association of Petroleum Geologists (MAPG) in association with the American Association of Petroleum Geologists (AAPG), Marrakesh, October.

Comas, M., et al. (1999). 44. The origin and tectonic history of the Alboran Basin: insights from Leg 161 results. Proceedings of the Ocean Drilling Program Scientific Results.

Copard, K., et al. (2012). "Late Holocene intermediate water variability in the northeastern Atlantic as recorded by deep-sea corals." Earth and Planetary Science Letters **313-314**: 34-44.

Corbera, G., et al. (2019). "Ecological characterisation of a Mediterranean cold-water coral reef: Cabliers Coral Mound Province (Alboran Sea, western Mediterranean)." Prog Oceanogr **175**: 245-262.

Corrège, T. (2006). "Sea surface temperature and salinity reconstruction from coral geochemical tracers." Palaeogeography, Palaeoclimatology, Palaeoecology **232**(2-4): 408-428.

Cuny-Guirriec, K., et al. (2019). "Coral Li/Mg thermometry: Caveats and constraints." Chemical Geology.

Cutler, K., et al. (2004). "Radiocarbon calibration and comparison to 50 kyr BP with paired 14 C and 230 Th dating of corals from Vanuatu and Papua New Guinea." Radiocarbon **46**(3): 1127-1160.

d'Ortenzio, F. and M. Ribera d'Alcalà (2009). "On the trophic regimes of the Mediterranean Sea: a satellite analysis." Biogeosciences **6**(2): 139-148.

Dafner, E. V., et al. (2003). "The N: Si: P molar ratio in the Strait of Gibraltar." Geophysical Research Letters **30**(10).

Davies, A. J., et al. (2009). "Downwelling and deep-water bottom currents as food supply mechanisms to the cold-water coral Lophelia pertusa (Scleractinia) at the Mingulay Reef Complex." Limnology and Oceanography **54**(2): 620-629.

Davies, A. J. and J. M. Guinotte (2011). "Global habitat suitability for framework-forming cold-water corals." PLoS One **6**(4): e18483.

Davies, A. J., et al. (2008). "Predicting suitable habitat for the cold-water coral Lophelia pertusa (Scleractinia)." Deep Sea Research Part I: Oceanographic Research Papers **55**(8): 1048-1062.

de Haas, H., et al. (2008). "Morphology and sedimentology of (clustered) cold-water coral mounds at the south Rockall Trough margins, NE Atlantic Ocean." Facies **55**(1): 1-26.

De Mol, B., et al. (2002). "Large deep-water coral banks in the Porcupine Basin, southwest of Ireland." Marine Geology **188**(1-2): 193-231.

Delanghe, D., et al. (2002). "New TIMS constraints on the uranium-238 and uranium-234 in seawaters from the main ocean basins and the Mediterranean Sea." Marine Chemistry **80**(1): 79-93.

Denton, G. H., et al. (2010). "The last glacial termination." Science **328**(5986): 1652-1656.

Desprat, S., et al. (2007). 25. Climate variability of the last five isotopic interglacials: Direct land-sea-ice correlation from the multiproxy analysis of North-Western Iberian margin deep-sea cores. Developments in Quaternary Sciences, Elsevier. **7:** 375-386.

Desprat, S., et al. (2006). "Climatic variability of Marine Isotope Stage 7: direct land–sea–ice correlation from a multiproxy analysis of a north-western Iberian margin deep-sea core." Quaternary Science Reviews **25**(9-10): 1010-1026.

Dorschel, B., et al. (2007). "Hydrodynamics and cold-water coral facies distribution related to recent sedimentary processes at Galway Mound west of Ireland." Marine Geology **244**(1-4): 184-195.

Dorschel, B., et al. (2005). "Carbonate budget of a cold-water coral carbonate mound: Propeller Mound, Porcupine Seabight." International Journal of Earth Sciences **96**(1): 73-83.

Dorschel, B., et al. (2005). "Growth and erosion of a cold-water coral covered carbonate mound in the Northeast Atlantic during the Late Pleistocene and Holocene." Earth and Planetary Science Letters **233**(1-2): 33-44.

Douarin, M., et al. (2013). "Growth of north-east Atlantic cold-water coral reefs and mounds during the Holocene: A high resolution U-series and 14C chronology." Earth and Planetary Science Letters **375**: 176-187.

Dubois-Dauphin, Q., et al. (2016). "South Atlantic intermediate water advances into the North-east Atlantic with reduced Atlantic meridional overturning circulation during the last glacial period." Geochemistry, Geophysics, Geosystems **17**(6): 2336-2353.

Duineveld, G. C. A., et al. (2004). "Particle flux and food supply to a seamount cold-water coral community (Galicia Bank, NW Spain)." Marine Ecology Progress Series **277**: 13-23.

Dullo, W. C., et al. (2008). "Cold-water coral growth in relation to the hydrography of the Celtic and Nordic European continental margin." Marine Ecology Progress Series **371**: 165-176.

Dunk, R., et al. (2002). "A reevaluation of the oceanic uranium budget for the Holocene." Chemical Geology **190**(1-4): 45-67.

Ehrmann, W., et al. (2016). "A distal 140 kyr sediment record of Nile discharge and East African monsoon variability." Climate of the Past **12**(3): 713-727.

Eiler, J. M. (2011). "Paleoclimate reconstruction using carbonate clumped isotope thermometry." Quaternary Science Reviews **30**(25-26): 3575-3588.

Eisele, M., et al. (2011). "Productivity controlled cold-water coral growth periods during the last glacial off Mauritania." Marine Geology **280**(1-4): 143-149.

Eisele, M., et al. (2008). "Growth history of a cold-water coral covered carbonate mound—Galway Mound, Porcupine Seabight, NE-Atlantic." Marine Geology **253**(3-4): 160-169.

Elderfield, H., et al. (2012). "Evolution of ocean temperature and ice volume through the mid-Pleistocene climate transition." Science **337**(6095): 704-709.

Elliot, M., et al. (2019). "Onset and demise of coral reefs, relationship with regional ocean circulation on the Wyville Thomson Ridge." Marine Geology **416**: 105969.

Eltgroth, S. F., et al. (2006). "A deep-sea coral record of North Atlantic radiocarbon through the Younger Dryas: Evidence for intermediate water/deepwater reorganization." Paleoceanography **21**(4).

Emeis, K.-C., et al. (2000). "The sapropel record of the eastern Mediterranean Sea — results of Ocean Drilling Program Leg 160." Palaeogeography, Palaeoclimatology, Palaeoecology **158**(3-4): 371-395.

Emiliani, C., et al. (1978). "Oxygen and carbon isotopic growth record in a reef coral from the Florida Keys and a deep-sea coral from Blake Plateau." Science **202**(4368): 627-629.

Emiliani, C. and J. D. Milliman (1966). "Deep-sea sediments and their geological record." Earth-Science Reviews **1**(2-3): 105-132.

Eriş, K. K., et al. (2011). "Late glacial to Holocene sea-level changes in the Sea of Marmara: new evidence from high-resolution seismics and core studies." Geo-Marine Letters **31**(1): 1-18.

Esat, T. M. and Y. Yokoyama (2006). "Variability in the uranium isotopic composition of the oceans over glacial–interglacial timescales." Geochimica et Cosmochimica Acta **70**(16): 4140-4150.

Eynaud, F., et al. (2009). "Position of the Polar Front along the western Iberian margin during key cold episodes of the last 45 ka." Geochemistry, Geophysics, Geosystems **10**(7).

Fabres, J., et al. (2002). "Composition and spatio-temporal variability of particle fluxes in the Western Alboran Gyre, Mediterranean Sea." Journal of Marine Systems **33-34**: 431-456.

Faure, G. (1977). "Principles of isotope geology."

Feenstra, E. J., et al. (2020). "Palaeo-environmental variability and the proliferation of cold-water coral growth at the onset of the last deglaciation in the Western Mediterranean (East Melilla Mound Field, Alboran Sea)." in prep.

Fentimen, R., et al. (2020). "The influence of climatic variability on the long-term growth history of a Mediterranean cold-water coral mound (Melilla Mound Field)." submitted.

Ferdelman, T. G., et al. (2006). "IODP Expedition 307 drills cold-water coral mound along the Irish continental margin." Scientific Drilling **2**: 11-16.

Fink, H. G., et al. (2015). "Spatio-temporal distribution patterns of Mediterranean cold-water corals (Lophelia pertusa and Madrepora oculata) during the past 14,000 years." Deep Sea Research Part I: Oceanographic Research Papers **103**: 37-48.

Fink, H. G., et al. (2013). "Cold-water coral growth in the Alboran Sea related to high productivity during the Late Pleistocene and Holocene." Marine Geology **339**: 71-82.

Fletcher, W. J., et al. (2013). "Mid-Holocene emergence of a low-frequency millennial oscillation in western Mediterranean climate: Implications for past dynamics of the North Atlantic atmospheric westerlies." The Holocene **23**(2): 153-166.

Flögel, S., et al. (2014). "Geochemical and physical constraints for the occurrence of living cold-water corals." Deep Sea Research Part II: Topical Studies in Oceanography **99**: 19-26.

Flügel, E. (2013). Microfacies of carbonate rocks: analysis, interpretation and application, Springer Science & Business Media.

Frank, N., et al. (2011). "Northeastern Atlantic cold-water coral reefs and climate." Geology **39**(8): 743-746.

Frank, N., et al. (2005). Deep-water corals of the northeastern Atlantic margin: carbonate mound evolution and upper intermediate water ventilation during the Holocene. Cold-water corals and ecosystems, Springer**:** 113-133.

Frank, N., et al. (2004). "Eastern North Atlantic deep-sea corals: tracing upper intermediate water Δ14C during the Holocene." Earth and Planetary Science Letters **219**(3-4): 297-309.

Frank, N., et al. (2009). "The Holocene occurrence of cold water corals in the NE Atlantic: Implications for coral carbonate mound evolution." Marine Geology **266**(1-4): 129-142.

Freiwald, A. (2002). Reef-forming cold-water corals. Ocean margin systems, Springer**:** 365-385.

Freiwald, A., et al. (2009). "The White Coral Community in the Central Mediterranean Sea Revealed by ROV Surveys." Oceanography **22**(1): 58-74.

Freiwald, A., et al. (2004). "Cold water coral reefs: out of sight-no longer out of mind."

Freiwald, A. and J. M. Roberts (2005). "Cold-water corals and ecosystem."

Freiwald, A., et al. (2017). "Global distribution of cold-water corals (version 4.0). Third update to the dataset in Freiwald et al. (2004) by UNEP-WCMC, in collaboration with Andre Freiwald and John Guinotte. Cambridge (UK): ." UN Environment World Conservation Monitoring Centre.

Freudentahl, T. and G. Wefer (2010). "Kernbohrung am Mee-res-bo-den-Bohr-ge-rät MeBo." DVS-Be-rich-te **261**: 47-52.

Frigola, J., et al. (2008). "Evidence of abrupt changes in Western Mediterranean Deep Water circulation during the last 50kyr: A high-resolution marine record from the Balearic Sea." Quaternary International **181**(1): 88-104.

Fuda, J. L., et al. (2002). "Warming, salting and origin of the Tyrrhenian Deep Water." Geophysical Research Letters **29**(19).

Füger, A., et al. (2019). "Effect of growth rate and pH on lithium incorporation in calcite." Geochimica et Cosmochimica Acta **248**: 14-24.

Gacic, M., et al. (1996). "Thermohaline properties and circulation in the Otranto Strait." BULLETIN-INSTITUT OCEANOGRAPHIQUE MONACO-NUMERO SPECIAL-: 117-146.

Garcia-Gorriz, E. and M. E. Carr (1999). "The climatological annual cycle of satellite-derived phytoplankton pigments in the Alboran Sea." Geophysical Research Letters **26**(19): 2985-2988.

Gass, S. E. and J. M. Roberts (2006). "The occurrence of the cold-water coral Lophelia pertusa (Scleractinia) on oil and gas platforms in the North Sea: colony growth, recruitment and environmental controls on distribution." Mar Pollut Bull **52**(5): 549-559.

Gasse, F. (2000). "Hydrological changes in the African tropics since the Last Glacial Maximum." Quaternary Science Reviews **19**(1-5): 189-211.

Gasse, F. and C. N. Roberts (2004). Late Quaternary hydrologic changes in the arid and semiarid belt of northern Africa. The Hadley circulation: present, past and future, Springer**:** 313-345.

Ghosh, P., et al. (2006). "13C–18O bonds in carbonate minerals: a new kind of paleothermometer." Geochimica et Cosmochimica Acta **70**(6): 1439-1456.

Glogowski, S., et al. (2015). "The Eugen Seibold coral mounds offshore western Morocco: oceanographic and bathymetric boundary conditions of a newly discovered cold-water coral province." Geo-Marine Letters **35**(4): 257-269.

Grazzini, C. V. and C. Pierre (1991). "High fertility in the Alboran Sea since the last glacial maximum." Paleoceanography **6**(4): 519-536.

Grousset, F., et al. (1993). "Patterns of ice-rafted detritus in the glacial North Atlantic (40–55° N)." Paleoceanography **8**(2): 175-192.

Hahn, O., et al. (1943). "Geologische Altersbestimmungen mit der strontiummethode." Chem. Zeitung **67**: 55-56.

Hanz, U., et al. (2019). "Environmental factors influencing cold-water coral ecosystems in the oxygen minimum zones on the Angolan and Namibian margins." Biogeosciences Discussions: 1-37.

Hathorne, E. C., et al. (2013). "Lithium in the aragonite skeletons of massivePoritescorals: A new tool to reconstruct tropical sea surface temperatures." Paleoceanography **28**(1): 143-152.

Hayes, A., et al. (2005). "Glacial Mediterranean sea surface temperatures based on planktonic foraminiferal assemblages." Quaternary Science Reviews **24**(7-9): 999-1016.

Hays, J. D., et al. (1976). "Variations in the Earth's orbit: pacemaker of the ice ages." Science **194**(4270): 1121-1132.

Hebbeln, D. (2019). Highly variable submarine landscapes in the Alborán Sea created by cold-water corals. Mediterranean Cold-water Corals: Past, Present and Future. Orejas C and Jiménez C, Springer Series. **Coral Reefs of the World**.

Hebbeln, D., et al. (2019). "Thousands of cold-water coral mounds along the Moroccan Atlantic continental margin: Distribution and morphometry." Marine Geology **411**: 51-61.

Hebbeln, D., et al. (2019). Key Environmental Drivers for Cold-water Coral Growth. ICP 13. Sydney.

Hebbeln, D., et al. (2016). "Good neighbours shaped by vigorous currents: Cold-water coral mounds and contourites in the North Atlantic." Marine Geology **378**: 171-185.

Hebbeln, D., et al. (2009). "Report and preliminary results of RV Poseidon cruise POS 385 “Cold-Water corals of the Alboran Sea (Western Mediterranean Sea)”." Berichte aus dem Fachbereich der Geowissenschaften der Universität Bremen **273**: 1-79.

Hebbeln, D., et al. (2015). "MoccoMeBo Climate-driven development of Moroccan cold-water coral mounds revealed by MeBo-drilling: Atlantic vs. Mediterranean settings." MARIA S. MERIAN-Berichte **MSM36**: 47.

Hebbeln, D., Wienberg, C., Bender, M., Bergmann, F., Dehning, K., Dullo, W.-C., Eichst¨adter,, et al. (2016). "ANNA: Cold-Water Coral Ecosystems off Angola and Namibia." Cruisereport.

Heburn, G. W. and P. E. La Violette (1990). "Variations in the structure of the anticyclonic gyres found in the Alboran Sea." Journal of Geophysical Research: Oceans **95**(C2): 1599-1613.

Heinrich, H. (1988). "Origin and Consequences of Cyclic Ice Rafting in the Northeast Atlantic Ocean During the Past 130,000 Years." Quaternary Research **29**(02): 142-152.

Hemsing, F. (2017). "Cold-Water Corals as Archives for Ocean Dynamics, Environmental Conditions and Glacial Reef Accumulation." PhD thesis - Heidelberg University.

Henderson, G. M. (2002). "New oceanic proxies for paleoclimate." Earth and Planetary Science Letters **203**(1): 1-13.

Henderson, G. M. (2002). "Seawater (234 U/ 238 U) during the last 800 thousand years." Earth and Planetary Science Letters **199**(1-2): 97-110.

Henderson, G. M., et al. (2006). "Control on (234U/238U) in lake water: A study in the Dry Valleys of Antarctica." Chemical Geology **226**(3-4): 298-308.

Henriet, J. P., et al. (1998). "Gas hydrate crystals may help build reefs." Nature **391**(6668): 648-649.

Henriques, A. F. D. B. (2014). Cold-water coral communities in the Azores: Diversity, Habitat and Conservation. PhD thesis - Universidade dos Acores.

Hernández-Molina, F. J., et al. (2014). "Contourite processes associated with the Mediterranean Outflow Water after its exit from the Strait of Gibraltar: Global and conceptual implications." Geology **42**(3): 227-230.

Hernández-Molina, F. J., et al. (2006). "The contourite depositional system of the Gulf of Cádiz: A sedimentary model related to the bottom current activity of the Mediterranean outflow water and its interaction with the continental margin." Deep Sea Research Part II: Topical Studies in Oceanography **53**(11-13): 1420-1463.

Hillaire-Marcel, C. and A. De Vernal (2007). Proxies in Late Cenozoic Paleoceanography, Elsevier.

Hua, Q., et al. (2001). "Progress in radiocarbon target preparation at the ANTARES AMS Centre." Radiocarbon **43**(2A): 275-282.

Hubbard, G. D. and C. G. Wilder (1930). "Validity of the Indicators of Ancient Climates." Bulletin of the Geological Society of America **41**(2): 275-292.

Huvenne, V. A. I., et al. (2009). "Sediment dynamics and palaeo-environmental context at key stages in the Challenger cold-water coral mound formation: Clues from sediment deposits at the mound base." Deep Sea Research Part I: Oceanographic Research Papers **56**(12): 2263-2280.

Inoue, M., et al. (2011). "Effects of seawater pH on growth and skeletal U/Ca ratios of Acropora digitifera coral polyps." Geophysical Research Letters **38**(12).

Ivanovich, M. (1994). "Uranium series disequilibrium: concepts and applications." Radiochimica Acta **64**(2): 81-94.

Ivanovich, M. and R. S. Harmon (1992). "Uranium-series disequilibrium: applications to earth, marine, and environmental sciences. 2."

Jimenez-Espejo, F. J., et al. (2008). "Detrital input, productivity fluctuations, and water mass circulation in the westernmost Mediterranean Sea since the Last Glacial Maximum." Geochemistry, Geophysics, Geosystems **9**(11): n/a-n/a.

Jiménez-Amat, P. and R. Zahn (2015). "Offset timing of climate oscillations during the last two glacial-interglacial transitions connected with large-scale freshwater perturbation." Paleoceanography **30**(6): 768-788.

Kaboth-Bahr, S., et al. (2018). "Monsoonal Forcing of European Ice-Sheet Dynamics During the Late Quaternary." Geophysical Research Letters **45**(14): 7066-7074.

Kaboth, S., et al. (2016). "New insights into upper MOW variability over the last 150kyr from IODP 339 Site U1386 in the Gulf of Cadiz." Marine Geology **377**: 136-145.

Kaboth, S., et al. (2017). "Mediterranean Outflow Water dynamics during the past~ 570 kyr: Regional and global implications." Paleoceanography **32**(6): 634-647.

Kageyama, M., et al. (2006). "Last Glacial Maximum temperatures over the North Atlantic, Europe and western Siberia: a comparison between PMIP models, MARGO sea–surface temperatures and pollen-based reconstructions." Quaternary Science Reviews **25**(17-18): 2082-2102.

Kaminski, M. A., et al. (2002). "Late Glacial to Holocene benthic foraminifera in the Marmara Sea: implications for Black Sea–Mediterranean Sea connections following the last deglaciation." Marine Geology **190**(1-2): 165-202.

Kandiano, E. S., et al. (2012). "The meridional temperature gradient in the eastern North Atlantic during MIS 11 and its link to the ocean–atmosphere system." Palaeogeography, Palaeoclimatology, Palaeoecology **333**: 24-39.

Kano, A., et al. (2007). "Age constraints on the origin and growth history of a deep-water coral mound in the northeast Atlantic drilled during Integrated Ocean Drilling Program Expedition 307." Geology **35**(11).

Keller, N. and N. Os'kina (2008). "Habitat temperature ranges of azooxantellate scleractinian corals in the world ocean." Oceanology **48**(1): 77-84.

Kiriakoulakis, K., et al. (2004). "Organic biogeochemistry of the Darwin Mounds, a deep-water coral ecosystem, of the NE Atlantic." Deep Sea Research Part I: Oceanographic Research Papers **51**(12): 1937-1954.

Konijnendijk, T. Y. M., et al. (2014). "Chronological constraints on Pleistocene sapropel depositions from high-resolution geochemical records of ODP Sites 967 and 968." Newsletters on Stratigraphy **47**(3): 263-282.

Krengel (2016). "Temporal and spatial cold-water coral occurrence in the Alboran Sea and the Gulf of Cádiz during previous glacial-interglacial cycles."

Krijgsman, W., et al. (1999). "Chronology, causes and progression of the Messinian salinity crisis." Nature **400**(6745): 652.

Kronfeld, J. and J. Vogel (1991). "Uranium isotopes in surface waters from southern Africa." Earth and Planetary Science Letters **105**(1-3): 191-195.

Ku, T. L. (1965). "An evaluation of the U234/U238 method as a tool for dating pelagic sediments." Journal of Geophysical Research **70**(14): 3457-3474.

Kuhlemann, J., et al. (2008). "Regional synthesis of Mediterranean atmospheric circulation during the Last Glacial Maximum." Science **321**(5894): 1338-1340.

Laepple, T. and P. Huybers (2013). "Reconciling discrepancies between Uk37 and Mg/Ca reconstructions of Holocene marine temperature variability." Earth and Planetary Science Letters **375**: 418-429.

Larrasoaña, J., et al. (2003). "Three million years of monsoon variability over the northern Sahara." Climate Dynamics **21**(7-8): 689-698.

Lascaratos, A. (1993). "Estimation of deep and intermediate water mass formation rates in the Mediterranean Sea." Deep Sea Research Part II: Topical Studies in Oceanography **40**(6): 1327-1332.

Lausecker, M. (2015). Das Lithium - Magnesium -Verhältnis als Temperaturproxy in Tiefseekorallen - Temperaturkalibration und Temperaturrekonstruktion -. Institute of Environmental Physics, Heidelberg. **Bachelor Thesis**.

Lindberg, B. and J. Mienert (2005). Sedimentological and geochemical environment of the Fugløy Reef off northern Norway. Cold-Water Corals and Ecosystems, Springer**:** 633-650.

Lionello, P., et al. (2004). "The Mediterranean climate: basic issues and perspectives." White Paper on Mediterranean climate variability and predictability, Technical Report: 5-17.

Lisiecki, L. E. and M. E. Raymo (2005). "A Pliocene-Pleistocene stack of 57 globally distributed benthic δ18O records." Paleoceanography **20**(1): n/a-n/a.

Lo Iacono, C., et al. (2014). "The West Melilla cold water coral mounds, Eastern Alboran Sea: Morphological characterization and environmental context." Deep Sea Research Part II: Topical Studies in Oceanography **99**: 316-326.

Lo Iacono, C., et al. (2018). Cold-water carbonate bioconstructions. Submarine Geomorphology, Springer**:** 425-455.

Lohr, J., et al. (2007). "Characterization of a latent virus-like infection of symbiotic zooxanthellae." Appl. Environ. Microbiol. **73**(9): 2976-2981.

Lohrenz, S. E., et al. (1988). "Interrelationships among primary production, chlorophyll, and environmental conditions in frontal regions of the western Mediterranean Sea." Deep Sea Research Part A. Oceanographic Research Papers **35**(5): 793-810.

Lomitschka, M. and A. Mangini (1999). "Precise Th/U-dating of small and heavily coated samples of deep sea corals." Earth and Planetary Science Letters **170**(4): 391-401.

Ludwig, W., et al. (2009). "River discharges of water and nutrients to the Mediterranean and Black Sea: major drivers for ecosystem changes during past and future decades?" Progress in Oceanography **80**(3-4): 199-217.

Lutringer, A., et al. (2005). Paleotemperatures from deep-sea corals: scale effects. Cold-water corals and ecosystems, Springer**:** 1081-1096.

Major, C., et al. (2002). "Constraints on Black Sea outflow to the Sea of Marmara during the last glacial–interglacial transition." Marine Geology **190**(1-2): 19-34.

Malanotte-Rizzoli, P. (2001). Currents systems in the Mediterranean Sea. Encyclopedia of Ocean Sciences (Second Edition)**:** 605-612.

Mangini, A., et al. (2010). "Deep sea corals off Brazil verify a poorly ventilated Southern Pacific Ocean during H2, H1 and the Younger Dryas." Earth and Planetary Science Letters **293**(3-4): 269-276.

Mangini, A., et al. (1998). "Coral provides way to age deep water." Nature **392**(6674): 347-348.

Marriott, C. S., et al. (2004). "Temperature dependence of δ7Li, δ44Ca and Li/Ca during growth of calcium carbonate." Earth and Planetary Science Letters **222**(2): 615-624.

Martrat, B., et al. (2004). "Abrupt temperature changes in the Western Mediterranean over the past 250,000 years." Science **306**(5702): 1762-1765.

Martrat, B., et al. (2007). "Four climate cycles of recurring deep and surface water destabilizations on the Iberian margin." Science **317**(5837): 502-507.

Martrat, B., et al. (2014). "Similarities and dissimilarities between the last two deglaciations and interglaciations in the North Atlantic region." Quaternary Science Reviews **99**: 122-134.

Matos, L., et al. (2015). "Interglacial occurrence of cold-water corals off Cape Lookout (NW Atlantic): first evidence of the Gulf Stream influence." Deep Sea Research Part I: Oceanographic Research Papers **105**: 158-170.

Matos, L., et al. (2017). "Coral mound development at the Campeche cold-water coral province, southern Gulf of Mexico: Implications of Antarctic Intermediate Water increased influence during interglacials." Marine Geology **392**: 53-65.

McCulloch, M., et al. (2010). "Proliferation and demise of deep-sea corals in the Mediterranean during the Younger Dryas." Earth and Planetary Science Letters **298**(1-2): 143-152.

McCulloch, M., et al. (2012). "Resilience of cold-water scleractinian corals to ocean acidification: Boron isotopic systematics of pH and saturation state up-regulation." Geochimica et Cosmochimica Acta **87**: 21-34.

McCulloch, M. T. (1999). "Coral Record of Equatorial Sea-Surface Temperatures During the Penultimate Deglaciation at Huon Peninsula." Science **283**(5399): 202-204.

McManus, J. F., et al. (2004). "Collapse and rapid resumption of Atlantic meridional circulation linked to deglacial climate changes." Nature **428**(6985): 834.

Mienis, F., et al. (2007). "Hydrodynamic controls on cold-water coral growth and carbonate-mound development at the SW and SE Rockall Trough Margin, NE Atlantic Ocean." Deep Sea Research Part I: Oceanographic Research Papers **54**(9): 1655-1674.

Mienis, F., et al. (2006). "Carbonate mound development at the SW Rockall Trough margin based on high resolution TOBI and seismic recording." Marine Geology **233**(1-4): 1-19.

Mikucki, J. A., et al. (2015). "Deep groundwater and potential subsurface habitats beneath an Antarctic dry valley." Nature communications **6**: 6831.

Millot, C. (1985). "Some features of the Algerian Current." Journal of Geophysical Research: Oceans **90**(C4): 7169-7176.

Millot, C. (1987). "Circulation in the Western Mediterranean." Oceanol Acta **10(2)**: 143-149.

Millot, C. (1999). "Circulation in the Western Mediterranean Sea." Journal of Marine Systems **20**(1-4): 423-442.

Millot, C. (2009). "Another description of the Mediterranean Sea outflow." Progress in Oceanography **82**(2): 101-124.

Millot, C. (2013). "Levantine Intermediate Water characteristics: an astounding general misunderstanding!" Scientia Marina **77**(2): 217-232.

Millot, C. (2014). "Heterogeneities of in- and out-flows in the Mediterranean Sea." Progress in Oceanography **120**: 254-278.

Millot, C. and I. Taupier-Letage (2005). Circulation in the Mediterranean Sea. The Mediterranean Sea**:** 29-66.

Millot, C. and I. Taupier-Letage (2005b). "Additional evidence of LIW entrainment across the Algerian subbasin by mesoscale eddies and not by a permanent westward flow." Progress in Oceanography **66**(2-4): 231-250.

Mitsuguchi, T., et al. (1996). "Mg/Ca thermometry in coral skeletons." Science **274**(5289): 961-963.

Montagna, P., et al. (2014). "Li/Mg systematics in scleractinian corals: Calibration of the thermometer." Geochimica et Cosmochimica Acta **132**: 288-310.

Montagna, P., et al. (2007). "The non-tropical coral Cladocora caespitosa as the new climate archive for the Mediterranean: high-resolution (~ weekly) trace element systematics." Quaternary Science Reviews **26**(3-4): 441-462.

Montero-Serrano, J.-C., et al. (2011). "The climate influence on the mid-depth Northeast Atlantic gyres viewed by cold-water corals." Geophysical Research Letters **38**(19): n/a-n/a.

Morán, X. A. G. and M. Estrada (2001). "Short-term variability of photosynthetic parameters and particulate and dissolved primary production in the Alboran Sea (SW Mediterranean)." Marine Ecology Progress Series **212**: 53-67.

Moreno, A., et al. (2005). "Links between marine and atmospheric processes oscillating on a millennial time-scale. A multi-proxy study of the last 50,000yr from the Alboran Sea (Western Mediterranean Sea)." Quaternary Science Reviews **24**(14-15): 1623-1636.

Moreno, A., et al. (2002). "Saharan Dust Transport and High-Latitude Glacial Climatic Variability: The Alboran Sea Record." Quaternary Research **58**(3): 318-328.

Mortensen, P. B., et al. (2001). "Distribution, abundance and size of Lophelia pertusa coral reefs in mid-Norway in relation to seabed characteristics." Journal of the Marine Biological Association of the United Kingdom **81**(4): 581-597.

Murthy, V. R., et al. (1971). "Rb-Sr ages and elemental abundances of K, Rb, Sr, and Ba in samples from the Ocean of Storms." Geochimica et Cosmochimica Acta **35**(11): 1139-1153.

Ollivier, P., et al. (2011). "Major and trace element partition and fluxes in the Rhône River." Chemical Geology **285**(1-4): 15-31.

Orejas, C., et al. (2008). "Growth rates of live Lophelia pertusa and Madrepora oculata from the Mediterranean Sea maintained in aquaria." Coral Reefs **27**(2): 255-255.

Pailler, D. and E. Bard (2002). "High frequency palaeoceanographic changes during the past 140 000 yr recorded by the organic matter in sediments of the Iberian Margin." Palaeogeography, Palaeoclimatology, Palaeoecology **181**(4): 431-452.

Palmer, M. and J. Edmond (1993). "Uranium in river water." Geochimica et Cosmochimica Acta **57**(20): 4947-4955.

Perkins, H., et al. (1990). "The Atlantic inflow in the Western Alboran Sea." Journal of Physical Oceanography **20**(2): 242-263.

Picotti, V., et al. (2014). The geological origins and paleoceanographic history of the Mediterranean Region: Tethys to present. The Mediterranean Sea, Springer**:** 3-10.

Pierre, C. (1999). "The oxygen and carbon isotope distribution in the Mediterranean water masses." Marine Geology **153**(1-4): 41-55.

Pisias, N. G. and T. Moore Jr (1981). "The evolution of Pleistocene climate: a time series approach." Earth and Planetary Science Letters **52**(2): 450-458.

Raddatz, J., et al. (2013). "Stable Sr-isotope, Sr/Ca, Mg/Ca, Li/Ca and Mg/Li ratios in the scleractinian cold-water coral Lophelia pertusa." Chemical Geology **352**: 143-152.

Raddatz, J., et al. (2016). "Environmental constraints on Holocene cold-water coral reef growth off Norway: Insights from a multiproxy approach." Paleoceanography **31**(10): 1350-1367.

Raddatz, J., et al. (2014). "The influence of seawater pH on U / Ca ratios in the scleractinian cold-water coral Lophelia pertusa." Biogeosciences **11**(7): 1863-1871.

Raddatz, J., et al. (2014). "Environmental boundary conditions of cold-water coral mound growth over the last 3 million years in the Porcupine Seabight, Northeast Atlantic." Deep Sea Research Part II: Topical Studies in Oceanography **99**: 227-236.

Raddatz, J., et al. (2011). "Paleoenvironmental reconstruction of Challenger Mound initiation in the Porcupine Seabight, NE Atlantic." Marine Geology **282**(1-2): 79-90.

Reeder, R. J., et al. (2001). "Coprecipitation of uranium (VI) with calcite: XAFS, micro-XAS, and luminescence characterization." Geochimica et Cosmochimica Acta **65**(20): 3491-3503.

Repschläger, J., et al. (2017). "Holocene evolution of the North Atlantic subsurface transport." Climate of the Past **13**(4).

Revel, M., et al. (2010). "100,000 Years of African monsoon variability recorded in sediments of the Nile margin." Quaternary Science Reviews **29**(11-12): 1342-1362.

Roberts, J. M., et al. (2006). "Reefs of the deep: the biology and geology of cold-water coral ecosystems." Science **312**(5773): 543-547.

Roberts, W., Freiwald (2009). "Cold-Water Corals The Biology and Geology of Deep-Sea Coral Habitats."

Robinson, A. R., et al. (2001). Mediterranean Sea Circulation. Encyclopedia of Ocean Sciences**:** 1689-1705.

Robinson, L. F., et al. (2006). "Primary U distribution in scleractinian corals and its implications for U series dating." Geochemistry, Geophysics, Geosystems **7**(5).

Robinson, L. F., et al. (2007). "Deep-sea scleractinian coral age and depth distributions in the northwest Atlantic for the last 225,000 years." Bulletin of Marine Science **81**(3): 371-391.

Robinson, L. F., et al. (2004). "Climatic control of riverine and seawater uranium-isotope ratios." Science **305**(5685): 851-854.

Robinson, S. G., et al. (1995). "Magnetic susceptibility variations in Upper Pleistocene deep-sea sediments of the NE Atlantic: Implications for ice rafting and paleocirculation at the Last Glacial Maximum." Paleoceanography **10**(2): 221-250.

Rodellas, V., et al. (2015). "Submarine groundwater discharge as a major source of nutrients to the Mediterranean Sea." Proceedings of the National Academy of Sciences **112**(13): 3926-3930.

Rogerson, M., et al. (2008). "A dynamic explanation for the origin of the western Mediterranean organic-rich layers." Geochemistry, Geophysics, Geosystems **9**(7): n/a-n/a.

Rogerson, M., et al. (2004). "The azores front since the last glacial maximum." Earth and Planetary Science Letters **222**(3-4): 779-789.

Rogerson, M., et al. (2012). "Paleoceanography of the Atlantic-Mediterranean exchange: Overview and first quantitative assessment of climatic forcing." Reviews of Geophysics **50**(2).

Rohling, E., et al. (2002). "African monsoon variability during the previous interglacial maximum." Earth and Planetary Science Letters **202**(1): 61-75.

Rohling, E., et al. (1998). "Abrupt cold spells in the northwest Mediterranean." Paleoceanography **13**(4): 316-322.

Rohling, E. J., et al. (2014). "Sea-level and deep-sea-temperature variability over the past 5.3 million years." Nature **508**(7497): 477-482.

Rohling, E. J., et al. (2015). "Mediterranean climate and oceanography, and the periodic development of anoxic events (sapropels)." Earth-Science Reviews **143**: 62-97.

Rossignol-Strick, M. (1985). "Mediterranean Quaternary sapropels, an immediate response of the African monsoon to variation of insolation." Palaeogeography, Palaeoclimatology, Palaeoecology **49**(3-4): 237-263.

Roveri, M., et al. (2014). "The Messinian Salinity Crisis: Past and future of a great challenge for marine sciences." Marine Geology **352**: 25-58.

Ruddiman, W. F. and A. McIntyre (1981). "The North Atlantic Ocean during the last deglaciation." Palaeogeography, Palaeoclimatology, Palaeoecology **35**: 145-214.

Rüggeberg, A., et al. (2005). "Environmental changes and growth history of a cold-water carbonate mound (Propeller Mound, Porcupine Seabight)." International Journal of Earth Sciences **96**(1): 57-72.

Rüggeberg, A., et al. (2007). "Environmental changes and growth history of a cold-water carbonate mound (Propeller Mound, Porcupine Seabight)." International Journal of Earth Sciences **96**(1): 57-72.

Rüggeberg, A., et al. (2008). "Stable strontium isotopes (δ88/86Sr) in cold-water corals — A new proxy for reconstruction of intermediate ocean water temperatures." Earth and Planetary Science Letters **269**(3-4): 570-575.

Rüggeberg, A., et al. (2016). "Paleoseawater density reconstruction and its implication for cold-water coral carbonate mounds in the northeast Atlantic through time." Paleoceanography **31**(3): 365-379.

Russell, A. D., et al. (1994). "Uranium in foraminiferal calcite as a recorder of seawater uranium concentrations." Geochimica et Cosmochimica Acta **58**(2): 671-681.

Saenger, C., et al. (2012). "Carbonate clumped isotope variability in shallow water corals: Temperature dependence and growth-related vital effects." Geochimica et Cosmochimica Acta **99**: 224-242.

Sánchez Goñi, M., et al. (2005). "Increasing vegetation and climate gradient in Western Europe over the Last Glacial Inception (122–110 ka): data-model comparison." Earth and Planetary Science Letters **231**(1-2): 111-130.

Sanyal, A., et al. (1995). "Evidence for a Higher Ph in the Glacial Ocean from Boron Isotopes in Foraminifera." Nature **373**(6511): 234-236.

Sarhan, T. (2000). "Upwelling mechanisms in the northwestern Alboran Sea." Journal of Marine Systems **23**(4): 317-331.

Schleinkofer, N., et al. (2019). "Environmental and biological controls on Na/Ca ratios in scleractinian cold-water corals." Biogeosciences **16**(18): 3565-3582.

Schlitzer, R. (2018). Ocean data view. odv.awi.de.

Schott, W. (1938). "Stratigraphie rezenter Tiefseesedimente auf Grund der Foraminiferenfauna." Geologische Rundschau **29**(3): 330-333.

Schröder-Ritzrau, A., et al. (2005). U/Th-dating of deep-water corals from the eastern North Atlantic and the western Mediterranean Sea. Cold-water corals and ecosystems, Springer**:** 157-172.

Schröder-Ritzrau, A., et al. (2003). "Deep-sea corals evidence periodic reduced ventilation in the North Atlantic during the LGM/Holocene transition." Earth and Planetary Science Letters **216**(3): 399-410.

Shaltout, M. and A. Omstedt (2014). "Recent sea surface temperature trends and future scenarios for the Mediterranean Sea." Oceanologia **56**(3): 411-443.

Shen, G. T. and R. B. Dunbar (1995). "Environmental controls on uranium in reef corals." Geochimica et Cosmochimica Acta **59**(10): 2009-2024.

Sherwood, O. A. and M. J. Risk (2007). "Chapter twelve deep-sea corals: New insights to paleoceanography." Developments in marine geology **1**: 491-522.

Sierro, F., et al. (1998). Origin of the youngest western Mediterranean organic-rich layer: productivity or stagnation. 6th International Conference on Paleoceanography.

Sierro, F. J., et al. (2005). "Impact of iceberg melting on Mediterranean thermohaline circulation during Heinrich events." Paleoceanography **20**(2): n/a-n/a.

Simon, D. (2017). Gateway exchange, climatic forcing and circulation of the Mediterranean Sea during the late Miocene: A model perspective, UU Dept. of Earth Sciences.

Sinclair, D. J. (2005). "Correlated trace element “vital effects” in tropical corals: a new geochemical tool for probing biomineralization." Geochimica et Cosmochimica Acta **69**(13): 3265-3284.

Sinclair, D. J., et al. (2006). "A biological origin for climate signals in corals—Trace element “vital effects” are ubiquitous in Scleractinian coral skeletons." Geophysical Research Letters **33**(17).

Singh, A., et al. (2015). "Planktic foraminiferal responses to orbital scale oceanographic changes off the western Iberian margin over the last 900 kyr: Results from IODP site U1391." Global and Planetary Change **135**: 47-56.

Skliris, N. (2014). Past, present and future patterns of the thermohaline circulation and characteristic water masses of the Mediterranean Sea. The Mediterranean Sea, Springer**:** 29-48.

Smith, J. E., et al. (1997). "Rapid climate change in the North Atlantic during the Younger Dryas recorded by deep-sea corals." Nature **386**(6627): 818-820.

Smith, J. E., et al. (2000). "Paleotemperatures from Deep-Sea Corals: Overcoming 'Vital Effects'." Palaios **15**(1).

Smith, J. R., et al. (2004). "Constraints on Pleistocene pluvial climates through stable-isotope analysis of fossil-spring tufas and associated gastropods, Kharga Oasis, Egypt." Palaeogeography, Palaeoclimatology, Palaeoecology **206**(1-2): 157-175.

Snoussi, M., et al. (2002). "Effects of the construction of dams on the water and sediment fluxes of the Moulouya and the Sebou Rivers, Morocco." Regional Environmental Change **3**(1-3): 5-12.

Soto-Navarro, J., et al. (2010). "Estimation of the Atlantic inflow through the Strait of Gibraltar from climatological and in situ data." Journal of Geophysical Research: Oceans **115**(C10).

Soulet, G., et al. (2010). "Glacial hydrologic conditions in the Black Sea reconstructed using geochemical pore water profiles." Earth and Planetary Science Letters **296**(1-2): 57-66.

Soulet, G., et al. (2011). "Black Sea “Lake” reservoir age evolution since the Last Glacial—hydrologic and climatic implications." Earth and Planetary Science Letters **308**(1-2): 245-258.

Sparnocchia, S., et al. (1999). "Dynamics and mixing of the Eastern Mediterranean outflow in the Tyrrhenian basin." Journal of Marine Systems **20**(1-4): 301-317.

Squires, D. F. (1964). "Fossil coral thickets in Wairarapa, New Zealand." Journal of Paleontology: 904-915.

Stalder, C., et al. (2018). "Large-scale paleoceanographic variations in the western Mediterranean Sea during the last 34,000 years: From enhanced cold-water coral growth to declining mounds." Marine Micropaleontology **143**: 46-62.

Stalder, C., et al. (2015). "Microfossils, a Key to Unravel Cold-Water Carbonate Mound Evolution through Time: Evidence from the Eastern Alboran Sea." PLoS One **10**(10): e0140223.

Stanley, G. D. and S. D. Cairns (1988). "Constructional azooxanthellate coral communities: an overview with implications for the fossil record."

Stuut, J.-B., et al. (2009). "Aeolian dust in Europe: African sources and European deposits." Quaternary International **198**(1-2): 234-245.

Taviani, M., et al. (2016). "Reprint of'On and off the beaten track: Megafaunal sessile life and Adriatic cascading processes'." Marine Geology **375**: 146-160.

Taviani, M., et al. (2005). "First geo-marine survey of living cold-water Lophelia reefs in the Ionian Sea (Mediterranean basin)." Facies **50**(3-4): 409-417.

Terhzaz, L., et al. (2018). "Carbonate mounds of the Moroccan Mediterranean margin: Facies and environmental controls." Comptes Rendus Geoscience **350**(5): 212-221.

Theocharis, A., et al. (1999). "Climatic changes in the Aegean Sea influence the Eastern Mediterranean thermohaline circulation (1986–1997)." Geophysical Research Letters **26**(11): 1617-1620.

Thompson, W. G., et al. (2011). "Sea-level oscillations during the last interglacial highstand recorded by Bahamas corals." Nature Geoscience **4**(10): 684.

Thornalley, D. J., et al. (2009). "Holocene oscillations in temperature and salinity of the surface subpolar North Atlantic." Nature **457**(7230): 711.

Tintore, J., et al. (1988). "A Study of an Intense Density Front in the Eastern Alboran Sea: The Almeria–Oran Front." Journal of Physical Oceanography **18**(10): 1384-1397.

Titschack, J., et al. (2015). "Aggradation and carbonate accumulation of Holocene Norwegian cold-water coral reefs." Sedimentology **62**(7): 1873-1898.

Tjallingii, R., et al. (2008). "Coherent high-and low-latitude control of the northwest African hydrological balance." Nature Geoscience **1**(10): 670.

Toucanne, S., et al. (2015). "Tracking rainfall in the northern Mediterranean borderlands during sapropel deposition." Quaternary Science Reviews **129**: 178-195.

Toucanne, S., et al. (2012). "A 130,000-year record of Levantine Intermediate Water flow variability in the Corsica Trough, western Mediterranean Sea." Quaternary Science Reviews **33**: 55-73.

Toucanne, S., et al. (2010). "The first estimation of Fleuve Manche palaeoriver discharge during the last deglaciation: Evidence for Fennoscandian ice sheet meltwater flow in the English Channel ca 20–18 ka ago." Earth and Planetary Science Letters **290**(3-4): 459-473.

Tzedakis, P. (2005). "Towards an understanding of the response of southern European vegetation to orbital and suborbital climate variability." Quaternary Science Reviews **24**(14-15): 1585-1599.

Tzedakis, P., et al. (2004). "The duration of forest stages in southern Europe and interglacial climate variability." Science **306**(5705): 2231-2235.

van de Flierdt, T., et al. (2010). "Deep-sea coral aragonite as a recorder for the neodymium isotopic composition of seawater." Geochimica et Cosmochimica Acta **74**(21): 6014-6032.

Van Engeland, T., et al. (2019). "Cabled ocean observatory data reveal food supply mechanisms to a cold-water coral reef." Progress in Oceanography **172**: 51-64.

Van Rooij, D., et al. (2013). EUROFLEETS Cruise Summary Report. The Mediterranean-Atlantic Gateway Code: The Late Pleistocene Carbonate Mound Record.

van Weering, T. C. E., et al. (2003). "Structure and development of giant carbonate mounds at the SW and SE Rockall Trough margins, NE Atlantic Ocean." Marine Geology **198**(1-2): 67-81.

Victorero, L., et al. (2016). "Reconstruction of the formation history of the Darwin Mounds, N Rockall Trough: How the dynamics of a sandy contourite affected cold-water coral growth." Marine Geology **378**: 186-195.

Vidal, L., et al. (1997). "Evidence for changes in the North Atlantic Deep Water linked to meltwater surges during the Heinrich events." Earth and Planetary Science Letters **146**(1-2): 13-27.

Viúdez, Á. and J. Tintoré (1995). "Time and space variability in the eastern Alboran Sea from March to May 1990." Journal of Geophysical Research: Oceans **100**(C5): 8571-8586.

Voelker, A., et al. (2006). "Mediterranean outflow strengthening during northern hemisphere coolings: A salt source for the glacial Atlantic?" Earth and Planetary Science Letters **245**(1-2): 39-55.

Voelker, A. H., et al. (2010). "Variations in mid-latitude North Atlantic surface water properties during the mid-Brunhes (MIS 9–14) and their implications for the thermohaline circulation."

Vogler, S., et al. (1998). "230Th in the eastern north atlantic: the importance of water mass ventilation in the balance of230Th." Earth and Planetary Science Letters **156**(1-2): 61-74.

Volkov, D. L. and L. L. Fu (2011). "Interannual variability of the Azores Current strength and eddy energy in relation to atmospheric forcing." Journal of Geophysical Research: Oceans **116**(C11).

Wang, H., et al. (2019). "Cold-water coral mounds in the southern Alboran Sea (western Mediterranean Sea): Internal waves as an important driver for mound formation since the last deglaciation." Marine Geology **412**: 1-18.

Weaver, A. J., et al. (2003). "Meltwater pulse 1A from Antarctica as a trigger of the Bølling-Allerød warm interval." Science **299**(5613): 1709-1713.

Weber, J. N. (1973). "Deep-sea ahermatypic scleractinian corals: isotopic composition of the skeleton." Deep Sea Research and Oceanographic Abstracts **20**(10): 901-909.

Wefer, G. (1999). Use of Proxies in Paleoceanography: Examples from the South Atlantic; with 43 Tables, Springer Science & Business Media.

Wefer, G. and T. Freudentahl (2016). "MeBo200–Entwicklung und Bau eines ferngesteuerten Bohrgerätes für Kernbohrungen am Meeresboden bis 200 m Bohrteufe, Schlussbericht." Berichte, MARUM–Zentrum für Marine Umweltwissenschaften, Fachbereich Geowissenschaften, Universität Bremen(308): 9.

Wefing, A.-M., et al. (2017). "High precision U-series dating of scleractinian cold-water corals using an automated chromatographic U and Th extraction." Chemical Geology **475**: 140-148.

Wefing, A. M. (2016). "Fully Automated Chromatographic Extraction of Th and U: Performance of the prepFAST-MC and its Application to Cold-Water Corals from the Angolan Margin." Master thesis - Heidelberg University: 95.

Wheeler, A., et al. (2007). "Morphology and environment of cold-water coral carbonate mounds on the NW European margin." International Journal of Earth Sciences **96**(1): 37-56.

White, M. (2007). "Benthic dynamics at the carbonate mound regions of the Porcupine Sea Bight continental margin." International Journal of Earth Sciences **96**(1): 1-9.

White, M. and B. Dorschel (2010). "The importance of the permanent thermocline to the cold water coral carbonate mound distribution in the NE Atlantic." Earth and Planetary Science Letters **296**(3-4): 395-402.

White, M., et al. (2005). Deep-water coral development as a function of hydrodynamics and surface productivity around the submarine banks of the Rockall Trough, NE Atlantic. Cold-water corals and ecosystems, Springer**:** 503-514.

Wienberg, C., et al. (2010). "Glacial cold-water coral growth in the Gulf of Cádiz: Implications of increased palaeo-productivity." Earth and Planetary Science Letters **298**(3-4): 405-416.

Wienberg, C., et al. (2009). "Scleractinian cold-water corals in the Gulf of Cádiz—First clues about their spatial and temporal distribution." Deep Sea Research Part I: Oceanographic Research Papers **56**(10): 1873-1893.

Wienberg, C. and J. Titschack (2017). "Framework-forming scleractinian cold-water corals through space and time: a late Quaternary North Atlantic perspective." Marine Animal Forests: The Ecology of Benthic Biodiversity Hotspots: 699-732.

Wienberg, C., et al. (2018). "The giant Mauritanian cold-water coral mound province: Oxygen control on coral mound formation." Quaternary Science Reviews **185**: 135-152.

Willett, S. D., et al. (2006). "Messinian climate change and erosional destruction of the central European Alps." Geology **34**(8): 613-616.

Xu, X., et al. (2007). "A regional modeling study of the entraining Mediterranean outflow." Journal of Geophysical Research: Oceans **112**(C12).

Yanko-Hombach, V. (2003). Noah's Flood" and the Late Quaternary history of the Black Sea and its adjacent basins: A critical overview of the flood hypotheses. 2003 Seattle Annual Meeting.

Ziegler, M., et al. (2010). "The precession phase of the boreal summer monsoon as viewed from the eastern Mediterranean (ODP Site 968)." Quaternary Science Reviews **29**(11-12): 1481-1490.

Acknowledgements

I would like to pay my special regards to the the German Science Foundation (DFG), who founded my project: “Das Meerwasser $^{234}U/^{238}U$-Verhältnis in der Vergangenheit” and this thesis.

I wish to express my sincere appreciation to my supervisor Norbert Frank, who accepted me as his first Earth Science PhD student. Norbert afforded me the possibilities to take part in numerous research cruises, conferences and research stays around the globe. His passion for paleo-oceanography and especially for corals motivated me, ever since I retrieved my first coral-bearing gravity core during MSM36. During my PhD, I got to know a lot of interesting and talented scientists, who I’m glad to call colleagues and friends.

I met Jacek Raddatz, my second supervisor at a coral conference, where we lead heated but interesting discussions. Over the last 4 years, we have met regularly on conferences and research cruises. I wish to show my gratitude to Jacek for helping me improve my thesis and great evenings with fun discussions and entertainment over the past years.

I would like to pay my special regards to Oliver Friedrich for being my second referee on this thesis.

Furthermore, I wish to thank the chief scientists of the cruises MSM36, M144 and M151, for having me aboard and giving me the opportunity to work on numerous gear and diverse scientific topics. Through these cruises and resultant scientific cooperation, I wish to show my gratitude to Dierk Hebbeln, Claudia Wienberg, Jürgen Titschak and André Freiwald for helping me improve my scientific thinking and supporting me during sampling campaigns and other scientific tasks.

Special regards to René Eichstädter and Andrea Schröder-Ritzrau for supporting me during sample processing, sample analysis and the extensive support during my thesis. For helping me to improve my thesis greatly over the last weeks and months, I want to especially thank Stefanie Kaboth-Bahr and André Bahr.

I wish to thank all the people, Post-Docs, PhD students, MSc students and Hiwis from the research group Physics of Environmental Archives. The last years were simply amazing. Especially the darts and table soccer sessions with my office mates and the 5th floor of the IUP. Additionally, I want to thank the Friday-after-work group, for an entertaining start into weekends.

I wish to sincerely thank my roommates from the Werderstraße 6 (Timmi, Leander, Lotti, David, Elias and Jule) and my best friends since the first bachelor semester (Joe, Jakob and Max). Over the last years, I had a lot of fun going on epic fishing trips, playing Skat or Durak for entire evenings, celebrating wicked parties and starting one of the greatest hobbies there is; beekeeping.

Lastly, I want to thank my family. I am truly a lucky person to have family, which can give the moral support of an entire army if necessary. Over the last decade, I could count on my family, even if I was living halfway around the globe or on a ship, somewhere in the middle of an ocean. However, over the last years, I received the greatest, everlasting support from my girlfriend Marleen. Hopefully, our exciting and adventurous journeys on road trips, on mountain tops, in the middle of the ocean, under the sea and down under were only the beginning of many more memorable journeys to come. Thank you so much for the last weeks, months and years.

NATURWISSENSCHAFTLICH-MATHEMATISCHE GESAMTFAKULTÄT

COMBINED FACULTY OF NATURAL SCIENCES AND MATHEMATICS

RUPRECHT-KARLS-
UNIVERSITÄT
HEIDELBERG

Eidesstattliche Versicherung gemäß § 8 der Promotionsordnung für die Naturwissenschaftlich-Mathematische Gesamtfakultät der Universität Heidelberg / Sworn Affidavit according to § 8 of the doctoral degree regulations of the Combined Faculty of Natural Sciences and Mathematics

1. Bei der eingereichten Dissertation zu dem Thema / The thesis I have submitted entitled

   550,000 years of marine climate variability in the western Mediterranean Sea revealed by cold-water corals

   handelt es sich um meine eigenständig erbrachte Leistung / is my own work.

2. Ich habe nur die angegebenen Quellen und Hilfsmittel benutzt und mich keiner unzulässigen Hilfe Dritter bedient. Insbesondere habe ich wörtlich oder sinngemäß aus anderen Werken übernommene Inhalte als solche kenntlich gemacht. / I have only used the sources indicated and have not made unauthorised use of services of a third party. Where the work of others has been quoted or reproduced, the source is always given.

3. Die Arbeit oder Teile davon habe ich ~~wie folgt~~/bislang nicht[1)] an einer Hochschule des In- oder Auslands als Bestandteil einer Prüfungs- oder Qualifikationsleistung vorgelegt. / I have not yet/have already[1)] presented this thesis or parts thereof to a university as part of an examination or degree.

   Titel der Arbeit / Title of the thesis: ……

   Hochschule und Jahr / University and year: ……

   Art der Prüfungs- oder Qualifikationsleistung / Type of examination or degree: ……

4. Die Richtigkeit der vorstehenden Erklärungen bestätige ich. / I confirm that the declarations made above are correct.

5. Die Bedeutung der eidesstattlichen Versicherung und die strafrechtlichen Folgen einer unrichtigen oder unvollständigen eidesstattlichen Versicherung sind mir bekannt. / I am aware of the importance of a sworn affidavit and the criminal prosecution in case of a false or incomplete affidavit.

Ich versichere an Eides statt, dass ich nach bestem Wissen die reine Wahrheit erklärt und nichts verschwiegen habe. / I affirm that the above is the absolute truth to the best of my knowledge and that I have not concealed anything.

Heidelberg, 12.01.2020 ……

Ort und Datum / Place and date

…… Unterschrift / Signature

[1)] Nicht Zutreffendes streichen. Bei Bejahung sind anzugeben: der Titel der andernorts vorgelegten Arbeit, die Hochschule, das Jahr der Vorlage und die Art der Prüfungs- oder Qualifikationsleistung. / Please cross out what is not applicable. If applicable, please provide: the title of the thesis that was presented elsewhere, the name of the university, the year of presentation and the type of examination or degree.

The German text is legally binding.